Alma Mater Studiorum
– Università degli Studi di Bologna –

Dipartimento di Ingegneria Industriale

**Dottorato di Ricerca in Ingegneria Energetica
Nucleare e del Controllo Ambientale**

– Ciclo XXIX –

**Settore Concorsuale di afferenza: 09/C2
Settore Scientifico Disciplinare di afferenza: ING-IND 18**

Development of Core Design
Methods and Tools for Gen-IV
Heavy Liquid Metal Cooled Reactors

Presentata da:

Dott. Ing. Francesco Lodi

Coordinatore Dottorato: **Tutor:**

Chiar.mo Prof. Nicolò Cavina   Prof. Ing. Marco Sumini

Correlatore:

Dott. Ing. Giacomo Grasso

Esame finale anno 2017

ABSTRACT

Development of Core Design Methods and Tools for Gen-IV Heavy Liquid Metal Cooled Reactors

Heavy Liquid Metal Cooled Reactors (HLMCRs) are among the concepts, fostered by the Generation IV International Forum, as potentially able to comply with stringent safety, economical, sustainability, proliferation resistance and physical protection requirements. The increasing interest around these innovative systems has highlighted the lack of tools specifically dedicated to their core design stage. The present PhD thesis, therefore, summarizes the three years effort of, partially, closing the mentioned gap, by rationally defining the role of codes in core design and by creating a development methodology for core design oriented codes (DOCs) and its subsequent application to the most needed design areas. The covered fields are, in particular, the fuel assembly thermal-hydraulics and the fuel pin thermo-mechanics. Regarding the former, following the established methodology, the sub-channel code ANTEO+ has been conceived. Initially restricted to the forced convection regime and subsequently extended to the mixed one, ANTEO+, via a thorough validation campaign, has been demonstrated a reliable tool for design applications. To what pertains to the fuel pin thermo-mechanics, the will to include safety-related considerations at the outset of the pin dimensioning process, has given birth to the safety-informed DOC TEMIDE. The DOC development methodology, followed for ANTEO+, has also been applied to TEMIDE; given the complex interdependence patterns among the numerous phenomena involved in the fuel pin during irradiation, to optimize

....

the code final structure, a sensitivity analysis has been performed, in the anticipated TEMIDE's application domain. The development methodology has also been tested in the verification and validation phases; the latter, due to the low availability of experiments, in the open literature, truly representative of TEMIDE's application domain, has only been a preliminary attempt to test TEMIDE's capabilities in fulfilling the DOC requirements upon which it has been built. In general, the capability of the proposed development methodology for DOCs in delivering tools able to help the core designer in preliminary setting the system configuration has been proven.

ACKNOWLEDGMENTS

The three years time span of my PhD have surely been a roller-coaster of emotions and events, so I really want to start the thesis thanking who has been part of the ride.

It is only natural to start thanking my supervisor, prof. Sumini, who made the beginning of this journey possible, also giving me the opportunity to spend the PhD period in ENEA.

A very special thank you goes also to ing. Grasso of ENEA that, besides being an affectionate friend, has hosted, unconditionally supported and taught me, with genuine passion, the precious art of core design.

In ENEA, I must also thank all the people that made me, since the beginning, feel home: ing. Mattioli for the many fruitful discussions and natural congeniality, dr. Petrovich for being a wonderful office mate, friend and my reference philosopher (hoping ing. Giusti does not take it personally) and also ing. Rocchi, dr. Sarotto, ing. Polidori, ing. Ferrucci, ing. Lombardo, ing. Console Camprini, ing. Pergreffi, ing. Guglielmelli (for a while) a PhD fellow, ing. Cervone, ing. Bandini all of them exceptional workmates and friends. I must thanks also dr. Padoani and ing. Meloni who fully supported my permanence at ENEA. Finally, I want to thank all the people working in the ENEA center in Bologna for their kindness.

Thanks also to all the friendly people I met in my six months abroad period at KTH in Stockholm starting with prof. Wallenius who made it possible in the first place. Thanks to all the people of the Reactor Physics Division including: ing. Messina precious office mate and city guide in the very first period, prof. Olsson, dr. Adorno Lopes, ing. Bortot and the (ex-)PhD fellows ing. Claisse, ing. Johnson, ing. Samuelsson and ing. Toijer for all the

. . . .

The Author
Francesco Lodi

Education

Master degree in Energy and Nuclear Engineering, March 2013

Alma Mater Studiorum University, Bologna, Italy. M.S. degree with honours in Energy and Nuclear Engineering. Advisor: prof. Marco Sumini. Assistant supervisors: Dr. Andrea Alfonsi, Dr. Aaron Epiney, Dr. Cristian Rabiti, Dr. Alexander Stanculescu, Dr. James Wolf. Dissertation: "A PHISICS/RELAP5-3D coupled benchmark of a Pressurized Water Reactor".

Bachelor degree in Energy Engineering, October 2010

Alma Mater Studiorum University, Bologna, Italy. B.S. degree with honours in Energy Engineering. Advisor: prof. Domiziano Mostacci. Assistant supervisors: Dr. Giacomo Grasso. Dissertation: "Elementary cell preliminary design of the Generation IV lead cooled demonstrative reactor ALFRED".

Awards

Rotary Club, May 2013

Guido Paolucci award for the best graduate in the field "School of Engineering and Architecture" of the Alma Mater Studiorum University, Bologna, Italy, for the academic year 2011-2012. Institution: Rotary Club - Bologna section.
....

University of Bologna, June 2012

Award for outstanding acamedic performances in the field "School of Engineering and Architecture" of the Alma Mater Studiorum University, Bologna, Italy, for the academic year 2010-2011. Institution: Alma Mater Studiorum University, Bologna.

Ph.D courses and schools, International conferences and meetings

NuMat, November 2016

NuMat, Nuclear Material Conference. Venue: Montpellier, France. Date: 7-11th November 2016. Poster: "Quantitative guidelines for the development of a fuel pin thermo-mechanic safety-informed design-oriented tool for HLM cooled reactors".

ESNII plus, May 2016

2nd ESNII plus Summer School: "The challenges of the future Gen-IV Reactors: safety issues in support to the design and operation". Venue: Pisa, Italy. Date: 9-11th May 2016. Presenting: "Design oriented tools development supporting the conceptual core design phase of heavy liquid metal cooled reactors".

ESNII plus, March 2016

ESNII plus International Workshop: "Thermophysical Properties of Mixed oxide Fuels for Fast Reactor". Venue: Aix-en-Provence, France. Date: 10-11th March 2016.

ESNII plus, September 2015

EU research project ESNII plus work package 6 - Core Safety, progress meeting. Venue: Cadarache research center, France. Date: 14-15th September 2015. Presenting: "Impact of propagation of uncertainties and tolerances: preliminary thermal-hydraulics analysis".

Summer School, June 2015

8th Summer School on Actinide Science & Applications. Venue: Karlsruhe, Germany. Date: 15-19th June 2015. Organizer: JRC-ITU (old organization

name).

PHYSOR, November 2014

PHYSOR, Reactor Physics Topical Meeting. Venue: Kyoto, Japan. Date: 28th September - 3rd October 2014. Oral: "PHISICS improvements and comparative study with ERANOS 2.2 on the Gen-IV lead cooled fast reactor concept, ALFRED".

Summer School, May 2014

23rd Summer School on Parallel Computing. Venue: Bologna, Italy. Date: 19-30th May 2014. Organizer: CINECA.

Publications

2017

M. Sarotto, G. Grasso, **F. Lodi**, G. Bandini, M. Sumini. Impact of an accidental control rod withdrawal on the ALFRED core: tridimensional neutronic and thermal-hydraulic analyses", In 3rd *International Conference on Fast Reactors and Related Fuel Cycles: Next Generation Nuclear Systems for Sustainable Development*, Yekaterinburg, June 26-29th (2017). (Accepted).

N. Garcia-Herranz, P. Romojaro, G. Grasso, **F. Lodi**, F. Alvarez-Velarde, D. Lopez. Impact of nuclear data uncertainties on the reactivity coefficients of ALFRED. In 3rd *International Conference on Fast Reactors and Related Fuel Cycles: Next Generation Nuclear Systems for Sustainable Development*, Yekaterinburg, June 26-29th (2017). (Accepted).

G. Grasso, G. Bandini, **F. Lodi**, L. Cinotti. The core of the LFR-AS-200: robustness for safety. In 3rd *International Conference on Fast Reactors and Related Fuel Cycles: Next Generation Nuclear Systems for Sustainable Development*, Yekaterinburg, June 26-29th (2017). (Accepted).

F. Lodi, G. Grasso, D. Mattioli. Evaluation of data and model uncertainties and their effect on the fuel assembly temperature field of the ALFRED Lead-cooled Fast Reactor. In 3rd *International Conference on Fast Reactors and Related Fuel Cycles: Next Generation Nuclear Systems for Sustainable Development*, Yekaterinburg, June 26-29th (2017). (Accepted).

F. Lodi, G. Grasso, M. Sumini. Extension to Heavy Liquid Metal coolants of the validation database of the ANTEO+ sub-channel code. In *3rd International Conference on Fast Reactors and Related Fuel Cycles: Next Generation Nuclear Systems for Sustainable Development*, Yekaterinburg, June 26-29th (2017). (Accepted).

G. Grasso, N. Garcia-Herranz, P. Romojaro, **F. Lodi**, E. Bubelis, G. Bandini, F. Alvarez-Velarde, D. Lopez, E. Corsetti, D. Gugiu. ALFRED core safety parameters and influence of model uncertainties on transients. ESNII plus project, Deliverable D6.1.6-1 (2017).

2016

F. Lodi, G. Grasso, D. Mattioli, M. Sumini. ANTEO+: a subchannel code for thermal-hydraulic analysis of liquid metal coolant systems. *Nuclear Engineering and Design*, 301:128–152 (2016).

M. Sarotto, G. Grasso, **F. Lodi**, G. Bandini, M. Sumini. Tridimensional analysis of local perturbations on the core reactivity and thermal-hydraulics of the fuel elements. RdSE, Tech. Rep. ADPFISS-LP2-113 (2016).

F. Lodi, G. Grasso, P. Meloni. LFR-120 Core neutronic verifications. ENEA, Tech. Rep. SICNUC-P000-007 Rev. 1 (2016).

2015

F. Lodi, G. Grasso, C. Rabiti, M. Sumini. PHISICS improvements and comparative study with ERANOS 2.2 on the Gen-IV lead cooled fast reactor concept, ALFRED. In *Proceedings of the International Conference on Physics of Reactors* (PHYSOR 2014), Kyoto, September 28th - October 3rd. Tech. Rep. JAEA-Conf 2014-003 (2015).

F. Lodi, G. Grasso, A. Cammi, S. Lorenzi, C. Petrovich, D. Mattioli, M. Sumini. Characterization of the new ALFRED core configuration. RdSE, Tech. Rep. ADPFISS-LP2-085 (2015).

G. Grasso, **F. Lodi**, C. Petrovich. On the viability of In-Vessel Storage in the new ALFRED configuration. RdSE, Tech. Rep. ADPFISS-LP2-086 (2015).

2014

G. Grasso, **F. Lodi**, C. Petrovich, D. Mattioli, M. Sumini. Ottimizzazione del progetto di nocciolo di ALFRED. RdSE, Tech. Rep. ADPFISS-LP2-050 (2014).

A. Guglielmelli, G. Grasso, **F. Lodi**, R. Lo Frano, D. Mattioli, C. Petrovich, M. Sumini. Studi preliminari di tecniche di monitoraggio del nocciolo di ALFRED. RdSE, Tech. Rep. ADPFISS-LP2-051 (2014).

2013

F. Lodi, C. Rabiti, A. Alfonsi, A. Epiney, M. Sumini. Hot zero and full power validation of PHISICS RELAP-5 coupling. In *Transactions of the American Nuclear Society*, American Nuclear Society, 108, pp. 709 - 713 (2013).

CONTENTS

xxi

LIST OF TABLES

. . . .

Part I

Latin symbols

$\vec{C_A}$	vector containing actual constrained quantities
$\vec{C_T}$	vector containing target constraints
f	function summarizing the design process
$\vec{P_A}$	vector containing actual reactor performances
$\vec{P_T}$	vector containing target reactor performances
x	core configuration including geometry and materials

Part II

Latin symbols

A	empirical constant for the friction factor [-]
A_b	bundle flow area [m^2]
A_i	flow area of the i-th SC [m^2]
A'_1	bare interior SC area [m^2]
A_{r1}	projected wire area in the interior SC [m^2]
A_{wr}	contact surface for thermal exchange between SC and wrapper [m^2]
b	geometry shape factor [-]

....

C_1	dimensionless transverse velocity [-]
C'_{f1}	friction factor constant for a bare rod [-]
C_{fi}	friction factor constant depending on SC geometry [-]
C_h	correction parameter accounting for the annulus approximation in the Nusselt's number [-]
C_i	correction parameter accounting for the annulus approximation in the Nusselt's number [-]
C_s	correction parameter accounting for the annulus approximation in the Nusselt's number [-]
c_s	grid loss coefficient [-]
C_t	correction parameter accounting for the annulus approximation in the Nusselt's number [-]
D	pin diameter [m]
D_{an}	outer diameter of the SC equivalent annulus [m]
D_H	bundle hydraulic diameter [m]
D_{Hi}	hydraulic diameter of the i-th SC [m]
D_{Hij}	mean hydraulic diameter of SCs i and j [m]
D_w	wire wraps diameter [m]
E_i	coupling term of SC i between momentum and energy discretized equation [J/kg]
EEX_i	energy exchange term between SC i and its neighbors [W/m^2]
F_i	momentum term in the discretized equations for SC i [Pa s/m]
f^*	modified friction factor [-]
$f_{1,L}$	laminar friction factor for interior SC [-]
$f_{1,T}$	turbulent friction factor for interior SC [-]
$f_{1,tr}$	transition friction factor for interior SC [-]
f_i	Darcy friction factor with the walls surrounding the i-th SC [-]
G^*	empirical constant for the friction factor [-]
G_i	hydrostatic pressure loss term for SC i [Pa]
g	gravitational acceleration [m/s^2]
Gr	Grashof's number based on the axial temperature rise [-]
Gr_q	Grashof's number based on the applied heat flux [-]
H	lead of the wire wraps [m]
H^*	average effective enthalpy transported by cross flow [J/kg]
h^*	effective enthalpy transported by cross flow [J/kg]
h_i	enthalpy of the i-th SC [J/kg]
J	number of SCs adjacent to i [-]
K	friction factor constant depending on SC geometry [-]
K_{ij}	coefficient accounting for both frictional and form losses for the crossflow between SCs i and j [-]

K_{tot}	bundle average of the SC's K [-]
k_{cool}	coolant thermal conductivity [W/(m K)]
k_p	equivalent internal pin structure thermal conductivity [W/(m K)]
k_w	wrapper thermal conductivity [W/(m K)]
L	bundle length [m]
m	friction factor index depending on the flow regime [-]
$\dot{m}$	FA mass flow rate [kg/s]
$\dot{m}_B$	bundle mass flow rate [kg/s]
$\dot{m}_{BP}$	bypass mass flow rate [kg/s]
$\dot{m}_i$	mass flow rate of the i-th SC [kg/s]
MEX_i	momentum exchange term between SC i and its neighbors [Pa]
N_i	number of SCs of the i-th type [-]
N_{pin}	number of pins in the bundle [-]
N_{sub}	number of SCs [-]
N_{typ}	total number of SCs types [-]
Nu	Nusselt's number [-]
Nu_{wr}	Nusselt's number for thermal exchange between SC and wrapper [-]
P	bundle pin pitch [m]
P_i	pressure of the i-th SC [Pa]
p_{w1}	wire spaced rod wetted perimeter [m]
p'_{w1}	bare rod wetted perimeter [m]
p_{wb}	bundle wetted perimeter [m]
p_{wi}	wetted perimeter of the i-th SC [m]
$p_{w,nw}$	wetted perimeter of the bundle without the duct [m]
Pe	Peclet's number [-]
Pr	Prandtl's number [-]
Pr_T	turbulent Prandtl's number [-]
Q_{out}	bundle outward heat flux [W/m^2]
Q_{tr}	bundle transverse heat flux [W/m^2]
q_{wr}	power deposited in the wrapper [W]
R_t	thermal resistance between the SC and wrapper [K/W]
Re_i	Reynolds number based on the hydraulic diameter of SC i [-]
S_i	fractional area occupied by SCs of type i [-]
s	clearance between fuel rods [m]
s_w	wrapper thickness [m]
St_g	gap Stanton's number [-]
Str	Strouhal's number [-]
T_b	average bundle outlet temperature [K]

T_{bp}	representative bypass temperature [K]
T_{co}	outer cladding temperature [K]
T_i	coupling term of SC i between momentum and energy discretized equation [$\mathrm{W\,s/m^3}$]
T_{in}	FA inlet temperature [K]
T_{sc}	representative SC [K]
U_i	energy term in the discretized equations for SC i [$\mathrm{W\,m/kg}$]
u	speed in the direction x [m/s]
V^*	average effective speed transported by cross flow [m/s]
v^*	effective speed transported by cross flow [m/s]
v_{eff}	effective velocity created by the swirl flow of the wire [m/s]
v_i	coolant axial speed in the i-th SC [m/s]
v_{ij}	mean axial speed in SCs i and j [m/s]
W	maximum pin-duct distance [m]
W_d	wire drag constant [-]
W_{ij}	transverse mass flow rate per unit length between SCs i and j [$\mathrm{kg/(s\,m)}$]
W_{ij}^C	rod thermal conduction analog of W_{ij}^H [$\mathrm{kg/(s\,m)}$]
W_{ij}^H	effective mass exchange rate per unit length between SCs i and j for energy transfer [$\mathrm{kg/(s\,m)}$]
$W_{ij,wire}^H$	mass exchange for energy transfer solely due to the wire [$\mathrm{kg/(s\,m)}$]
W_{ij}^M	effective mass exchange rate per unit length between SCs i and j for momentum transfer [$\mathrm{kg/(s\,m)}$]
W_s	empirical constant of proportionality for the friction factor [-]
x	transverse flow direction [m]
$X_{BP,B}$	bypass-bundle mass flow rate ratio [-]
X_i	flow split parameter of the i-th SC [-]
Y	parameter discriminating forced and mixed convection [-]
Y^*	normalized Y parameter [-]
Y_{mix}	parameter discriminating mixed and natural convection [-]
Y_{mix}^*	normalized Y_{mix} parameter [-]
y	ratio between the external and internal radius of the SC equivalent annulus [-]
z	axial coordinate [m]
$\frac{z_{FP}}{D}$	path length to diameter ratio for mixing purposes [-]

Greek symbols

α	mixing empirical constant [-]

α_{ij}	average thermal diffusivity of SCs i and j [m^2/s]
α'_{ij}	wire wrap phase entering the j-th SC from the i-th one [-]
α_p	convection coefficient between coolant and clad [W/(m^2 K)]
α_{wr}	convection coefficient for thermal exchange between SC and wrapper [W/(m^2 K)]
β	mixing empirical constant [-]
χ_i	linear power discharged to SC i from the surrounding fuel pins [W/m]
χ_p	linear power of the p-th pin [W/m]
δ	effective mixing length [m]
δ_w	distance between wrappers' nodes [m]
Δ_z	axial discretization step [m]
$\Delta P_{form,i}$	form pressure loss per unit length in the i-th SC [Pa]
$\Delta T_{c,norm}$	normalized clad temperature [-]
ΔT_{norm}	normalized SC temperature gain [-]
ΔT_w	temperature difference between two wrapper nodes [K]
ε	grid flow area blockage ratio [-]
$\bar{\varepsilon}$	average absolute error [%]
$\bar{\varepsilon}_{rel}$	average relative error [%]
ϵ_i	convergence threshold relative error for quantity i [-]
ϵ_{ij}	eddy diffusivity of the mixing between SCs i and j [m^2/s]
η	characteristic distance between SCs [m]
γ	empirical constant for the friction factor in the transition region [-]
$\gamma 1$	mixing empirical constant [-]
κ	conduction shape factor [-]
ν	empirical constant for the friction factor in the transition region [-]
Φ	empirical mixing related function [-]
Ψ	empirical mixing related function [-]
Ψ_1	intermittency factor [-]
ρ_i	coolant density in the i-th SC [kg/m^3]
ρ_{ij}	average coolant density of SCs i and j [kg/m^3]
σ'	parameter relating efficiencies in mass and energy transfer [-]
σ	standard deviation [%]
θ	wire wrapping angle [-]
ξ_i	concentrated loss coefficient of the grid spacers [-]

Part III

Latin symbols

A	h_{gas} a model coefficient [-]
$\boldsymbol{A}_i$	link matrix of radial node i [-]
$A_{h_{gas}}$	target accuracy on h_{gas} [-]
A_j	fractional area covered by the j region (either columnar col, equiaxed eq and unrestructured unr) [-]
$\overrightarrow{B}_i$	link vector of radial node i [Pa]
BU_{max}	maximum BU reached by the pellet [at.%]
BU_{JOG}	BU at which JOG formation starts [at.%]
$\boldsymbol{C}$	stress boundary conditions matrix [-]
C_i	integration constant
c_p	specific heat [J/(kg K)]
D	plutonium diffusion coefficient [m^2/s]
$\overrightarrow{D}$	stress boundary conditions vector [Pa]
D_g	fuel grain diameter [m]
D_{g0}	as-fabricated fuel grain diameter [m]
D_{ox}	oxygen diffusion coefficient [m^2/s]
d_i	uncertainty of quantity i [-]
dw_k	axial displacement of slice k [m]
E	Young modulus [Pa]
$e(r)$	plutonium enrichment radial distribution function [-]
$\overline{e}$	average pellet plutonium enrichment [-]
e_c	clad emissivity [-]
e_f	fuel emissivity [-]
e_{MA}	fuel minor actinides enrichment [-]
e_{max}	radial maximum fuel plutonium enrichment [-]
e_{Pu}	fuel plutonium enrichment [-]
F	user defined fraction for plutonium migration model [-]
F_a	axial force [N]
F_{intra}	corrective term for fuel gaseous swelling [-]
F_j	FGR from the j region (either columnar col, equiaxed eq and unrestructured unr) [-]
$f(r)$	power radial distribution function in the pellet [-]
f_{ax}	axial form factor [-]
f_{crack}	fraction of cesium trapped in cracks [-]
$f_{failure}$	failure threshold for the molten area fraction of a pellet [-]

f_{melt} molten area fraction of a pellet [-]

f_{norm} O/M normalization factor [-]

f_j maximum allowable variation with j equal to *creep, geo, bound, res, Pu* or *contact* for creep, geometry, boundary conditions, restructuring, plutonium migration, fuel-clad contact respectively [-]

f_U safety factor for ultimate tensile strength [-]

f_Y safety factor for yield strength [-]

g function relating the clad temperature and its mechanical response [K]

g_c jump distance for the clad [m]

g_f jump distance for the fuel [m]

H Meyer hardness [Pa]

h heat transfer coefficient between the pellet and the environment [W/(m^2 K)]

h_{con} contact contribution of the gap conductance [W/(m^2 K)]

h_{gap} gap conductance [W/(m^2 K)]

h_{gas} conductive contribution of the gap conductance [W/(m^2 K)]

h_{JOG} JOG conductance [W/(m^2 K)]

h_{rad} radiative contribution of the gap conductance [W/(m^2 K)]

$I_{x,y}$ sensitivity coefficient on parameter y of parameter x [-]

K grain growth model parameter [m^n/s]

k_c clad thermal conductivity [W/(m K)]

k_f fuel thermal conductivity [W/(m K)]

k_{gas} plenum gas mixture thermal conductivity [W/(m K)]

k_{JOG} JOG thermal conductivity [W/(m K)]

k_{ox} oxide scale thermal conductivity [W/(m K)]

$\boldsymbol{M}$ fuel pin inertia matrix [W/K]

M_{JOG} JOG molar volume [cm^3/mole]

$\dot{m}$ coolant mass flow rate [kg/s]

mol_{FG} moles of FGs released to the plenum by the whole pin [mole]

$mol_{FGR,k}$ number of FG moles released in the fuel axial slice k [mole]

$mol_{g,k}$ number of FG moles generated in the fuel axial slice k [mole]

$mol_{gCs,k}$ moles of generated cesium in axial slice k [mole]

mol_{He} helium moles in the plenum [mole]

mol_{ret} number of moles retained per unit volume in the fuel matrix [mole/m^3]

mol_{Xe} xenon moles in the plenum [mole]

N number of points of the radial discretization [-]

n	grain growth model parameter [-]
N_{cr}	number of cracks in the pellet [-]
P_{con}	fuel-clad contact pressure [Pa]
P_{con}^*	fuel-clad contact pressure without fuel creep [Pa]
P_{con}^∞	asymptotic fuel-clad contact pressure [Pa]
P_γ	fuel bubbles surface tension [Pa]
P_{gas}	plenum gas mixture pressure [Pa]
P_h	hydrostatic pressure [Pa]
P_i	inner cladding pressure [Pa]
P_o	outer cladding pressure [Pa]
P_p	plenum pressure [Pa]
P_{ss}	steady-state clad inner pressure [Pa]
P_{tr}	ULOF transient clad inner pressure [Pa]
Po	fuel porosity [-]
Po_{ave}	average fuel porosity [-]
$Po_{gas,i}$	bubbles porosity fraction at point i [-]
Po_{max}	radial maximum fuel porosity [-]
Po_{sin}	fuel sintered porosity [-]
$Po_{sin,min}$	minimum allowable sintered porosity in the pellet [-]
$Po_{sin,i}^t$	sintered porosities at point i and time t [-]
Q	characteristic activation energy for grain growth [J]
Q^+	characteristic plutonium heat of transport [J]
Q_{ox}	characteristic heat of transport for oxygen migration [J]
$\boldsymbol{Q_{ss}}$	fuel pin power matrix in steady-state [W]
$\boldsymbol{Q_{tr}}$	fuel pin power matrix in transient conditions [W]
q'	rod linear power [W/m]
q'_{max}	maximum rod linear power [W/m]
q''	thermal flux at the pellet radial periphery [W/m^2]
q'''	radially averaged power density [W/m^3]
q'''_0	power density of the source at time $t = 0$ [W/m^3]
$q'_{melting}$	linear power-to-fuel melting [W/m]
q'_{UTOP}	linear excursion during an UTOP [W/m]
R_c	clad roughness [m]
R_f	fuel roughness [m]
R_j	target uncertainty on the performance parameter j [-]
$R_{j,Mat}$	material properties contribution to the uncertainty [-]
$R_{j,Mod}$	modeling contribution to the uncertainty [-]
$R_{j,Ss}$	steady state uncertainty on the j performance parameter [-]
$R_{j,Tot}$	global uncertainty on the j performance parameter [-]

$R_{j,Tr}$	transient uncertainty on the j performance parameter [-]
$\boldsymbol{R_{ss}}$	fuel pin resistance matrix in steady-state [W/K]
$\boldsymbol{R_{tr}}$	fuel pin resistance matrix in transient conditions [W/K]
r_b	radius inside which significant plutonium redistribution has occurred [m]
r_{col}	columnar region outer boundary [-]
r_{eq}	equiaxed region outer boundary [-]
r_{ci}	clad inner radius [m]
r_{ci0}	as-fabricated clad inner radius [m]
r_{fi}	internal pellet radius [m]
r_{fi0}	as-fabricated fuel inner radius [m]
r_{fo}	external pellet radius [m]
r_{fo0}	as-fabricated fuel outer radius [m]
r_{gap}	gap radius [m]
$r_{i,0}$	input radius of point i [m]
r_{ci}^{mech}	mechanical field clad inner radius [m]
$r_{ci}^{thermal}$	thermal field clad inner radius [m]
s_c	clad thickness [m]
s_{gap}	gap thickness [m]
s_{JOG}	JOG thickness [m]
s_{ox}	oxide scale thickness [m]
s_w	cladding wastage thickness due to fuel corrosion [m]
T	difference between the maximum fuel temperature and the clad outer temperature [K]
$\overrightarrow{T}$	pin temperature vector [K]
T_∞	environment temperature for heat exchange [K]
T_0	initial system temperature [K]
T_c	coolant temperature [K]
T_{co}	clad outer temperature [K]
T_{col}	temperature at r_{col} [K]
T_{eq}	temperature at r_{eq} [K]
T_{fi}	maximum fuel temperature [K]
T_{fo}	fuel pellet surface temperature [K]
T_{in}	FA inlet temperature [K]
$T_{melting}$	fuel melting temperature [K]
T_{norm}	normalized pin temperature [-]
t	time [s]
t_{con}	time at which fuel-clad contact started [s]
t_{grace}	target grace time in an ULOF transient [s]

t_{Pu}	normalized time relative to the plutonium time constant [-]
$t_{rupture}$	time-to-rupture due to creep action [s]
u_i	radial displacement of point i [m]
v	coolant axial speed [m/s]
v_p	pore migration velocity [m/s]
VP	fraction of volatile fission products released from the pellet
$\frac{V}{T}_j$	volume-to-temperature ratio of region j (either p, lp, up, cv and gap for the total plenum, lower plenum, upper plenum, central void and fuel-clad gap) [m^3/K]
X_{Xe}	xenon concentration in the plenum gas mixture [-]
x	average deviation from stoichiometry [-]
x_{max}	maximum radial deviation from stoichiometry [-]
x^l_{ave}	average deviation from stoichiometry calculated at iteration l [-]
x^t_{ave}	average deviation from stoichiometry at time t [-]
x^t_i	deviation from stoichiometry at point i at time t [-]
z	axial coordinate [m]

Greek symbols

α	linear thermal expansion coefficient [1/K]
α_f	fuel thermal diffusivity [m^2/s]
χ	linear power discharged to the coolant [W/m]
$\Delta A_{den,i}$	area decrease due to densification at node i [m^2]
$\Delta \varepsilon^j_{k,i}$	strain in direction i of component k for phenomenon j (see $\varepsilon^j_{k,i}$) during Δt [-]
Δr	radial discretization step [m]
Δt	time discretization step [s]
ΔT_c	radial temperature difference across the clad [K]
ΔT_f	radial temperature difference across the fuel [K]
ΔT_{gap}	radial temperature difference across the gap [K]
ΔT_{ox}	radial temperature difference across the oxide scale [K]
ΔT_{ULOF}	cladding temperature increase during the ULOF [K]
ΔT_{UTOP}	fuel temperature excursion during an UTOP [K]
Δt_j	time step control variable with j equal to *creep*, *geo*, *bound*, *res*, *Pu*, *contact* or *max* for creep, geometry, boundary conditions, restructuring, plutonium migration, fuel-clad contact and maximum allowable, respectively [s]
$\Delta u_{th,c}$	thermal displacement of the clad for the axial slice k [m]
$\Delta u_{th,f}$	thermal displacement of the fuel for the axial slice k [m]

Δz	axial discretization step [m]
$\Delta z_{k,0}$	input axial height of slice k [m]
ε_c	clad strain [-]
$\varepsilon'_{c,i}$	clad modified total strain in direction i [-]
ε_{con}	fictitious fuel-clad contact strain [-]
ε^{et}	effective modified total strain [-]
ε^{ex}	non-elastic component of the strain [-]
ε_f	fuel strain [-]
$\varepsilon_{f,i}^{sw,g,\infty}$	equilibrium gaseous swelling strain [-]
$\varepsilon_{ss}^{sw,g}$	fuel gaseous swelling during steady-state operations [-]
$\varepsilon_{tr}^{sw,g}$	fuel transient volumetric swelling [-]
ε_i	strain in direction i equal to radial r, tangential t and axial a [-]
$\varepsilon_{k,i}^{j}$	strain in direction i of component k (either f for fuel or c for clad), with j equating el, th, sw, (sw,g), (sw,s), hp, $crack$, re, de, cr (cr,th) (cr,ir) and pl for the elastic, thermal, void swelling, gaseous swelling, solid fission products swelling, hot pressing, cracking, relocation, densification, total creep, thermal creep, irradiation creep and plastic component respectively [-]
$\dot{\varepsilon}_{k,i}^{j}$	strain rate in direction i of component k for phenomenon j (see $\varepsilon_{k,i}^{j}$) [1/s]
$\boldsymbol{\varepsilon^{p}}$	pin strain state from the previous time step or gap loop iteration [-]
ε_{eff}^{p}	calculated effective plastic strain [-]
$\varepsilon_{failure}^{p}$	allowable effective plastic strain [-]
ε_i^{tr}	strain in direction i after an ULOF transient [-]
ε^{tot}	sum of the strains in all directions [-]
ε_w	fictitious wastage strain [-]
λ	fuel-clad contact pressure relaxation constant [1/s]
λ_i	cost parameter related to i [-]
ν	Poisson ratio [-]
ρ_{col}	columnar region density [kg/m^3]
ρ_{eq}	equiaxed region density [kg/m^3]
$\rho_f(r)$	fuel density radial distribution function [kg/m^3]
$\overline{\rho_f}$	average pellet density [kg/m^3]
$\rho_{f,0}$	as-fabricated fuel density [kg/m^3]
ρ_{max}	radial maximum fuel density [kg/m^3]
ρ_{unr}	unrestructured region density [kg/m^3]
σ	stress tensor [Pa]
$\overrightarrow{\sigma}_1$	boundary conditions stress vector [Pa]

σ_i	stress in direction i equal to radial r, tangential t and axial a [Pa]
$\vec{\sigma}_{i+1}$	principal stress vector at point $i+1$ [Pa]
σ_{eff}	effective/Von Myses stress [Pa]
$\boldsymbol{\sigma^p}$	pin stress state from the previous time step or gap loop iteration [Pa]
σ_{eff}^{tr}	effective/Von Mises stress after an ULOF transient [Pa]
σ_U	ultimate tensile strength [Pa]
σ_Y	yield strength [Pa]
$\tau_{cr,ir}$	clad irradiation swelling time constant [s]
τ_D	concentration gradient diffusion time constant for radial migration [s]
τ_{ox}	characteristic time for oxygen migration [s]
τ_p	pore migration characteristic time constant [s]
τ_{sw}	clad swelling time constant [s]
τ_T	temperature gradient diffusion time constant for radial migration [s]
τ_{tr}	characteristic transient time after which the initial power has doubled [s]

CHAPTER 1

INTRODUCTION

In this particular historical moment there is a great scrutiny, from the general public and, by reflex, from governmental institutions towards the sustainability of our society; this, however, turns out combined with a prolonged period of recession and slow growth rates of the major economies - especially in Europe - which dictates, as a mandatory requirement, that any sustainable initiative be also economically competitive and with a high social return. Such a considerable challenge, pertains to all the numerous - yet intrinsically linked - facets of the present day society, thus encompassing transportation, life styles, commodity production, waste management and energy generation. The last one, in particular, is at the center of the debate due to the growing concerns around climate change and greenhouse gases emissions, recently culminated in, the so called, Paris agreement at the 21th **C**onference **O**f the **P**arties (COP21) [30].

The strive for sustainability and economic viability must be coupled, in the specific case of the energy sector, with the security and reliability of supply forming what is commonly known as The Energy Trilemma. Currently, the main energy portion comes from fossil fuels: they score high in economy[1] and reliability but very poorly in sustainability producing about $3.2 \cdot 10^{10}$ t of CO_2 per year (in 2014) [2] and thus significantly contributing to the anthropogenic global warming. Taking into account the fact that according to [2], the energy system, to meet the COP21 goals, should reach a Carbon-free footprint before 2100, it is evident that a major transition towards alterna-

---

[1]This is true if the environmental cost is discharged, as presently done, on the consumers and not on the producers.

tive energy sources is mandatory; following The Energy Trilemma such a transition should however not be penalizing for the economy and reliability. Nowadays, the major candidates for such a shift are renewables - meaning mainly solar and wind - and nuclear - meaning nuclear energy from fission - both of them, however, are still facing a number of non-trivial challenges:

- Renewables are seeking economical viability, being still profitable only if local governments carry on subsidizing policies[2]. There are also a number of physical and technical issues to be tackled, like their intermittent nature - reducing the reliability score - and the low energy density, along with the necessary storage technology development which are still hindering the impact of renewables on the energy system.

- Nuclear would be ideal for making up for the base-load character of fossil fuel plants scoring high in reliability but, it struggles to survive in a subsidized energy market and suffers a negative perception, by the public opinion, of its safety performances. There are also sustainability issues concerning the very-long-term management of the radioactive waste it produces.

Regarding nuclear, steps have been done, over the years, trying to alleviate some of the mentioned issues like: increasing sustainability, by means of a more efficient use of natural resources and a reduction of the waste volume and radiotoxicity, and increasing safety, by improving operational procedures and updating emergency systems. Besides the various incidents in the last decades which have, in a way or another, compromised the industry appeal, the key aspect is recognizing that just asymptotically improving the state of the art technology would not be enough to settle all the mentioned issues; instead, a scientific leap must be pursued. This passes through a different approach in conceiving and designing nuclear systems both from a mindset and technological point of view; indeed, quoting Professor Oren Harari *"The electric light did not come from the continuous improvement of candles"*.

The quest for innovating the current scientific approach, that should be the harbinger of technological advancement, has therefore been the founding leitmotiv of the present PhD thesis. The work focuses in particular on the preliminary core design of innovative **F**ast **R**eactors (FR).

---

[2]Some exceptions concerning isolated islands projects are present but are characterized by very peculiar environmental conditions not transferable to global proportions.

. . . .

Part I

The Role of Methods and Tools in Core Design of Fast Reactors

Abstract In Part I of the thesis focus is given in creating and explaining the context around the work. The Generation IV initiative is introduced along with its main philosophy; one of the most promising candidate to fully implement it, the HLMFR, is analyzed, presenting the advantages and weaknesses peculiar to this concept which, in recent years, has gained significant momentum and attracted various industrial stakeholders.

Being the core a critical component for actually achieving the required degrees of sustainability, safety, economics, proliferation resistance and physical protection, its design is of paramount importance; the adopted rationale approach forming the boundary conditions of the work is therefore presented. This gives the possibility of introducing the concept of a design-oriented code along with its importance and salient features. Finally, inside the given context of Generation IV HLMFRs, the main objectives of the thesis are presented and motivated.

. . . .

. . . .

CHAPTER 2

FAST REACTORS AND THE GENERATION IV INITIATIVE

The interest in FRs is as old as the nuclear industry itself thanks to their intrinsic characteristics favoring sustainability. A great number of experimental and prototype reactors have been constructed and operated during the years aiming at proving the viability of concepts and technological readiness. Unfortunately, due to the Three Mile Island incident in 1979 and mostly to the Chernobyl tragedy in 1986, generating an adverse political context, along with a variety of technical problems and difficulties during the prototypes operation, many research programmes were canceled or halted, significantly delaying the FRs deployment. More recently, however, due to growing concerns about global warming, and recognizing the prominent role that nuclear can play in the fight against climate changes, attention to FRs has bloomed again under the framework of the Generation IV endeavor [41]. The **G**eneration IV **I**nternational **F**orum (GIF) listed a number of FRs types of interest including concepts cooled by **L**iquid **M**etals (LMs) like, sodium and **H**eavy **LMs** (HLMs), such as lead and lead-bismuth; the bulk of the operational experience on these systems have, however, been accumulated using sodium. With the rising enthusiasm, at the beginning of the 1990s, in **A**cceleretor-**D**riven **S**ystems (ADSs) but, soon spread to critical systems, a considerable amount of research has been devoted to HLMs. In the very recent years, HLMs cooled concepts have gained an eminent spot in the FRs international panorama, boosted by the engagement of various industrial stakeholders and emerging economies, attracted by their unique safety features.

....

2.1   A brief history of Fast Reactors

To substantially solve the sustainability issues related to the inefficient uti-
lization of uranium natural resources, and to reduce the level, both in quan-
tity and hazard, of the radioactive waste, the role of FRs has been, since the
early days, recognized as crucial.

Clementine, the first fast reactor ever operated, indeed, dates back to
1946 and was located at the Los Alamos National Laboratory. The project
was soon followed, driven by the enthusiasm of Fermi, by the **E**xperimental
fast **B**reeder **R**eactor (EBR-I) which became - on December 20, 1951 - the
first reactor ever to generate electricity. EBR-I operations also proved the
concept of breeding, generally meaning the ability of a reactor to generate
more fissile mass than it consumes to operate. The advancement of breed-
ing capabilities was at the core of the **R**esearch and **D**evelopment (R&D)
programmes spreading worldwide in the upcoming years; under the effort of
integrating breeding with low doubling times, the need for high power den-
sities arose, soon pinpointing sodium-cooled designs as the reference choice.
The R&D attempts were then almost universally (see Section 2.4 for excep-
tions) addressed to this cooling option, culminating in various experimental
reactors among which are: the **D**ounreay **FR** (DFR) in the United Kingdom,
EBR-II in the USA, Rapsodie in France and BOR-60 in Soviet Union.

The knowledge and confidence gained from the experimental activities
lead many countries, in the 70's, to develop prototype reactors, paving the
way for the full deployment of commercial power plants. The most notorious
examples are: the **P**rototype **FR** (PFR) in the United Kingdom, Phénix in
France, BN-350 in USSR and Monju in Japan.

The maintenance and operation of such prototypes were, however, less
smooth than anticipated, with a number of technical and managerial prob-
lems frequently forcing reactors in a shutdown state. Emblematic is the case
of the Monju reactor that the Japanese government has recently decided to
decommission. The reactor reached the first criticality in 1994 but, since
then, has accumulated only about 250 days of operation in 22 years. Such a
poor availability was mainly due to repeated accidents and mismanagements
like sodium leaks, fires and problems with the in-vessel transfer machine.
The French Phénix and Russian BN-350 experiences have also been char-
acterized by a series of events but, overall, after the initial learning curve,
satisfactory availability factors and performances were obtained. Both the
prototypes operated as breeders demonstrating the feasibility of the concept
on a larger scale; moreover, in the BN-350 case, the reactor was used for
water desalinization producing around $1.2 \cdot 10^5$ m^3/day of drinkable water.

. . . .

It was when those prototypes reactors were operating for many years and various commercial-sized plants were starting to be commissioned or constructed that two major nuclear accidents happened: the Three Mile Island partial core melting in 1979 in the USA and mostly the Chernobyl disaster in 1986. The last one was greatly amplified by the absence of a real containment building - especially at the roof of the reactor - and consequent high interaction between the environment and the radioactive inventory of the molten core. Besides the peculiar reasons behind the Chernobyl tragedy, the impact on the public opinion, worldwide, was enormous and led many countries to immediately abandon nuclear - like Italy - or to plan a phase-out - like Sweden. Repercussions on the individual FR projects were also conspicuous, with many of them canceled, halted or undergone to heavy financial cuts and thus significantly slowing down their deployment on a commercial scale. Some notable exceptions are the **C**hinese **E**xperimental **FR** (CEFR) connected to the grid in 2011 and the Russian BN-800 that achieved full power - after a 20 years hiatus in construction - in 2016.

It must be said, that while the motivations just described are surely a vital part of the picture, they are not the only reason for the unsuccessful history of FRs. Other main contributors have been:

- FRs were mostly envisaged as breeders able to produce plutonium from fertile isotopes and consequently contributing to the nuclear system sustainability; from the 50's to the 80's, the urge to increase the stockpiles of fissile material was not felt due to the abundant availability of Uranium at low prices, making the need for the more expensive FRs less pressing.

- The use of sodium as coolant, although seemingly featuring a milder technological effort, at the outset, relative to other LMs, has posed a great number of challenges to designers and operators significantly increasing costs and deployment times.

Recently, the interest around FRs has increased again, mainly due to threat of global warming and the recognized need, by many countries, of sustainable nuclear in an energy mix able to pass the climate challenge. The opportunity of resetting the standards for the design and deployment of a new generation of FRs, along with other reactors concepts, has been grasped by the GIF with the Generation IV endeavor.

....

2.2 The Generation IV initiative: motivations and philosophy

The GIF is a cooperative international effort organized to carry out the R&D needed to establish the feasibility and performance capabilities of the next generation nuclear energy systems. Presently, the GIF signatory countries are 14: Argentina, Brazil, Canada, France, Japan, the Republic of Korea, the Republic of South Africa, the United Kingdom, the United States of America, Switzerland, Euratom, the People's Republic of China, the Russian Federation and Australia. The GIF envisages also for the participation of the **I**nternational **A**tomic **E**nergy **A**gency (IAEA) and the **N**uclear **E**nergy **A**gency of the **O**rganisation for **E**conomic **C**o-operation and **D**evelopment (OECD/NEA) as permanent observers.

The term Generation IV comes from the fact that the civil nuclear energy history is commonly subdivided in generations representing a group of technologies and design, construction, economical and managerial philosophies which have characterized a historical period. As depicted in Figure 2.1, it all started with the early experimental reactors and prototypes - Generation I - followed by their large scale commercial counterparts - Generation II - representing the bulk of the reactors in operation today. The evolution of such designs like the Westinghouse AP1000 and the French **E**uropean **P**ressurized **R**eactor (EPR) along with other Japanese, Korean and Chinese proposals are usually labeled Generation III or III+, representing the majority of reactors presently in construction. The Generation IV should therefore symbolize an evolution from the current state of the art; at the backbone of the GIF philosophy, however, there is the idea that the evolution should transform in a revolution pursuing the scientific leap mentioned in Chapter 1.

The attempt of the GIF to rationalize such a revolution has been categorized in eight technology goals covering four broad areas: sustainability, economics, safety and reliability and proliferation resistance and physical protection. They establish a framework and identify concrete targets for focusing GIF R&D efforts. Following [41], the eight goals are:

Sustainability-1 Generation IV nuclear energy systems will provide sustainable energy generation that meets clean air objectives and provides long-term availability of systems and effective fuel utilization for worldwide energy production.

Sustainability-2 Generation IV nuclear energy systems will minimize and manage their nuclear waste and notably reduce the long-term steward-

....
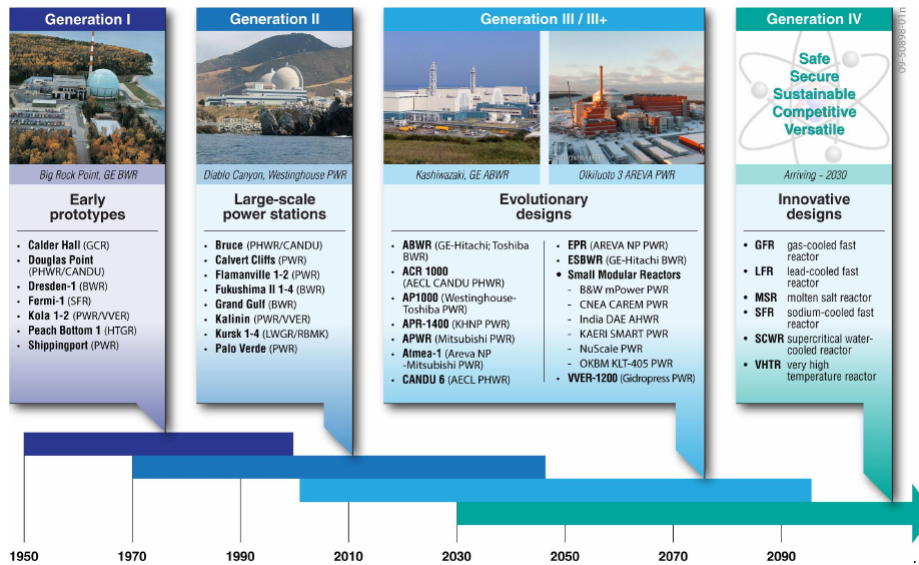
Figure 2.1: The Generation IV context in the nuclear history. Taken from [41].

ship burden, thereby improving protection for the public health and the environment.

Economics-1 Generation IV nuclear energy systems will have a clear life-cycle cost advantage over other energy sources.

Economics-2 Generation IV nuclear energy systems will have a level of financial risk comparable to other energy projects.

Safety and Reliability-1 Generation IV nuclear energy systems operations will excel in safety and reliability.

Safety and Reliability-2 Generation IV nuclear energy systems will have a very low likelihood and degree of reactor core damage.

Safety and Reliability-3 Generation IV nuclear energy systems will eliminate the need for offsite emergency response.

Proliferation Resistance and Physical Protection Generation IV nuclear energy systems will increase the assurance that they are very unattractive and the least desirable route for diversion or theft of weapons-usable materials, and provide increased physical protection against acts of terrorism.

. . . .

With these goals in mind, some 100 experts evaluated 130 reactor concepts before GIF selected six reactor technologies for further research and development. The selected systems are based on a variety of reactor, energy conversion and fuel cycle technologies. Their designs include thermal and fast neutron spectrum cores, closed and open fuel cycles. The reactors range in size from very small to very large. Depending on their respective degree of technical maturity, the first Generation IV systems are expected to be deployed commercially around 2030-2040.

The six selected concepts are:

- the **G**as-cooled **FR** (GFR),

- the **L**ead-cooled **FR** (LFR),

- the **M**olten **S**alt **R**eactor (MSR),

- the **S**uper-**C**ritical **W**ater-cooled **R**eactor (SCWR),

- the **S**odium-cooled **FR** (SFR) and

- the **V**ery **H**igh **T**emperature **R**eactor (VHTR).

The SCWR and the VHTR are thermal spectrum concepts, the GFR, LFR and SFR are fast spectrum while the MSR can be both, even if recent interest is more oriented to the fast spectrum side.

2.3   Heavy liquid metal cooled Fast Reactors

Putting the accent on the FRs concepts, thanks to their higher ranking on the sustainability goals, the GIF fosters, as the most promising candidates, the GFR, LFR, SFR and MSR. LFRs in particular, or more broadly HLMFRs, are, among the FRs concepts, the ones offering the wider design space for substantial innovations so to achieve unprecedented levels of sustainability, safety and economics in a relatively short time frame. Compliance with the GIF goals can be achieved by exploiting the pros and coping with the cons as detailed in the following sub-sections and summarized in Table 2.1

2.3.1   Pros

There are a considerable number of interesting benefits descending from the intrinsic nature of HLMs.

. . . .

Table 2.1: Summary of HLMs pros and cons in relation to the GIF goals.

	Pros	Cons
Sustainability	Excellent neutronic properties	
Economics	Chemical inertness	Elevated melting point[a]
	Great thermal properties	Harsh neutron damage
	Shielding	High density
	Low vapor pressure	Corrosion
	High boiling point	Erosion
		Coolant activation
Safety and Reliability	Chemical inertness	High fissile inventory
	Fast reactor dynamics	Great thermal properties
	High density	High density
	High boiling point	Corrosion
	Shielding	Erosion
	Low vapor pressure	Poisonous
	Excellent neutronic properties	Eleveted melting point[a]
	Great Fission Products retention	
PR&PP[b]	Chemical inertness	High fissile inventory
	High boiling point	Activation products
	Shielding	Poisonous
	Low vapor pressure	

[a] It must still be established if the risk of freezing in HLMFRs is a safety or investment protection concern.
[b] PR&PP stands for **P**roliferation **R**esistance and **P**hysical **P**rotection.

Extremely high boiling point

In virtue of the extremely high boiling point (compared to other coolants), in any accidental scenario, huge safety margins are made available before reaching coolant boiling; this leads to practically exclude, from design, the voiding of the core - that would greatly complicate any accidental scenario - leaving as possible cases, only reductions of lead density. From this directly descends a strong reduction of the positive reactivity potentially inserted into the system, further relieving design constraints.: as a matter of facts, for a given temperature increase, the relative reduction of the coolant density is lower than for other LMs, thereby reducing the physical component of the effect

Linked to the the high boiling point, there is the very low vapor pressure and consequent low volatility, significantly reducing the risk of toxic HLMs aerosols production and consequent pollution of the cover gas plenum.

Chemically inert coolant

HLMs are chemically inert (in practice, i.e.: they do not react violently) with both air and water implying a significant reduction of the potential energy stored in the primary system along with the elimination of fire risks on the nuclear island. The possibility of using air or water as ultimate heat sinks for **D**ecay **H**eat **R**emoval (DHR) systems without safety threats for their operation, drastically improves their reliability and effectiveness. Finally, the chemical inertness allows for the declassification of coolant leakages from a safety point of view (simplifying the requirements for leak monitoring).

High density of the coolant

The high density of HLMs brings about considerable advantages; indeed, in spite of the low relative expansion coefficient (with respect to other fluids), HLMs high density implies large absolute variations of density itself and thus favoring the onset of natural circulation at affordable temperatures, easing plant management.

Great thermal properties

HLMs feature a balanced set of thermal properties: the high thermal capacity implies an enormous reserve for accumulating heat, like a flywheel, thereby accommodating large releases of energy with slow and acceptable changes of the system temperature; the optimal capacity of heat removal (meaning
....

the thermal capacity and conductivity) makes heat exchange effective even in tight bundles or lattices.

Excellent neutronic properties

HLMs are characterized by low absorption cross sections entailing that they do not penalize the system criticality even in case of large coolant volumetric fractions; the extremely low moderation action, on the other hand, allows for a particularly hard neutron spectrum with benefits on:

- breeding capabilities, with a consequent decrease of the reactivity swing along an irradiation cycle and hence lower risks in case of an accidental withdrawal of a control rod; this also means low surplus of reactivity at the beginning of cycle, reducing the inventory of fissile material.

- The burning of **M**inor **A**ctinides (MAs), with low equilibrium concentrations, allowing for more flexibility in waste transmutation; indeed, at fixed performances, the lower negative impact to the total average fraction of delayed neutrons (due to the low contribution associated to MAs) represents a larger operability margin to what concerns such a stringent constraint for reactor control.

- Reduction of the spectrum hardening phenomenon, in case of coolant density reduction, which is the main positive contributor to the associated reactivity effect.

Shielding ability

HLMs are commonly used (especially lead) in radiation protection for gamma-ray shielding; low doses to personnel and the general population are therefore expected.

Great fission products retention capabilities

As proven, up until 800°C, HLMs feature great fission products retention capabilities with scrab factors lower than 10^{-5}; this, further reduces expected source terms in accidental scenario with cladding breaches.

2.3.2   Cons

Some of the safety-related weaknesses of HLMFRs are in common with all the other LM-cooled FR concepts:

. . . .

- for many practical engineering reasons the core is not designed in its most reactive configuration meaning that a reduction of coolant mass inside the core will increase power - positive reactivity feedback effect - and that risks of re-criticality after postulated fuel failure cannot be ruled out;

- the short neutron lifetime combined with a low fraction of delayed neutron and modest feedback coefficients implies faster reactor dynamics and slower counteractions;

- the elevated melting point of LMs, particularly for pure lead, increase the risk of local freezing in stagnation zones and consequent occlusions of the cooling channels or primary circuit segments;

- the hard neutron spectrum implies a severe damaging of the core and nearby structures;

- in-service inspections are complicated by the opaque nature of the coolant.

There are also a number of threats directly stemming from the characteristics of HLMs.

High density of the coolant

Already cited in Section 2.3.1 among the pros, the high density of the coolant brings also some cons: being, higher than the structural materials and the fuel - in the case of oxides - it entails a net positive buoyancy force; all components immersed in the coolant must therefore be anchored. High density means also higher loads on the structures via fluid-structure interactions, this being of special relevance under seismic solicitations.

Corrosive action

The corrosive action of the coolant subtracts mass from the steels in contact with it reducing their actual thickness able to withstand loadings; moreover, the removal action is selective on some alloy elements (e.g. Nickel) compromising the steel micro-structure and its mechanical resistance. Finally, the removed agents pollute the coolant with the possibility of oxide compound formation and subsequent sedimentation with risk of cooling channels occlusion.

. . . .

Erosive action

The erosive action, similarly to the corrosive one, subtracts mass from the steels in contact with flowing coolant reducing their actual thickness able to withstand loadings; moreover, coating or protective layers fabricated or formed on the structures surfaces, in order to protect them from the coolant corrosion, could be gradually removed generating a local unprotected exposition to the HLM. Finally, as for the corrosion, the removed agents pollute the coolant with the possibility of oxide compound formation and subsequent sedimentation with risk of cooling channels plugging.

Activation products

For all the HLMs, but particularly in the case of LBE, coolant activation can be a concern. Bismuth, indeed, can, via neutron capture, generate polonium, a strong alpha emitter, significantly complicating refueling operations and the coolant disposal during the plant decommissioning stage. For pure lead the polonium activity is around four orders of magnitude lower than for LBE drastically reducing this cons.

Poisonous

HLMs are poisonous agents; they do not pose significant threats while in solid or liquid form but, their vapors are toxic representing a possible health hazard. Their management is however common practice in many industrial sectors.

2.3.3 GIF goals achievement

Given all the features described in the previous sections, it is possible to understand the great potential of HLMFRs in successfully achieving the GIF goals mentioned in Section 2.2.

Sustainability

Resource utilization Thanks to the excellent neutronic properties, due to the high atomic number of lead (and bismuth), a core with a hard neutron spectrum even with large coolant fractions can be attained. This allows achieving high conversion ratios - without a blanket - and high fuel burn-ups greatly enhancing resources utilization together with a flexible management of fuel loadings including homogeneously diluted MAs. The latter, in particular, its possible in virtue of the lower impact - with respect to SFRs - of

. . . .

MAs on the major safety coefficients (see Section 2.3.1), like the void effect, the delayed neutron fraction and the Doppler.

To what concerns the coolant, lead is not expensive and abundant and can be considered to be always available, even in the case of deployment of a large number of LFRs. The same cannot be said for LBE, however, due to the limited availability of bismuth.

Waste minimization and management   The combination of the mentioned features with plutonium recycling in a close fuel cycle, makes the residual amount of waste greatly lower in volume and with a much shorter-termed radiotoxicity - affordable for safe management in human times. The opportunity to safely load significant quantities of MAs into the fuel and recycle them is a mandatory requirement for waste minimization adding attractiveness to HLMFRs.

Economics

Life cycle cost   The relatively inert coolant which does not violently react with water or air, also featuring good thermal exchange properties, offers enormous potential for plant design simplifications, thereby overnight capital cost reduction and investment protection such as:

- a compact reactor pool configuration operating at low pressure with a simple design for the internals along with

- the elimination of the degrading, in terms of energy balance, reliability and economics, intermediate heat exchange loop typical of SFRs.

- The possibility of long refueling intervals increasing the availability of the system.

- Potential for replaceable/removable in-vessel components simplifying in-service inspection, to the sake of cost and plant availability.

The cost advantages of the HLMFR are therefore expected to result from relatively low capital cost, short construction duration.

Risk to capital   For small, transportable systems, a limitation to the risk to capital results from the small reactor size. In addition, and with particular emphasis to the moderate- or large-size central station systems, a reduction in the risk to capital results from the potential for removable/replaceable in-vessel components.

. . . .

Safety and Reliability

Operation will excel in safety and reliability   Apart from operating at low pressure, intrinsic safety is guaranteed by the high compatibility existing between the oxide fuel and HLMs and, from the ability of the latter to retain significant quantities of fission products; to this, the notorious gamma radiation shielding abilities and the very high boiling point (higher than many structural materials) must be added. Moreover, the moderate ΔT between core inlet and outlet temperatures, coupled with the high thermal inertia, reduces the thermal stresses during transients and minimizes the creep effects in steels.

Other cross-cutting advantages for safety come from engineering design solutions eliminating or diminishing potential initiator events such as the **S**team **G**enerator **T**ube **R**upture (SGTR). The SGTR could, in principle, generate pressure waves inside the pool, moving a vast mass of lead, damaging reactors internals or leading to the ingress of steam bubbles in the core and thus possible reactivity insertions; proposing steam generator concepts that, by design, avoid the propagation of such a scenario to the whole primary system and notably to the core is therefore and added safety and economic value.

Low likelihood and degree of core damage   In order to have extremely low likelihood and degree of core damage, it is necessary to arrange fuel pins with an elevated pitch-to-diameter ratio and so a high coolant volume fraction in the elementary cell - feasible from the neutronic point of view as described in Section 2.3.1. This allows for reduced pressure drops in the core which, combined with the high lead density, improve the capabilities for heat removal through natural circulation in the primary system and consequently increasing system grace time before operator intervention. The pool configuration makes also possible to design the reactor so that the coolant free-level never drops under a value impairing circulation throughout the system. Last, the high boiling point permits accommodating huge margins, thereby excluding the risk for coolant boiling and all associated (severe) accident scenarios.

No need for off site emergency response   The need for offsite emergency response is greatly reduced in virtue of the extremely low potential energy stored in the primary system (including also any potential exotermic reaction with the fuel air and water) on one hand, and the huge thermal capacity to accommodate such energy before incurring in the release of ra-

. . . .

dioactivity from the core. Even postulating the possibility of core damage, the density similarities between HLMs and the fuel - at least when in oxide form - favor fuel dispersion over compaction; the risk of re-criticality in the case of postulated fuel failure, which could lead to further heating and system damaging and consequent release, is thus strongly decreased. In addition, the ability of lead to trap and retain fission products, in particular iodine and cesium, forming an additional, extremely effective, inherent barrier to release and the fact that a loss of coolant accident will not result in significant pressurization of the containment are features of primary importance in reducing the potential consequences of severe accidents.

Proliferation Resistance and Physical Protection

The core long life, combined with the possibility of using mixed oxide fuels containing MAs, fabricated without the need for specific separation of the fissile largely, reduces the risk of diversion of the spent fuel for nuclear weapons production. For proliferation resistance, nevertheless, international safeguards for each of the major elements of the system fuel cycle remain a necessary independent assurance.

The protection against acts of terrorism is markedly augmented by the chemical compatibility of HLMs with air and water and the atmospheric pressure operations. Being physical protection and safety tightly interlinked, all the technical considerations in Section 2.3.3 are impacting, more or less, also on the ability of the system to withstand acts of terrorism.

2.4   History of HLMFR and major projects

2.4.1   Early days

HLMs were proposed and investigated as coolants for FRs as early as the 1950s (e.g., in the USA). In that historical period, the main driver for FRs development was breeding, making HLMs less attractive than sodium due to the higher power density achievable with this coolant, which resulted in lower doubling times; sodium then quickly became the reference coolant in the USA. However, the Soviet (and then Russian) scientists and industries who have actively pursued lead-cooled reactor technology for more than 50 years have significantly contributed in the development of lead technology [13].

In the early 1950s in the Soviet Union, the principal objective of the R&D activities was the design and construction of nuclear reactors for sub-

....

marine propulsion. The first of these systems, a 70 MW$_{th}$ land prototype reactor, achieved criticality and started full power operation at the Institute of Physics and Power Engineering (IPPE) in 1959. Soon after, in 1963, the first nuclear submarine with an HLM-cooled reactor was put into operation featuring two 73 MW$_{th}$ reactors. From 1971, the new series of nuclear powered submarines termed "Alfa class" was started, characterized by a single, bigger unit of 155 MW$_{th}$ [28]; during their life-time more than 80 reactors-years of experience have been accumulated.

A comprehensive R&D program focusing on HLMs coolant technology and materials was carried out, looking in particular at the chemical control of the HLMs to avoid the possibility of slag formation and consequent plugging (for example by corrosion/erosion products), and to enhance corrosion resistance of internal components made from specially developed steels.

As happened for the major sodium industry a stall hit the research programs after the Chernobyl accident. However, in the 1990s in Russia, there was a renewed interest regarding HLMs as coolants for civilian FRs, giving rise to the lead-cooled BREST-300 concept; a short while after, with the surge of the ADS programs driven by Carlo Rubbia, interest on HLMs bloomed worldwide with a variety of configurations proposed, quickly spreading efforts also to the field of critical reactors.

BREST-300

BREST-300 was designed as a multipurpose reactors simultaneously generating electricity, consuming or producing plutonium, producing radioisotopes for industry and medical applications, and transmuting long-lived fission products and actinides generated during reactor operations. Differently from other concepts, the fuel is envisaged in nitride form - opposed to the more classical oxide - mainly to exploit their higher fissile density, thermal conductivity and margins to fuel melting; being nitride less tested then oxide and posing serious swelling and mechanical problems, R&D efforts are still under way to fully qualify the BREST fuel.

2.4.2   ADS

At the very beginning of the ADS concept history, around the mid-1990s, it was recognized that the unique features of HLMs would make them ideal as both coolants and neutron spallation targets; they soon became the reference for the various ADS projects under development in the USA, Europe, Japan, and the Republic of Korea.

. . . .

At the Korea Atomic Energy Research Institute and Seoul National University in the Republic of Korea, the **HY**brid **P**ower **E**xtraction **R**eactor (HYPER) LBE cooled concept was developed, primarily intended for transmutation of long-lived nuclear wastes. In Japan, at the Japan Atomic Energy Research Institute, another LBE cooled ADS with the thermal power of 800 MW_{th} has been conceived, where 250 kg of MA and some long-lived fission products can be transmuted annually. At SCK•CEN in Belgium, studies in the field of LBE technology have been performed under the framework of the subcritical **M**ulti-purpose **HY**brid **R**esearch **R**eactor for **H**igh-tech **A**pplications (MYRRHA) project. The MYRRHA design coalesced since 2005 with the European project IP-EUROTRANS, which includes also the detailed design of the associated linear proton accelerator and a generic conceptual design of the **E**uropean **F**acility for **I**ndustrial **T**ransmutation (EFIT), with pure lead used as both coolant and spallation target.

2.4.3   Critical systems

Thanks to the various ADS programs, the high versatility, safety and economical potential of HLM coolants became known to the world; soon curiosity, to quantitatively probe the aforementioned promises also for critical systems, started. Several research programs were supported and experimental facilities built and operated in order to define the feasibility domain and the main design criteria along with the selection of the candidates materials. The R&D efforts culminated in various designs among which are: the **C**onstant **A**xial **N**eutron **D**uring the **L**ife of **E**nergy (CANDLE) reactor, the **P**b–Bi-cooled direct-contact **B**oiling **W**ater **FR** (PBWFR) concept and the **P**roliferation-resistant **E**nvironment-friendly **A**ccident-tolerant **C**ontinuable-energy **E**conomical **R**eactor (PEACER) design.

Among the several proposed concepts, two of the HLMFRs community reference systems, expressing different needs for the electricity market and highlighting the design adaptability of HLMs are: the battery concept **S**mall **S**ecure **T**ransportable **A**utonomous **R**eactor (SSTAR) and the large scale plant **E**uropean **L**ead-Cooled **SY**stem (ELSY), both cooled by pure lead.

SSTAR

SSTAR, developed by the Lawrence Livermore National Laboratory (USA), is a small reactor with a nominal thermal power of 45 MW_{th} and generating 20 MW_e of electricity with an efficiency close to 44% obtained with a supercritical CO_2 Brayton cycle; the system features an extremely long refueling
....

interval - around 30 years - and a modular core cooled by lead in natural circulation. SSTAR main purpose is to economically generate electricity, heat and drinkable water [120] even in geopolitical areas with a lowly developed industry; the idea is to assemble the reactor in factories and then shipping it to the desired location.

ELSY

On the other hand, ELSY, developed within the 6th EURATOM Framework Program **E**uropean **U**nion (EU), has, as it main purpose, the base-load generation of electric power. The principal objective of the project was to *"demonstrate the possibility to design a safe lead-cooled fast reactor adopting innovative and simple engineering features"* [8]. The reactor power is rated at 600 MW$_e$ believed to be the most suited for the European market and to reduce reactor vessel dimensions and consequently the contained lead mass and mechanical loadings. Given the lead high density, and the will to reduce pumping power, pressure drops have been limited thanks to innovative design of components like the spiral tubes steam generator. To enhance investment protection all the components have been made removable and the DHR system designed to work in natural circulation.

Present efforts

Thanks to the success of the SSTAR and mainly ELSY projects, that have established a number of simple and innovative design solutions to complicated engineering problems, other R&D efforts have started.

The natural prosecution of the ELSY project focused on the **A**dvanced **L**ead-Cooled FR **E**uropean **D**emonstrator (ALFRED), conceived and developed inside the 7th EURATOM Framework Program project **L**ead-Cooled **E**uropean **A**dvanced **DE**monstrator **R**eactor (LEADER), with the aim of preliminarily designing a LFR demonstrator so to prove the general concept and to support the deployment of successive LFRs by allowing its licensing, procurement and construction in a relatively short time frame [45]. After the end of the LEADER project, the ALFRED design has progressed further under the aegis of the **F**ostering **AL**FRED **CON**struction (FALCON) consortium signed by Italian, Romanian and Czech organizations.

China is also one of the countries pushing more on nuclear energy and in particular on HLMs technology. In 2009, the **C**hinese **A**cademy of **S**ciences (CAS) started a new effort to develop an ADS based on a LBE cooled reactor. In 2011, CAS launched the Strategic Priority Research Program of

....

"the Future Advanced Nuclear Fission Energy-ADS transmutation system". The **I**nstitute of **N**uclear **E**nergy **S**afety **T**echnology (INEST) proposed the concept of the **C**hina **LEA**d-based **R**eactor (CLEAR), which was selected as the reference reactor. The CLEAR reactor development plan includes three stages: a 10 MW$_{th}$ LBE-cooled research reactor (CLEAR-I), a 100 MW$_{th}$ lead-based experimental reactor (CLEAR-II) and a 1000 MW$_{th}$ lead demonstration reactor (CLEAR-III) [143].

Besides public and governmental institutions, the attractiveness of HLM-FRs has engaged various industrial partners - besides the ones involved from the very beginning in international projects. Westinghouse has declared interest in the lead technology and is actively pursuing the design of a demonstrator reactor; Hydromine is also heavily involved in the development of the LFR-AS-200 reactor concept featuring original engineering solutions in many critical components aimed at increasing the power per unit system volume. Worth of mention is also the LeadCold company effort to commercialize a very small reactor named **Sw**E**dish **A**dvanced **LE**ad **R**eactor (SEALER) for electricity generation in remote arctic regions.

CHAPTER 3

A RATIONALE APPROACH TO CORE DESIGN

As seen in Chapter 2, HLMFRs are on the research spotlight in the FRs community thanks to the ability, proven in several projects throughout the years, of delivering systems fully complying with the GIF directives. Of the many plant components whose function is critical in order to unlock the desired levels of sustainability, safety, economics, proliferation resistance and physical protection, the core is surely the most important; all the other components, indeed, must be chiefly evaluated, especially for safety aspects, through their interaction with the core. Its careful and consistent design is therefore of the utmost relevance.

3.1   Core design rationales

Core design is the discipline aiming at determining the main parameters which unequivocally define a reactor configuration providing the desired performances while complying with all the thermal-hydraulic, technological, thermo-mechanical, and economical constraints both in nominal and accidental conditions. Given the very different nature of the constraints and the multidisciplinary essence of the task, core design is principally an art of engineering compromise and harmonization. Using a mathematical analogy, if one defines the "reactors space" as a hyper-space with axes representing the independent core parameters, core design can be visualized as the optimal operating point search in this multi-dimensional diagram: the technological limits define boundaries contracting the viability domain, the parameter inter-dependence laws define hyper-surfaces symbolizing the con-

....

nections between degrees of freedom and constraints, and the goal features provide criteria to guide the choice for the most suitable operating point in the design domain [44].

3.1.1   Core design philosophy

To enlighten the proposed philosophy it could be introduced, in opposition to the Maxwell's demon, a core designer's god; such a god, given all the technological and safety limits along with the energy and economic targets, would be able to exactly translate them in relations among the core geometric, material and physical parameters and to easily retrieve the optimal system configuration. This is, indeed, the essence of a designer task but the step *"to exactly translate them* [constraints and performances] *in relations among the core geometric, material and physical parameters"* is definitely a non-trivial one. On a scale going from a blind trial and error procedure, probing every possible point in the design domain and then selecting the optimum, to the core designer's god approach, it can confidently be stated that the quality of a core designer can be measured on how clearly he is able to link constraints and goals in the resultant core configuration. Such an ability, can originate from experience, from the use of simple physical relations or with the aid of dedicated tools (see Chapter 4) depending on the particular task and system.

In line with the Generation IV philosophy, among the previously mentioned constraints, safety related considerations must also be added to the picture from the outset of the core conceptualization, paving the way for what is called safety-informed design. This means translating safety relevant situations in limits to or relationship among the main core parameters. Practically, this implies achieving safety by a proper combination of materials and design in which the latter comes in aid when the former ends. In the specific case of HLMFRs such a process involves the examination of all lead (or LBE) properties so that all weaknesses are coped with (Section 2.3.2), while all advantages are exploited (Section 2.3.1). The design is then set orienting choices so to take profit of intrinsic features, thus making it more robust and the configuration safety-embedding; finally, engineering provisions are foreseen to complete the protection against threats. This is also in line with the defense in depth philosophy putting prevention first - through the combination of a safety-embedding system and proper safety margins - and then containment and mitigation - via engineering provisions.

The aforementioned approach can, in principle, be applied to any peculiar performance objective deemed of relevance. Sustainability, for example, could be treated exactly as safety, contributing to a core configuration which

. . . .

is sustainability-embedding. To achieve such a goal, fuel cycle considerations must again be translated in core designer language: limits or relationship to or among parameters.

The more evident advantage of the presented approach is the enormous gain in flexibility during the optimization phase; indeed, for a change in any of the core design boundary conditions the previously retrieved relations among parameters could be fully exploited to immediately point out how to arrange the core in the new optimal configuration; on the other hand, the trial and error strategy, would require to examine, all over again, the entire available design space before selecting the new optimum. The latter approach, besides being a less robust time consuming task, goes in the exact opposite direction of the scientific leap mentioned in Chapter 1.

3.1.2 Core design paths

All the logic explained in Section 3.1.1 substantiates in the following general process:

1. technological, safety and sustainability constraints are first considered narrowing the design viability region then,

2. relations among parameters are established and exploited so to make the core configuration safety/sustainability-embedding and finally,

3. protection against any foreseeable threats is achieved via dedicated engineering solutions.

It is not possible to indicate a universal path to put in action this generic recipe but, for HLMFRs, a possible way to proceed could be (see Figure 3.1), after having performed #1:

- guess from experience, similar systems or simple considerations all the necessary input parameters (e.g. shape factors);

- taking into account the limits coming from the thermo-mechanical capabilities of the system, like clad and fuel temperatures or the mechanic resistance of the cladding, the pin radius, gap thickness and pellet dimensions can be designed;

- the elementary cell can then be set-up by including thermal-hydraulic considerations so to guarantee sufficient natural circulation capabilities and limit erosive processes and, finally

. . . .
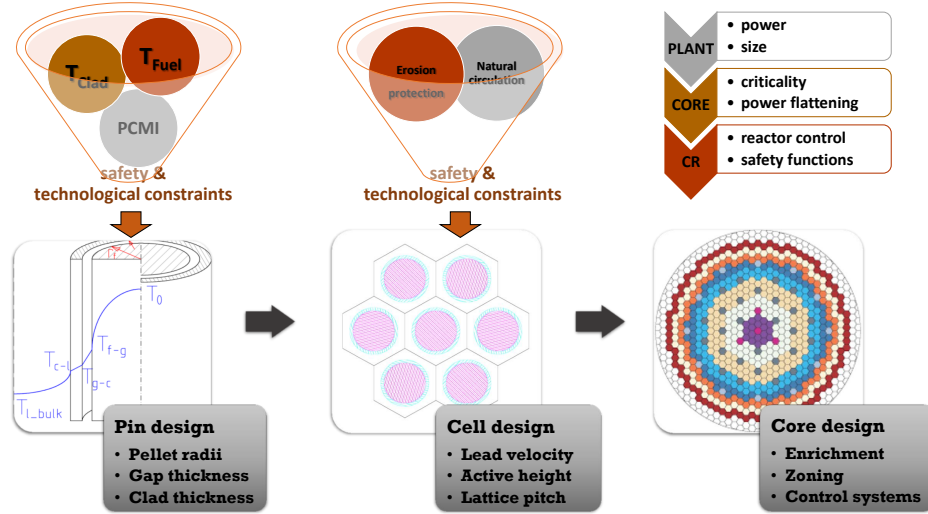
Figure 3.1: Logical scheme of the core design process. PCMI stands for
Pellet-**C**lad **M**echanical **I**nteraction.

- combining the plant rated power, the criticality needs throughout the
  envisaged cycles, the reactivity control requirements and the target
  power shape factors[1], the enrichment and its zoning, along with the
  reactivity control system can be designed.

If the final configuration does not respect any of the constraints or it results
to be not satisfactory optimized, the whole process can be repeated updating
guesses and taking advantage of the parameters relations.

   The presented picture is a simplified one because, in reality, all the con-
straints and elements - the pin, cell and core - are intimately connected mak-
ing the design exercise more cross-cutting then depicted. Moreover, some of
the described steps could be substantially different if the desire to include,
by design, specific aspects emerges; embedding sustainability, indeed, would
modify the core set-up step due to the arising constraints on the fuel compo-
sition and enrichment [44] and consequently, making power a variable rather
than an input (see Section 3.5.3).

   In the following, therefore, a more detailed sketch - yet not complete -
of the various core design steps, encompassing the fuel pin, elementary cell,

---

[1]The shape factors have transformed from guess to a sort of constraint (i.e. a recom-
mendation) because in any coherent design process early assumptions must be respected
- or at least proved to be adequate - in all the subsequent steps.

. . . .
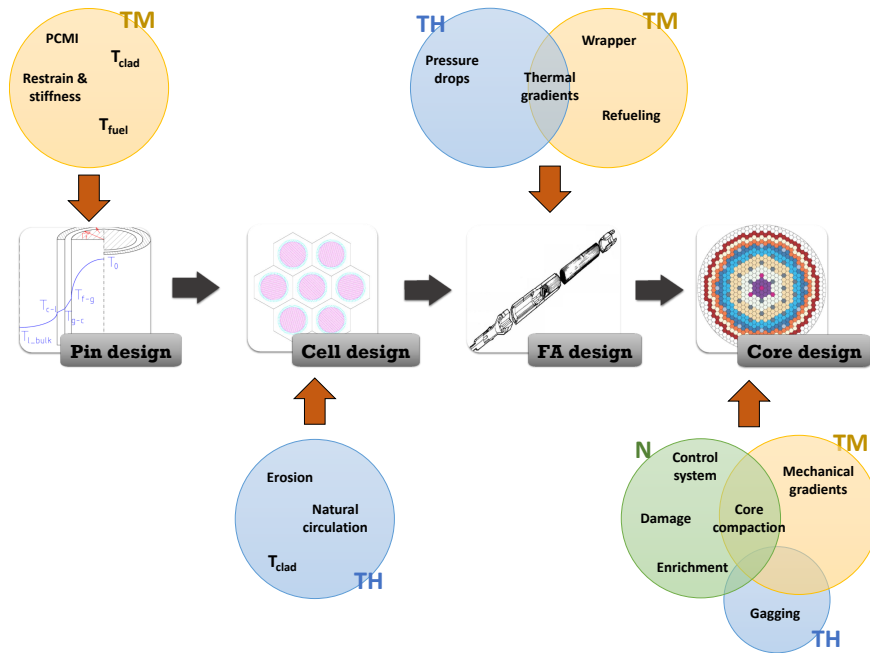
Figure 3.2: A more complete view of the various steps and components of the core design process. TH stands for **T**hermal-**H**ydraulics, TM for **T**hermo-**M**echanics and N for **N**eutronics.

Fuel **A**ssembly (FA) and core dimensioning is presented so to make clearer the impact of the thermal-hydraulics, thermo-mechanics and neutronics fields and to introduce the scope, context and motivations of the present thesis as described in Chapter 5. A graphical synopsis is also proposed in Figure 3.2.

3.2   Fuel Pin

The fuel pin is the most crucial element of the core lattice structure and its dimensioning is mainly driven by thermo-mechanic considerations, even if, interactions with other fields are present due to the inherent cross-cutting nature of core design, as previously discussed. In the following, the main aspects of its design will be analyzed in some detail.

3.2.1   Thermal-hydraulics

The fuel pin design, is mainly linked to the thermal-hydraulic one, by the clad outer radius dimensioning, constrained by corrosion considerations; this

. . . .

and other aspects will be reviewed in Section 3.3.1 under the elementary cell design.

3.2.2 Thermo-mechanics

The pin internal structure is chiefly dictated by thermal and mechanical factors which are, in a way, less dependent on the peculiarities of HLMs and as such, it is set-up similarly to other FRs concepts (e.g. SFR).

From the thermal point of view it must be ensured that the fuel temperature is lower then the melting one, allowing margins for uncertainties, in all nominal and accidental conditions, with particular regard to the **U**nprotected **T**ransient of **O**ver-**P**ower (UTOP); on the other hand, from a mechanical point of view, it must be assured the integrity of the cladding via its ability to withstand both the internal pin pressure, arising from **F**ission **G**as **R**elease (FGR), and PCMIs stemming from the fuel swelling, thermal expansion and cracking.

Another notable consideration applies to the structural stiffness of the fuel pin as a whole, meaning that mechanical provisions against bending must be taken - especially in high load situations such as earthquakes. Possible solutions are, for example, limiting the total height of the pin or via suitable radial constraints. The latter solution must also satisfy a number of requirements:

- it must guarantee adequate lateral restrain without creating significant mechanical interaction with the pin;

- it should prevent or dump flow induced oscillations;

- it should avoid high frequency fretting against the cladding so to prevent both clad failure (major effect) and the eradication of coating or protective layers, fabricated or formed on the surface in order to protect it from coolant corrosion (minor effect).

3.3 Elementary Cell

The elementary cell design is heavily guided by thermal-hydrualics considerations with an important interface with the mechanic field concerning the cladding behavior in both nominal and accidental conditions.

....

3.3.1 Thermal-hydraulics

Apart from the minimum operating temperature which is fixed by the margin to coolant freezing[2], all the upper bounds are actually established by the ability of the steel structures to safely operate in a HLM environment, meaning to limit corrosion processes to acceptable levels. The elementary cell must therefore be sized to guarantee the respect of the clad temperature constraint - allowing for uncertainty margins - and to limit coolant velocity and the consequent erosion dynamics.

Another important, safety related, objective is to assure the onset of natural circulation at affordable temperatures; this is particularly important in the case of an **L**oss **O**f **F**low (LOF) accidents (notably under **U**nprotected conditions - ULOF) in order to avoid excessive cladding temperatures and the risk of a short time creep failure or even melting. To achieve this, low pressure drops through the fuel bundle are necessary; a suitable dimensioning of the elementary cell must therefore be pursued.

3.4 Fuel Assembly

As a collection of fuel pins and with a marked structural nature the FA design is influenced, in equal measure, by both thermal-hydraulics and thermo-mechanics aspects.

3.4.1 Thermal-hydraulics

The main objective during the FA thermal-hydraulic sizing is to guarantee a uniform coolant temperature radial profile and adequate cooling for all the pins in the bundle; this is important, especially, for enclosed FA concepts[3]. The primary objective is to avoid local hot spots, cold bypasses and to reduce thermal gradients which could create unwanted mechanical stresses (see Section 3.4.2).

The pressure drops through the main components of the FA such as spacers, foot and any other relevant area change or narrow paths must also be such that the benefits of a wide elementary cell are not overshadowed by excessive pressure losses in other FA components.

---

[2]Another lower limit could also be the so called LMs embrittlement, a micro-structural phenomenon by which LMs reduce ferritic-martensitic steel ductility at low temperatures, should these steels be used.

[3]The majority of fast reactors designs indeed envisages the use of closed fuel assembly.

. . . .

From the safety point of view, the threat of a flow blockage due to cooling channel plugging via corrosion/erosion products sedimentation, coolant solidification or any foreseeable occlusion agent must be taken into account by means of appropriate instrumentation, a judicious design of the FA foot and a wary positioning of the spacers grids (if present).

3.4.2   Thermo-mechanics

The FA is a complicated system from the thermo-mechanical standpoint, chiefly for the enclosed concepts. Any interaction among fuel pins and between pins and wrapper, due to bowing, swelling and differential thermal expansion, must be avoided or at least limited to acceptable values; moreover, an adequate mechanical stiffness and resistance must be guaranteed, similarly to the fuel pin previously discussed: although - differently from SFRs - the pressure difference between the coolant outside and inside the elements is not the driving parameter for sizing the wrapper thickness, an adequate resistance is to be set for the wrapper to minimize loads-induced deformations of the FA . Of particular mechanical apprehension are the points of contact among adjacent elements, as well as the connections of the FA with the diagrid and the upper core plate (if present).

One more issue concerns the FA handling during refueling operations; the residual mechanical resistance in every moment of its lifetime must allow its movement, implying that it should be able to sustain the maximum expected insertion and withdrawal loads.

3.5   Core

Naturally, the core, being the most crucial element of the entire reactor layout is interested by a sizable number of different requirements encompassing thermal-hydrualics, thermo-mechanic and neutronic. The core is, indeed, the point of contact of all these fields, where all the dimensioning of the previously discussed components comes into play together.

3.5.1   Thermal-hydraulics

The core thermal-hydraulic design is, in a way, similar to the FA one; cold bypasses must be avoided, especially for closed FA, but, at the same time, excessive thermal gradients among opposite faces of the FA ducts prevented. This means assuring a suitable coolant flow outside the FA itself; such a flow

....

must be determined given the bypass - the space between FAs - geometry, established by the thermo-mechanical design (see Section 3.5.2).

If a wrapped FA is used, the possibility of gagging arises giving an extra degree of freedom to the designer for actually leveling thermal gradients at the FA outlet. During the core thermal-hydraulic design, the amount of pressure drops necessary to balance the coolant flow with the FA power must be calculated and a gagging zoning proposed so to achieve a lifetime optimum configuration, while still keeping low fabrication costs.

3.5.2   Thermo-mechanics

The mechanical core design is strongly related to several points of the Section 3.4.2. The FAs arrangement must be such that sufficient clearance is provided between them and along their whole height, so that friction forces during handling phases remains below limiting values even when distortions due to the flux (i.e. creep and mainly swelling) gradients are taken into account; at the same time, as mentioned in Section 3.5.1, excessive clearances must also be avoided not to incur in cold by-passes jeopardizing the thermal efficiency of the system, nor to imply a penalizing reactivity reduction due to the lower fuel volume fraction. The latter is also one of the main sources of positive reactivity insertion, thereby enhancing the risk associated to core compaction events upon external actions (e.g. earthquake). Therefore, in analogy with the pin and FA, also the core must be restrained; such a restraint system should fulfill three functions [139]:

1. provide compaction and structural stiffness to the core within the limits imposed by reactivity insertion considerations (encompassing also long-term irradiation effects and transient conditions),

2. maintain the heads of the assemblies in a position such that their handling grips can be remotely located and engaged by the refueling machine, and

3. provide clearance - and possibly margins for the introduction of measures able to magnify the clearance itself at shutdown - for spent (hence distorted) elements extraction and fresh elements insertion in a distorted lattice, with minimal vertical friction, during refueling conditions.

It would be also much desirable, to have a restrain system that maximizes the insertion of negative reactivity upon structures heat-up and consequent core thermal expansion during transient conditions. Finally, the lower and upper
. . . .

core plates (or diagrids), if present, are to be duly designed in order to provide i) the correct positioning of the elements in the core; ii) the concentrated pressure drops allowing for the assumed by-pass flow rate; iii) a limited - but sufficient - play alleviating the mechanical stresses that would otherwise be implied by the distortion and mutual interaction of the assemblies.

3.5.3   Neutronics

The neutronics design involves the core and the radiation shielding of the nearby structures along with the definition of the control and safety system layouts.

Core

The main purposes of the core neutronic design involve the definition of the fuel enrichment and enrichment zoning which will allow to guarantee the operability of the reactor for the foreseen time span, respecting all the constraints on the maximum burn-up along with requirements on the cladding and fuel temperatures. With operability, it is intended the capability of the core to sustain a chain reaction throughout the whole fuel irradiation cycle.

In the case in which sustainability is a direct constraint, the target of the neutronic design shifts from the enrichment, which is now fixed, to the core dimensions and, sometimes, the power density, which otherwise is driven by economics towards maximization; they must be determined so to guarantee an adequate reserve of reactivity for compensating the expected criticality swing. The power flattening, necessary for enhancing fuel utilization and easing compliance with the various thermal-hydraulic and thermo-mechanic constraints, must be achieved, not via enrichment zoning, but exploiting alternative strategies (e.g. different fuel volume fractions in the core layout) [44].

On the fringes of the core neutronic design, there is the evaluation of the core reactivity coefficients so to allow safety analysis and dynamic studies to be performed. Although HLMFRs, thanks to the huge margins offered by the coolant, usually present a very forgiving behavior in accidental conditions, it could be the case that the optimization of the reactivity coefficients enter the core design process, mainly at the level of neutronics (even if also thermo-mechanics and thermal-hydraulics play important roles).

. . . .

Control system

In designing the control system, the capacity of the latter to properly manage the core reactivity status in normal and off-normal situations must be assured; this means designing a system able to perform a variety of tasks, like:

- control of reactivity in safety related situations assuring redundancy, diversification and independence;

- reactor control, encompassing start-up and normal shutdown, power excursions, refueling and criticality compensation during a cycle;

- the fine reactivity tuning during a cycle.

All the target objectives necessary to fulfill these functions must be met even when uncertainties due to nuclear data or design methods are taken into account.

Structural damage

Besides persuading that the cladding damage remains below acceptable limits, the neutronic design must also ensure the respect of structural damage constraints, deriving from mechanical considerations, on all the internals and notably on those having core supporting functions like the diagrid(s) and the inner vessel. Appropriate shielding must be envisaged to protect the mentioned components or, at least, original engineering solutions have to be adopted.

3.6   Verification phase

Once the system configuration has been unequivocally set-up, it must be verified that the system does comply with the design constraints upon which has been built while achieving the target performances: this is commonly known as the verification phase which is basically the inverse problem of the design one. During the verification the system is tested in all the possible situations of interest to quantify the safety, economic and sustainability performances (i.e. the GIF goals); if any of the constraints is not respected with sufficient margins or space for optimization is available, the design process has to be repeated taking into account the feedback of the verification stage. The procedure just highlighted, is graphically proposed in Figure 3.3

. . . .
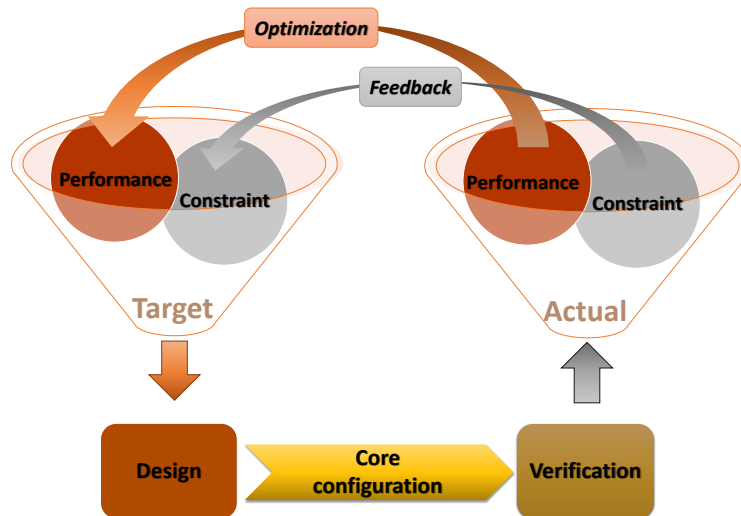
Figure 3.3: Logical scheme of the core design and verification processes.

It is a common practice to perform verification activities just after the various design steps previously outlined; they are known as preliminary verifications. Their objective is test small subsets of the overall design process so to increase confidence, in the designer, about the evolving configuration, avoiding possible criticalities to propagate further in the design.

CHAPTER 4

DESIGN-ORIENTED CODES

From Chapter 3 has positively emerged the importance, during the whole core design process, of clearly linking constraints/performances with the resulting core configuration; such a link could be inferred from experience or from the use of simple physical relations - a sort of a **P**aper and **P**encil (P&P) method. Both of them are valuable and essential tools for walking through a balance and consistent design path reaching a core configuration with an optimal degree of compromise but, they have also peculiar shortcomings:

- experience and engineering judgment can fall short when applied to new and innovative systems where unforeseen issues are a concrete risk;

- the P&P method, by its very nature, is ideal for the early conceptual design stage, when first guesses have to be put forward, or to orient thinking in the right direction for optimization purposes, after the feedback of the verification phase, but it encounters difficulties when more detail is needed and many phenomena come into play together.

The gap left by these methods is therefore the domain of application of a **D**esign-**O**riented **C**ode (DOC) as will be outlined in the following.

4.1 Definition

Due to the similarities between the design and verification phases, it is very easy to confuse them and be tempted with the possibility of using

....
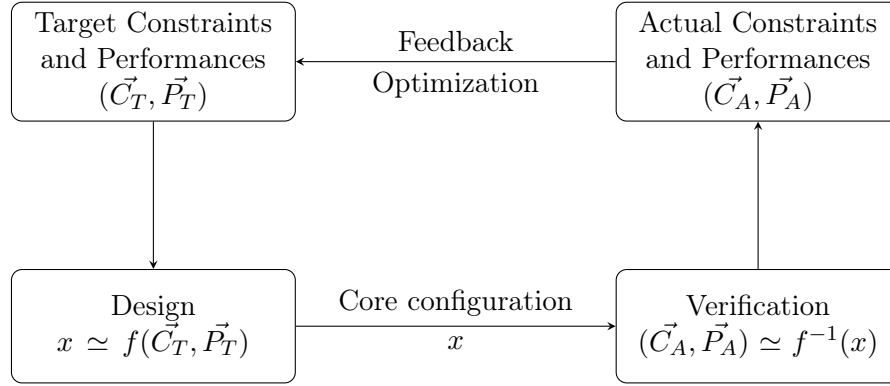
Figure 4.1: Mathematical description of the core design process.

Verification-**O**riented **C**odes (VOCs), featuring sophisticated numerical methods and models, also for the design stage; this is however as much tempting as dangerous. Remembering from Section 3.1.1, the mantra of core design is *"to translate* [constraints and performances] *in relations among the core geometric, material and physical parameters"* that can in turn be used to set up a preliminary system configuration; it can be understood that, in order to put into practice this design philosophy, tools in which such relations are explicit or at least easily retrievable by the user, must be used. A VOC is built with exactly the reverse intention: it takes all the core geometric, material and physical parameters and calculates the system performances and constraint-related observables value. The clarity of the connections among parameters is shadowed and sacrificed in the name of accuracy, dedicated tools are therefore needed to actually help the designer in this translation process: the DOCs.

To better comprehend what is meant with DOC, the logical scheme of the overall design procedure depicted in Figure 3.3 can be mathematically rendered as reported in Figure 4.1. It can then be said that

Definition. *A DOC must help in a priori understanding of properties and features of the function f - the design process - while keeping the relation among x - the core configuration - and $\vec{C_A}, \vec{P_A}$ - constraints and performances - clear to the user.*

Safety, a top priority for Gen-IV systems, is pervasively present in the constraints vector $\vec{C_T}$ and so it can also be defined a safety-informed design-oriented code:

. . . .

Definition. *When the properties of the function f are studied in safety related situations, the attribute safety-informed can be added to design-oriented (see Chapter 12), forming what is called a safety-informed design-oriented code.*

A safety-informed DOC can then be used to retrieve information on the main dependencies of safety margins - $(\vec{C_T} - \vec{C_A})$.

4.2   Principal characteristics

To ensure consistency with the intended application and to perform the constraints-configuration translation step in the clearer way possible, a DOC (and also a safety-informed DOC) must possess a number of features that are instrumental for bringing out its full potential. They are essentially:

- equilibrium,

- fast running and

- application domain.

Each of them will be discussed in the following.

4.2.1   Equilibrium

With equilibrium it is intended a good balance between the ability of a DOC in reproducing experimental data and the complexity of the implemented models and code structure so to maintain a clear relationship among the various core parameters. It should therefore represent an improvement over the P&P methods for what concerns accuracy and possibilities while still keeping their clarity in relating constraints/performances and core parameters. This objective is believed to be crucial because a very complex tool will hinder the user's understanding of the system under study (the f function), while an inaccurate one will render unusable or less significant the results, reducing the confidence of the user in utilizing them. To better illustrate this concept, it can be assumed that the curve relating accuracy with model complexity - in the form of degree of completeness of the phenomena description - has the form reported in Figure 4.2; the DOC general structure should therefore be placed on the point of optimal trade-off, where the minimum degree of complexity allows a satisfactory accuracy.

Even if vaguely introduced, the term *"satisfactory accuracy"* has actually a precise meaning. Equilibrium, indeed, also means that the various sources,

. . . .
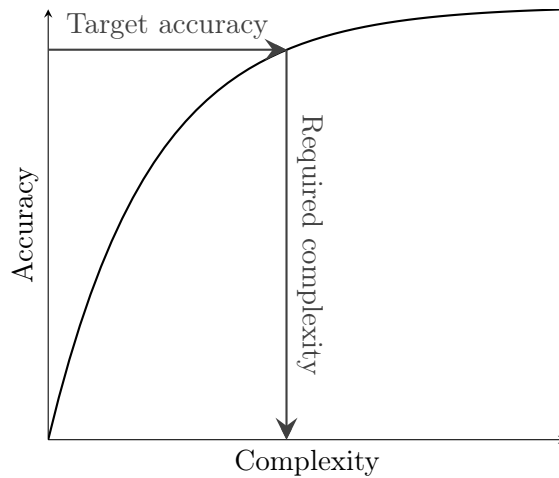
Figure 4.2: Hypothetical relation between complexity and accuracy of a
model.

contributing to the overall uncertainties, are balanced so to avoid excessive
efforts to increase accuracy on terms that are already poorly contributing to
the uncertainty on the final results. The terms in questions can be essentially
divided in three categories:

1. input,

2. material properties and

3. models.

Input

The first term indicates the available quality (and quantity) of input param-
eters; a DOC should indeed require a level of input detail fitting with the
current design stage. Many input values are often not yet known and only
a rough first estimate is usable; for such kind of parameters an extremely
accurate (and thus complex) tool would be oversized, besides hindering the
constraints-core configuration relation understanding.

Material properties

The second term indicates the only approximate knowledge that stems from
measurement campaigns or the difficulty in reproducing particular condi-
....

tions (e.g. irradiation effects). Depending on the particular physical field covered by the DOC under development, material properties can contribute significantly to the final uncertainties.

Models

The third term indicates the modeling errors and is the one directly under control of the DOC developer. Reducing this error, as previously discussed (see Figure 4.2), implies a stronger modeling effort and thus code complexity. The contribution of this term should then be balanced with the effect of the other two so to avoid the coupling of a very refined and time consuming model with poor material properties or input data. This will enforce code homogeneity and modeling efficiency, both helping in keeping clear the link between constraints and the resulting core configuration.

4.2.2   Fast running

While it is true that a DOC will help in understanding the features of the f function, its form is never truly known; this means that a DOC can help in rationally orienting choices for setting up a coherent core configuration but, such a process, would remain tentative in nature. Due to this, it could be desirable to test a number of configuration options and, as such, a DOC should be fast running with a low computational burden. Moreover, a sensitivity analysis could be performed to span the operational space looking for quantitative correlations substantiating intuitive optimization strategies or for understanding safety margins in key parameters; since these are all generally time consuming tasks, short computational times must be pursued.

4.2.3   Application domain

To enhance confidence in the DOC results, simplifying their interpretation phase - necessary in a rational design process -, facilitate **V**erification and **V**alidation (V&V) activities and enable a clear comprehension of the calculation flow by the user side, the application and validity domain must be openly stated. To carry this concept to the extreme, the application domain must be decided beforehand, so that it is unequivocally known, and equations and models derived accordingly. The idea is, therefore, not to solve a set of equations and models and to see *a posteriori* their validity range - the approach historically followed - but, to perform the equations and models selection in order to be consistent with an *a priori* decided application range; this will maximize efficiency in code development and simplify V&V

....

activities. Being this point of particular relevance, it will be recalled and stressed throughout the thesis.

4.3   Development logic

The previously mentioned characteristics of a DOC are synergistic, in the sense that they point in the same direction and, as such, they can effectively be meet together. To ease the achievement of such an objective, it can be of help to answer the following questions:

1. Which approach to choose among those found in the literature?

2. Which application and validity domain to select?

3. Which equations and models to adopt given the decided validity domain?

Some more details about the meaning of these interlinked questions will now be disclosed.

Which approach to choose among those found in the literature?

In order to ensure equilibrium and low running times the correct approach must be selected. This means opting for a numerical method able to efficiently operate on the particular scale of interest without requiring an excessively complex structure or computational burden. Again, too simple methods will probably fulfill the running time condition, but the risk of not reaching the wanted accuracy can be significant; on the contrary, very sophisticated ones will most certainly attain the required accuracy, but fail the computational time and structural requirements.

Answering this question, taking into account the foreseen application domain, is possibly the most important part of a DOC development effort because, it will directly influence the ability of the code to truly accomplish the DOC preconditions outlined in Section 4.2.

Which application and validity domain to select?

Depending on the specific tasks and goals of the DOC under development and the position in the core design process introduced in Section 3.1.2, the application and validity domain must be established. They ought to be coherent with the selected numerical method and the design requirements for the addressed category of systems.

....

Which equations and models to adopt given the decided validity domain?

Once the application domain has been selected, the choice of the most appropriate set of equations and models must be done trying to enforce the equilibrium requirements on accuracy and complexity. This means that the various terms of the governing equations must be analyzed, identifying those that do not contribute significantly to the particular problem; if compatible with the accuracy requirements they can be discarded or at least roughly modeled in proportion to their lower importance.

During the V&V phase it then becomes crucial to actually check that the anticipated and actual validity domains coincide so to prove the correctness of the adopted modeling strategy.

. . . .

. . . .

CHAPTER 5

THESIS MOTIVATIONS AND GOALS

To completely unlock the desired levels of sustainability, safety, economics, proliferation resistance and physical protection, the core design step of HLM-FRs is vital. Such a process should therefore be approached in the most rationale and aware fashion possible; a way of designing matching these requirements demand that the relation among constraints (whatever their nature) and performances on one hand, and the resultant core configuration on the other, be kept as clear as possible, as outlined in Section 3. To this regard the use of DOCs is deemed mandatory to fully exploit the advantages of the drafted core design procedure.

Given the growing interest in HLMFRs thanks to their potential in achieving the GIF goals, as highlighted in Chapter 2, numerous projects have emerged during the years; in the most recent times, the engagement of various industrial stakeholders has boosted research activities as discussed in Section 2.4.3. All these endeavors have made clear either - best case - the lack of specific DOCs for this kind of systems, that are usually designed with tools borrowed, *mutatis mutandis*, from previous SFRs projects; or - worst case - the lack of DOCs at all, these systems being designed with verification-oriented tools, hence mostly according to a try-and-fail approach.

5.1 State of the Art and Current Gap

The set of DOCs dedicated to HLMFRs, in the open literature, is not particularly populated due to the quite recent interest in these systems, especially for critical configurations, as discussed in Chapter 2; for this reason, state of
....

the art DOCs, with the meaning of Chapter 4, are actually few.

Between the fields of thermal-hydraulics, thermo-mechanics and neutronics, discussed in Section 3.1.2 and graphically summarized in Figure 3.2, the more advanced, from the available tools point of view, is possibly the latter. Neutronics, indeed, is, by nature, less dependent on the specific FR concept analyzed being the fuel isotopes the same for all the systems; the sole effect of the coolant must be assessed via dedicated validation activities, like the one in [116], and via sensitivity and uncertainty analysis, like the one in [39]. A suitable neutronic DOC specifically conceived for FRs applications is, for example, the deterministic code ERANOS [113] which can boast a wide-spread history of utilization in the core design community.

Regarding the other two, gaps have indeed surfaced. Going in logical order in Figure 3.2, for the thermal-hydraulics side, there are no evident lacks of tools for what pertains the elementary cell sizing; being the critical point the natural circulation onset already addressed by the safety-informed DOC BELLA [16], specifically developed for LM-cooled FRs. The next step would be the FA dimensioning: for this process a dedicated DOC has not been found in the open literature and, as such, its development has been one of the major purposes of the present work.

For what concerns the thermo-mechanics side, shortcoming in the area of DOCs have appeared for the fuel pin dimensioning; while it is true that this area has a lot to share with the other FR systems during the nominal operations, the same cannot be said for safety related situations. Transients in HLMFRs are characterized by time scales, temperatures and dynamics remarkably different from the other concepts (e.g. SFRs) due to the peculiarities of HLMs as highlighted in Section 2.3. A specific safety-informed DOC, presently not available in the open literature, is therefore necessary so to ease the process of conceiving a safety-embedding core configuration.

5.2 Objectives

The broad objective of the thesis is therefore to bridge the present gap concerning DOCs, and notably for the HLMFRs core design. Summarizing, the objectives of the present thesis involve the development, basically from scratch, of DOCs, with the meaning illustrated in Chapter 4, in the area of:

- FA thermal-hydraulics and

- fuel pin thermo-mechanics,

. . . .

and their subsequent validation so to prove the correctness of the overall process and quantitatively state their degree of reliability inside their anticipated validity domains.

. . . .

. . . .

Part II

Fuel Assembly Thermal-Hydraulics: ANTEO+

Abstract   In Part II of the thesis the focus is on the development of the FA thermal-hydraulics DOC, ANTEO+. The development logic outlined in Chapter 4 is here followed trying to truly fulfill all the main DOC requirements concerning equilibrium, running times and validity domain. After having answered the three pillar questions of any DOC, the code structure is deeply presented stressing the main simplification and model selection criteria. To test that the actual and anticipated validity domains coincide, along with the overall accuracy to recognize to ANTEO+ results, a through validation campaign has been conducted, proving the correctness of the adopted development methodology.

To allow the application of ANTEO+ to core layouts cooled, even at rated power, in mixed convection, the initial forced convection regime is extended, always employing the same rationale approach. The new code structure is laid out and discussed, highlighting the application domain boundaries. Again, a validation campaign is performed proving the solidity of the methodology, with a code able to smoothly translate from forced to mixed convection maintaining a consistent accuracy. The validation campaign will also outline the need of dedicated HLM-cooled experiments to fully validate SC codes in pin bundles.

. . . .

. . . .

CHAPTER 6

ANTEO+ DEVELOPMENT RATIONALES

As pointed out in Chapter 5 there is a lack of DOCs for the FA thermal-hydraulic analysis in HLMFRs. The effort to close this gap has given rise to the **S**ub-**C**hannel (SC) code ANTEO+[1] (acronym from the italian **AN**alisi **TE**rmoidraulica **O**ttimizzata) [68], stemming from the original ANTEO [19], initially conceived for forced convection simulations of light water reactors. The generalized version of ANTEO, applicable to LMs (particularly the heavy ones), presented in this thesis, labeled ANTEO+, features improved modeling and geometrical capabilities encompassing bare, gridded and wire spaced bundles as better discussed in Chapter 7.

The guidelines fostered in Chapter 4 have been here followed to fully achieve the benefits that a well constructed DOC can deliver to the core designer.

6.1 Intended use and objectives

As a DOC for the thermal-hydraulic design of a HLMFR FA, ANTEO+ should help in:

- reducing thermal gradients among the sub-channels (hence across the pins),

---

[1]Besides the models and equations presented in the following, this new version of ANTEO features a user manual and a (Python written) post-processor data viewer [67] along with a Doxygen of the Fortran 90 source [66]. For more information on ANTEO history, the reader is directed to [68].

. . . .

- estimating the effect of the bypass on the temperature field and

- assessing the pressure drops through the pin bundle.

The first point is important so to avoid hot spot factors which could result in locally-enhanced corrosion; besides, due to the fact that constraints on the clad temperature are enforced on the hottest point, a particularly high distance from this point to the average one will go to the detriment of the overall core performances. A flat temperature profile, notably for FA with strong internal power gradients, is also crucial for relaxing the mechanical interaction among the FA components and thus significantly easing its mechanical design.

The second point is particularly relevant for the enclosed FA concepts because, as explained in Section 3.5.2, a clearance is left among the FA so to allow refueling operations due to the foreseen mechanical deformations during the whole irradiation life; this clearance serves also for cooling the FA from the outside so to avoid thermal gradients, and thus stresses, on the wrapper. During the FA thermal-hydraulic dimensioning can therefore be of interest to understand the effect of such a bypass on the temperature field inside the bundle.

Finally, the assessment of the pressure drops through the pin arrangement can be exploited so to double-check the results obtained during the elementary cell dimensioning, employing the higher degree of information during the FA design phase.

6.1.1   ANTEO+ purposes

Given the intended use of ANTEO+, its main purposes as a DOC are: to deliver a code able to simplify the problem description without penalizing accuracy and with a clear interface for the user (i.e. the core designer) having an explicit and easily identifiable application domain so to ease the results interpretation phase - necessary in a rationale design process - and to increase confidence in them so to aid in the FA dimensioning.

6.2   Development rationales

The development of ANTEO+ has been guided by the considerations discussed in Chapter 4 and summarized in the three questions reported in Section 4.3.

....
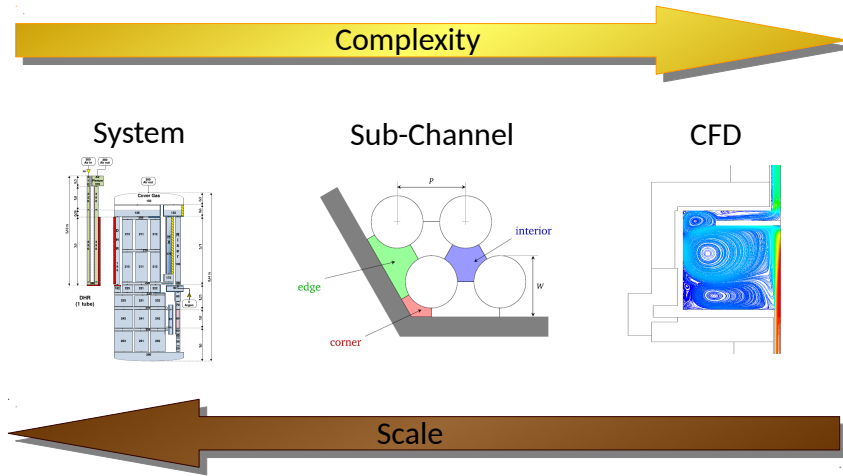
Figure 6.1: Representation of the main numerical approaches in relation to their target scale and complexity. The system image has been taken from [36] while the CFD one from [131].

Which approach to choose among those found in the literature?

Many methods have been conceived, over the years, for solving thermal-hydraulics related problems, covering various scales of interest and encompassing diverse numerical techniques. As summarized in Figure 6.1, methods going from the detailed **C**omputational **F**luid **D**ynamic (CFD) down to component-size one dimensional approaches are available. As the scale decreases, generally, the code complexity and running times increase but, at the same time, accuracy grows and a balance must be struck out so to fulfill the equilibrium condition discussed in Section 4.2.1; therefore, going through a compromise exercise, the most suitable candidate for fully achieving the requirements of a DOC, has been located in the SC method. Indeed, it covers the exact scale of interest for the FA thermal-hydraulic design, still allowing sufficient accuracy and structural simplicity; moreover, it has a widespread history of applications in core design of water- and sodium-cooled reactors as reviewed in [124] and [68] with reference VOCs like the COBRA and MATRA families.

It is worth to stress the meaning of *"sufficient accuracy"* in reference to the selected validity range (see answer to the next question): due to the low contribution of material properties like densities, specific heats and conductivities [93] to the overall uncertainty, along with the modest contribution of

. . . .

input quantities[2], it can be said that the main contribution is coming from modeling. As described in Section 4.2.1, the effort to equalize the various contributions meets here - due to the dominance of modeling - the lower bound of experimental uncertainties that are, therefore, the target accuracy of ANTEO+.

Which application and validity domain to select?

The reference has been set in steady-state conditions being the one usually of interest in the preliminary design phase of a power reactor and the most important for what pertains corrosion constraints. In steady-state the dominant flow regime, and thus the one selected, is typically forced convection. Being the focus on steady-state conditions the single-phase domain has been naturally selected.

Summarizing, the selected application and validity domain is the steady-state, single-phase, forced convection regime.

Which equations and models to adopt given the decided validity domain?

The answer to this question involves the analysis of the various terms appearing in the main equations of thermal-hydraulics, like the mass, energy and momentum balances, and their subsequent simplification. The salient results of such an investigation are reported in Chapter 7.

---

[2]At the FA design stage many input quantities have preliminary been fixed during the fuel pin and elementary cell dimensioning but, uncertainties on power distribution and pressure drops are still pending.

. . . .

CODE STRUCTURE

As reported in Section 6.1.1, the main objective of ANTEO+ as a DOC is to simplify the problem description without penalizing accuracy, thus enabling a more transparent interface with the user and, at the same time, considerably speeding up the calculation; for achieving this twofold task the SC method has been selected.

The reference validity and application domain has been set as the steady-state, single-phase, forced convection regime. The final step to implement the problem simplification while preserving a satisfactory degree of accuracy (with the meaning put forward in Section 6.2) is, therefore, to analyze the various terms of the governing equations, identifying those that do not contribute significantly to the particular problem; these terms could then be discarded or roughly modeled. This procedure allows to maximize modeling efficiency and, at the same time, to reduce the development effort.

7.1 Equation analysis

At the core of the SC method there is the idea to integrate the conservation equations over a channel, representing the flow area between fuel pins or between pins and duct, if present (Figure 7.1). This integration or "lumping" procedure assumes constant physical variables (i.e. temperature, pressure and velocity) across the control volume while mass, energy and momentum exchange phenomena between SCs are modeled via empirical correlations (more information on the SC method equations and approximations are available in [130]).

....
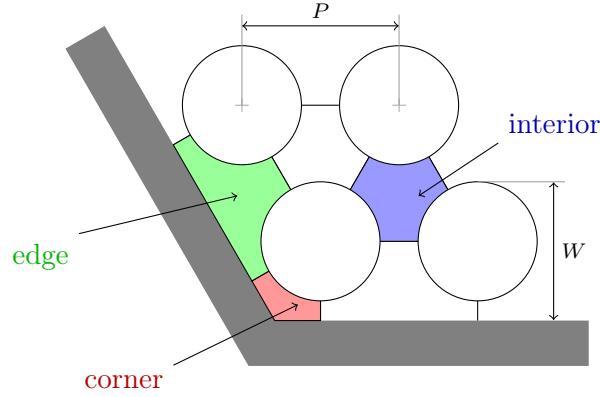
Figure 7.1: Sub-channel definitions for an hexagonal assembly (rods in a triangular lattice).

In the following, therefore, each steady-state constitutive equation is analyzed and the adopted simplifications highlighted and discussed.

7.1.1 Mass conservation

The mass conservation equation for a SC reads

$$\frac{d\dot{m}_i}{dz} = -\sum_{j=1}^{J} W_{ij} \quad , \tag{7.1}$$

where $\dot{m}_i$ is the mass flow rate of the i-th SC, z is the axial coordinate, J is number of SCs adjacent to i and W_{ij} is the transverse mass flow rate per unit length between SCs i and j, which accounts for diversion cross flows due to pressure differences on the plane orthogonal to z, usually induced by boiling, density gradients or geometric variations. In single-phase forced flow, these pressure and density gradients have a negligible effect (especially in an axially averaged sense) as the flow has a strong axial character, and so the diversion term can be eliminated from equation (7.1). The resulting mass conservation equation in ANTEO+ is then

$$\dot{m}_i = const \quad , \tag{7.2}$$

where SCs do not exchange mass with their neighboring ones.

....

7.1.2   Axial momentum conservation

The axial momentum conservation equation can be expressed as

$$
\begin{aligned}
\frac{d(P_i A_i)}{dz} = & - \frac{d(\dot{m}_i v_i)}{dz} - A_i \rho_i g - \frac{1}{2} \rho_i v_i^2 A_i \frac{f_i}{D_{Hi}} \\
& - A_i \Delta P_{form,i} - \sum_{j=1}^{J} W_{ij} v^* - \sum_{j=1}^{J} W_{ij}^M (v_i - v_j) \quad ,
\end{aligned}
\tag{7.3}
$$

where P_i is the pressure of the i-th SC, A_i its flow area, v_i is the coolant axial speed in the SC, ρ_i is the coolant density in the SC, g is the gravitational acceleration, f_i is the Darcy friction factor with the walls surrounding the i-th SC, D_{Hi} is the hydraulic diameter defined as $D_{Hi} = 4A_i/p_{wi}$ with p_{wi} indicating the wetted perimeter, $\Delta P_{form,i}$ is the form pressure loss per unit length due to changes in flow direction or geometry like the ones in the presence of spacers or at the inlet and outlet of the fuel bundle, v^* is the effective speed transported by cross flow and W_{ij}^M is the effective mass exchange rate per unit length between SCs i and j for momentum transfer purposes. The last term is labeled as *effective* because it is a fictitious mass flow defined in order to preserve the turbulent (including flow pulsation and secondary flow) and wire-induced momentum exchange between SCs; in single phase, indeed, turbulent mixing does not result in a net exchange of mass, even if, there is a net exchange of momentum and energy.

The diversion term is neglected as in equation (7.1); W_{ij}^M can be eliminated form equation (7.3) because in forced convection the SCs are weakly hydro-dynamically connected and, if necessary, this effect can be partially accounted for in the flow split model (see Section 7.2). Finally the SC index on the pressure can be dropped because it is uniform on the FA cross section as we shall see (equation (7.6)). Equation (7.3) can be then simplified as

$$
\begin{aligned}
\frac{d(P A_i)}{dz} = & - \dot{m}_i^2 \frac{d}{dz} \left(\frac{1}{\rho_i A_i} \right) - A_i \rho_i g \\
& - \frac{1}{2} \rho_i v_i^2 A_i \frac{f_i}{D_{Hi}} - A_i \Delta P_{form,i} \quad .
\end{aligned}
\tag{7.4}
$$

7.1.3   Transverse momentum conservation

The transverse momentum equation can be written as

$$
\frac{\partial(v^* W_{ij})}{\partial z} + \frac{\partial(u W_{ij})}{\partial x} = (P_i - P_j)\frac{s}{\eta} - K_{ij}\frac{W_{ij}^2}{2\rho_i s \eta} \quad ,
\tag{7.5}
$$

. . . .

where x is the transverse flow direction, u is the speed in the direction x, s is the clearance between fuel rods, η is a characteristic distance between SCs (i.e. centroid-to-centroid distance) and K_{ij} is a coefficient accounting for both frictional and form losses for the crossflow. Because W_{ij} is assumed equal to zero, the pressure is uniform on the SA cross section and the transverse momentum equation simply states that

$$P_i = P_j \quad \forall i,j \quad . \tag{7.6}$$

7.1.4   Energy conservation

The energy equation has the following form

$$\frac{d(\dot{m}_i h_i)}{dz} = \chi_i - \sum_{j=1}^{J} W_{ij} h^* - \sum_{j=1}^{J} W_{ij}^H (h_i - h_j)$$
$$- \sum_{j=1}^{J} \rho_{ij} \alpha_{ij} \left(\frac{s}{\delta}\right) (h_i - h_j) \quad , \tag{7.7}$$

where h_i is the enthalpy of the i-th SC, χ_i is the linear power discharged to SC i from the surrounding fuel pins, h^* and W_{ij}^H are the energy counterparts of v^* and W_{ij}^M, ρ_{ij} is the average coolant density of SCs i and j, α_{ij} is the average thermal diffusivity and δ is an effective mixing length usually taken as the ratio of η and the conduction shape factor κ [23]. Contrarily to W_{ij}^M in the momentum equation, W_{ij}^H is important even in forced convection - especially in the presence of a wire spacer - and must be accounted for. Eliminating the diversion term and considering equation (7.2) we arrive at

$$\dot{m}_i \frac{dh_i}{dz} = \chi_i - \sum_{j=1}^{J} W_{ij}^H (h_i - h_j) - \sum_{j=1}^{J} \rho_{ij} \alpha_{ij} \left(\frac{s}{\delta}\right) (h_i - h_j) \quad . \tag{7.8}$$

The term W_{ij}^H can also be properly enhanced to model flow sweeping due to a wire spacer or flow scattering due to grid spacers; this *effective* exchange term make possible to take into account energy exchange phenomena which are characterized by zero (or almost zero) net mass exchange (especially in an axially averaged sense), effectively decoupling the mass and energy equations with considerable gain in computational efficiency. One of the drawback of this approach is, however, that the flow rate in a channel cannot be computed from the above system of equations, namely, (7.2), (7.4), (7.6), (7.8), but it must be evaluated before starting the actual solution process; a flow split
. . . .

model is therefore necessary in order to define the inlet conditions of every SC in the bundle.

As can be seen, the final set of equations solved by ANTEO+ is remarkably different from the one usually solved by the standard COBRA-like VOCs [141], being more simple, avoiding to solve the transverse momentum equation and thus avoiding convergence problems with the possibility of maximizing modeling efficiency for the selected validity range.

Summarizing, the modeling adopted in ANTEO+ corresponds to a system of SCs dynamically connected only at the inlet and energetically connected throughout the whole simulated length.

7.1.5   Coolant temperature calculation scheme

The simplifications highlighted lead to a decoupling of the energy and momentum equations, now only related through the temperature dependency of the physical properties of the coolant. The decoupling considerably simplifies the numerical solution scheme because, once the inlet conditions are known from the flow split model, the energy equation can be solved at a particular axial location with the Gauss elimination method, the pressure drop computed from (7.4) and then the sequence repeated for the next axial step. The above procedure is also depicted in Figure 7.2.

The solution computed at an axial location is based only on the upstream nodes and does not depend on the subsequent ones: consequently, the scheme is a forward one, coherently with the parabolic nature of the energy equation; this means that situations with a strong axial flow redistribution, like flow blockage, cannot be simulated; this is, however, consistent with the forced convection assumption.

7.1.6   Cladding temperature calculation

Once the coolant temperature distribution is known, the external cladding temperature can be calculated. ANTEO+ assumes unirradiated conditions and cold geometry.

The outer cladding temperature T_{co} is calculated at each axial step as

$$T_{co}(z) = T_b(z) + \frac{\chi_p(z)}{\pi D \alpha_p(z)} \quad , \tag{7.9}$$

where T_b is the bulk coolant temperature surrounding the pin under analysis, χ_p is the linear power of the pin, D is the pin diameter and α_p is the convection coefficient.

. . . .
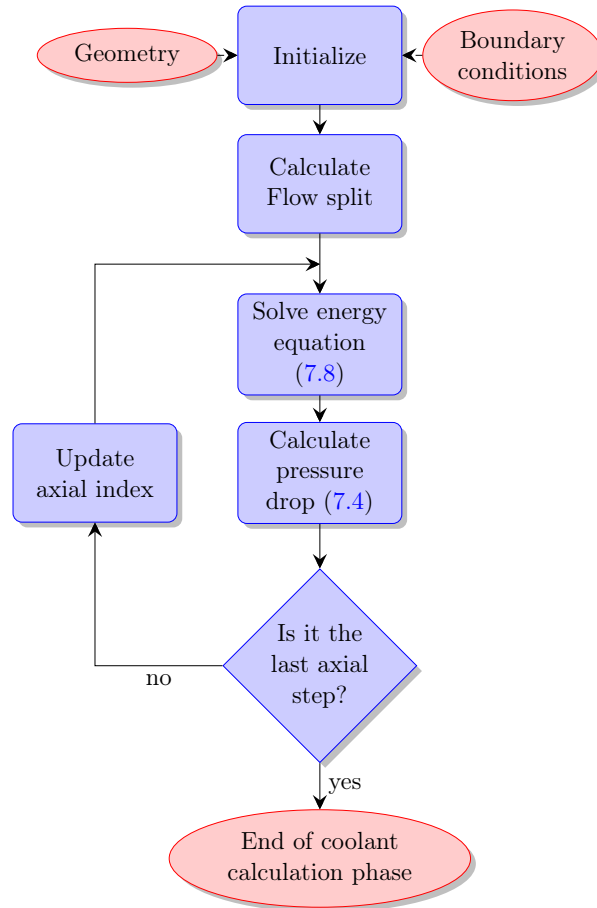
Figure 7.2: Flow diagram of the coolant temperature calculation scheme in ANTEO+.

7.1.7   State equations

For practically solving the momentum and energy equations on coolant side, and the heat equations for the cladding, a set of state equations is needed for the physical properties of the coolant and clad. The available correlations in ANTEO+ are not reported here but, are presented in [68].

7.2   Constitutive relations for balance equations

Besides the physical properties, constitutive relations are needed in order to eliminate some of the unknowns present in the conservation equations. In

....
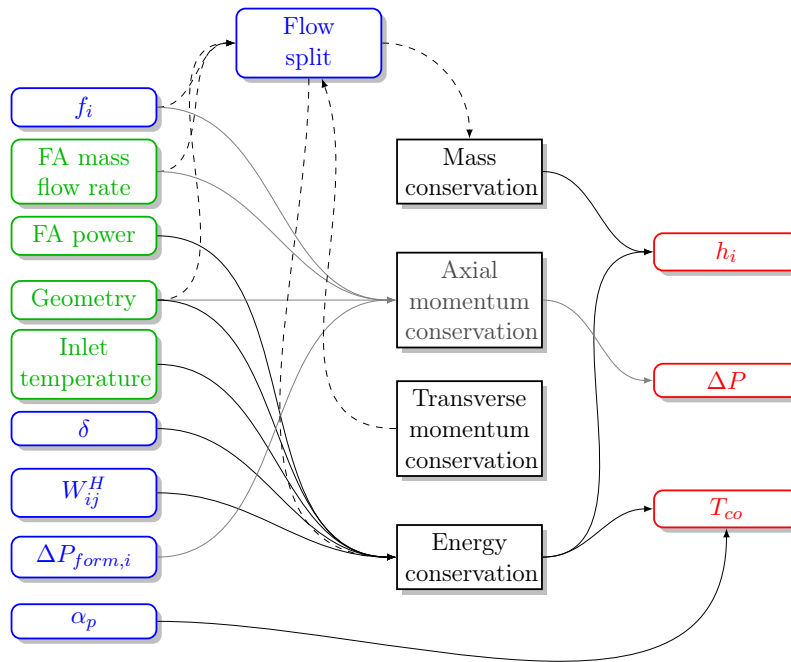
Figure 7.3: Summary of all the input (green) and models (blue) parameters
to ANTEO+ , along with their interaction with the output (red) SC
enthalpy, clad temperature and bundle pressure drops.

the system given by equations (7.2), (7.4), (7.6), (7.8), f_i, $\Delta P_{form,i}$, W_{ij}^H
and δ must be specified. Moreover, χ_i and m_i are available, directly or
indirectly, from the boundary conditions: the linear power transferred to a
SC is calculated from the power input supplied by the user while the mass
flow in a SC is calculated from the flow split model and the total flow of the
assembly, which is another input from the user.

The summary of all the input and models parameters - besides material
properties - necessary to ANTEO+, along with their interaction with the
calculated results, including SC and clad temperatures and bundle pressure
drops, is graphically reported Figure 7.3.

In this section the adopted flow split model and the correlations imple-
mented as constitutive relations are presented, highlighting their expected
range of validity.

. . . .

7.2.1   Friction factor

A great deal of attention was given in the 70's and 80's [111] to the pressure drops in wire wrapped and bare fuel assemblies, and an important effort was undertaken, in order to establish robust and multipurpose semi-empirical correlations for friction factors. From these experimental results and the ones reported in [22], four correlations were selected for both bare and wire spaced bundles in both hexagonal and square geometries.

In ANTEO+ the friction factor is actually used twice for two different purposes: the flow split and the bundle average pressure drop (see equation (7.4)). The accuracy and detail requirements can be different, so some model, even if not suited for flow split calculation, can still produce acceptable results in an average sense; nonetheless, selection's consistency is always recommended.

Blasius   The simple correlation proposed by Blasius [14] for the friction factor in a smooth circular tube reads

$$f_i = \frac{0.316}{Re_i^{0.25}} \quad , \tag{7.10}$$

where Re_i is the Reynolds number based on the hydraulic diameter of SC i. Blasius does not differentiates among SC types and it is not suited for wire spaced bundles; on the other hand has the advantage of being simple and applicable to a wide range of flow conditions and can thus be used as a first estimate correlation. The range of validity is:

- turbulent $\leq Re \leq 10^5$.

Rehme-bare   As suggested in [112] the use of the hydraulic diameter equivalence, coupled with friction factors for circular tubes can lead to misleading results. To overcome this limitation, in [111] a methodology was developed, applicable to laminar and turbulent flow regimes and suited for both hexagonal and square geometries.

In the case of fully developed laminar flow the friction factor can be expressed as

$$f = \frac{K}{Re} \quad , \tag{7.11}$$

where K is a constant depending on SC geometry. The latter is determined by the pitch to diameter ratio P/D (where P is the bundle pitch) for central SCs and, additionally, by the W/D ratio (where W is the maximum pin-duct distance) for edge and corner SCs (see Figure 7.1). For every SC family

....

K was computed and plotted over a wide range of P/D and W/D ratios as explained in [112]. By considering a parallel of all the SCs, the bundle average K_{tot} can also be computed as

$$\frac{1}{K_{tot}} = \sum_i \frac{1}{K_i} \left(\frac{p_{wb}}{p_{wi}}\right)^2 \left(\frac{A_i}{A_b}\right)^3 \quad , \tag{7.12}$$

where p_{wb} is the bundle wetted perimeter.

For turbulent flow a method was developed to predict the bundle friction factor f_b on the basis of laminar results; the following implicit formula was derived

$$\sqrt{\frac{8}{f_b}} = A \left[2.5\ln\left(Re \cdot \sqrt{\frac{8}{f_b}}\right) + 5.5\right] - G^* \quad , \tag{7.13}$$

where A and G^* are empirical factors graphically determined. In order to make the implementation of the model possible in ANTEO+ the interpolating formulae developed by [76] were used, which are very similar to the ones reported in [24], namely

$$A = \begin{cases} 1.89 - 0.215\ln(K_{tot}) & \text{if } K_{tot} \leq 64 \\ 1 & \text{if } K_{tot} > 64 \end{cases} \tag{7.14}$$

$$\begin{aligned} G^* =& 3.3618 + 0.1898\ln(K_{tot}) + 0.0902[\ln(K_{tot})]^2 + \\ & 0.0007[\ln(K_{tot})]^3 \quad . \end{aligned} \tag{7.15}$$

For dealing with the transition region no indication is reported by Rehme. A possible choice for the extrapolation could be the one used in [24] (see equation (7.21)), but, in order not to double the approach, a different one has been taken in ANTEO+; specifically, given the Reynolds number, the friction factor is calculated with both the laminar and turbulent formulas, then, the higher is selected as the reference friction factor.

Rehme's correlations for bare bundles can predict friction factors differentiated by SC type or bundle averaged and so it can be used both in the flow split model and in the pressure drops calculation phase.

This model was proved to give reliable results for a broad range of geometric arrangements [111] and flow conditions. No explicit validity domain is specified.

....

Rehme-wire   While the pressure drop due to a spacer grid is linearly added, the wire spacer effect is usually included in the distributed pressure losses. For this reason correlations developed for bare bundles are not transferable to wire spaced ones (although the opposite can be true) for which, in turn, they must be specifically determined. Among the many correlations proposed for wire spaced bundles the one by [110] has been selected and implemented in ANTEO+.

The model is based on an effective velocity v_{eff} created by the swirl flow of the wire, which is a function of P/D and $H/(D + D_w)$, where H is the lead of the wire wraps and D_w is its diameter. The relation is

$$F = \left(\frac{v_{eff}}{v_b}\right)^2 = \sqrt{\frac{P}{D} + \left[7.6\frac{D + D_w}{H}\left(\frac{P}{D}\right)^2\right]^{2.16}} \quad , \tag{7.16}$$

so that the friction factor is finally calculated as

$$f_b = F\left(\frac{p_{w,nw}}{p_{wb}}\right)f^* \quad , \tag{7.17}$$

where $p_{w,nw}$ is the wetted perimeter of the bundle without the duct and f^* is a modified friction factor expressed as

$$f^* = \frac{64}{Re_b\sqrt{F}} + \frac{0.0816}{(Re_b\sqrt{F})^{0.1333}} \quad . \tag{7.18}$$

It is declared that this equation is able to predict 92% of around 1400 experimental points within $\pm 5\%$ for $Re \geq 2 \times 10^4$.

This model does not discriminate among SCs and so is less suited for flow split calculations, similarly to Blasius. The validity domain is:

- $1.125 \leq \frac{P}{D} \leq 1.417$

- $8 \leq \frac{H}{D} \leq 50$

- $7 \leq N_{pin} \leq 61$

- $10^3 \leq Re_b \leq 3 \times 10^5$.

Cheng-Todreas   The correlation which was found to give the best agreement over a very wide range of geometries and flow conditions ([22] and [26]) for wire wrapped bundles is the one by **C**heng and **T**odreas (CT) [24]. This model is based on theoretical considerations of flow pattern in different types

....

of SCs, enabling different friction factors among SCs to be calculated. From the last point emerges that it can be efficiently cast in a flow split model; moreover, it can be applied to bare or gridded bundles.

A general relationship for f_i can be expressed as (see also Rehme-bare)

$$f_i = \frac{C_{fi}}{Re_i^m} \quad, \tag{7.19}$$

where m is an index that depends on the flow regime (laminar, turbulent) and C_{fi}, similarly to K, is a function of the SC geometry. The correlation moves from this general form to be detailed for every SC type[1].

Interior It is postulated that the pressure loss originates from two effects:

1. the friction loss caused by the fuel rod surface and

2. the drag loss caused by the wire.

Under these assumptions the friction factor for central SCs is expressed as

$$
\begin{aligned}
f_1 = &\frac{C_{f1}}{Re_1^m} = \frac{1}{Re_1^m} \left[C'_{f1} \left(\frac{p'_{w1}}{p_{w1}} \right) + \right.\\
&\left. 3W_d \left(\frac{A_{r1}}{A'_1} \right) \left(\frac{D_{H1}}{H} \right) \left(\frac{D_{H1}}{D_w} \right)^m \right] \quad,
\end{aligned}
\tag{7.20}
$$

where C'_{f1} is the friction factor constant for a bare rod, p'_{w1} and p_{w1} are respectively the bare and wire spaced rod wetted perimeters, W_d is the wire drag constant, A_{r1} is the projected wire area in the SC, A'_1 is the bare SC area, H and D_w are the wire lead pitch and diameter respectively. The coefficient m is 1 for laminar and 0.18 for turbulent flow regimes. For a bare bundle A_{r1} is zero and the wetted perimeter ratio is one; the correlation correctly reduces to the bare rod case.

The empirical constants C'_{f1} and W_d are correlated for laminar and turbulent conditions, so that they define two different friction factors, named $f_{1,L}$ in laminar and $f_{1,T}$ in turbulent flow regime. In the transition region f_1 is found using

$$f_{1,tr} = f_{1,L}(1 - \Psi_1^\nu)(1 - \Psi_1)^\gamma + f_{1,T}\Psi_1^\gamma \quad, \tag{7.21}$$

where γ and ν are chosen so to best fit the data and Ψ_1 is the intermittency factor.

---

[1]In the following the interior SC is denoted with index 1, the edge with 2 and the corner with 3.

. . . .

Edge   Since near the wall the wires sweep the SCs always in the same direction, a swirl flow originates and the coolant is assumed to follow the wire; so only a small velocity component slips over the wire and the drag losses can be assumed negligible compared to the skin friction. The friction factor can therefore be expressed as

$$f_2 = \frac{C_{f2}}{Re_2^m} = \frac{C'_{f2}}{Re_2^m} \left[1 + W_s \left(\frac{A_{r2}}{A'_2} \right) \tan^2 \theta \right]^{\frac{3-m}{2}} \quad , \qquad (7.22)$$

where W_s is an empirical constant of proportionality, function of geometry, and θ is the wrapping angle. The meaning of the other parameters is identical to the one described for the interior SC as is the transition flow regime calculation.

Corner   Since the flow characteristics are similar to the edge SC the same kind of relationship is assumed for f_3, namely

$$f_3 = \frac{C_{f3}}{Re_3^m} = \frac{C'_{f3}}{Re_3^m} \left[1 + W_s \left(\frac{A_{r3}}{A'_3} \right) \tan^2 \theta \right]^{\frac{3-m}{2}} \quad . \qquad (7.23)$$

The validity domain of the CT correlation for all types of SCs is reported to be:

- $1 \leq \frac{P}{D} \leq 1.42$

- $4 \leq \frac{H}{D} \leq 52$

- $19 \leq N_{pin} \leq 217$

- $50 \leq Re_b \leq 10^6$.

It is claimed that the correlation can predict bundle friction factors with $\pm 14\%$ accuracy for turbulent flow and within $\pm 30\%$ for laminar flow conditions (due to the higher experimental uncertainties in this regime).

In Figure 7.4 the correlations are compared (the bare results are for the same bundle but without spacers). In the turbulent region the agreement is good, while the maximum discrepancies are found in the transition region. The Blasius model is highly distant from the others in the laminar region, which is outside the correlation domain.

....
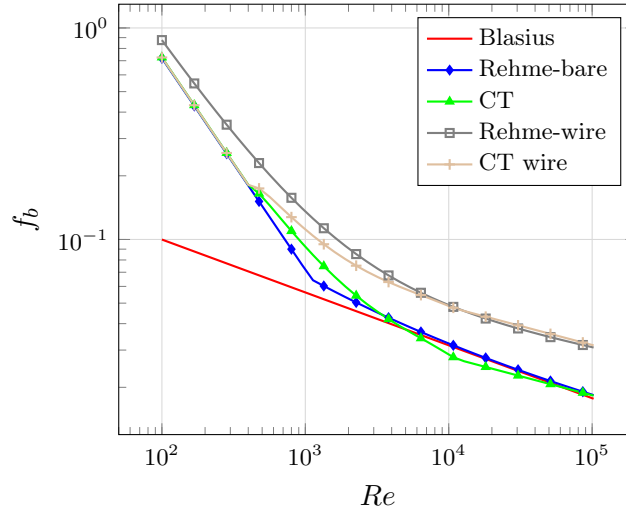
Figure 7.4: Comparison between friction factor correlations implemented in ANTEO+ for bare and wire-wrapped bundles. The following parameters were assumed: $\frac{P}{D} = 1.1$, $\frac{W}{D} = 1.1$ and $\frac{H}{D} = 10$.

7.2.2   Grid loss coefficient

The concentrated pressure loss for a grid are quite dependent from the spacer design, and no general correlation can be stated applicable to every grid typology. For this reason in ANTEO+ the user can supply in the input his own correlation of the form proposed in [27]

$$
\begin{aligned}
c_v = & \ \ \text{MIN}\left(a + b \cdot Re^c + d \cdot Re^e, \frac{f}{\varepsilon^g}\right) \\
c_s = & \ \ c_v \cdot \varepsilon^g
\end{aligned}
\tag{7.24}
$$

with c_s the grid loss coefficient and ε the area blockage ratio. Pressure drops are then calculated as

$$
\Delta P_{grid} = c_s \frac{1}{2} \rho v_b^2 \quad ,
\tag{7.25}
$$

and are linearly added to the other pressure drops contribution (i.e. friction along the bare bundle).

7.2.3   Flow split

Before starting the actual calculation, a way for specifying how the total flow rate distributes in every SC is needed; this task is performed by the flow split

. . . .

model. The main idea behind the model is to follow the hydrodynamic description depicted in 7.1.4 namely, a set of parallel SCs connected only at the inlet and outlet sections; with this picture, and assuming a radially uniform pressure distribution in the inlet and outlet plenum of the pin bundle, the pressure drops of all SCs must be equal. This constraint is translated in the transverse momentum equation (7.6) or equivalently in its difference form as

$$\Delta P_i = \Delta P_j \quad \forall i,j \quad . \tag{7.26}$$

The pressure drop is the sum of terms reported in equation (7.4). Assuming an axially constant flow area, neglecting the acceleration pressure term (first term on the right hand side) and eliminating the hydrostatic pressure, which is equal for every SC, it is possible to recast (7.26) in the form

$$v_i^2 \frac{f_i}{D_{Hi}} L + \xi_i v_i^2 = v_j^2 \frac{f_j}{D_{Hj}} L + \xi_j v_j^2 \quad \forall i,j \quad , \tag{7.27}$$

where L is the bundle length and ξ_i is the concentrated loss coefficient of the grid spacers which is equal to the product of the spacers number and c_s described in 7.2.2. The form pressure drop term has been related to the dynamic pressure and the term $\frac{1}{2}\rho$ has been simplified, neglecting density variations between SCs [2]. The flow split parameters are defined as the ratio between the SC's velocity and the average bundle velocity, so equation (7.27) can be written as the ratio of two flow split parameters as

$$\frac{X_i}{X_j} = \sqrt{\frac{f_j(X_j)\frac{L}{D_{Hj}} + \xi_j}{f_i(X_i)\frac{L}{D_{Hi}} + \xi_i}} \quad \forall i,j \tag{7.28}$$

where the dependency of the friction factor on Reynolds number and thus on the velocity and flow split parameters is explicitly reported. It is seen that equation (7.28) is non-linear.

The system of equations composing the flow split model is closed with the continuity condition

$$\sum_{i=1}^{N_{typ}} S_i X_i = 1 \quad where \quad S_i = \frac{N_i A_i}{A_b} \quad , \tag{7.29}$$

where N_{typ} is the total number of SCs types (Figures 7.1 and 7.11) in the bundle, S_i is the fractional area occupied by SCs of type i, N_i is the number

---

[2]This is consistent with the forced flow assumption.

of SCs of the i-th type and A_b is the bundle flow area. Given the generally non-linear character of the model [3] the system is solved cycling on successive approximations is used.

Various flow split models can be constructed from the general one just described, depending on the correlation used for the friction factors. Some models account for the difference in friction among SC types (e.g. CT) while others use the same f_i formula for all the SCs (e.g. Blasius) and are essentially based on the hydraulic diameter concept. The former type is generally more accurate, but the latter can still produce reliable results if all the f_i are close to each other; this is partially true for turbulent flow conditions, where geometric characteristics become less and less important (see Figure 7.5). In laminar flow, however, not considering the difference among SCs can produce unacceptably inaccurate results. With wire spacer the situation worsens. For these reasons it is always recommended to rely on models which differentiates f_i by SC type [106].
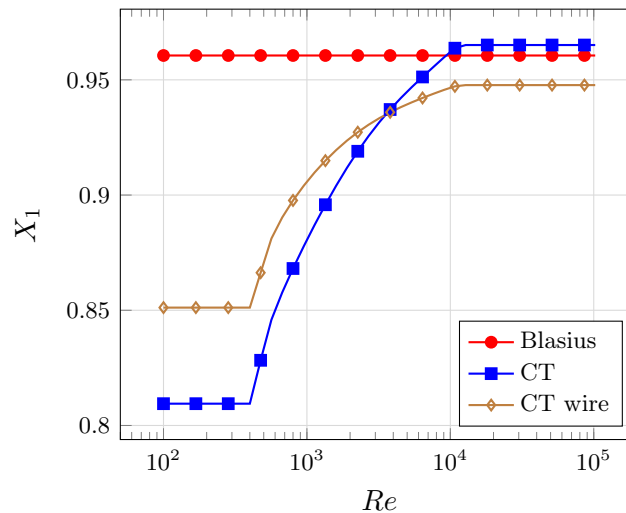
Figure 7.5: Comparison between flow split models implemented in ANTEO+ for bare and wire-wrapped bundles. The following parameters were assumed: $\frac{P}{D} = 1.1$, $\frac{W}{D} = 1.1$ and $\frac{H}{D} = 10$.

---

[3]If the concentrated loss coefficient is set to zero the equation can be cast in an explicit form which does not need non-linear iterations.

. . . .

7.2.4   Mixing coefficient

Temperature prediction is probably the most important task of thermal-hydraulic design and so a high degree of accuracy must be targeted in a wide range of situations compatibly with the anticipated range of application of ANTEO+. For this, correlations for W_{ij}^H encompassing both bare and wire spaced bundles have been implemented. The additional mixing effect of the grid spacer is not directly modeled, but it is partially accounted for in the flow split model.

The reference correlation implemented in ANTEO+ for bare or grid spaced bundles, taken from [57], is firstly presented.

Bare bundle

Kim   In the model proposed in [57] the mixing rate is estimated on the basis of a scale analysis on the flow pulsation generated by periodic vortices, that is indicated to be the main cause of mixing in rod bundles. Based upon the assumption that turbulent mixing is the sum of molecular motion, isotropic turbulent motion and flow pulsations (anisotropic turbulence due to heterogeneity effects), the scale relation is derived as a function of P/D, Re, and the Prandtl's number Pr.

The effective mass exchange rate between SCs for energy transfer per unit length can be expressed as

$$W_{ij}^H = \rho_{ij}v_{eff}s = \rho_{ij}v_{ij}St_g s \quad , \qquad (7.30)$$

where v_{eff} is the effective mixing velocity, possibly different from v^*, v_{ij} is the mean axial speed in SCs i and j, and St_g is the gap Stanton number which is expressed as

$$St_g = \frac{v_{eff}}{v_{ij}} = \frac{2}{\gamma_1^2}\sqrt{\frac{\alpha}{8}}\frac{D_{Hij}}{s}\left[\left(\frac{\gamma_1^2}{2PrRe^{(1-\frac{\beta}{2})}}\frac{8}{\alpha}\right.\right.$$
$$\left.\left.+\frac{1}{Pr_T}\right)\frac{s}{b\eta} + a_x\frac{z_{FP}}{D}Str\right]Re^{-\frac{\beta}{2}} \quad , \qquad (7.31)$$

where α, β and γ_1 are empirical constants, b is as shape factor equal to 1 in square and $2/3$ in hexagonal geometry, D_{Hij} is the mean hydraulic diameter of SCs i and j, Pr_T is the turbulent Prandtl's number relating eddy diffusivity of momentum and energy, Str is the Strouhal's number, calculated with the formula found in [142], and $\frac{z_{FP}}{D}$ is the path length to diameter ratio.

....

The correlation already includes the effect of conduction and so the last term in equation (7.8) is automatically included in W_{ij}^H. This correlation can be applied to both square and hexagonal pins' arrangements and was found in good agreement with the published experimental results with various Prandtl number fluid flows, especially for liquid metal coolants ($Pr \ll 1$).

Wire spaced bundle

Wire wrapping spacers have been extensively used in assembly design of LM-FRs (mostly sodium-cooled ones) [139] because, besides holding the fuel pin in position, they enhance mixing mechanisms, although increasing pressure drops over the core. The presence of the helical wire generates a periodic transverse flow pulsation, with frequency inversely proportional to the wire lead pitch. In the interior SCs the wire sweeps the flow in all directions, while in the peripheral SCs it passes in only one direction thus originating a swirl flow (i.e. the flow follows the wire). This pulsation creates pressure waves which are responsible for the enhanced pressure drops and mixing.

The flow pulsation is a local effect since it depends on the position of the wire relative to the gap: when the wire passes the gap the actual mass and energy exchange takes place. ANTEO+, however, does not deal with local correlations or phenomena but with quantities averaged over a representative length (i.e. the wire lead pitch), for this reason the position of the wire will be ignored. To be sure that this average is truly representative the lead pitch must be shorter than the bundle axial height.

Three correlations have been implemented in the code with various degrees of modeling and empiricism, in order to give the user a broad spectrum of choices, as was done for the friction factor.

Nijsing The correlation proposed in [86] is based only on theoretical geometric considerations and it does not involve any kind of data fitting; for this reason it is probably the simplest of all the wire mixing models.

The main idea behind this method is that the wire sweeps an annular sector as it passes through the gap between channels; this, considering that the mixing is a periodic event with period proportional to half the wire lead pitch, suggests that the average mixing rate per unit length can be written as

$$W_{ij,wire}^H = \frac{1}{2}D_w\pi\frac{D+D_w}{H}\rho_{ij}v_{ij} \quad , \tag{7.32}$$

where $W_{ij,wire}^H$ is the mass exchange for energy transfer solely due to the wire; to complete the range of mixing phenomena, pure turbulent and con-

....

duction effects must be linearly added. These effects are taken into account
in the model by Kim previously highlighted that can thus be used for this
superposition.

The above relation is valid for internal SCs only; for edge and corner
SCs, the sweep is unidirectional so that the expression becomes

$$W_{ij,wire}^{H} = D_w \pi \frac{D + D_w}{H} \rho_{ij} v_{ij} \quad . \tag{7.33}$$

Neglecting differences in velocity, the wire effect is, in the wall region, twice
the one in the internal zone. Because no data fitting was performed, no
specific validity range is prescribed.

Zhukov Contrary to the correlation by Nijsing this one is mainly experi-
mental. The founding theoretical consideration of the model is the periodic
nature of the sweeping effect assumed to be represented only by the first
harmonic [15]. The mixing rate is expressed as

$$W_{ij,wire}^{H} = \rho_{ij} v_{ij} \frac{A_i + A_j}{2} \frac{1.047 \sigma'}{H} \Phi \left(\frac{P}{D} \right) \Psi(Re) \sin(\varphi_{ij}) \quad , \tag{7.34}$$

where $\varphi_{ij} = \frac{2\pi z}{H} - \alpha'_{ij}$ and α'_{ij} is the wire wrap phase entering the j-th SC
from the i-th one. Averaging the last expression over the wire lead pitch we
finally arrive at

$$W_{ij,wire}^{H} = \rho_{ij} v_{ij} \frac{A_i + A_j}{2} \frac{\sigma'}{3H} \Phi \left(\frac{P}{D} \right) \Psi(Re) \quad , \tag{7.35}$$

where σ' is a parameter relating efficiencies in mass and energy transfer
assumed equal to 0.7, Φ is an empirical function of the pitch-to-diameter
ratio and Ψ is an empirical function of the Reynolds number. A similar
approach is used for wall SCs. This model, similarly to the one by Nijsing,
calculates only the wire contribution to thermal mixing and must thus be
coupled to the model by Kim.

The formula accuracy is claimed to be 10% inside the validity domain:

- $1.01 \leq \frac{P}{D} \leq 1.4$

- $2 \leq \frac{H}{D} \leq 50$

- $2000 \leq Re_b \leq 2 \times 10^5$.

....

Cheng-Todreas   Consistently with the friction factor another correlation Cheng and Todreas (CTm) [24] has been implemented. Contrarily to other correlations this one is of the comprehensive type since it encompasses all principal types of mixing and not just the flow sweeping of the wire (see also 7.2.5). The flow sweeping effect is handled in different ways for interior and wall SCs; in fact in the internal ones the wire sweeps flow in a bidirectional fashion similar to what happens with turbulent exchange, and so these two mechanisms are grouped together, while for wall SCs the sweep effect is unidirectional and so is treated separately from other terms (i.e. linearly added).

Interior   In the interior SCs the wire sweeping and the turbulence effects are correlated together by means of the eddy diffusivity ϵ_{ij} concept, which is linked to W_{ij}^H by

$$W_{ij}^H = \frac{\rho_{ij}\epsilon_{ij}s}{\eta} \quad . \tag{7.36}$$

In the actual correlation the dimensionless parameter $\frac{\epsilon_{ij}}{v_{ij}\eta}$, similar to the Stanton's number, is used.

Wall   For wall SCs (i.e edge and corner) the unidirectional flow sweeping effect is expressed as

$$W_{ij,wire}^H = s\rho_{ij}v_{ij}C_1 \quad , \tag{7.37}$$

where C_1 is the dimensionless transverse velocity defined as the ratio between the transverse and axial velocity components. In the last equation it was supposed that the transverse velocity is the same for all wall SCs (this assumption stems from considerations on the continuity equation and the constant mass flow assumption).

$\epsilon_{ij}/(v_{ij}\eta)$ and C_1 are correlated for both laminar and turbulent conditions; in the transition region, the intermittency function is used similarly as for the friction factors (Section 7.2.1).

The proposed validity range is:

- $1.067 \leq \frac{P}{D} \leq 1.35$

- $4 \leq \frac{H}{D} \leq 52$

- $7 \leq N_{pin} \leq 217$

- $400 \leq Re_b \leq 10^6$

. . . .

in which $\epsilon_{ij}/(v_{ij}\eta)$ and C_1 can be predicted with 25% and 15% accuracy respectively.

The three correlations for wire spaced bundles are compared in Figure 7.6. The simple approach proposed by Nijsing is in poor agreement with the other experimental correlations for this geometric arrangement, increasingly with higher Reynolds numbers.
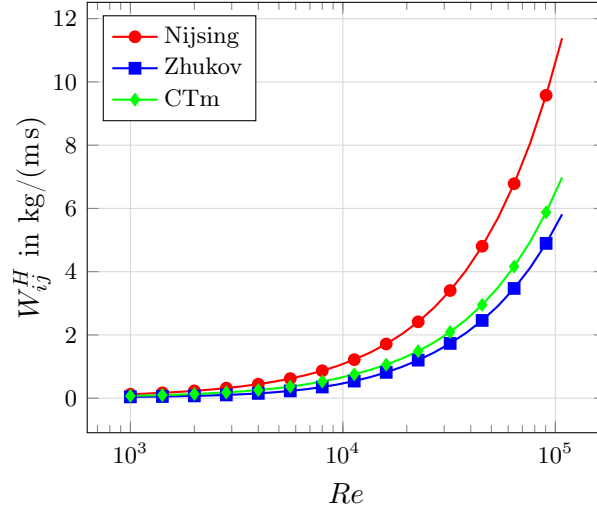
Figure 7.6: Comparison between wire thermal mixing correlations implemented in ANTEO+. The following parameters were assumed: $\frac{P}{D} = 1.1$, $\frac{W}{D} = 1.1$, $\frac{H}{D} = 10$ and $Pr = 0.025$ corresponding to lead. The contribution given by Kim's correlation has been added to Zhukov and Nijsing.

7.2.5   Conduction shape factor

The conduction shape factor κ appears in the conduction term of the energy equation (7.8). In this, the temperature gradient is approximated as a finite difference and the representative length is taken as the centroid-to-centroid distance η which is not, however, the correct one. The conduction shape factor is introduced in order to correct the finite difference and stems from the lumped nature of the SC approach.

In ANTEO+ two correlations have been implemented.

....

Cheng-Todreas As stated in paragraph 7.2.4 the mixing correlation of Cheng and Todreas [23] is comprehensive, and as such even molecular heat conduction is modeled. In particular κ is expressed as

$$\kappa = 0.66 \left(\frac{P}{D} \right) \left(\frac{s}{D} \right)^{(-0.3)} \quad , \tag{7.38}$$

which was proposed for bare bundles and is assumed to be applicable also to wire spaced ones. It has to be mentioned that it can only be applied to hexagonal arrangements.

Ma In [72] a method was developed to make use of the correlations and experimental data of annuli to obtain the heat transfer rate of LMCs flowing in rod bundles. Their interaction correction factor was found to be generally related to the conduction shape factor and correlated as

$$\kappa = 0.5 \left(\frac{\frac{D_{an}}{D} - 1}{\frac{P}{D} - 1} \right) \quad , \tag{7.39}$$

where D_{an} is the outer diameter of the equivalent annulus. The correlation can be applied to square and hexagonal bundles.

The two correlations are compared in Figure 7.7 for hexagonal geometry. They are in good agreement in the plotted range.

7.2.6 Nusselt number

For calculating the cladding outer temperature with equation (7.9) the convection coefficient α_p must be determined; this can be done via the Nusselt's number.

In ANTEO+ two categories of correlation have been implemented:

- the first, for the interior pins, includes the correlation by Mikityuk [79] for hexagonal bundles and that by Ma [72] - conceived in parallel with the conduction shape factor described in Section 7.2.5 - applicable to both square and hexagonal pin arrangements;

- the second, for near-wall pins only, includes the correlation by Zhukov [49] for hexagonal bundles.

The second category is built with a pin-center logic, meaning that the Nusselt's number relates the average coolant temperature of the SCs surrounding a pin with the average cladding temperature of that pin; since for

. . . .
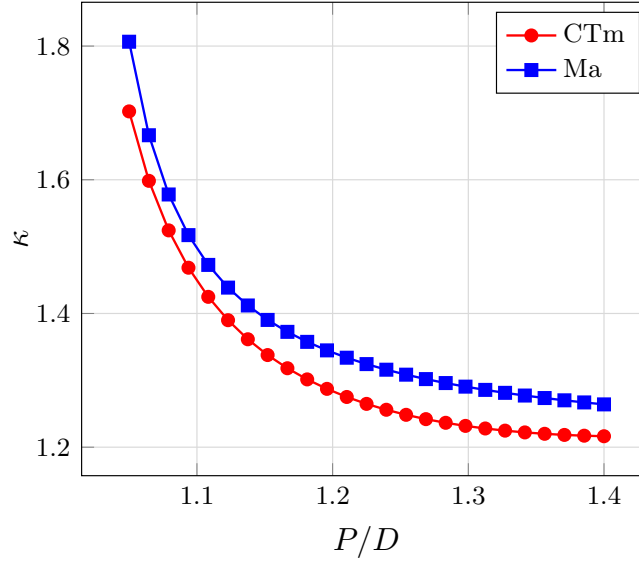
Figure 7.7: Comparison between correlations for the conduction shape factor implemented in ANTEO+.

near wall pins the difference among the SCs can be significant it is important to apply it correctly. On the contrary, the first category, can be reasonably employed both in a pin- or SC-center logic because the temperature variation around an interior pin is generally low[4].

Mikityuk

The correlation for Nu has the form

$$
\begin{aligned}
Nu = &4.7 \times 10^{-2} \left(1 - \exp \left(-3.8 \left(\frac{P}{D} - 1 \right) \right) \right) \\
&(250 + (Re \cdot Pr)^{0.77}) \quad .
\end{aligned}
\tag{7.40}
$$

Recently in [99] the authors compared this correlation with experimental data for lead-bismuth in hexagonal geometry; satisfactory agreement was found.

---

[4]It can be non negligible only if very strong power gradients are present or for tightly packed pin bundles.

....

Ma

The correlation has the following form,

$$Nu = \left(4.82 + 0.697 \cdot y + 0.022 \left(\frac{Re \cdot Pr}{Pr_T}\right)^{0.758 \cdot y^{0.053}}\right) \cdot$$
$$C_h C_t C_i C_s \quad, \tag{7.41}$$

where y is the ratio between the external and internal radius of the equivalent annulus while C_h, C_t, C_i and C_s are correction parameters accounting for the annulus approximation.

Zhukov

The correlation has the following form for edge pins,

$$Nu = 4.69\frac{P}{D} - 4.131 + \left(0.577\frac{P}{D} - 0.566\right) \cdot$$
$$(Re \cdot Pr)^{\left(3.53\frac{P}{D}^2 - 8.71\frac{P}{D} + 5.97\right)} \quad, \tag{7.42}$$

and for corner pins,

$$Nu = 7.13\frac{P}{D} - 6.972 + \left(0.331\frac{P}{D} - 0.342\right) \cdot$$
$$(Re \cdot Pr)^{\left(5.27\frac{P}{D}^2 - 13.12\frac{P}{D} + 8.83\right)} \quad. \tag{7.43}$$

The declared validity range is:

- $1.04 \leq \frac{P}{D} \leq 1.3$

- $0.39 \leq \frac{W-D}{P-D} \leq 0.52$

- $30 \leq Pe \leq 3000$.

Outside this range the correlation is not reliable and must not be used.

The correlations are compared in Figure 7.8 where we see the decreasing Nusselt value going from interior to edge and the corner pins indicating the effect of the wrapper.

. . . .
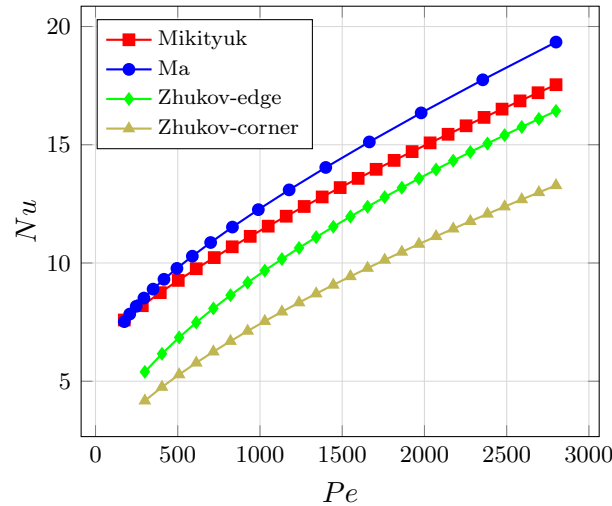
Figure 7.8: Comparison between Nusselt's number correlations implemented in ANTEO+. A $\frac{P}{D} = 1.2$ has been used and the pin arrangement has been assumed hexagonal.

7.3   Bypass model

Usually thermal hydraulic calculations at FA level are performed with the hypothesis that the bundle is adiabatic and so no heat is lost to the wrapper or other FAs. This holds true if thermal gradients between FAs are small, as near the core center (in standard configurations, e.g. without internal blankets) and the bypass flow rate is set proportional to the power directly deposited in the coolant so to maintain the nominal temperature gain for fuel elements also in the bypass. If a FA is placed side-by-side with a dummy element, a control or safety rod assembly, or if we are near the periphery; or in any case in which the coolant in the bypass has a remarkably different temperature than that inside the fuel elements, this could not hold true. Assuming that a pins bundle is adiabatic is however a conservative assumption, especially for the hottest one, so for safety reasons is acceptable. The above procedure has one disadvantage, namely, that the wrapper temperature itself cannot be estimated with some accuracy; moreover the effect the bypass has on the outer rows of pins is not accounted for. In order to calculate such effects a simple model has been devised and implemented in ANTEO+. The model is divided into two parts: first comes the calculation of the bypass flow rate if requested, otherwise a selected flow rate can be used; second is the

. . . .

calculation of the temperature distribution of the assembly coupled to the wall and bypass regions. The following sections briefly describe the model's features and range of applicability.

7.3.1 Bypass flow rate

A flow split model conceptually identical to the one presented in section 7.2.3 has been implemented where distributed and concentrated friction coefficients must be supplied, along with geometrical details of the flow path of the bypass and bundle regions (see Figure 7.9).

Equating pressure drops in both paths we find for the mass ratio bypass-bundle, labeled as $X_{BP,B} = \frac{\dot{m}_{BP}}{\dot{m}_B}$

$$X_{BP,B}^2 = \frac{\sum_{i'} \frac{K_{i'}}{A_{i'}^2} + \sum_{l'} f_{l'} \frac{L_{l'}}{D_{l'} A_{l'}^2}}{\sum_i \frac{K_i}{A_i^2} + \sum_l f_l \frac{L_l}{D_l A_l^2}} \quad , \tag{7.44}$$

where primed quantities refer to the bundle path while un-primed ones refer to the bypass path, K indicates the concentrated pressure loss coefficient. To close the system, equation (7.44) must be coupled with the mass conservation,

$$\dot{m} = \dot{m}_B + \dot{m}_{BP} \quad . \tag{7.45}$$

7.3.2 Heat transfer

To comprehend what level of detail is reasonable to retain in order to have reliable results compatibly with the structure of ANTEO+, a scale analysis has been performed. The key indicator is the ratio between the bundle outward Q_{out} and the transverse (i.e. perpendicular to the outward direction) Q_{tr} heat fluxes that, in typical fast reactor operating conditions, can be approximated as

$$\frac{Q_{out}}{Q_{tr}} = \frac{\Delta T_w}{T_{sc} - T_{bp}} \left(\frac{s_w}{P}\right)^2 \quad , \tag{7.46}$$

where ΔT_w is a temperature difference between two wrapper nodes, T_{sc} and T_{bp} are respectively a representative SC and bypass temperatures and s_w is the wrapper thickness. The above ratio measures how much two nodes are thermally similar: if it is low the nodes could be ideally grouped together without much loss of accuracy, but if it is high the nodes must be treated separately, accounting for their coupling. It is usually small [5], but in presence

---

[5]A similar analysis leads to the same conclusions for the transverse heat flux in the bypass region.

. . . .
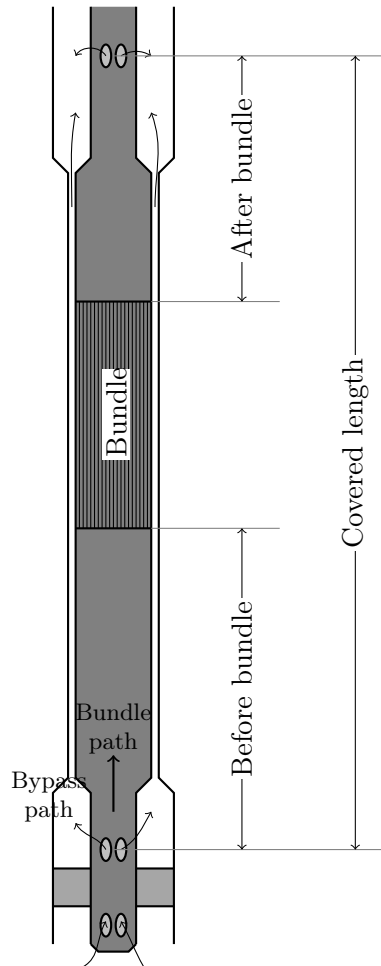
Figure 7.9: Example of a FA geometry with the bypass and bundle flow
paths.

of strong power gradients or uneven cooling of corner and edge SCs, however,
the flux ratio can increase. For properly modeling these phenomena the most
logical subdivision for the wrapper and bypass region is the same one used
in the SC definition (see Figure 7.10).

The energy conservation equation presented in section 7.1.4 must be aug-
mented with the exchange term between SCs and wrapper, which has the
form

$$\frac{T_w - T_i}{R_t} \quad ; \tag{7.47}$$

. . . .
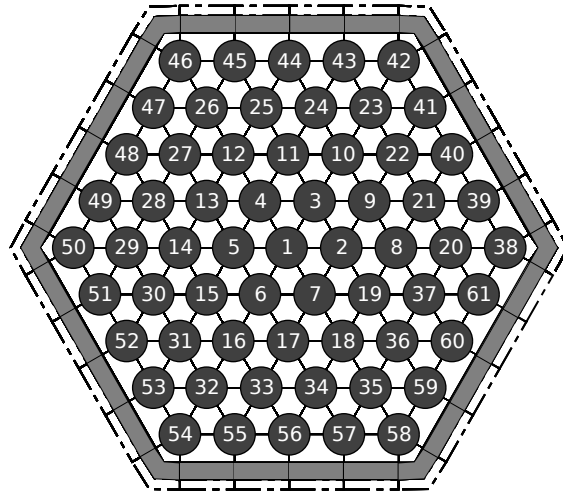
Figure 7.10: Representation of the nodalization scheme used in ANTEO+ for performing calculations including the bypass region between assemblies.

R_t is the thermal resistance between the SC and wrapper node centers, which is written as

$$R_t = \frac{1}{\alpha_{wr} A_{wr}} + \frac{s_w/2}{k_w A_{wr}} \quad , \tag{7.48}$$

where α_{wr} is the convection coefficient for thermal exchange between SC and wrapper, A_{wr} is the contact surface for the exchange and k_w is the wrapper thermal conductivity. The selected Nu_{wr} correlation used to calculate α_{wr} is the one presented in [119] for pipe flows, which was proven in [56] to have the closest agreement with **D**irect **N**umerical **S**imulation (DNS) calculations for a uniformly heated rectangular duct. This correlation is also recommended in [92] and has the following form

$$\begin{aligned} Nu_{wr} &= 5 + 0.015 \cdot Re^a \cdot Pr^b \\ a &= 0.88 - \frac{0.24}{4+Pr} \\ b &= \tfrac{1}{3} + 0.5 \exp(-0.6Pr) \quad . \end{aligned} \tag{7.49}$$

The reported validity range is:

- $Pr \leq 10$

- $10^4 \leq Re \leq 10^6$.

The energy balance of the bypass region is identical to the one outlined for the bundle SCs (as is the Nu correlation), but without the power discharged

. . . .

by the pin. A term for simulating power deposition/removal in this region
has also been added.

The conservation statement for a generic node in the duct region, equating the energy exiting the bundle (i.e. from SC to wrapper) to the power
directly deposited - by gamma rays - in the wrapper, the energy leaving the
wrapper (towards the by-pass) and the energy exchanged by conduction with
other wrapper nodes, can be written as

$$\frac{T_{sc} - T_w}{R_t} = q_{wr} + \frac{T_w - T_{bp}}{R_t} + \sum_j \Delta z \frac{s_w k_w}{\delta_w}(T_w - T_{w,j}) \quad , \qquad (7.50)$$

where q_{wr} is the power deposited in the wrapper and δ_w is the distance
between wrappers' nodes. The R_t factors in the right and left hand sides of
equation (7.50) are different only for a geometrical effect, solely present in
hexagonal bundles. The first term

7.4   Geometric capabilities

ANTEO+ has extended geometric capabilities which encompass both hexagonal and square arrangements enclosed in a casing duct. The possibility of
simulating pins of different size, structural rods, guide tubes with or without
control rods and edge channel displacers has been implemented into the code
in order to give the user some modeling flexibility. Internal structural walls,
like in the ELSY design [8], are also available both in hexagonal and square
geometries. Finally the innovative design feature proposed in [129] is also
present in ANTEO+; this consist of an inner discharge duct which prevents
coherent motion of the molten fuel within the bundle lattice and so reducing risk of recriticality, which is the main issue in case of **C**ore **D**isruptive
Accidents (CDAs). The above geometrical features are schematically illustrated in Figure 7.11.

(a) guide tube, with (as in the figure) or without a rod inside

(b) wrapper with rounded corners

(c) pin with different diameter

(d) wrapper displacers

(e) internal structural wall

(f) inner discharge duct
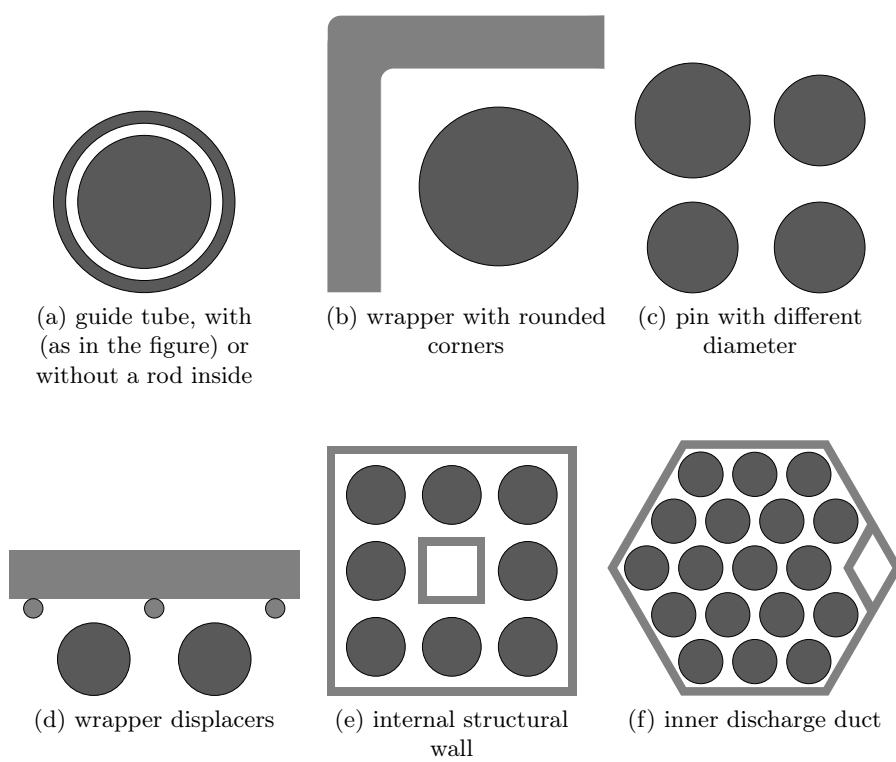
Figure 7.11: Examples of ANTEO+ geometrical modeling capabilites.

CHAPTER 8

VALIDATION

To ultimately estimate, in a quantitative way, the degree of reliability and range of application of a code, the comparison with experimental data, representative of the operating conditions and geometric configurations to which the code will be applied, is a mandatory step. This is part of the validation phase of a code.

SC codes, in particular, have empirical bases so understanding and clearly identifying their application domain can heavily help the user in the results interpretation phase. For this, in ANTEO+, the application range was decided beforehand (see Section 4.2.3) and thus validation takes on a slightly different scope, namely, to verify that the anticipated and actual validity domains coincide, thus supporting the derived set of equations and modeling approximations. As explained in Section 6.2 the expected range of application for ANTEO+ is the steady-state, single-phase forced convection regime, and consequently this is the main focus of the present work. Nonetheless, experiments falling out of this regime are analyzed in order to quantify extrapolation errors.

In this chapter, the models previously presented, encompassing flow split, pressure drops, SC temperatures and Nusselt's number are thoroughly validated; then, results are critically discussed.

To better contextualize ANTEO+ accuracy, a quantitative comparison with other SC codes, like COBRA-IV-I-MIT [37] and ENERGY-II [23], is reported. This will also highlight the advantages of ANTEO+, within its validity domain, over the standard development approach.

. . . .

8.1   Flow split

As explained in section 7.2.3 the flow split model could be coupled with any one of the friction factors described in section 7.2.1. In ANTEO+ however the flow split model can be used only in combination with Blasius or CT friction factor models; the former does not account for the different friction factors in each SC type and so can only be used for bare or gridded bundles in the turbulent region. The latter is more general encompassing wired, gridded and bare bundles in every flow regime.

The experimental data used in the validation are listed in Table 8.1. The data set is basically the one used in [23] with the addition of three cases. The results are summarized in Table 8.2 and Figures 8.1a and 8.1b; in these, three cases are reported: the whole ensemble of data point analyzed, the data in the turbulent region only and the data for bare bundles in the turbulent region. The last category is chosen according to the validity range of the Blasius based flow split model.

(a) CT model.

(b) Blasius model.
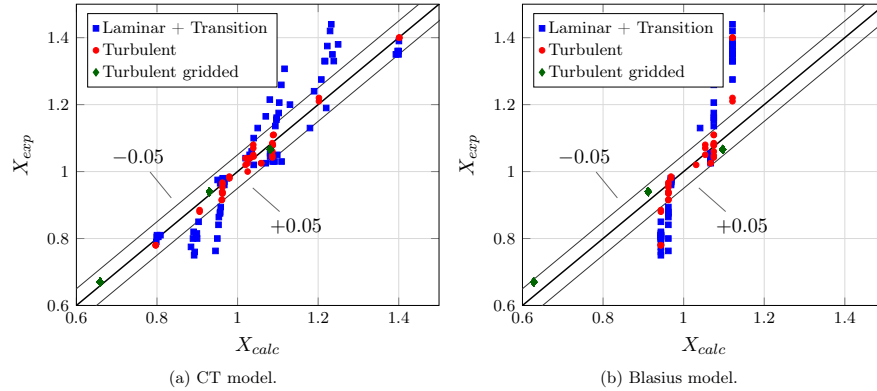
Figure 8.1: Comparison of ANTEO+ flow split models with experimental data used in the validation.

The flow split validation covers the following range:

- $1.067 \leq \frac{P}{D} \leq 1.3$

- $0 \leq \frac{H}{D} \leq 52$

- $19 \leq N_{pin} \leq 217$

- $320 \leq Re_b \leq 7.3 \times 10^5$,

which is deemed extensive and representative for ANTEO+ applications.

. . . .

Table 8.1: Collection of experiments used for flow split
models validation.

Ref.	N_{pin}	P/D	H/D	$Re(\times 10^3)$
Laminar				
Chen (1974)[a]	61	1.250	24.0	0.64
Chen (1974)[a]	61	1.250	48.0	0.64
Efthimiadis (1983)[a]	19	1.245	35.2	0.32
Turbulent				
Davidson (1971)[a]	217	1.283	48.0	20.0
Chen (1974)[a]	61	1.250	24.0	4.50
Chen (1974)[a]	61	1.250	48.0	4.50
Pederson (1974)[a]	91	1.210	48.0	20.0
Othake (1976)[a]	37	1.190	34.8	14.0
Bartholet (1976)[a]	217	1.257	51.7	73.0
Lorenz (1977)[a]	91	1.240	48.0	20.0
[81]	169	1.210	47.1	32.0-58.0
[112][b]	19	1.300	bare	60.0
Complete range				
[25]	37	1.155	21.0	3.00-13.9
Chiu (1978a)[a]	61	1.067	4.0	2.00-14.6
Chiu (1978b)[a]	61	1.067	8.0	1.00-21.8
Symolon (1981)[a]	217	1.250	51.7	1.80-12.7
Cheng (1982)[a]	37	1.154	13.4	3.47-26.3

[a] See [23] for reference.

[b] Only data set for gridded bundle.

Table 8.2: Summary of flow split models validation. Results
are presented differentiating flow regimes.

	$\bar{\varepsilon}[\%]^{\mathrm{a}}$	$\sigma[\%]^{\mathrm{b}}$	RMS $[\%]^{\mathrm{c}}$
Total (117 points)			
CT	4.8	6.8	6.8
Blasius	9.8	19.3	13.2
Turbulent region (43 points)			
CT	1.8	2.1	2.2
Blasius	5.9	9.7	9.6
Turbulent gridded bundle (3 point)$^{\mathrm{d}}$			
CT	1.2	-	1.2
Blasius	3.4	-	3.4

[a] defined as $\frac{\sum_{i=1}^{n} |x_{exp}-x_{calc}|}{n}$.
[b] standard deviation.
[c] Root Mean Square.
[d] no standard deviation is reported due to insufficient statistic.

Discussion   In [24] it is reported that the CT model can predict flow
split parameters within 5% error. In our finding this is not true in the whole
range, due to higher errors in the laminar region; in the turbulent region
however, accuracy drastically increases, and the error drops well below the
5% limit. This is especially true for bare bundles.

The Blasius correlation gains some accuracy only in the turbulent region
and for bare or gridded bundles, as expected.

Given the presented results, the recommended correlation to be used
in ANTEO+ is therefore the CT one. Blasius could be used in screening
calculations, inside its validity domain, for evaluating complex geometric
options.

8.2   Pressure drops

The bundle pressure drop ΔP_b can be expressed as

$$\Delta P_b = f_b \frac{1}{2} \rho v_b^2 \frac{L}{D_H} \quad , \tag{8.1}$$

....

Table 8.3: Collection of experiments used for pressure drops validation. Experiments cover only grid spaced bundles.

Ref.	Liquid	N_{pin}	P/D	$Re(\times 10^3)$
[117]	Water	19	1.40	8.0-73.0
[65]	Lead-Bismuth	19	1.40	21.1-55.5

where D_H is the bundle hydraulic diameter. From equation (8.1) we see that, neglecting geometric uncertainties, the validation of the friction factor and pressure drops are equivalent, and, as such, the latter is used for validating the friction factor models presented in section 7.2.1.

The friction factor must be validated for bare, grid spaced and wire spaced bundles; concerning the latter, in a recent article [22], the authors compared a number of correlations with a broad set of experimental data. In their analysis the two correlations for wired bundles presented in section 7.2.1, namely CT and Rehme-wire, were among the correlations analyzed. The authors concluded that the CT correlation has the best performances while Rehme-wire ranked lower. Because we deem their analysis representative of the anticipated application range of ANTEO+, the validation of the friction factor and pressure drops for wire spaced bundles is not reported here, but borrowed from [22].

The present section is therefore focused on the validation of gridded bundles pressure drops; experimental grid pressure losses, however, are subtracted from the overall ones in order to retrieve bare bundle results which are, in turn, directly comparable to the correlation reported in section 7.2.1. This choice stems from the wish of keeping the two effects separated and from the already proven ability of the general form of the grid loss coefficient presented in 7.2.2 of reproducing experimental data [34].

The experiments used in the validation are reported in Table 8.3. One, among the selected, employs water as a coolant, but because it is an isothermal zero power experiment, it is still a representative case for validating pressure drops of LMs. A summary of the results can be found in Table 8.4 and Figure 8.2.

The pressure drop validation for gridded bundles (the one for wire spaced bundles is borrowed from [22]) covers the following range:

- $\frac{P}{D} = 1.4$

- $N_{pin} = 19$

. . . .

Table 8.4: Results summary for pressure drops
validation of grid spaced bundles.

	$\bar{\varepsilon}_{rel}[\%]$[a]	$\sigma[\%]$	RMS [%]
Total (21 points)			
CT	3.3	4.1	3.9
Rehme	6.5	8.0	8.1
Blasius	4.6	5.8	5.7

[a] defined as $\dfrac{\sum_{i=1}^{n}\frac{|x_{exp}-x_{calc}|}{x_{exp}}}{n}$.
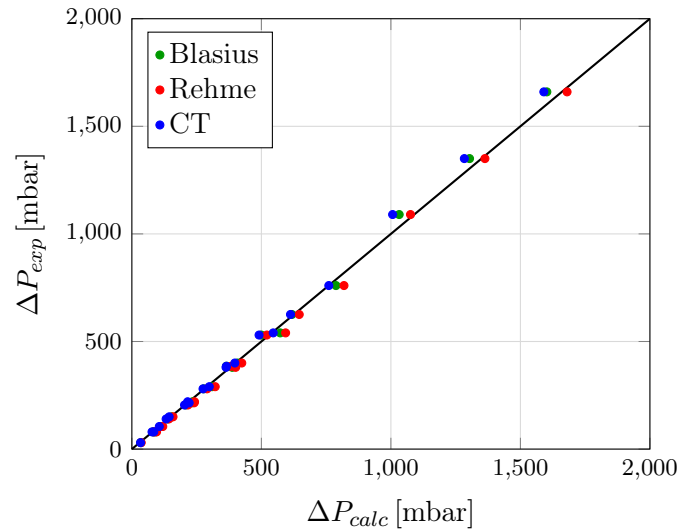
Figure 8.2: Comparison of models with experimental data used in the
validation of pressure drops for grid spaced bundles.

. . . .

Table 8.5: Comparison between calculated and
experimental bundle average temperature gain
for the experiment described in [65].

	$\bar{\varepsilon}_{rel}[\%]$	$\sigma[\%]$	RMS [%]
Total (24 points)	1.1	1.3	1.5

- $8.0 \times 10^3 \leq Re_b \leq 5.5 \times 10^5$,

which is not as extensive as the one used for the wired spaced bundles, principally due to the lack of experimental data for gridded bundles cooled by liquid metals.

Discussion   Of the three correlations analyzed in Section 8.2, the one with the best agreement with the data is CT ($\bar{\varepsilon}_{rel} = 3.3\%$), followed by Blasius (4.6%) and Rehme (6.5%). The agreement for the CT model with experimental data is deemed acceptable and is the recommended one to be used in ANTEO+.

8.3   Temperatures

The assessment of the ability of a SC code in reproducing experimental steady state SCs temperature distributions is of paramount importance. A SC temperature can effectively be a tight design constraint, moreover it is used in estimating the thermal-hydraulic feedback effects on neutronic performances and as initial condition in safety analyzes. Finally, in the evaluation of SC temperatures distribution, the overall performances of the code can be effectively tested, because, in solving the conservation equations all the models outlined in section 7.2 play along with the inherent approximations of ANTEO+. For these reasons a thorough validation is now presented.

8.3.1   Bundle temperature

Before starting with the local SC assessment an integral experiment is analyzed, in order to ascertain the accuracy of some of the equations of state presented in Section 7.1.7. The experiment taken from [65], already used in section 8.2, employs lead-bismuth as a coolant. The results are summarized in Table 8.5 and Figure 8.3.

. . . .

(a) $T_{in} = 200°C$

(b) $T_{in} = 350°C$
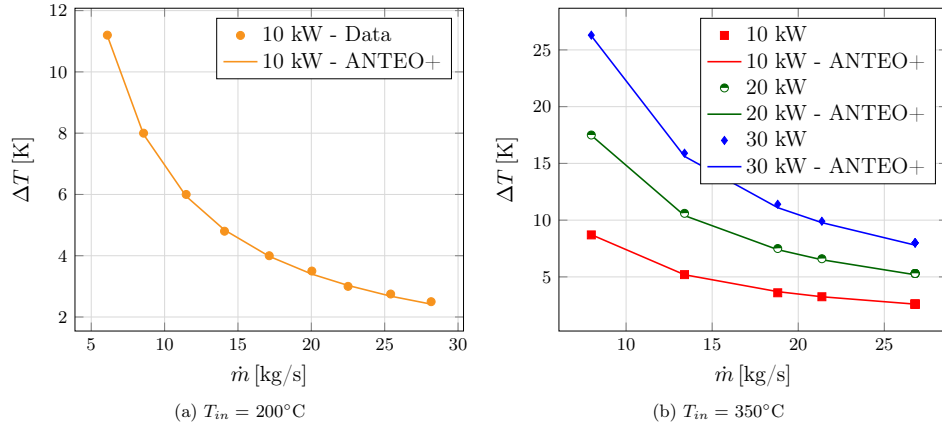
Figure 8.3: Graphical representation of calculated and experimental bundle average temperature gain for the lead-bismuth experiment described in [65]. Dots represent experimental data, while continuous lines represent ANTEO+ results.

Discussion   ANTEO+ performs well in this experiment, with an error of 1.1%, proving the validity of the state equation implemented for this coolant. While sodium has been extensively used in the past, and so, some confidence on its physical properties has been gained, lead still needs further verification, even if LBE results are quite encouraging in this sense.

8.3.2   SC temperatures

A sizeable number of cases has been simulated as reported in Table 8.6, trying to cover the anticipated application domain of ANTEO+. The majority of them involves sodium as a coolant; they will be treated first[1]. Then the ones involving HLMs will be presented and discussed highlighting similarities and differences with sodium.

As stated at the beginning of the chapter, cases outside the anticipated validity range of ANTEO+, namely, single phase forced convection, have been also simulated; these cases fall in the so called mixed convection regime in which free and forced convection are equally important. Mixed convection cases are only used, in the present chapter, to highlight in a more quantita-

---

[1]Sodium-cooled cases are included in the validation due to the large availability of experimental campaigns with this coolant that, will help in understanding the degree of confidence to recognize to ANTEO+ results.

. . . .

tive way extrapolation errors and make the reader aware of the consequences of violating the validity range of ANTEO+. For a discussion on mixed convection modeling problems and specificities the reader is referred to Chapter 9. In order to roughly estimate the degree of natural convection and thus how much the operating conditions are far from ANTEO+ domain, a parameter called Y, similar to the Richardson's number, has been used; Y is defined as[2]

$$Y = \frac{Gr}{Re^2} \quad , \tag{8.2}$$

where Gr is the Grashof's number based on the axial temperature rise. Y is basically the ratio of the buoyancy forces, drivers of thermal mixing, and axial pressure drops, responsible for axial mass flow.

From the results outlined in [31] the value of $2.5 \cdot 10^{-5}$ has been detected as the discriminant between forced and mixed convection; this corresponds to a reduction of approximately 10% of the maximum temperature gain relative to fully forced convection. Henceforth the reported values of Y will be normalized to the reference value; if greater than unity, mixed convection is important and we are falling out of ANTEO+ validity domain. It must be said that this estimate is only qualitative because a complex phenomenon like the onset of mixed convection in a fuel pin bundle with spacers has been collapsed into a single number.

In order to ease data reading from the following tables, the rows which represent cases in the anticipated validity range of ANTEO+ have been highlighted with a gray background.

Sodium-cooled experiments

ORNL-19 In [35] a 19 pins bundle, part of the Fuel Failure Mockup facility, with the aim of testing operating conditions of liquid metal cooled systems has been used. The selected cases for this bundle are reported in Table 8.7, where COBRA-IV-I-MIT (hereafter simply referred to as COBRA) results taken from [37] are also included, when available. In Figure 8.4b a visual comparison is given where the SC labels on the abscissa are highlighted in Figure 8.4a; the ordinate is the normalized temperature gain expressed as

$$\Delta T_{norm} = \frac{T - T_{in}}{T_b - T_{in}} \quad , \tag{8.3}$$

---

[2]This definition differs from the one in [68] because it is believed to be more reliable and scalable to different coolants being inferred from more general grounds.

. . . .

Table 8.6: Collection of experiments used for SC temperature validation. Main physical and geometrical parameters are also given.

Ref.	Coolant	N_{pin}	P/D	H/D	$Re(\times 10^3)$
Hexagonal - wire spacer					
[35]	Na	19	1.243	52.2	0.90-68.9
[84]	Na	37	1.210	47.2	0.86-11.9
[83]	Na	61	1.243	52.2	49.0-73.0
[33]	Na	61	1.082	7.70	0.50-13.0
[108]	Na	91	1.067	11.4	0.60-3.27
[100]	LBE	19	1.279	40.0	37.8
[71]	LBE	61	1.116	25.0	49.8
Square - grid spacer					
[145]	NaK	25	Variable[a]	-	53.4

[a] Pins with different diameters are present.

where T_{in} is the inlet temperature and T_b is the average bundle outlet temperature.

In order to keep this subsection clean and understandable, all the results presented in the validation of SC temperatures for hexagonal wire spaced bundles cover only the CTm correlation, which is the best among the ones introduced in section 7.2.4 for this type of bundle. The other correlations results are summarized in Table 8.15.

Discussion   For this bundle various power skews have been analyzed and it can be seen, from Table 8.7, that the error seems to increase at higher skews. The highest error is in the internal SC near the wall, possibly due to the inaccurate value of the mixing coefficient in this region; it must be said that being the power almost uniform in Figure 8.4b, SCs 7 and 16 should have similar temperatures, as predicted by the code, but not experimental data, giving an hint on experimental uncertainties in this bundle. The general agreement is however satisfactory with an average error of 3.5% and, for the analyzed cases, lower than the one obtained with COBRA.

Toshiba-37   In [84] experiments performed on a 37 pins bundle used by the Toshiba Corporation Nuclear Engineering Laboratory in Japan are described. The bundle comprises three regions which can operate at different

. . . .

Table 8.7: Comparison summary between simulations and ORNL-19 bundle experimental data.

Identifier	Power (kW)	Flow rate (kg/s)	Y	$\bar{\varepsilon}[\%]$	
				ANTEO+	COBRA
Power Uniform					
Test 2 - Run 105	322.3	3.06	0.00	3.9	5.4
Power skew 1.25					
Test 4 - Run 105	31.13	0.27	0.38	3.7	-
Test 4 - Run 101	4.940	0.07	4.86	0.9	0.9
Power skew 3.0					
Test 14 - Run 101	16.52	2.99	0.00	5.4	-

(a) Experimentally instrumented SCs and corresponding ANTEO+ numeration.

(b) ANTEO+ simulations vs. experimental data for Test 2-Run 105
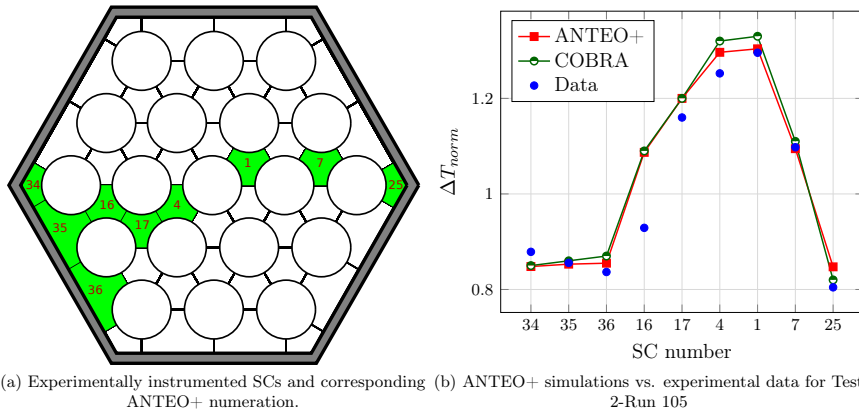
Figure 8.4: Representation of ANTEO+ simulations and SC temperature experimental data for Test 2-Run 105.

power levels, thus enabling transverse power skews to be simulated; moreover the axial power shape is a chopped cosine with an axial factor of 1.2. Three different skews, each one in three different flow conditions, were examined as reported in Table 8.8 along with the results of the simulations.

From Table 8.8 it can be seen that errors are higher for the skew cases; in [84] an estimate for the heat loss through the duct is given as 2.5 % of the

. . . .

Table 8.8: Comparison summary between simulations and Toshiba-37 bundle experimental data.

Identifier	Power (kW)	Flow rate (kg/s)	Y	$\bar{\varepsilon}[\%]$	
				ANTEO+	COBRA
Power uniform					
B37P02	53.60	1.37	0.01	3.6	3.6
C37P06	41.02	0.31	0.80	1.3	1.5
E37P13	13.40	0.09	11.5	1.5	0.6
Power skew 1.40 [a]					
E37P17	53.50	0.93	0.04	4.8	5.7
F37P20	53.82	0.31	1.00	1.9	1.9
F37P27	32.56	0.17	4.39	5.1	4.2
Power skew 1.96					
G37P22	54.57	0.92	0.04	8.5	9.0
G37P25	54.57	0.31	1.18	5.6	4.6
L37P43	34.13	0.14	7.75	6.6	2.3

[a] Skew defined as the maximum-to-minimum power ratio.

power discharged to the SCs, which can partially explain the higher errors just mentioned. To test this hypothesis simulations with the bypass model explained in section 7.3 were carried out adjusting the bypass flow in order to have approximately 2.5 % of heat losses. The same simulations were performed in [37] and results are outlined in Table 8.9. A visual comparison of COBRA and ANTEO+ can be found in Figure 8.6 where the SC numbers are the ones highlighted in Figure 8.5.

Discussion   As for the ORNL-19 bundle the error increases with the skew, while it decreases entering the mixed convection regime. The last effect is possibly due to the higher importance that heat losses have when buoyancy forces are not negligible anymore.

Results obtained by ANTEO+ and COBRA are quite in line for this bundle, with accuracy assessing around 4.3%.

. . . .

Table 8.9: Comparison summary between simulations and Toshiba-37 bundle experimental data when 2.5 % heat losses are taken into account.

Identifier	$\bar{\varepsilon}[\%]$			
	Adiabatic		2.5% heat losses	
	ANTEO+	COBRA	ANTEO+	COBRA
Power uniform				
B37P02	3.6	3.6	2.5	2.7
C37P06	1.3	1.5	2.3	2.1
E37P13	1.5	0.6	1.5	1.7
Power skew 1.40				
E37P17	4.8	5.7	4.0	3.8
F37P20	1.9	1.9	2.7	3.2
F37P27	5.1	4.2	3.0	2.3
Power skew 1.96				
G37P22	8.5	9.0	7.2	7.7
G37P25	5.6	4.6	4.5	3.4
L37P43	6.6	2.3	4.3	3.4

ORNL-61   The experimental bundle described in [83] is geometrically identical to the ORNL-19 bundle, only the number of pins and the axial shape of the power profile (which is a chopped cosine with form factor of 1.38) are different. Measurements at three different axial locations were taken. As in the Toshiba-37 bundle the possibility of simulating power skews is present, but with an higher spatial resolution, since each row of pins has a modular power.

Results are presented in Table 8.10, where distances are taken from the beginning of the heated length, and visually in Figure 8.8 where the SC numbers are the ones highlighted in Figure 8.7.

Discussion   For this 61 pins bundle the power skew effect seems to be less important; this suggests that for bigger pins arrangements the spatial power profile is bound to be less determinant. The error remains pretty low for the two simulated cases and along the heated length, assessing around 3.3%.

. . . .
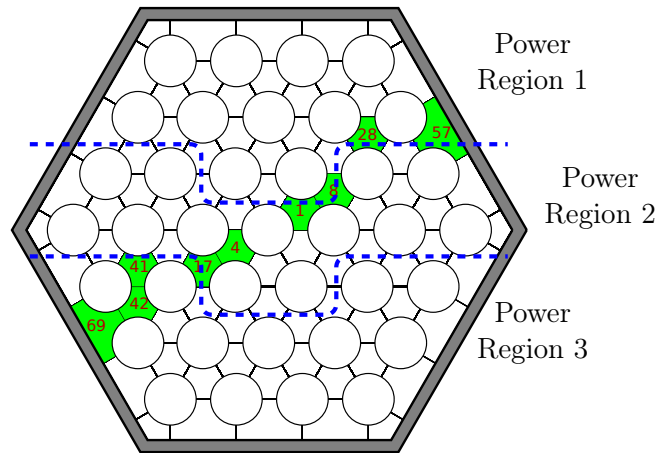
Figure 8.5: Experimentally instrumented SCs and corresponding ANTEO+ numeration for the Toshiba-37 bundle.

Table 8.10: Comparison summary between ANTEO+ simulations and ORNL-61 bundle experimental data.

Identifier	Power (kW)	Flow rate (kg/s)	Y	$\bar{\varepsilon}[\%]$		
				53.4 cm	63.5 cm	94.0 cm
Power uniform						
Run 1-4	1,220	8.490	0.00	2.9	4.5	2.1
Power skew 3.0						
Run 19-101	821.5	5.660	0.17	3.9	3.2	3.2

WARD-61   The **W**estinghouse **A**dvanced **R**eactors **D**ivision (WARD) experimental bundle has 61 electrically heated pins [33]. The WARD-61 bundle provides the largest collection of data of the present validation, thanks to the high number of operating conditions investigated. As the ORNL-61 bundle, each row of pins has modular power and the axial power shape is a chopped cosine with form factor of 1.4. Measurements were taken at a

. . . .

(a) Run B37P02

(b) Run F37P20

(c) Run L37P43 - Mixed Convection with
$Y = 1.89$
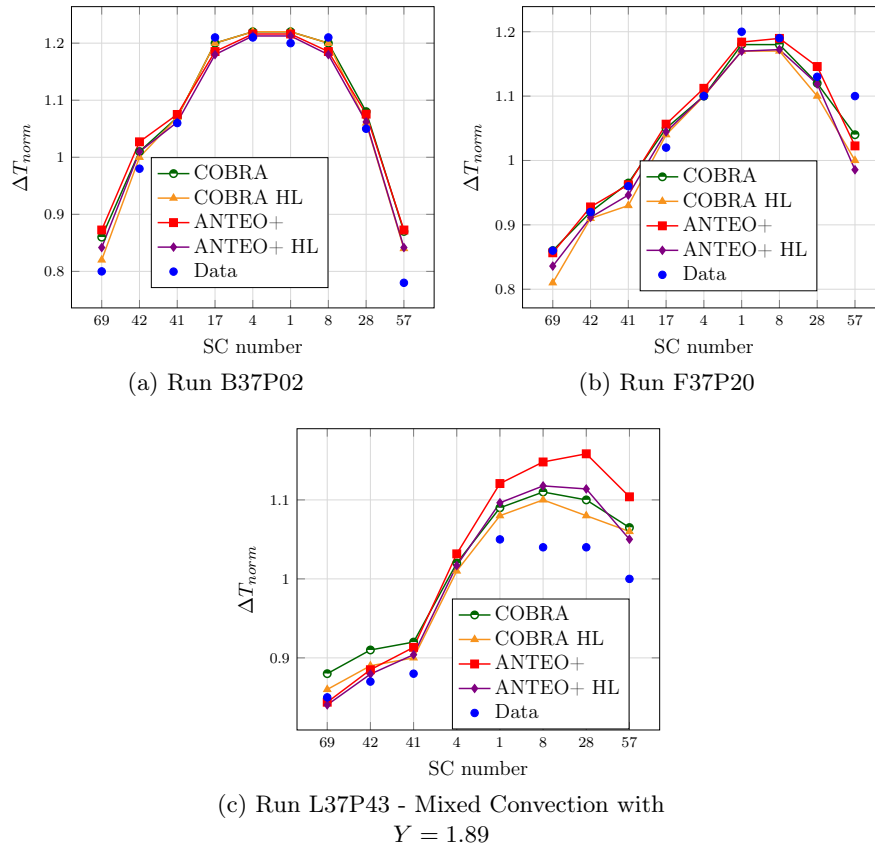
Figure 8.6: Representation of experimental and simulations results for some illustrative runs of the Toshiba-37 bundle. In the plots HL means simulation with heat losses.

number of axial locations giving the possibility for validating the axial distribution along with the radial one; planes downstream the heated length are present; moreover, thanks to thermocouples placed in the edge channels, a detailed representation of the near wall temperature distribution is available for comparisons.

The selected cases are reported in Table 8.11 where runs from 1 to 6 are not officials numbers; beside the uniform power case, three radial skews were simulated, where the one labeled 1.5:1:1.5 represents an U-shaped power profile. Simulations results are shown in Table 8.12 where the SC code
. . . .

Measured elevations

63.5 cm, 94.0 cm   53.4 cm
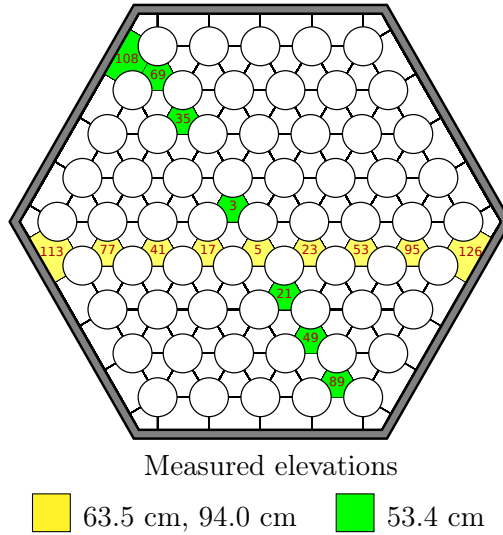
Figure 8.7: Experimentally instrumented SCs and corresponding ANTEO+ numeration for the ORNL-61 bundle.

(a) ANTEO+ simulations vs. experimental data results for Run 19-101. Dots represent experimental data, while continuous lines represent ANTEO+ results.

(b) ANTEO+ simulations vs. experimental data results for Run 19-101. Dots represent experimental data, while continuous lines represent ANTEO+ results.
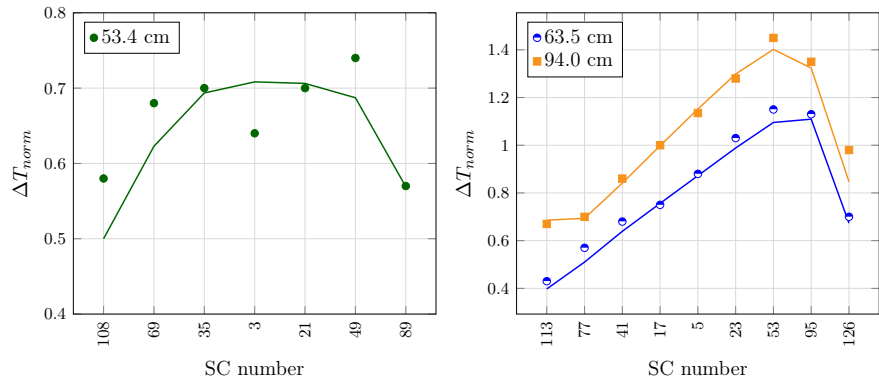
Figure 8.8: Representation of experimental and ANTEO+ simulations results for the Run 19-101 of the ORNL-61 bundle.Dots represent experimental data, while continuous lines represent ANTEO+ results.

ENERGY-II [23] is included in the comparison[3]; distances are relative to the beginning of the heated section which is 114.3 cm long. A graphical

---

[3]hereafter simply labeled ENERGY.

. . . .

representation of the results is given in Figure 8.10 where SCs numbers are highlighted in Figure 8.9. In Figure 8.11a the near wall SCs temperature distribution is compared with ANTEO+, while in Figure 8.11b the axial distribution of three SCs, comprising both heated and unheated lengths, is plotted along with COBRA results.

Table 8.11: Main parameters of the simulated runs for the WARD-61 bundle.

Run	Power (kW)	Flow rate (kg/s)	Y
Power uniform			
1	440.0	3.346	0.07
224	260.0	2.033	0.19
218	130.0	0.978	0.86
2	34.00	0.257	12.3
Power skew 1.5:1:1.5			
3	440.0	3.200	0.08
4	165.0	1.132	0.70
5	44.00	0.283	11.9
6	22.00	0.141	47.7
Power skew 2.0			
403	264.0	2.033	0.19
Power skew 2.8			
313	440.0	3.346	0.07
223	260.0	2.033	0.19
221	130.0	0.978	0.86
231	34.00	0.257	12.3
229	17.00	0.129	49.1

Discussion A great number of cases was simulated for this bundle giving the possibility of better studying the effects of power skews and buoyancy on ANTEO+ accuracy.

It seems that for uniform skews the effect of buoyancy is less prominent due to the already flat temperature profile; increasing the skew however

....

Table 8.12: Comparison summary between simulations and WARD-61 bundle experimental data.

Run	$\bar{\varepsilon}$ [%]								
	57.2 cm			115.6 cm			179.1 cm		
	ANTEO+	COBRA	ENERGY	ANTEO+	COBRA	ENERGY	ANTEO+	COBRA	ENERGY
Power uniform									
1	-	-	-	5.3	13.3	-	-	-	-
224	2.0	2.5	2.4	2.4	3.9	2.6	1.1	5.5	2.2
224 edge	-	-	-	2.1	-	-	-	-	-
218	2.4	1.2	-	3.8	3.9	-	1.3	3.5	-
2	5.3	2.7	1.6	4.1	2.1	2.7	1.2	1.2	-
Power skew 1.5:1:1.5									
3	7.1	8.7	-	4.3	4.5	-	1.4	4.7	-
4	4.4	6.1	-	2.7	2.4	-	1.1	3.8	-
5	3.1	1.4	-	4.7	2.1	-	6.1	7.3	-
6	1.8	4.9	-	1.8	3.3	-	3.8	4.4	-
Power skew 2.0									
403	5.1	-	4.5	5.7	-	5.4	3.2	-	4.4
403 edge	-	-	-	6.0	-	-	-	-	-
Power skew 2.8									
313	3.7	7.3	-	2.8	15.8	-	3.5	16.2	-
223	3.0	10.9	2.5	3.8	10.2	3.6	2.9	14.4	3.7
223 edge	-	-	-	6.1	-	-	-	-	-
221	2.7	2.3	6.7	6.3	9.0	2.9	3.0	12.6	5.1
231	8.8	4.2	6.2	12.4	5.6	4.2	6.5	5.1	4.4
229	10.6	3.1	3.5	11.5	1.4	3.9	8.0	4.5	3.1
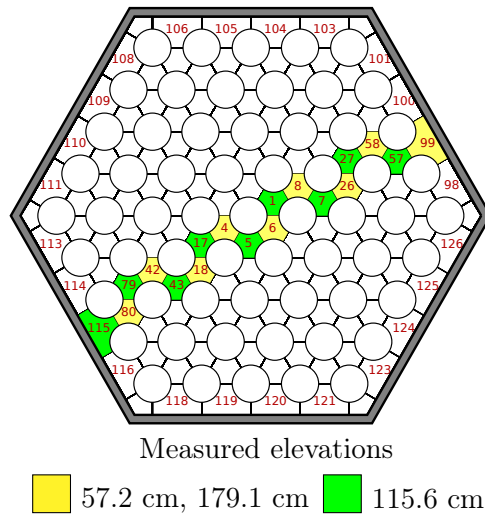
Figure 8.9: Experimentally instrumented SCs and corresponding ANTEO+ numeration for the WARD-61 bundle.

magnifies the effect of flow redistribution and the error grows larger (e.g. from 2.8% to 12.4% for the maximum skew analyzed).

The error drastically decreases far downstream the heated section, down to 2.2%, due to the mixing flattening effect and as before it is less sensitive to flow redistribution (5.1 % in the mixed regime).

Comparing with other SC codes we see that inside its validity range, ANTEO+ performs usually better than COBRA and in line with ENERGY. In the mixed convection cases the error increases and the other codes are able to better reproduce experimental results.

This bundle offered also the possibility of testing the capability of predicting also the near-wall SC temperature distribution, which was done providing more than acceptable results (error around 4.7%) as shown in Figure 8.11a. Similarly the axial temperature shape has been investigated, as shown in Figure 8.11b, with some success. ANTEO+ is better able to follow the experimental shape compared to COBRA with accuracies respectively of 3.6% and 8.2%. In particular, it can be seen that COBRA does not follow the data after the end of the heated length where the only non-zero term in the energy equation is thermal mixing. ANTEO+, thanks to its simplified and robust models, seems able to correctly reproduce the observed trend.

. . . .

(a) Run 224

(b) Run 3

(c) Run 403

(d) Run 313

(e) Run 229 - Mixed Convection with $Y = 3.2$
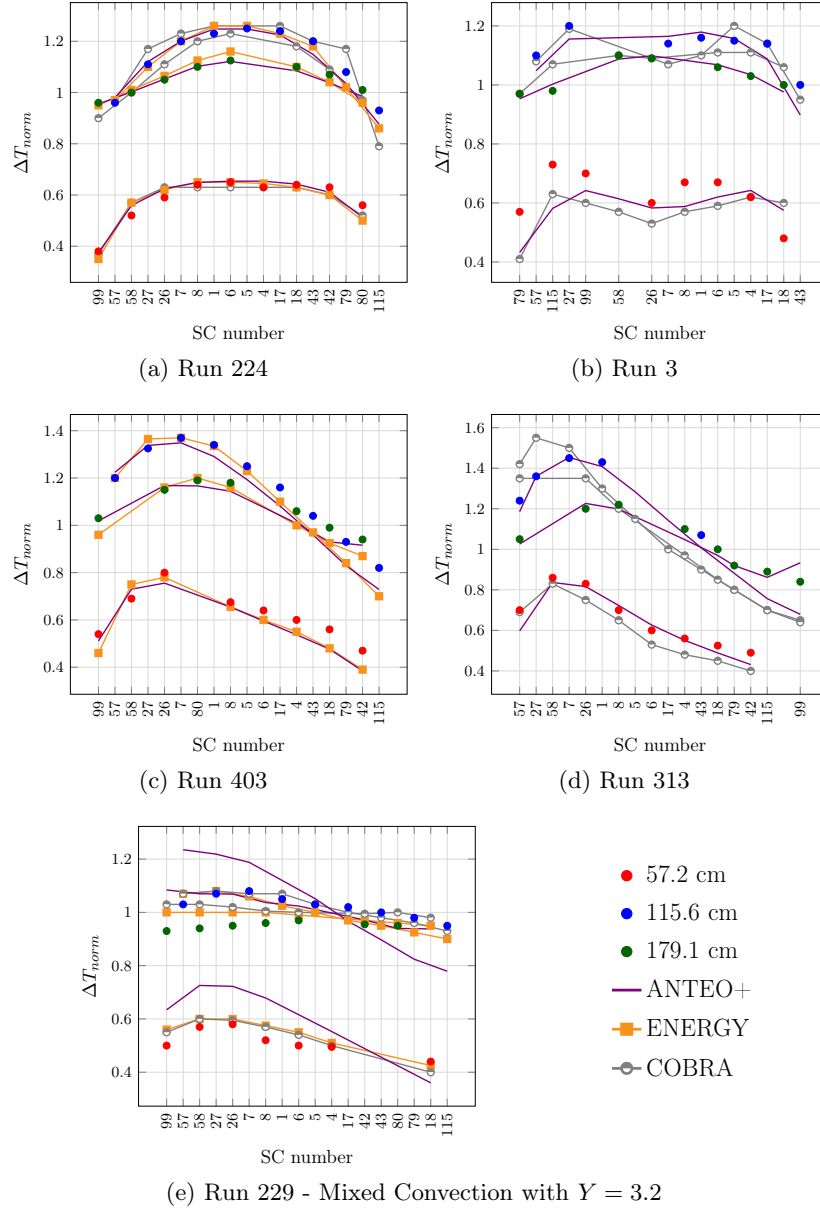
Figure 8.10: Representation of experimental and simulations results for some illustrative runs of the WARD-61 bundle.

(a) Experimental vs. simulations results for the near wall SCs temperature distribution at 115.6 cm.

(b) Experimental vs. simulations results for the axial SCs temperature distribution.
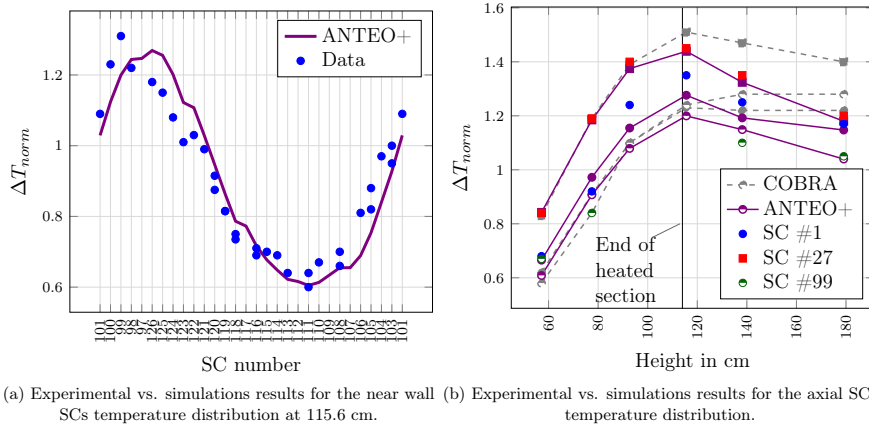
Figure 8.11: Representation of experimental and simulations results for the near wall (left) and axial (right) SCs temperature distribution for the WARD-61 bundle.

FETUNA-91   The last wire spaced hexagonal bundle analyzed is the mock-up described in [108], which is an ensemble of 91 electrically heated pins. Only a uniform power profile and mixed convection cases are analyzed. Results are summarized in Table 8.13 and visually in Figure 8.12.

Table 8.13: Comparison summary between ANTEO+ and FETUNA-91 bundle experimental data.

Run	Power (kW)	Flow rate (kg/s)	Y	$\bar{\varepsilon}[\%]$
1a	141.9	1.332	1.21	3.9
1b	71.34	0.676	4.67	4.3
1c	25.00	0.025	34.0	7.1

Discussion   In the FETUNA-91 bundle only mixed convection cases were analyzed, and we see that, even with a uniform power profile, if the buoyancy gets strong enough, the error is bound to increase up to 7.1% and the maximum SC temperature overestimated.

Hexagonal results summary   Given the high number of simulated cases it's worth to summarize the validation results just outlined for the hexagonal

. . . .
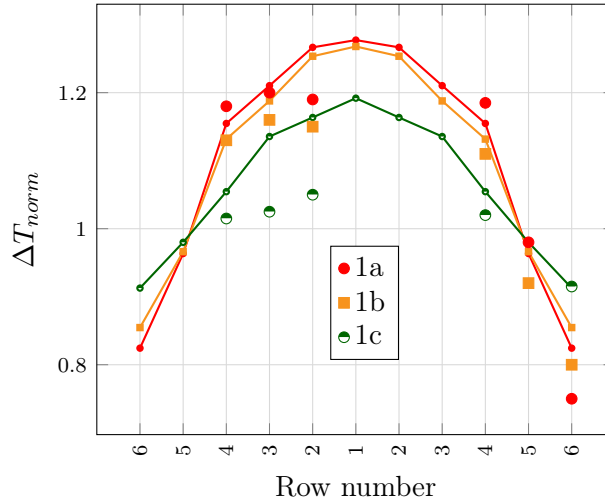
Figure 8.12: Representation of ANTEO+ simulations and experimental data for the FETUNA-91 bundle.

bundles. The covered range in the SC temperatures validation for sodium-cooled hexagonal bundles cases is:

- $1.067 \leq \frac{P}{D} \leq 1.34$

- $0 \leq \frac{H}{D} \leq 52$

- $19 \leq N_{pin} \leq 91$

- $0.00 \leq Y \leq 49.9$

- $500 \leq Re_b \leq 7.3 \times 10^5$.

Even if not complete, this range is still quite extensive and can be used as a guide to understand ANTEO+ targeted accuracy, at least in first approximation.

The comparison with COBRA results is presented in Table 8.14 for both the mixed and forced convection cases.

The results for the whole ensemble of data points, including the correlations mentioned in 7.2.4 are shown in Table 8.15, where distinction is made between the two flow regimes. The errors reported are referred to the normalized temperature, but because the average temperature gain is around 100 K, the error on the true SC temperature gain (the numerator of equation (8.3)) is basically the same.

. . . .

Table 8.14: Comparison between ANTEO+ and COBRA average $\varepsilon[\%]$ for the hexagonal SC temperatures. Results are displayed by operating flow condition.

	Forced	Mixed
ANTEO+[a]	3.3	5.5
COBRA	6.4	3.4

[a] Only points where COBRA results were available are considered.

Table 8.15: Results summary for SC temperature validation on hexagonal wire spaced bundles. All correlations for wire-spaced bundles implemented in ANTEO+ are reported.

	CTm	Nijsing	Zhukov
Forced convection (406 points)			
$\bar{\varepsilon}[\%]$	3.9	5.6	4.9
90% confidence interval [%][a]	8.6	10.8	10.0
Mixed convection (162 points)			
$\bar{\varepsilon}[\%]$	5.2	3.8	6.2
90% confidence interval [%]	12.8	8.7	15.1

[a] 90 % of the points have an error ε less than the reported value.

The cumulative distribution and the comparison with experimental results for the CTm correlation are reported in Figure 8.13.

Discussion   Due to experimental uncertainties in measuring the SC temperature, in the energy balance, flow rate and the graphical acquisition of data, an error can be labeled as acceptable if it remains below 5% (see Section 6.2). With this discriminant we can see from Table 8.14 that ANTEO+ is more effective than COBRA in the forced convection regime (with errors respectively equal to 3.3% and 6.4%) thus confirming the code philosophy and modeling efficiency; in the mixed regime COBRA is able to handle flow redistribution and so the situation is reversed (with errors respectively equal to 5.5% and 3.4%).

If we focus only on the SC with the maximum temperature gain (i.e.

. . . .

(a) Cumulative distributions

(b) ANTEO+ simulated versus experimental SC temperatures
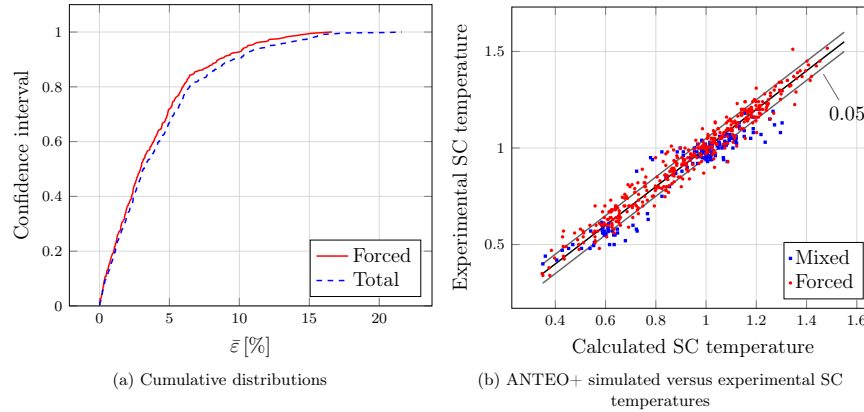
Figure 8.13: Graphical results summary for the validation of the CTm correlation, for thermal mixing, in wire spaced hexagonal bundles.

the hottest SC), which can be of particular interest for safety/design considerations, the error is considerably lower and equal to 2.7 % for the CTm correlation in forced convection; in mixed situations, instead, it is usually overestimated due to the higher flow redistribution in this regime.

From Table 8.15, where results for hexagonal wire spaced bundles are summarized for all the correlations implemented in ANTEO+, it is seen that in the forced convection regime the CTm correlation for thermal mixing is the closest to the analyzed experimental data, followed by Zhukov and Nijsing. In the mixed convection regime Nijsing performs better, probably because it usually overestimates mixing; since there are no physical bases under the success of Nijsing in the mixed regime, results must be taken with care.

As a final remark, it should be noted that in the analysis, the transition from the cold to the hot geometry was never taken into account, even if it can have some impact, especially for the near wall SCs. Simplified models of thermal expansion were proposed in literature [106], but they are not always capable of improving results; for this reason ANTEO+ actually deals only with cold geometries.

Zhukov-25   For the validation, a peculiar square bundle, which relies on grid spacers for holding the simulation pins in position, has been included; the coolant, differently from all the previous cases, is a sodium-potassium alloy (22 % sodium, 78 % potassium).

During the 11-th meeting of the International Association for Hydraulic

. . . .

Research a standard problem was presented in [145] with the aim of assessing the reliability and accuracy of thermal-hydraulic codes. The model assembly is representative of the BREST-type reactor. The bundle has 25 pins with different diameters (see Figure 8.14) and modular power capabilities, enabling different power skews to be investigated; in particular, there are two power regions that can be tuned corresponding to the two different diameters zones. The flow rate is fixed and so is the Reynolds' number, which is around 53400. In the simulations 200 axial nodes were used.
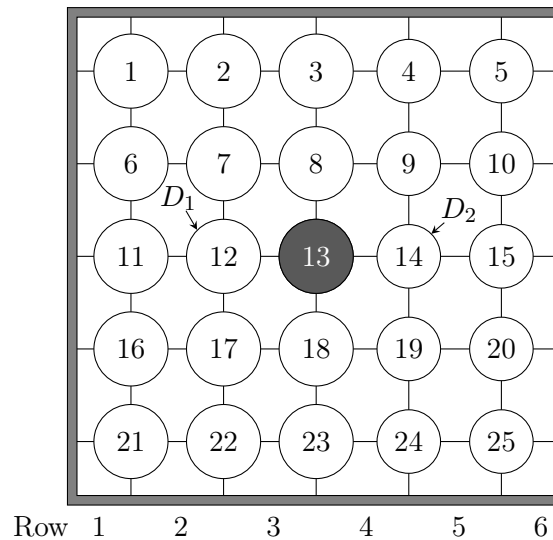
Figure 8.14: Cross section of BREST-type model assembly used in the experiment by Zhukov et al. (2004). In figure $D_1 > D_2$ and the gray filled pin indicates the instrumented rod.

The benchmark was tackled by many specialists ([95], [104], [18] and [123]) with a variety of tools encompassing SC, distributed resistance and CFD codes.

Results, reported in Table 8.16 and visually in Figure 8.15, were obtained using Kim's mixing model described in section 7.2.4. The physical properties for the coolant were borrowed from [145]. In Table 8.16 the results of the BRS-TVS code [1] are only reported, being the one with the overall best agreement with the data among the benchmark participants as reported in [146]; in Figure 8.15 some of the other participants results are also included, in order to better contextualize ANTEO+ accuracy. The error bars reported in Figure 8.15 correspond to an experimental uncertainty of 10% as suggested in [145].

. . . .

Table 8.16: Comparison summary between simulations and Zhukov-25 bundle experimental data.

Identifier	N_{15}/N_{10} (kW/kW) [a]	Y	$\bar{\varepsilon}_{rel}[\%]$	
			ANTEO+	BRS-TVS
1	1.35/2.00	0.01	10.3	13.0
2	1.65/2.00	0.01	4.9	6.1
3	2.00/2.00	0.02	7.2	5.1
4	2.00/1.65	0.01	13.2	10.3
5	2.00/1.35	0.01	14.8	11.2

[a] N_{15} and N_{10} represent the power of the pin with diameter D_1 and D_2 respectively.

(a) Operating condition 2.   (b) Operating condition 5.
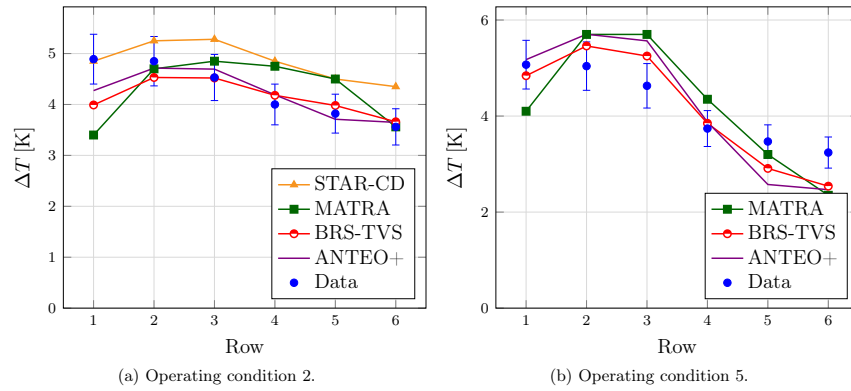
Figure 8.15: Representation of experimental and simulations results for some illustrative operative conditions of the Zhukov-25 bundle. Results for STAR-CD [18] and MATRA [123] codes are also included.

Discussion It can be seen that ANTEO+, using the correlation for thermal mixing by Kim, performs in line with BRS-TVS, which was the code closest to the experimental results as explained in [146]. Increasing the power skew increases the error because the experimental power shape is less sensitive to the skew than ANTEO+ (and BRS-TVS). This could be explained by errors in the flow split model, in the mixing coefficient or due to flow redistribution; the latter in particular, due to the low Y, should not be dominant. Other possibilities are: the mixing coefficient is not high enough or the grid effect on the flow split is much higher than predicted.

. . . .

Nonetheless, ANTEO+ accuracy for this bundle, assessing around 10%, has been proven to be one of the highest compared to other SC codes and CFD tools, especially considering the 10% experimental uncertainties suggested in [145].

HLM-cooled experiments

It is to be noted that the HLM coolant is, in all the available cases (see Table 8.6), the lead-bismuth eutectic and so, no pure lead experimental data are available; this is not of particular concern relatively to the SC temperatures due to the similar values and behavior of the physical parameters of interest (Prandtl's number for example), especially in forced convection. The following validation can thus be directly transferred to lead with a high degree of confidence.

KALLA-19   An experimental campaign on a 19-pin electrically heated hexagonal bundle (see Figure 8.16a) with wire spacers cooled by LBE was conducted at the **KA**rlsruhe **L**iquid metal **LA**boratory (KALLA) [100] in the frame of the EU research project **S**afe **E**xploit**A**tion **R**elated **C**hemistry for **H**LM reactors (SEARCH). The geometry and operating conditions were chosen so to be representative of the MYRRHA [115] fuel assembly.

The simulated case features an axially and radially uniform power profile, with a total power of 197 kW, a mass flow rate of 15.97 kg/s and a Y equating 0.06.

ANTEO+ calculations for this bundle – and also for the other case with a wire spacer – have been performed using, for the flow split and energy mixing, the CT and CTm correlations that were proven to be the most reliable in Sections 8.3.2 and in the sodium validation.

Results are presented in Figure 8.16b; the average $\bar{\varepsilon}_{rel}$ amounts to 11.9%.

Discussion   For what concerns the SC temperature distribution it can be noted that ANTEO+ over-predicts the temperature for the interior SCs while, for the edge and corner ones, overestimates mixing. In the simulations, indeed, the edge and corner SCs have almost the same temperature while the data show that the corner one is colder. An important consideration must however be made: the difference between the SC center temperature (where the thermocouple is located) and the clad temperature oscillates between 10°C and 25°C which must be compared with a SC temperature increase

....

(a) Experimentally instrumented SCs and
corresponding ANTEO+ numeration.

(b) ANTEO+ simulations vs. experimental data
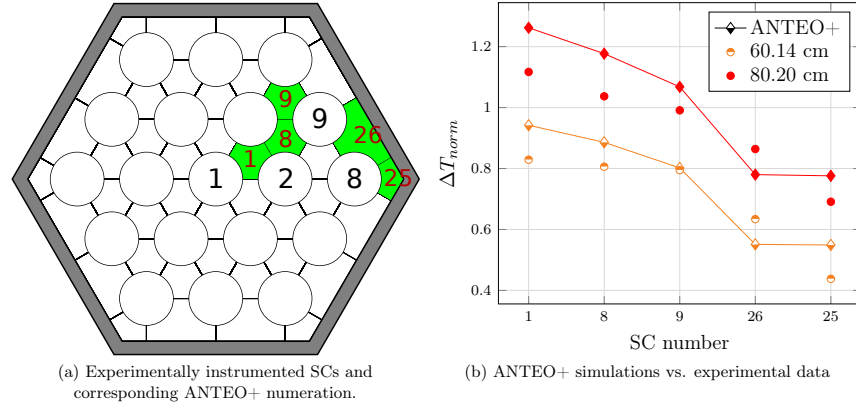
Figure 8.16: Representation of ANTEO+ simulations and SC temperature
experimental data for the KALLA-19 bundle.

around $100°C$[4] – for the hottest SC at the location near the end of the heated
length and much lower for other SCs or elevations. This means that the SC
center temperature is not representative (i.e. lower) of the bulk temperature,
the quantity actually calculated by ANTEO+ and SC codes in general. This
is partially proven by the good agreement between the predicted and exper-
imental clad temperature (see Figure 8.20); error compensation between the
SC temperature rise and the clad-coolant temperature difference predictions
is a possibility but, alone, could not explain why the relative error drops
from 11.9 to only 2.6 going from the SCs to clad (see Section 8.4).

KYLIN-61   In the frame of the ADS research project launched by the CAS,
the INEST undertook the design of a reactor cooled by LBE named CLEAR-
I. To support CLEAR-I design, the KYLIN-II [71] multi-functional facility
including material, thermal-hydraulic and safety loops has been established;
a test section composed of 61 electrically heated pins arranged in a hexagonal
bundle with wire spacers has also been installed and operated (Figure 8.17a).
The forced convection case from [71], with an axially and radially uniform
power profile, with a total power of 70 kW, a mass flow rate of 85.00 kg/s
and a Y equating 0.00 has been used for the validation.

Results are reported in Figure 8.17b; the average $\bar{\varepsilon}_{rel}$ amounts to 15.5%.

---

[4]As a comparison metric, the maximum value of the ratio between the bulk-clad tem-
perature difference and the SC temperature rise found in all the sodium experiments
previously presented encompassing every SC and elevation is 4.8%.

. . . .

(a) Experimentally instrumented SCs and
corresponding ANTEO+ numeration.

(b) ANTEO+ simulations vs. experimental data
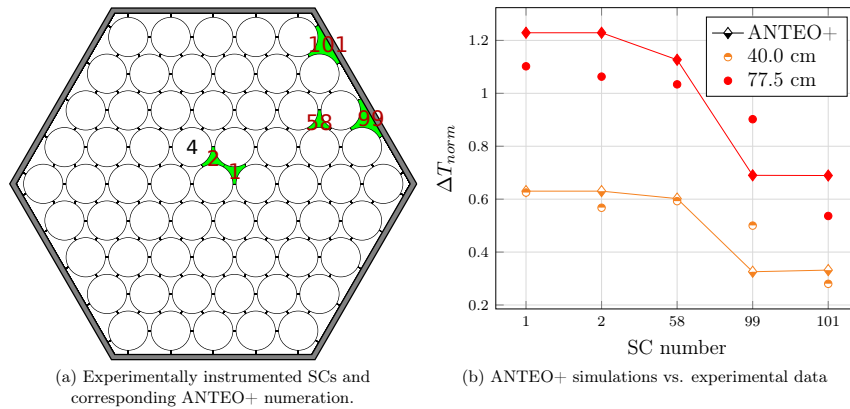
Figure 8.17: Representation of ANTEO+ simulations and SC temperature
experimental data for the KYLIN-61 bundle.

Discussion   The same considerations done for KALLA-19 hold true
also for this bundle, because the SC temperature increase is lower than 7°C
while the difference between the SC and clad temperatures is around 2°C
and so, percentage-wise, relevant, meaning that the measured temperature is
not representative of the bulk one. Similarly to KALLA-19, the wire mixing
effect is overestimated suggesting that, for HLMs, the correlations by CTm
may not be directly transferable, especially for such a tightly spaced bundle.

HLMs results summary   A graphical summary of the validation is re-
ported in Figure 8.18; the average $\bar{\varepsilon}_{rel}$ over 20 data points is 13.7%.

Discussion   The SC temperatures are generally overestimated and the
accuracy (error of 13.7%) substantially drops if compared to sodium-cooled
cases (see Table 8.15). The motivations behind this have been discussed in
the KALLA-19 and KYLIN-61 bundles. The proposed explanation is par-
tially proven by the satisfactory agreement with the outer clad temperature
(see 8.4), with an error lower than the one committed on the SC temperature.

8.4   Clad outer temperature

Once the SC temperature is known the Nusselt's number must be calculated
in order to compute the outer clad temperature, which is a tight design
. . . .
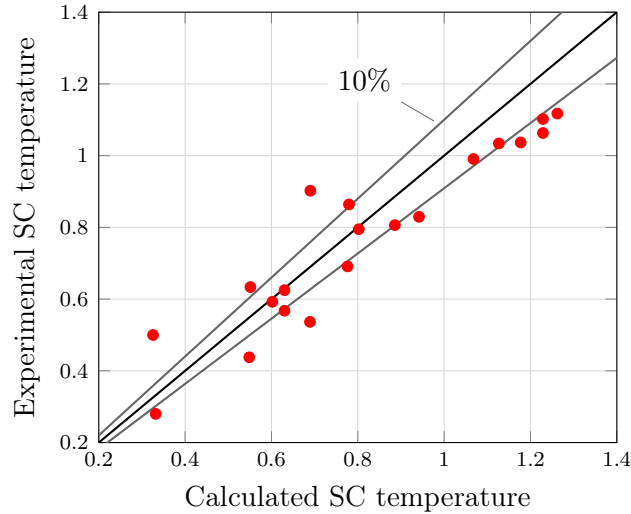
Figure 8.18: Experimentally instrumented SCs and corresponding
ANTEO+ numeration for the KYLIN-61 bundle.

constraint. Some accuracy is therefore needed in order to reduce uncertainty
margins and increase the degree of reliability of the overall core design.

For assessing the targeted accuracy of the correlations explained in sec-
tion 7.2.6 a comparison with experimental data has been carried out; the
used database is reported in Table 8.17.

As done in the previous section, first the sodium case will be discussed
and then the HLM ones, highlighting similarities and differences. An im-
portant variation in the results displaying style is also present because, as
previously discussed for the KALLA-19 and KYLIN-61, in the HLM-cooled
cases available, the difference between the measured SC and clad outer tem-
peratures is not representative of the difference between the bulk and clad
outer temperatures, the quantity actually calculated with the Nusselt's num-
ber. For this reason, for HLMs experiments, results are normalized, similarly
to equation (8.3), as

$$\Delta T_{c,norm} = \frac{T_{co} - T_{in}}{T_b - T_{in}} \quad , \tag{8.4}$$

thus merging together the SC temperature increase and the bulk-clad tem-
perature rise; for the sodium case the two effects can be separated and so
only the bulk-clad temperature difference will be analyzed.

....

Table 8.17: Collection of experiments used for the clad temperature validation. Main physical and geometrical parameters are also given.

Ref.	Coolant	N_{pin}	P/D	H/D	$Re(\times 10^3)$
Hexagonal - wire spacer					
[100]	LBE	19	1.279	40.0	37.8
[71]	LBE	61	1.116	25.0	49.8
Hexagonal - grid spacer					
[74]	LBE	37	1.800	-	108.7
Square - grid spacer					
[145]	NaK	25	Variable[a]	-	53.4

[a] Pins with different diameters are present.

8.4.1 Sodium-cooled experiments

Zhukov-25 The bundle in question is the one already presented in section 8.3.2; measurements where taken around the colored pin in Figure 8.14 and averaged over the two semicircles facing the different diameters regions; this process was repeated for 10 axial positions. Results for the five cases described in Table 8.16 are reported in Table 8.18 and graphically in Figure 8.19. The error reported in Table 8.18 is referred to the difference between SC bulk temperature and clad outer temperature, because it is the quantity actually used in uncertainty analysis. Finally the error bars plotted in Figure 8.19 are taken from [145].

Discussion The declared experimental uncertainties for the temperature film drop are around 0.1 degree which is about 5%. With this in mind we see from Table 8.18 that Ma correlation performs better than the one from Mikityuk in square geometries, with errors respectively around 7% and 20%[5]. We also notice that the entrance effect seems higher in the operating condition 2 than 5, giving an hint on the experimental uncertainties. Finally we see that the grid effect on heat transfer seems to be of the order of the uncertainties and so negligible in first approximation.

---

[5]If only the upper hottest part of the pin was studied, and so neglecting the thermal entrance effect, errors would be lower.

. . . .

Table 8.18: Comparison summary between simulations and Zhukov-25 bundle experimental data on Nusselt's number for the instrumented pin in Figure 8.14; errors relative to the clad-bulk temperature difference are given. D_1 and D_2 sides stand for the semi-perimeters of the instrumented pin facing the side of the bundle with the respectively corresponding diameter.

Identifier	D_1 side		D_2 side	
	Ma	Mikityuk	Ma	Mikityuk
1	4.2	21.8	4.7	22.0
2	7.7	26.1	5.1	19.2
3	3.9	22.7	12.5	13.9
4	7.4	20.0	13.6	16.3
5	3.1	22.0	8.1	16.7

8.4.2   HLM-cooled experiments

KALLA-19   This is the same bundle, with the same operating conditions presented in Section 8.3.2. Results are presented in Figure 8.20 and summarized in Table 8.19, where the nomenclature is the following:

- "Mikityuk+Zhukov" indicates that the Nusselt's number has been calculated by means of the Mikityuk's correlation for the central pins and the Zhukov's correlation for the edge and corner pins (see Section 7.2.6);

- "Mikityuk" indicates that the Nusselt's number, for all the pins, has been calculated based on Mikityuk's correlation.

- "Ma" indicates that the Nusselt's number, for all the pins, has been calculated based on Ma's correlation.

Discussion   As previously hinted, the error on $\Delta T_{c,norm}$ - clad - is much lower than the one on ΔT_{norm} - SC - partially confirming the hypothesis put forward in Section 8.3.2. From Table 8.19 it can also be seen how the correlations from "Mikityuk" and "Ma" perform similarly, both of them under-predicting the edge and corner pins temperatures. To increase accuracy, a dedicated correlation for these types of pin must be used, like the one from Zhukov.

. . . .

(a) Operating condition 2.

(b) Operating condition 5.
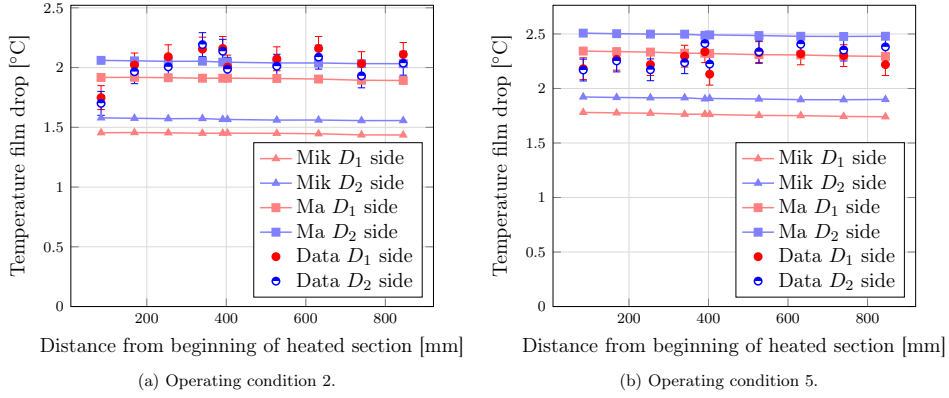
Figure 8.19: Representation of experimental and simulations Nusselt's numbers for some illustrative operative conditions of the Zhukov-25 bundle. Mik represents Mikytiuk correlation, while D_1 and D_2 sides stand for the perimeter of the instrumented pin facing the side of the bundle with the respectively corresponding diameter.

Table 8.19: Comparison summary between simulations and KALLA-19 bundle experimental data on clad temperature for the instrumented pins in Figure 8.16a.

	Correlation	$\bar{\varepsilon}_{rel}[\%]$
	Mikityuk+Zhukov	2.6
$\Delta T_{c,norm}$	Mikityuk	3.4
	Ma	3.4

KYLIN-61   This is the same bundle, with the same operating conditions presented in Section 8.3.2. Results are presented in Figure 8.21 and summarized in Table 8.20.

Table 8.20: Comparison summary between simulations and KALLA-19 bundle experimental data on clad temperature for the instrumented pins in Figure 8.17a.

	Correlation	$\bar{\varepsilon}_{rel}[\%]$
$\Delta T_{c,norm}$	Mikityuk	19.9
	Ma	17.8
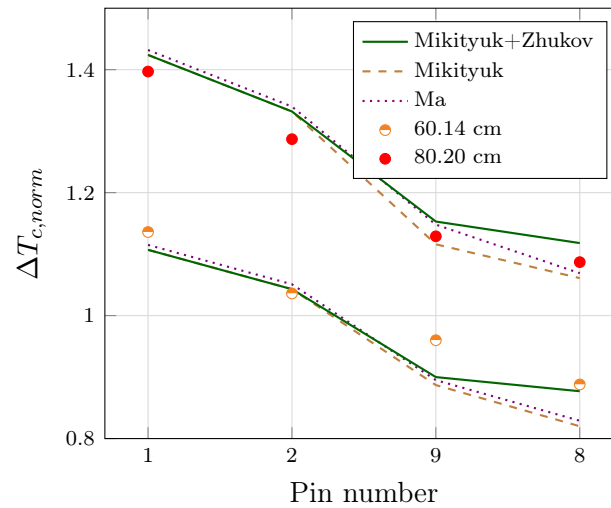
Figure 8.20: Representation of experimental and simulations clad
temperatures for the KALLA-19 bundle. The pin identification number is
explained in Figure 8.16a.

Discussion   The same considerations performed on the KALLA-19 re-
sults, hold true also for this bundle but, in this case, even neglecting the
thermal entrance region, the clad temperature is overestimated. This is par-
tially due to an over-prediction of the SC temperature but, mostly, to the
error committed in estimating the thermal exchange between the coolant
and the clad. The presence of the wire has heavy effects due to the low $\frac{P}{D}$ of
the bundle which enhances the thermal perturbation brought by the spacer.
It must be noted that this is a local measurement – for a specific angular
position of the pin[6] – which oscillates when the wire is close to the thermo-
couple meaning, that the average clad temperature should agree better with
ANTEO+ calculations[7]; nonetheless, correlations for the Nusselt's number
based on bare rods are not enough reliable for tightly packed pins with a
wire spacer.

CIRCE-37   Within the 6th EU Framework Program, ENEA assumed the
commitment to perform an integral experiment aimed at simulating the pri-

---

[6]In the KALLA-19 bundle the clad temperature was averaged over the pin perimeter.

[7]The average clad temperature should lie somewhere between the minimum (when the
wire is far away) and the maximum (when the wire is near the thermocouple) of the
experimental data; this is, indeed, where the simulations results approximately lie (see
Figure 8.21 where the local increment is due to the wire presence).

. . . .
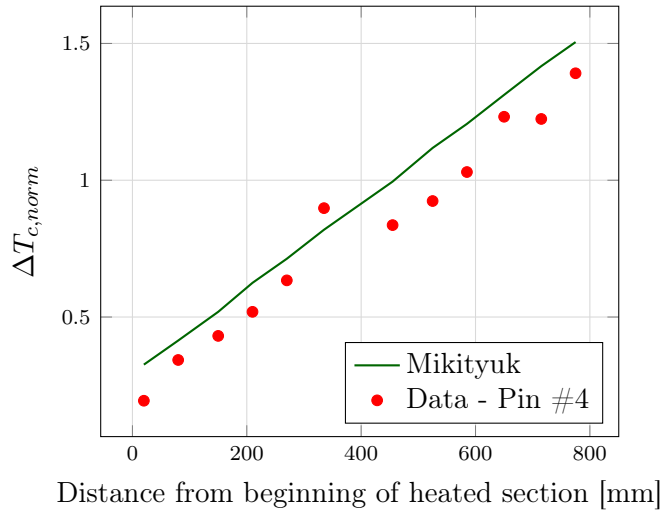
Figure 8.21: Representation of experimental and simulations clad temperatures for the KYLIN-61 bundle. The pin identification number is explained in Figure 8.17a.

mary flow path of a HLM cooled – pool-type – nuclear reactor, implementing a new experimental activity named **I**ntegral **C**irculation **E**xperiment (ICE) to be performed in the CIRCE facility [74]. The ICE test section includes an assembly of 37 pins, spaced by grids, arranged in a hexagonal bundle (see Figure 8.22a). Among the numerous transient tests, a forced convection steady state run was also performed featuring an axially and radially constant power profile with a total output of 600 kW, a mass flow rate of 63.50 kg/s and a Y equating 1.08.

Results for the clad outer temperature obtained with Mikityuk's correlation and a SC-centered logic are reported in Figure 8.22b; the error bars stem from the declared $\pm15\%$ uncertainty on the heat flux due to the use of bifilar-type pin rods [74] and so they do not take into account the other sources of uncertainty – like flow and power oscillations. A summary of the results is also reported in Table 8.21.

Discussion   This experimental set does not feature a wire spacer and so is particularly useful to evaluate the accuracy of the Nusselt's correlations implemented in ANTEO+. The agreement with the experimental data is, overall, satisfactory, with "Mikityuk" performing better than "Ma". Being the uncertainty, coming from the bifilar-type pin, on average, around 8.4%

....

Table 8.21: Comparison summary between simulations and CIRCE-37 bundle experimental data on clad temperature for the instrumented pins in Figure 8.22a.

	Correlation	$\bar{\varepsilon}_{rel}[\%]$
$\Delta T_{c,norm}$	Mikityuk[a]	5.9
	Ma	6.5

[a] The Zhukov's correlation is not used for the ICE test section because the $\frac{P}{D}$ is out of the range of the correlation.

(a) Experimentally instrumented SCs and corresponding ANTEO+ numeration. Clad temperatures are measured and evaluated at the locations marked by the blue bars.

(b) ANTEO+ simulations vs. experimental data using Mikityuk's correlation
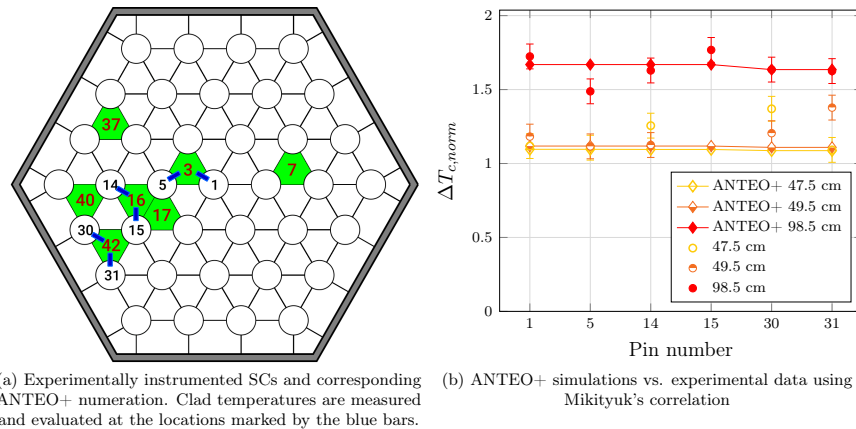
Figure 8.22: Representation of ANTEO+ simulations and clad temperature experimental data for the CIRCE-37 bundle.

for the $\Delta T_{c,norm}$, results in Table 8.21 can be better appreciated.

The axial elevation 49.5 cm is in the middle of the spacer grid but, a decisive effect of the latter cannot be seen and lies within the experimental uncertainty similarly to Section 8.4.1.

HLMs results summary   A graphical summary of the validation concerning the clad temperature for HLM-cooled bundles is reported in Figure 8.23 while a quantitative one is visible in Table 8.22.

Discussion   The agreement with experimental data is satisfactory for what concerns the clad outer temperature calculations and, in line, with the experimental uncertainty. As seen from Table 8.22, excluding the tightly
....

Table 8.22: Comparison summary between simulations and experimental data on clad temperature for the instrumented pins in Figure 8.22a.

	Correlation[a]	$\bar{\varepsilon}_{rel}[\%]$
36 points		
$\Delta T_{c,norm}$	Mikityuk	9.8
	Ma	9.5
24 points[b]		
$\Delta T_{c,norm}$	Mikityuk	4.8
	Ma	5.2

[a] Zhukov's correlation has been used for near wall pins when inside its validity range.

[b] Excluding KYLIN-61.

wire spaced bundle KYLIN-61 tainted by the local measurement effect that is not taken into account in ANTEO+ implemented correlations, the accuracy on the average clad temperature is around 5%. This is much lower than the error committed on the SC temperature alone indicating, that the validation on that parameters - for what pertains HLMs - previously presented, is not expressing the real accuracy of ANTEO+ and that, instead, the clad temperature accuracy should be taken as reference.

8.5 Validation summary

In the validation performed and discussed in the present chapter, basically all the models outlined in Chapter 7 were, at least preliminary, validated. The validation has highlighted the capabilities of the models implemented in ANTEO+ and their interactions in reproducing experimental data, with a relatively high degree of accuracy when compared to other classical SC tools like ENERGY-II, COBRA-IV-I-MIT and BRS-TVS:

- the flow split model is quite accurate for both wire spaced or gridded bundles, with an error of 4.8% which goes down to 1.8% in turbulent flow conditions;

- pressure drops can be predicted with some accuracy in basically every operative condition, even if validation is still needed for gridded

....
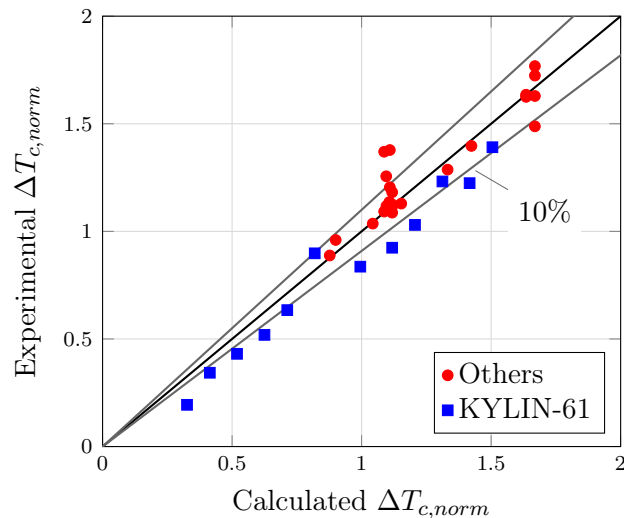
Figure 8.23: Representation of experimental and simulations Nusselt's
numbers for the HLM-cooled bundles.

bundles, where the error is 3.3%;

- SC temperatures are calculated with an accuracy around 3.9% in a variety of flow conditions and geometric arrangements. This figure has been derived with sodium-cooled data and further work is needed to prove it is transferable to HLMs. Moreover, in the case of mixed convection (as expected) accuracy decreases down to 5.2% or even more for small bundles with high power skews.

- Clad outer temperatures are calculated with an accuracy around 4.8% for HLM-cooled bundles in various geometric arrangements, suggesting, that the corresponding SC temperature should have an accuracy similar to the sodium cases.

In Table 8.23 results are summarized and compared with the estimated experimental uncertainties in their measurement, so to better contextualize the validation results. Information like the one given in Table 8.23, but more generally, throughout all this chapter, can be actively used in uncertainties quantification analyses - like the one performed on the ALFRED FA by means of ANTEO+ [69] - which are, in parallel to the direct use of the DOC, a keystone of any design procedure and, particularly, of the core one.

. . . .

Table 8.23: Summary of estimated uncertainties and confidence intervals of the main SC parameters in ANTEO+ validity range for HLMs. A reference experimental uncertainty is also given for qualitative comparison.

Parameters	$\bar{\varepsilon}_{rel}[\%]$	90% confidence interval [%]	experimental uncertainty [%]
X_i[a]	4.8 (1.8)	11.4 (5.2)	<10[b]
ΔP	3.3	10.0	5
ΔT_{norm}	3.9[c]	8.6	5
$\Delta T_{c,norm}$	4.8	14.4	8.4

[a] Values in parenthesis refer to turbulent flow conditions.
[b] Flow split uncertainties vary with flow regime being around 5% for turbulent flow and as high as 10% for the transition region.
[c] This value has been preliminary borrowed from sodium-cooled cases.

Work is still needed particularly for HLMs SC temperatures with dedicated experiments so to avoid measurement of temperatures not representative of the bulk one, making possible to understand the applicability of ANTEO+ models (e.g. CTm) specifically for near wall SCs in wire spaced bundles; for the clad temperature calculation with wire spacers and expressly for local measurement the development of new, dedicated, correlations is mandatory along with models for near wall pins with a validity range higher than the Zhukov's one.

. . . .

. . . .

CHAPTER 9

EXTENSION TO THE MIXED CONVECTION REGIME

With the increasing interest around HLMFRs, and thanks to the flexibility offered by the coolant (see Section 2.3), various battery concepts of very small size have been conceived [120]. To make the system more safe natural circulation in the primary circuit to cool the core, even at rated power, is often employed. While a direct link between the primary circuit convection and the in-core thermal exchange regimes cannot be established, because specifically depending from the envisaged core and plant layouts, generally, when the first relies on natural circulation the possibility of exiting the forced convection regime entering into the mixed one concretely exists for the second.

ANTEO+ validity range covers only the forced convection regime, with unacceptably low accuracy in the mixed one, as discussed in Chapter 8; in order to make it applicable also to this particular battery concepts, the validity range has been therefore extended.

The procedure followed in developing the code is identical to the one presented in Chapter 7 with the additional constraint of having a set of equations that smoothly reduces to the one previously solved by ANTEO+ in forced convection (see Section 7.1). This is important so to ensure a uniform predictive ability inside the validity domain and thus increasing the confidence of the user in interpreting the results.

....

9.1 Equation analysis

To better identify the framework inside which the equation analysis and subsequent model selection has to be performed, a parameter Y_{mix} similar to Y (see Chapter 8) can be defined

$$Y_{mix} = \frac{Gr_q}{Re} \quad , \tag{9.1}$$

where Gr_q is the Grashof's number based on the applied heat flux; following [51], [126] and [127] it can conservatively be said that mixed convection extends up to $Y_{mix} < 100$, when this condition is not fulfilled the bundle has entered the natural convection regime. The proposed criteria is subject to considerable uncertainties because it does not take into account the effect that geometry - $\frac{P}{D}$, number of pins and heated length - seems to have on the onset of the natural convection; indeed, for widely spaced pins arrangements the transition starts later.

9.1.1 Mass conservation

The mass conservation equation is not directly simplified and so equal to (7.1). The main implicit assumption is that W_{ij} - the transverse mass flow rate per unit length between SC i and its neighbors j - is thermally driven[1] (i.e. buoyancy); as discussed in Section 9.1.3, indeed, pressure is taken uniform on the FA cross section.

9.1.2 Axial momentum conservation

Regarding the axial momentum equation (7.3), the main simplification pertains the momentum transfer via diversion cross flow which is collapsed to a single term W_i, sum of the individual neighboring SCs j ($W_i = \sum_{j=1}^{J} W_{ij}$). The axial momentum equation to solve can then be cast as

$$\frac{d(P_i A_i)}{dz} = - \frac{d(\dot{m}_i v_i)}{dz} - A_i \rho_i g - \frac{1}{2} \rho_i v_i^2 A_i \frac{f_i}{D_{Hi}}$$
$$- A_i \Delta P_{form,i} - V^* W_i - \sum_{j=1}^{J} W_{ij}^M (v_i - v_j) \quad , \tag{9.2}$$

where V^* is theoretically defined as $\frac{\sum_{j=1}^{J} W_{ij} v^*}{\sum_{j=1}^{J} W_{ij}}$; it should therefore symbolize an average of the confining SCs v^*. In the present context, and assuming

---

[1]Contrarely to the forced convection, buoyancy related phenomena due not entails zero net mass exchange even in an axially averaged sense

. . . .

smooth velocity gradients, V^* is taken as v_i; this choice simplifies convergence while not impairing the overall accuracy (see Chapter 10).

9.1.3   Transverse momentum conservation

The vehicle of the diversion flow is assumed to be a redistribution of thermal origin (i.e. buoyancy); for this reason, the same assumption of uniform pressure on the FA cross section put forward in Section 7.1 is here utilized bringing again to equation (7.6).

9.1.4   Energy conservation

Similarly to the axial momentum, the energy equation (7.7) is simplified, in its diversion term, as

$$
\begin{aligned}
\frac{d(\dot{m}_i h_i)}{dz} =& \chi_i - H^* W_i - \sum_{j=1}^{J} W_{ij}^H (h_i - h_j) \\
& - \sum_{j=1}^{J} \rho_{ij} \alpha_{ij} \left(\frac{s}{\delta} \right) (h_i - h_j) \quad,
\end{aligned}
\tag{9.3}
$$

where H^* is the energy analog of V^*. The same assumption performed on V^* is done on H^* which is taken equal to h_i.

Again, having disregarded the transverse momentum equation a flow split model is necessary to establish the inlet conditions of each SC. Now, however, the mass flow can change in a SC due to thermally induced redistribution (i.e. W_i) and so, the effect of the flow split model on the final temperatures results is bound to be less important than in forced convection.

It can also be noticed that, for W_i approaching zero, the set of equations just described, reduces to the one solved in forced convection.

9.1.5   Method of solution

The system of equations for mixed convection is somewhat more difficult to solve than the forced one, because now, the energy and momentum equations are interlinked and must therefore be solved together. The idea suggested in [23] is to solve the system having as unknown the density and velocity variations in each SC along with the bundle pressure drop. To achieve this, first the mass conservation equation must be substituted into the energy and momentum ones so to eliminate the term W_i in favor of $\dot{m}_i = \rho_i v_i A_i$ and

....

then, the following axial discretizations on the node between z and $z + \Delta z$ performed:

$$
\begin{aligned}
d\dot{m}_i &\approx \Delta \dot{m}_i = (\rho_i v_i A_i)_{z+\Delta z} - (\rho_i v_i A_i)_z \quad , \\
d(\dot{m}_i h_i) &\approx \Delta(\dot{m}_i h_i) = (\rho_i v_i A_i h_i)_{z+\Delta z} - (\rho_i v_i A_i h_i)_z \quad , \\
d(\dot{m}_i v_i) &\approx \Delta(\dot{m}_i v_i) = (\rho_i v_i^2 A_i)_{z+\Delta z} - (\rho_i v_i^2 A_i)_z \quad , \\
d(P_i A_i) &\approx A_i \Delta P_i = A_i \Delta P \quad , \\
\rho_{z+\Delta z} &= \rho_z + \Delta \rho \quad , \\
h_{z+\Delta z} &= h_z + \Delta h \quad , \\
v_{z+\Delta z} &= v_z + \Delta v \quad .
\end{aligned}
\tag{9.4}
$$

Finally, to eliminate the enthalpy in favor of the density, advantage is taken of the relation $\Delta h \approx R \Delta \rho$ where $R = \left(\frac{\partial h}{\partial \rho} \right)_P$.

The final system of equations can then be expressed as

$$
\begin{aligned}
E_i \Delta \rho_i + F_i \Delta v_i + \Delta P &= G_i + MEX_i \quad \forall i = 1, N_{sub} \\
U_i \Delta \rho_i + T_i \Delta v_i &= \frac{\chi_i \Delta z}{A_i} + EEX_i \quad \forall i = 1, N_{sub} \quad ,
\end{aligned}
\tag{9.5}
$$

where N_{sub} is the number of SCs, E_i, F_i, U_i and T_i are coupling terms between momentum and energy, G_i is the hydrostatic pressure loss term while MEX_i and EEX_i are exchange terms between SCs for momentum and energy respectively, they include turbulent mixing, conduction effects and wire/grid contributions. Presently, there are $2N_{sub}$ equations and $2N_{sub} + 1$ unknowns - the density and velocity variations for each SC plus the bundle pressure drop - and so another equation, represented by the overall mass conservation, must be added,

$$
\sum_{i=1}^{N_{sub}} \Delta \dot{m}_i = \sum_{i=1}^{N_{sub}} A_i (\Delta \rho_i (v_{iz} + \Delta v_i) + \rho_{iz} v_i) = 0 \quad .
\tag{9.6}
$$

The above system of equations is non-linear because the coupling terms depend on $\Delta \rho_i$ and Δv_i which are the unknowns; an iteration schemed is therefore necessary. To ease convergence, phenomena are divided in two categories:

- the ones related to flow redistribution like $\Delta \rho$ and Δv and

- the ones not related to buoyancy like W^H and the conduction term.

....

The first category is treated implicitly and contributes to the non-linearity of the system being included in the coupling coefficients E_i, F_i, U_i and T_i, while elements of the second are treated explicitly and so approximated with their value at the previous iteration and thus contributing to G_i, MEX_i and EEX_i. This is acceptable because they are usually small compared to redistribution in mixed convection conditions and, at the same time, are characterized by a slower axial variation.

The adopted iteration procedure, depicted in Figure 9.2, starts, after the necessary flow split calculation, with a first guess of the density and velocity variations (e.g. $\Delta\rho_i = 0$ and $\Delta v_i = 0$ or the value of the previous axial step) then, the system is solved with the Greene's method[2] [46] or via Gauss elimination if a bypass is present (see Section 9.3), and the newly calculated values are used to update the coupling coefficients. The solution is believed to be converged when a set of physical conditions is satisfied, these include: the global mass balance, the bundle pressure drop difference, the temperature (and so the energy balance) and velocity (and so the momentum balance); convergence is achieved when all these errors are below some user defined value ϵ_i (with $i = m, P, T, v$). Generally, the most stringent criteria happen to be the temperature and velocity ones, with the global mass balance and pressure drops quickly converging, as visible in Figure 9.1. These set of criteria is believed sufficient to provide physically sound solutions (i.e. respecting the conservation equations) in spite of the problem non-linearity, particularly since the research domain starts close to the limiting case of forced convection; issues could be expected very far from this point but, they will fall outside the validity domain of ANTEO+ in mixed convection (see Section 10.1) and so not posing particular concerns.

Thanks to various optimization strategies - like under relaxation in the case of slow convergence - it has been found that the above procedure converges very well in every flow condition investigated, assuring calculation times lower than a minute on a standard personal computer.

Once the coolant temperature field has been calculated, the cladding temperature can be derived in the same way as explained in Section 7.1.6

---

[2]Due to the fact that Gauss elimination is not suitable for sparse matrices, like the one of the present problem, Greene devised a dedicated procedure based on the linear combination of matrix rows to transform the original in a diagonal one. This procedure, however, works only if a bypass is not present.

. . . .
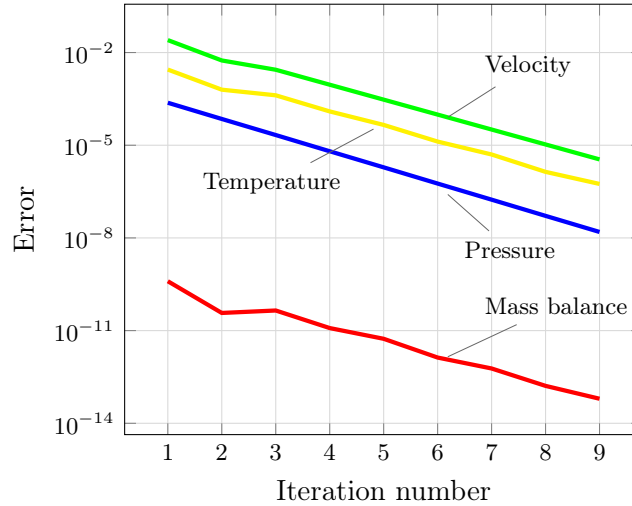
Figure 9.1: Example of ANTEO+ convergence in a typical mixed convection situation.

9.2 Constitutive relations for balance equations

As discussed in Section 7.2, constitutive relations are needed in order to eliminate some of the unknowns present in the conservation equations. In the system given by equations (9.5) and (9.6) f_i, $\Delta P_{form,i}$, W_{ij}^H, W_{ij}^M and δ must be specified. In this section, only models for quantities that are different from their forced convection counterparts or that are subject to constraints in the selected regime are discussed; they include f_i, W_{ij}^M and the conduction term.

9.2.1 Friction factor

At the beginning of Section 9.1 the parameter Y_{mix} was introduced; this discerning between the mixed and natural convection regimes comes in the sense that for $Y_{mix} > 100$ the main bundle parameters are completely dominated by buoyancy related effects.

The friction factor is one of such parameters; it has indeed been found that for increasing Y_{mix} the velocity field is more and more distorted, with mass flow pushed near the heated wall. Changing the velocity profile also changes the shear stress distribution and, ultimately, the friction factor [126], that increases, introducing an error in the pressure drop estimation

An additional problem arises in the evaluation of the gravity term of the

. . . .
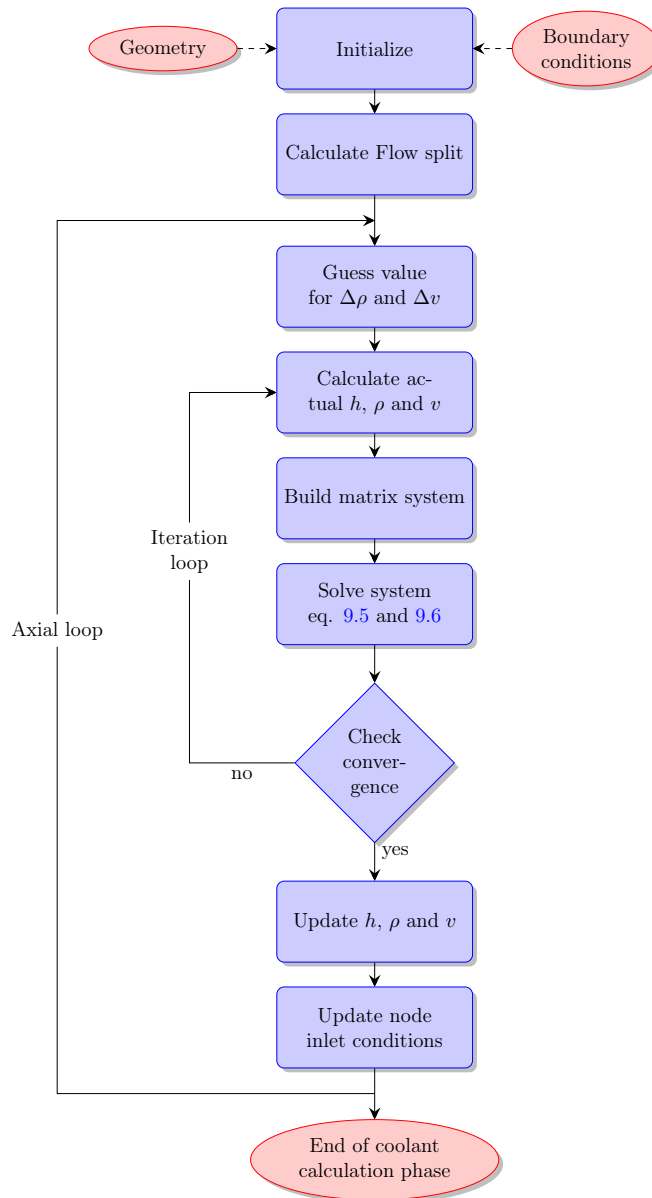
Figure 9.2: Flow diagram of the coolant temperature calculation scheme in ANTEO+ for the mixed convection regime.

momentum balance equations because, to properly assess it, the spatially-averaged coolant density should be used but, in lumped parameters tools

. . . .

like SC codes, only the bulk average is available. As Y_{mix} increases, the difference between the two densities can grow larger introducing an error in the hydrostatic pressure evaluation. To avoid this a corrective term should be added to the momentum equation or the friction factor suitably modified as suggested in [51].

Because, presently, ANTEO+ does not deal with the phenomena discussed in this section, calculation should be limited to $Y_{mix} < 100$, so to be confident that the error introduced by neglecting them is negligible.

9.2.2   Flow split

Due to the simplification of the transverse momentum equation a flow split model is needed exactly as explained in Section 7.2.3. The main input of this model is the friction factor and so the flow split is subject to the same problems and restrictions that affect it; an important consideration must however be made and it starts looking at equation (7.28). The flow split value of a SC does not depend on the absolute value of the friction factors but, on their ratio, meaning that is less sensitive to variations of the latter. High errors on f_i therefore do not necessarily imply high errors on X_i if in all the SCs the change of the friction factor is similar.

Moreover, due to flow redistribution, the temperature field is less sensitive to inlet conditions than in forced convection, further reducing the error on the SC temperature and so possibly aiding in keeping high ANTEO+ accuracy even near the boundary indicated by the Y_{mix} criteria.

9.2.3   Momentum mixing coefficient

The momentum mixing coefficient W_{ij}^M, representing the effective mass exchange rate between SCs i and j for momentum transfer per unit length is taken equal to its energy counterpart W_{ij}^H described in Section 7.2.4 because they are both driven by the same physical phenomena like turbulence (i.e. turbulent Prandtl's number $Pr_t \sim 1$), flow pulsation or wire sweeping.

9.2.4   Conduction

The main model modification, relatively to forced convection, pertains to the conduction term; while it is a minor contribution in the forced regime, in mixed convection, indeed, azimuthal conduction through the rod can help energy exchange between SCs, especially if the heat flux at the outer rod surface is not azimuthally uniform. For an actual pin using oxides as a fuel, the heat flux will be basically uniform at the inner cladding surface due to the

. . . .

low conductivity of the fuel and gap; at this point, coolant temperature non-uniformity around the pin - due for example to SC geometry variation in the azimuthal direction (see Figure 7.1) - can distort the heat flux distribution, making it azimuthally varying, due to the relatively high clad conductivity. This effect is bound to be magnified in tightly spaced rod bundles.

In [114] the authors suggest that the energy exchange via rod conduction is magnified, in many out-of-pile experimental setups, by the use of electric insulators like boron nitride featuring a thermal conductivity at least an order of magnitude higher than in the case of oxide, implying a stronger azimuthal gradient of the outer clad heat flux. To account for this phenomenon, a correlation, stemming from computer simulations on a multicell multiregion layout cooled by sodium (and assuming a $\frac{k_{clad}}{k_{cool}}$ ratio around 0.26), was proposed having the following form

$$W_{ij}^C = 0.52 \left(\frac{k_p}{k_{cool}} \right)^{0.38} \left(\frac{P}{D} \right)^{-1.04} \left(\frac{s_{ij}}{D} \right)^{0.016} \rho_{ij} \alpha_{ij} \quad , \qquad (9.7)$$

where W_{ij}^C is the rod thermal conduction analog of W_{ij}^H, k_p is the equivalent internal pin structure conductivity - meaning inside the inner surface of the cladding - and k_{cool} is the coolant thermal conductivity. In [114] k_p was selected equal to the boron nitride conductivity and specifically calibrated for its range of values; it is believed, however, that this correlation should be applicable also to real sodium-cooled fuel rods cases where the ratio $\frac{k_p}{k_{cool}}$ is quite low and the only contribution left is due to the cladding; indeed, boron nitride and the steel cladding typical of FRs have similar conductivities. Of course, for low k_p, the value of W_{ij}^C is bound to be small and thus not significantly contributing to the overall energy exchange dynamics, possibly making the proposed approximation acceptable.

Due to the low thermal conductivity of HLMs compared to sodium - around a factor of eight - the assumptions on which equation (9.7) is based do not longer hold:

- $\frac{k_p}{k_{cool}} < 0.4$ (in the case of boron nitride out-of-pile experiments) and

- $\frac{k_{clad}}{k_{cool}} \approx 0.26$.

The latter, in particular, makes the application of equation 9.7 to HLMs questionable; fortunately, a lower coolant conductivity means a lower overall impact of W_{ij}^C causing it to became negligible and, even more so, for real oxide fuel pins. Therefore, in ANTEO+, the present correlation is not applied to HLM-cooled cases.

....

9.2.5   Nusselt number

Similarly to the friction factor discussed in Section 9.2.1, the Nusselt's number is affected by the velocity distortion brought about by the increasing buoyancy (i.e. for increasing Y_{mix}). Again, however, with the shrewdness of the Y_{mix} criteria, this effect can be neglected and the Nusselt's number borrowed from Section 7.2.6.

9.3   Bypass model

The bypass model presented in Section 7.3 is also used for the mixed convection regime because the adopted nodalization is also suited for the expected values of $\frac{Q_{out}}{Q_{tr}}$. While the wrapper region treatment is identical in forced or mixed conditions for the bypass region, flow redistribution could occur between the different nodes; this effect is, however, presently neglected in ANTEO+ and the set of equations for the bypass nodes kept equal to their forced convection counterparts. This assumption needs further verification but, due to the low temperature, and thus density, gradients inside the bypass region, compared to the bundle, it is believed to be acceptable, at least as s first approximation[3].

Thanks to this simplification convergence is achieved much faster even if the efficient algorithm of Greene [46] cannot be used, being valid only for isolated pin arrangements; the standard Gauss elimination methods is therefore employed.

---

[3]Because the power-to-flow ratio of the bundle and bypass regions must be similar, if hot or cold bypasses have to be avoided, only very high power gradients on the different sides of the FA could make this assumption questionable.

. . . .

CHAPTER 10

VALIDATION IN MIXED CONVECTION

For the same motivations reviewed in Chapter 8 validation is a critical part of a SC code development effort. Due to the code structure delineated in Chapter 9 some of the models, like the friction factor and flow split, have been borrowed from forced convection and so, they do not need specific validation in the mixed regime; indeed, pressure drop and flow split are usually experimentally measured in isothermal conditions and so, simulation results among the mixed and forced convection in ANTEO+ are bounded to be identical. The present chapter is therefore devoted to the validation of SC and clad temperatures.

10.1 SC temperature

The list of mixed convection simulated experiments, to be added to the ones presented in Section 8.3.2, is reported in Table 10.1; the bundles analyzed are the same of Table 8.6, only the operational conditions are different. As done in Section 8.3.2 the sodium-cooled cases will be presented first and, after, the ones involving HLMs will be discussed highlighting similarities and differences with sodium.

The results will be presented highlighting the value of Y_{mix}, important in determining the degree of the velocity field distortion due to buoyancy, and thus friction factor and Nusselt's number. As explained in Section 9.1, ANTEO+ regime in mixed convection extends until $Y_{mix} < 100$; to ease readiness the reported value will be normalized to 100 (i.e. $Y_{mix}^* \to \frac{Y_{mix}}{100}$) so that a $Y_{mix}^* > 1$ implies falling outside ANTEO+ validity domain.

....

Table 10.1: Collection of experiments used for SC temperature validation in mixed convection, besides the one in Section 8.3.2. Main physical and geometrical parameters are also given.

Identifier	Power (kW)	Power skew	Flow rate (kg/s)	Y_{mix}^*
Hexagonal - wire spacer				
[83] Na				
Run 12-144	12.3	Uniform	0.12	0.00
Run 17-105	51.4	1.43	0.23	0.00
Run 18-105	50.1	1.67	0.23	0.01
Run 19-105	49.4	2.39	0.23	0.01
[33] Na				
Run 732	22.0	Uniform	0.18	0.00
Run 401	33.4	2.0	0.27	0.00
Run 720	14.2	2.0	0.13	0.00
Run 731	21.5	2.0	0.19	0.00
Run 731	21.5	2.0	0.19	0.00
[71] LBE				
NC	70.0	Uniform	5.6	0.22
Hexagonal - grid spacer				
[74] LBE				
Test 2 - NC	38.6	Uniform	9.0	10.8

Finally, it is mentioned that all the results for wire-spaced bundles are obtained with the CTm correlation while, for grid-spaced bundles, Kim's mixing model has been used; the choice stems from their proven ability, in forced convection, of accurately reproducing experimental trends (see Chapter 8).

10.1.1 Sodium-cooled experiments

For brevity, only a few selected cases, testing the ability of the code to properly reproduce forced convection results along with the capability of efficiently taking into account flow redistribution effects, will be presented in this chapter. The summary of the overall validation in sodium then follows.

. . . .
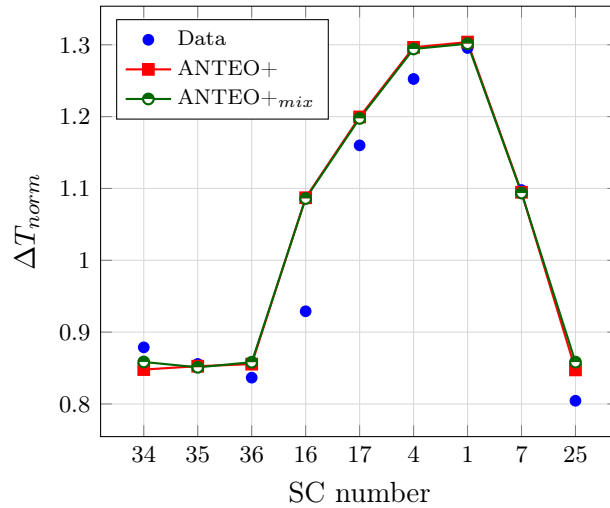
Figure 10.1: Test 2 - Run 105 of the ORNL-19 bundle ($Y = 0.00$ and $Y^*_{mix} = 0.00$). Comparison of ANTEO+ and ANTEO+ for mixed convection (ANTEO+$_{mix}$) in a pure forced convection case. Instrumented SCs are visible in Figure 8.4a.

Forced convection test

In Figure 10.1 it is clearly visible how, the set of equations and models presented in Chapter 9, smoothly reduces to the one of Chapter 7 when the limit of the forced convection regime is encounter (i.e. $Y \to 0$).

Mixed convection test

The mixed convection case with the highest Y but, with a Y^*_{mix} still much lower then one, is reported in Figure 10.2 comparing ANTEO+ for forced and mixed convection. It can be seen the ability to properly cope with the strong flow redistribution in this operative conditions, enhanced by the strong power skew (i.e. 2.8); the error on the ΔT_{norm}, indeed, drops from 10% - forced convection ANTEO+ - to 3.8% - mixed convection ANTEO+$_{mix}$.

Results summary

The overall results for the sodium cooled cases of Table 10.1 and Table 8.6 are displayed in Figure 10.3 and quantitatively in Table 10.2 where a comparison between the forced and mixed convection ANTEO+ is also reported.

. . . .
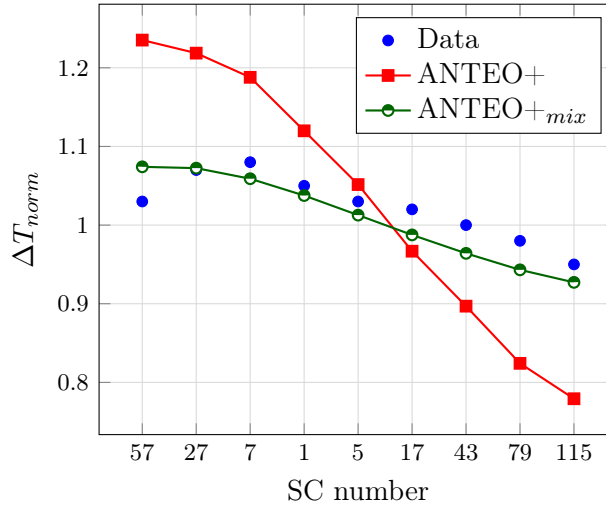
Figure 10.2: Run 229 of the WARD-61 bundle ($Y = 49.1$ and $Y^*_{mix} = 0.00$). Comparison of ANTEO+ and ANTEO+ for mixed convection (ANTEO+$_{mix}$) in a pure mixed convection case. Instrumented SCs are visible in Figure 8.9.

In Table 10.3 a comparison with the reference SC code COBRA is also presented.
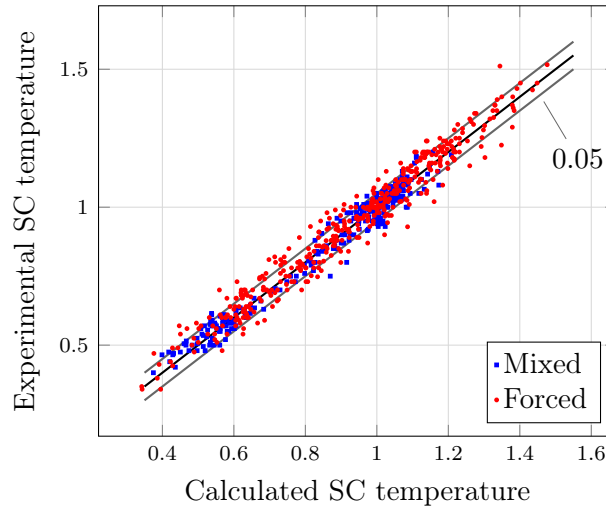
Figure 10.3: Graphical results summary for the SC temperature validation of ANTEO+$_{mix}$ in sodium-cooled bundles.

. . . .

Table 10.2: ANTEO+ and ANTEO+$_{mix}$ overall comparison in forced and mixed convection for sodium-cooled bundles.

	$\bar{\varepsilon}_{rel}[\%]$	90% confidence interval [%]
Forced convection (427 points)		
ANTEO+	3.8	8.6
ANTEO+$_{mix}$	3.9	8.6
Mixed convection (288 points)		
ANTEO+	4.9	11.7
ANTEO+$_{mix}$	2.9	5.7

Table 10.3: Comparison between ANTEO+$_{mix}$ and COBRA average $\varepsilon_{rel}[\%]$ for SC temperatures on sodium-cooled cases. Results are displayed by operating flow condition.

	Forced	Mixed
ANTEO+$_{mix}$[a]	3.5	3.1
COBRA	6.4	3.4

[a] Only points where COBRA results were available are considered.

Discussion In Figure 10.3 and Table 10.2 the ability of ANTEO+$_{mix}$ to homogeneously cope with both forced and mixed convection is evident; moreover, in Table 10.3, the direct comparison with COBRA well highlights the advantages of the adopted modeling approach, with ANTEO+ able to maintain a uniform accuracy inside its validity domain while, COBRA, showing difficulties approaching the forced convection regime.

10.1.2 HLM-cooled experiments

As reported in Table 10.1 two HLM-cooled cases in mixed convection have been simulated. In the following the main findings will be presented.

....

KYLIN-61

The same bundle of Section 8.3.2 was also investigated under mixed convection conditions (see Figure 8.17a) featuring, an axially and radially uniform power profile, with a total power of 70 kW and a mass flow rate of 5.60 kg/s as reported in Table 10.1.

Results are reported in Figure 10.4; the average $\bar{\varepsilon}_{rel}$ amounts to 15.4%.
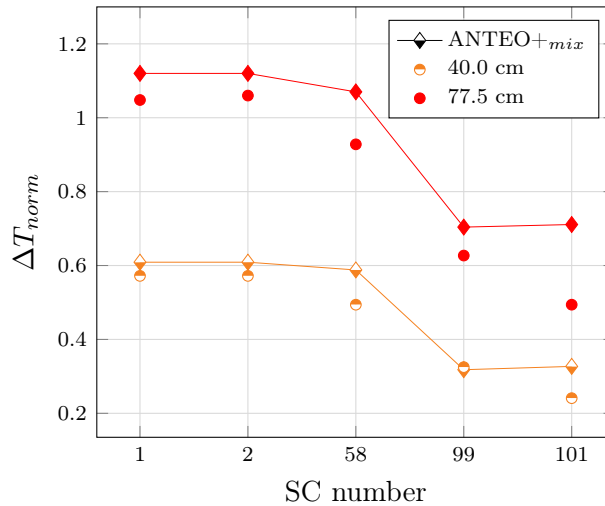
Figure 10.4: Representation of ANTEO+$_{mix}$ simulations and SC temperature experimental data for the KYLIN-61 bundle.

Discussion   Similarly to Section 8.3.2 an overestimation of the SC temperature occurs; this time, however, the difference between the SC center and bulk temperatures is bound to be much lower than in forced convection due to the higher SC temperature rise (their ratio being non negligible only near wall SCs). The effect discussed in Section 8.3.2 should therefore be lower for this operating conditions.

Again, the wire mixing effect seems to be over-predicted for near wall SCs, questioning the applicability of the CTm correlation for tightly spaced bundles cooled by HLMs. Finally, the fact that at 77.5 cm all the measured temperatures are lower than the calculated ones could also be a hint of energy balance errors or heat losses; with a simple average of the plotted results based on the number of SCs of each type and the inlet mass flow split values calculated by ANTEO+, a value of 0.950 for the average ΔT_{norm} (to be compared to the theoretical 0.969 at 77.5 cm) is obtained from ANTEO+ while

. . . .

the data give a 0.845[1]. While this is just a rough estimate, the difference is quite significant partially confirming uncertainties on the energy balance[2].

CIRCE-37

The same bundle of Section 8.4.2 was also investigated under mixed convection conditions (see Figure 8.22a), featuring an axially and radially uniform power profile, with a total power of 38.6 kW and a mass flow rate of 9.0 kg/s as reported in Table 10.1.

Results are reported in Figure 10.5; the average $\bar{\varepsilon}_{rel}$ amounts to 4.3%.
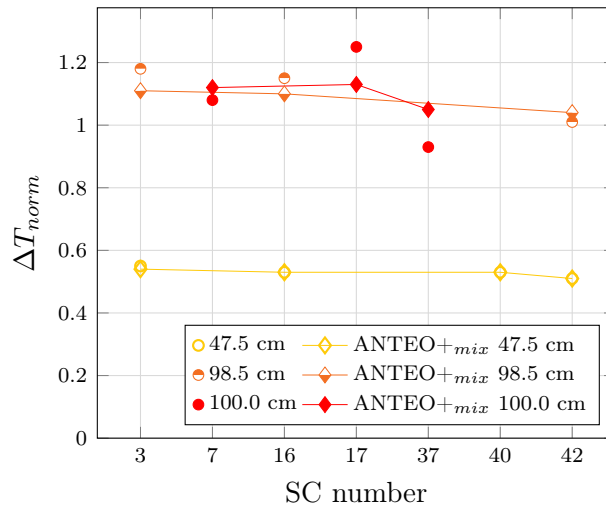
Figure 10.5: Representation of ANTEO+ simulations and SC temperature experimental data for the CIRCE-37 bundle.

Discussion   Even if, in the reported operating conditions, Y^*_{mix} is greater then unity results are more then satisfactory; this could be due to the flat power profile helping in reducing buoyancy effects or to the conservativeness of the Y^*_{mix} criteria. As discussed in Section 9.1, indeed, for widely spaced bundles - like CIRCE-37 - the onset of pure free convection effects could be

---

[1]The same conclusions would be drawn from the analysis at 40.0 cm

[2]Performing the same analysis in forced convection, with all the limitations concerning the representativeness of the SC center as a bulk temperature, it is found that the energy balance is much better respected than in the mixed regime: 0.99 against the theoretical 0.969 at 77.5 cm).

. . . .

delayed. Further investigations are however necessary in order to reach a more reliable conclusion.

Results summary

A graphical summary of the SC temperature validation on HLMs is reported in Figure 10.6 while a quantitative comparison between forced and mixed convection is reported in Table 10.4.

Table 10.4: ANTEO+ and ANTEO+$_{mix}$ overall comparison in forced and mixed convection for the SC temperature predictions in HLM-cooled bundles.

	$\bar{\varepsilon}_{rel}[\%]$
Forced convection (20 points)	
ANTEO+	13.7
ANTEO+$_{mix}$	12.6
Mixed convection (20 points)	
ANTEO+	11.8
ANTEO+$_{mix}$	9.8

Discussion   While in forced convection the measured quantities are not representative of the SC bulk temperature, in the mixed regime the difference between the two is bound to decrease; for this reason, the accuracy slightly increases but, still remains unsatisfactory low.

As previously seen the main source of error, in the available data, comes from the KYLIN-61 bundle featuring a tight lattice pitch in combination with a wire spacer; the correlations implemented in ANTEO+ presently seem to overestimate mixing, for near-wall SCs, in such HLM-cooled bundles (although energy balance errors may play an important role). For widely spaced pin arrangements with grid spacers, the accuracy is more then satisfactory suggesting that Kim's correlation well scales from sodium to HLMs.

Usually, in designing HLMFRs, relying on primary circuit natural circulation imposes high lattice pitches in the core layout and thus, going into the conditions currently better simulated by ANTEO+.

....
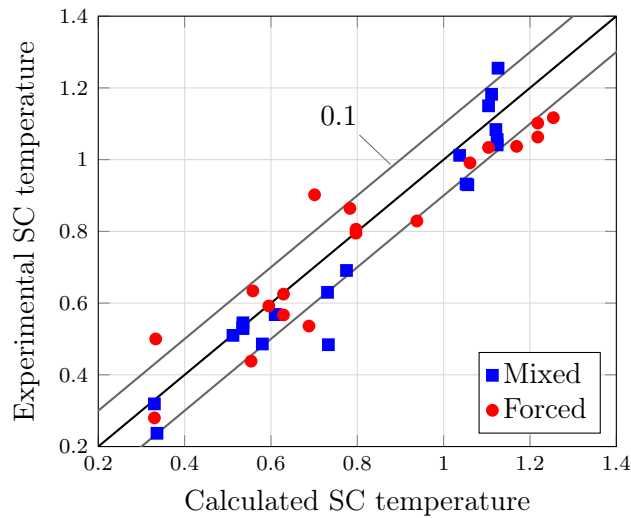
Figure 10.6: Graphical results summary for the SC temperature validation of ANTEO+$_{mix}$ in HLM-cooled bundles.

10.2   Clad temperature

The validation of the clad outer temperature, besides the forced convection cases analyzed in Section 8.4 covers the two HLM-cooled experiments previously discussed in Section 10.1.2 namely, KYLIN-61 and CIRCE-37. No new experiments in sodium are available and so this section covers only the HLMs results.

KYLIN-61

Results in term of $\Delta T_{c,norm}$ are reported in Figure 10.7, where only the correlation of Mikityuk has been used, Ma's one falling outside its validity range (Reynold's number too low). The average $\bar{\varepsilon}_{rel}$ assesses at 14.3%.

Discussion   In this operating conditions, due to the higher SC temperature rise, the wire effect is much less visible than in forced convection (see Figure 8.21) and is possibly less important in the overall thermal exchange dynamics. The bulk of the error, indeed, seems to come from the overestimation of the temperature in the interior SCs, as reported in Figure 10.4 and previously discussed.

. . . .
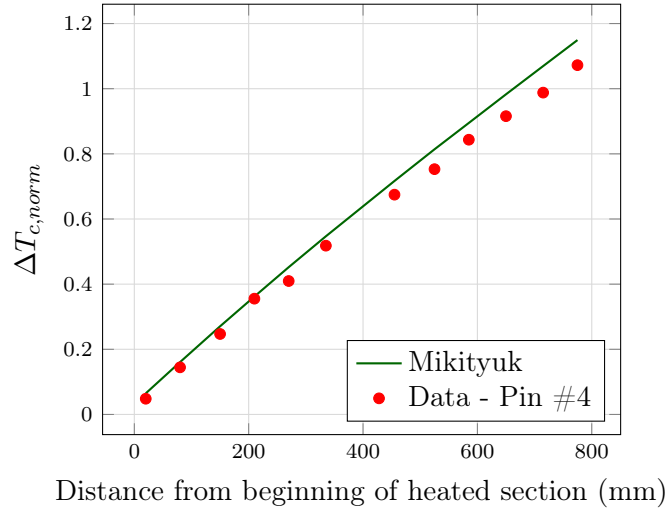
Figure 10.7: Representation of experimental and simulations clad temperatures for the KYLIN-61 bundle. The pin identification number is explained in Figure 8.17a.

CIRCE-37

Results for this bundle using Mikityuk's correlation for the Nusselt's number are reported in Figure 10.8, where pin numeration is the same as Figure 8.22a. Results are also summarized in Table 10.5.

Table 10.5: Comparison summary between simulations and CIRCE-37 bundle mixed convection experimental data on clad temperature for the instrumented pins in Figure 8.22a.

	Correlation	$\bar{\varepsilon}_{rel}[\%]$
$\Delta T_{c,norm}$	Mikityuk[a]	8.0
	Ma	8.5

[a] The Zhukov's correlation is not used for the ICE test section because the $\frac{P}{D}$ is out of the range of the correlation.

Discussion   The overall accuracy is satisfactory being the uncertainty, solely coming from the bifilar-type pin, on average, around 2.4% for the $\Delta T_{c,norm}$ and considering the Y^*_{mix} greater than unity.

. . . .
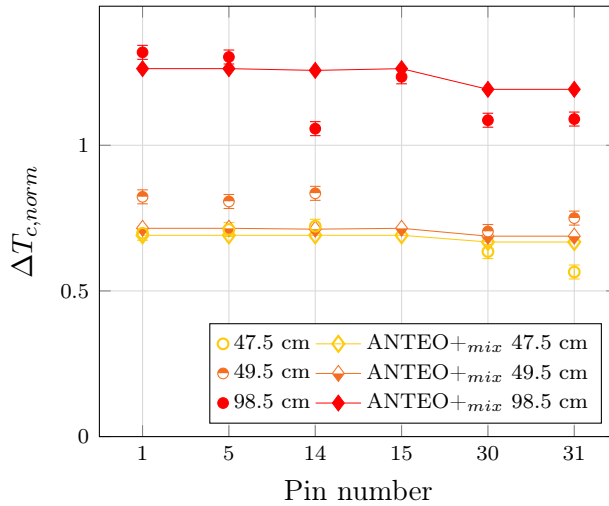
Figure 10.8: Representation of ANTEO+$_{mix}$ simulations and clad temperature experimental data for the CIRCE-37 bundle in mixed convection.

Contrarily to the forced convection experiments in Section 8.4.2, measurements at the grid plane (49.5 cm) are systematically higher than just upstream the spacer (47.5 cm) suggesting an influence of the latter when very small coolant bulk-clad temperature differences are present.

Finally, it is noticed, that some of the measured clad temperatures are lower then the corresponding SC temperatures, implying local effects at the measuring position that are not captured, by definition, by SC codes; the representativeness of such points is therefore questionable.

Results summary

The summary of the clad temperature validation is graphically reported in Figure 10.9, where Mikityuk's correlation has been used, and quantitatively in Table 10.6.

Discussion   Again the ability to smoothly translate from forced to mixed convection is visible in Figure 10.9, even with all the uncertainties previously discussed. The two Nusselt's correlations show similar performances although, KYLIN-61 mixed convection case falls outside Ma's one.

Finally it can be noticed how, comparing Table 10.6 and Table 10.4, in mixed convection the errors on ΔT_{norm} and $\Delta T_{c,norm}$ are in line with each
. . . .

Table 10.6: ANTEO+ and ANTEO+$_{mix}$ overall comparison in forced and mixed convection for the clad temperature predictions in HLM-cooled bundles.

		$\bar{\varepsilon}_{rel}[\%]$
Forced convection (36 points)		
ANTEO	Mikityuk	9.8
	Ma	9.5
ANTEO$_{mix}$	Mikityuk	9.8
	Ma	9.5
Mixed convection (28 points)		
ANTEO	Mikityuk	11.4
	Ma[a]	8.5
ANTEO$_{mix}$	Mikityuk	8.7
	Ma[a]	8.5

[a] Do not include KYLIN-61 mixed convection data because outside correlation application range.
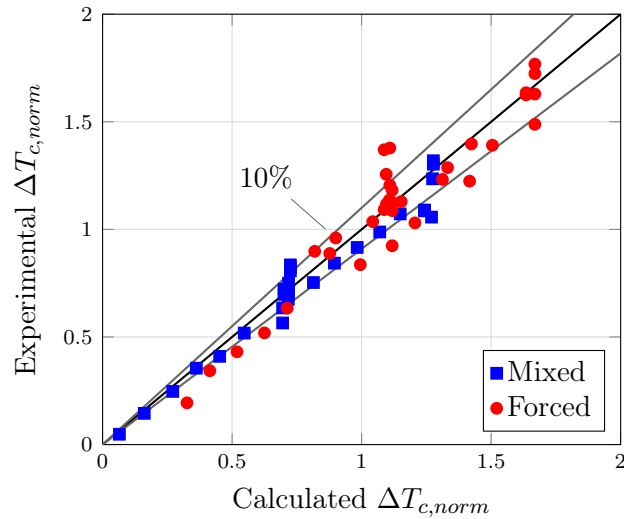
Figure 10.9: Graphical results summary for the clad temperature validation of ANTEO+$_{mix}$ in HLM-cooled bundles.

....

other, partially confirming the hypothesis put forward in forced convection about discrepancies between SC measured and actual bulk temperatures.

10.3   Validation summary

In the validation performed and discussed in the present chapter, the ability of the modeling approach presented in Chapter 9 to smoothly translate from forced to mixed convection has been proven both in sodium- and HLM-cooled cases. Having borrowed flow split and pressure drops from the previous forced convection validation campaign, attention has focused on SC and clad temperatures in mixed convection:

- SC temperatures are predicted with an average relative error of 2.9% for sodium-cooled bundles while, for HLM-cooled cases, accuracy decreases with a relative error up to 9.8%; excluding the KYLIN-61 bundle, suspected of energy balance errors, the error assesses at 4.3%, much more in line with the sodium result.

- For the clad temperature, only HLM-cooled experiments have been used, with an accuracy around 8.7% which, considering uncertainties and local effects, is deemed satisfactory.

In Table 10.7 results are summarized and compared with the estimated experimental uncertainties in their measurement, so to better contextualize the validation results. Similarly to what has been discussed in Section , results from this chapter can actively be incorporated in uncertainty quantification analyses, so to establish suitable margins for the nominal values of the main FA (thermal-hydraulically speaking) constrained parameters (e.g. clad outer temperature).

Work is still needed to extend the validation database in HLMs with particular emphasis on the SC temperatures in controlled conditions, along with measures of the clad temperatures avoiding local effects so to be truly representative of the quantity actually calculated by SC codes. Dedicated experiments to validation, indeed, will greatly enhance confidence in the final code accuracy assessment, easing its use in the design phase.

. . . .

Table 10.7: Summary of estimated uncertanties and confidence intervals of the main SC parameters in ANTEO+$_{mix}$ validity range for HLMs. A reference experimental uncertainty is also given for qualitative comparison.

Parameters	$\bar{\varepsilon}_{rel}[\%]$	experimental uncertainty [%]
ΔT_{norm}	4.3[a]	5
$\Delta T_{c,norm}$	8.7	5.6[b]

[a] Excluding KYLIN-61 bundle mixed convection results.
[b] Combination of the 5% uncertainty on the SC and 2.4% of bifilar-type simulator pins.

CHAPTER 11

CONCLUSIONS ON ANTEO+

In Part II the SC code for thermal-hydraulic analysis of HLMFRs, AN-
TEO+, has been extensively outlined. The main objectives of ANTEO+ as
a DOC were simplifying the problem description without penalizing accuracy
thus enabling a more transparent interface with the user having a clear and
identifiable application domain. In order to achieve these aims, in line with
the DOC development philosophy discussed in Chapter 4, a validity range
has been decided beforehand, namely, the steady-state, single-phase forced
convection regime.

The models and correlations implemented in the code have been pre-
sented, stressing the overall logical framework of their development along
with their target validity domain. These expectations have been tested dur-
ing the validation phase of the code, finding general agreement with ex-
periments. In particular, a thorough validation has been performed on the
models for flow split, pressure drops, SC temperatures and Nusselt's num-
ber quantifying the accuracy targeted by ANTEO+. Moreover, comparison
with other codes and tools has been performed revealing the generally high
level of ANTEO+ accuracy in its applicability domain. When falling outside
this domain, however, accuracy can drastically decrease and results start to
become excessively conservative.

For this reason, to tackle HLMFRs core layouts relying on mixed convec-
tion even at rated power, further work has been focused on the extension of
the validity domain to this regime. Again, the rationales of code development
have been stated and a consistent models selection performed; during the val-
idation phase the requirement of smoothly translating from forced to mixed

....

convection has been successfully tested, along with the level of accuracy targeted by the code. For both SC and clad temperatures, sodium-cooled experiments have revealed the great predictive abilities of ANTEO+$_{mix}$ while, some concerns are still pending on HLM-cooled cases, mainly due to the lower availability of experiments truly dedicated to validation of SC codes concerning these coolants; the first obtained results are however encouraging in this sense.

Concluding, ANTEO+ and ANTEO+$_{mix}$ are here presented as robust SC codes for the application in single phase forced and mixed convection regimes, which enable the user to more easily follow the calculation process and thus facilitating the results interpretation phase, including the identification of the confidence interval of the results.

Part III

Fuel Pin Thermo-mechanics: TEMIDE

Abstract   In Part III of the thesis the focus is on the development of the fuel pin thermo-mechanics DOC, TEMIDE. The development logics outlined in Chapter 4 and followed in Part II is here, again, implemented trying to enforce all the DOC requirements striving for a balanced tool. For answering the three pillar questions of any DOC, a sensitivity analysis is conducted so to understand the main phenomena contributing to the definition of the target parameters (i.e. fuel temperature and clad stresses and strains) inside the anticipated validity domain of TEMIDE. Results of the analysis are a series of guidelines helping in the code development phase, notably for models selection and the overall layout.

Following the derived guidelines, the code structure is deeply presented stressing the main simplifications and models selection criteria. To test the actual worth of the undertaken methodology, a verification campaign, first, and an early validation, after, are carried out. Due to the very preliminary nature of the performed validation, definitive conclusions cannot be drawn, but first results are encouraging.

. . . .

CHAPTER 12

TEMIDE DEVELOPMENT RATIONALES

As pointed out in Chapter 5 there is a lack of DOCs for the safety-informed fuel pin dimensioning in HLMFRs. The will to close this gap has given rise to the fuel pin thermo-mechanics code TEMIDE[1], from the italian **TE**ermo-**M**eccanica **I**mprontata al **DE**sign (design oriented thermo-mechanics). The guidelines fostered in Chapter 4 have here been followed to developed, from scratch, TEMIDE so to fully achieve the benefits that a well constructed DOC can deliver to the core designer exactly in the same way depicted in Part II.

12.1 Intended use and objectives

Being safety one of the milestones of Generation IV reactors, including it since the very beginning of the conceptual design phase is a mandatory step, paving the way for what is called safety-informed design; as discussed in Chapter 4, to enforce such a concept, the use of dedicated DOCs can be crucial. This is particularly true for the fuel pin dimensioning, the very first step of every core design, which is also the first safety barrier between the environment and the radioactive fuel and fission products. Therefore, the need to transform design constraints (e.g. $q' < q'_{melting}$ where q' is the linear power) deriving from safety requirements (e.g. UTOP) in pin dimensions that meet these constraints arises.

---

[1]TEMIDE descends from the female giant of the ancient Greek culture symbol of justice and order.

. . . .

As introduced in Chapter 5, due to the peculiar physical and neutronic characteristics of HLMs, the typical transients temperatures, time scales and global evolution are remarkably different from other LM coolants with particular emphasis for the UTOP- and ULOF-like transients; accordingly, they are assumed as references for TEMIDE.

12.1.1   UTOP

In UTOP-like transients the power suddenly rises due to some insertion of reactivity and, at the same time, it is assumed that no control or safety system is able to intervene; this scenario is one of the most threatening in terms of potential fuel melting. A possible scenario is depicted in Figure 12.1a, where the corresponding temperature evolution is reported in Figure 12.1b; to cope with such a situation the steady state maximum fuel temperature T_{fi} is to be lowered so to provide sufficient margin against melting $T_{melting}$, to accommodate any temperature excursion ΔT_{UTOP}, meaning

$$T_{fi} + \Delta T_{UTOP} < T_{melting}   . \tag{12.1}$$

This equation can be conveniently cast in terms of linear powers as

$$q' + \Delta q'_{UTOP} < q'_{melting}   . \tag{12.2}$$

This is the target relation that TEMIDE, as a DOC, should translate in relations among the main pin parameters.

(a) Reactor and **M**ain **H**eat e**X**changer (MHX) power evolutions.

(b) Maximum clad and fuel temperatures evolutions.
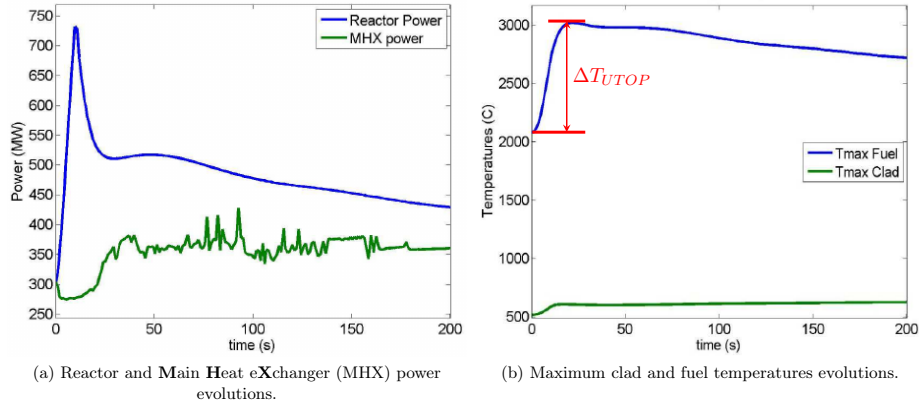
Figure 12.1: Typical powers (left) and temperatures (right) evolutions during an UTOP-like transient in a HLMFR (taken from [9]).

. . . .

12.1.2   ULOF

In ULOF-like transients, the pressure head contribution from the pumps is lost, and natural circulation is the only means for removing nominal heat (since any shutdown system is also supposed to fail) from the core. Due to the increase of the power-to-flow ratio in the system, the core outlet and, accordingly, the clad temperature rise[2] (see Figure 12.2); while a huge margin is available for coolant boiling, thanks to the very high boiling point of HLMs, elevated clad temperatures translate in a drastically weakened mechanical resistance of this component, enhancing risks of creep or plastic failures.
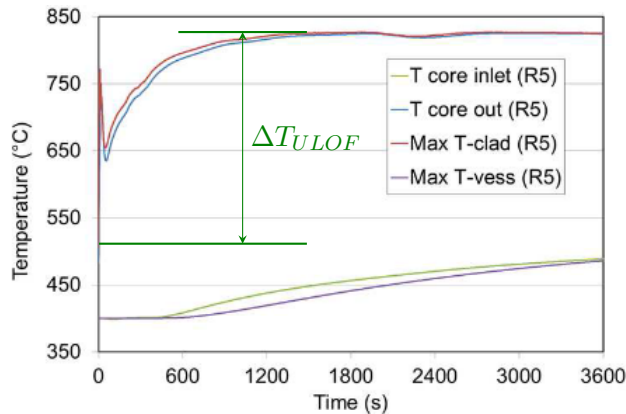
Figure 12.2: Typical temperatures evolutions during an ULOF-like transient in a HLMFR (taken from [9]).

To prevent core damage, the flow path must be arranged so as to provide low pressure drops, therefore the onset of natural circulation at affordable temperatures (see Section 3.3.1); the notion of *affordable* is linked with the stress state σ of the cladding and to the target grace time t_{grace} supposed before operator intervention. The relation could be formally stated as

$$T_{co} + \Delta T_{ULOF} = g(t_{grace}, \sigma) \quad , \tag{12.3}$$

where T_{co} is the steady state maximum clad outer temperature, ΔT_{ULOF} is the cladding temperature increase during the ULOF and g is the function relating the clad temperature and its mechanical response. The equality of equation (12.3) must be met in conditions where no clad failure is expected;

---

[2]In the case of a simultaneous loss of heat sink, the core inlet temperature will also increase, further aggravating the risk of clad failures.

. . . .

to achieve this, each member must be evaluated, understood and translated in core designer language: while ΔT_{ULOF} can be found via analytical pressure balances or dedicated DOCs like [16], the objective of TEMIDE, in ULOF, is the study of the function g.

It is implicit that, due to the strong interaction between the elementary cell - impacting on ΔT_{ULOF} - and pin - impacting on g - dimensioning, feedback retrofitting the design of both these elements are expected and, actually one of the main motivations for using a safety-informed DOC as explained in Chapter 4.

Given all the above, TEMIDE, as a safety-informed DOC for the thermo-mechanic design of a HLMFR fuel pin, should help in:

- dimensioning the pin so to avoid diffuse fuel melting during an UTOP and

- prevent clad damage and failure in the case of an ULOF so to allow sufficient grace time before operator intervention.

12.1.3   TEMIDE purposes

Given the intended use of TEMIDE, its main purposes as a safety-informed DOC are: to clearly translate the main transients of a HLMFR in constraints or relations among the main pin design parameters with a degree of accuracy and completeness superior to P&P methods, but without losing their degree of clarity, fundamental in a rationale design process.

12.2   Development rationales

The development of TEMIDE has been guided by the considerations discussed in Chapter 4 and summarized in the three questions reported in Section 4.3.

Which approach to choose among those found in the literature?

Differently from thermal-hydraulics, fewer methods have reached maturity, during the years, in the fuel pin thermo-mechanics field, mainly due to its superior intrinsic complexity cutting across numerous and diverse physical spheres; this rendered in prohibitive calculation times for the more sophisticated numerical techniques which have, therefore, lagged behind other,

....
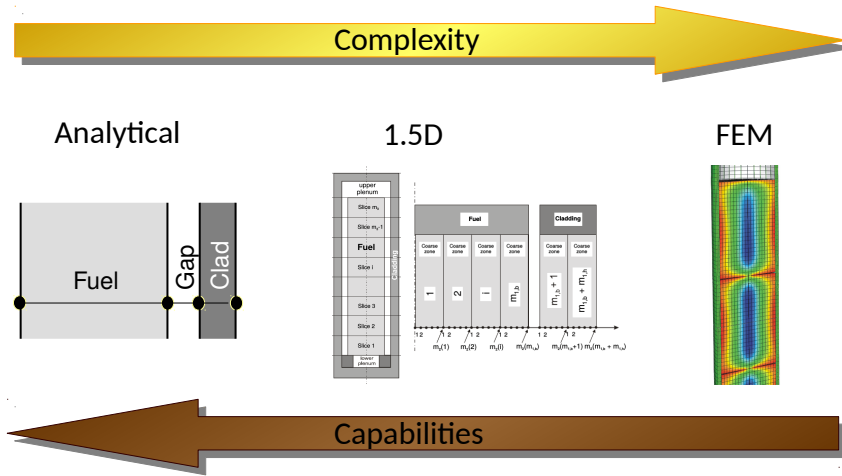
Figure 12.3: Representation of various numerical approaches in relation to their target scale and capabilities. The 1.5D image has been taken from [32].

more practical, approaches. Only recently, thanks to the increased availability of computational resources, classical mechanical engineering methods, like **F**inite **E**lements **M**ethods (FEMs) coupled to micro-structural analysis tools, have gained momentum. Similarly to Section 6.2, increasing accuracy and possibilities goes along with growing complexity as summarized in Figure 12.3; striking a balance between all the competing elements encompassing accuracy, complexity, running times and also including the degree of maturity as a variable - being it fundamental for reaching the required accuracy - the so called 1.5D approach has been pinpointed as the most promising candidate for reaching the DOC equilibrium requirement. It consists of an axial segmentation of the pellet stack where, each slice has an additional radial segmentation of the clad and fuel; the various slices are characterized by a weak axial connection and from this stems the additional 0.5D. Among the many 1.5D thermo-mechanics VOCs developed for water- and sodium-cooled reactors (a more comprehensive overview is given in [90]), so to verify fuel performances, TRANSURANUS [62], FRAPCON [40], CEPTAR [98] and FEMAXI [133] (in all the various versions produced during the many development years) are worth mentioning.

Establishing the target level of accuracy requires the analysis of all the components taking part into the global uncertainty on the final results of interest: input, material properties and models. While a more deep dis-

. . . .

cussion is presented in Chapter 13, here it is worth introducing some basic considerations:

- The input, meaning mainly power and clad outer temperature, are only approximately known; indeed, the clad temperature, especially in ULOF, depends on the elementary cell design which has been only tentatively fixed. Errors come from both nominal and transient conditions, with the latter possibly dominating; if, ideally, most of the input parameters are elaborations of other DOCs build with the same logic described in the present thesis, the error magnitude on such parameters should be similar to the other sources, thus ensuring code homogeneity.

- Material properties, differently from the case of FA thermal-hydraulics, give an important contribution to the global uncertainty, mainly due to the physical complexities of the various irradiation effects involved along with the practical difficulties of systematically measuring them; indeed, properties like the fuel thermal conductivity or the clad swelling are subject to conspicuous uncertainties.

- Models, therefore, should be tailored and selected so to avoid an excessive development effort, with a contribution to the overall uncertainty in line with the material properties ones; an extremely refined modeling tagged with poorly defined material properties would indeed not be particularly beneficial in terms of accuracy while surely hindering the constraints-configuration translation process (see Section 4.2.1).

While for ANTEO+ the modeling efforts were set by the lower limit of the experimental uncertainties, for TEMIDE the requirement is different: to ensure homogeneity between models and material errors.

Which application and validity domain to select?

The application domain has been selected based on the design parameters currently targeted by the main HLMFR concepts described in Section 2.4.3 which are, basically, technology demonstrator reactors or, at least, short-time deployment concepts. Among the possible fuels, the selected reference ones are oxides, due to the great amount of experience accumulated on their performances in FRs, with respect to other fuel types, significantly easing the achievement of the short deployment time requirement; for the same reason, the additional constraint of low MA load is added.

. . . .

To what concerns the clad temperature the main limitation comes from corrosion considerations and the ability of the clad steel to operate, for the foreseen irradiation life, while assuring the desired performances. Given the strategies currently investigated and deemed available in the short term, the maximum nominal temperature has been conservatively assumed lower than $550°C$ [45]. The lower limit of $400°C$ comes, instead, from the credible margin to freezing and the risk of LM embrittlement (for ferritic-martensitic steels) [28].

The validity domain has then been set, relatively to the peak pin - the one of interest for design purposes - as:

- **B**urn-**U**p (BU) < 10 $at.\%$,

- **D**isplacement **P**er **A**tom (DPA) < 100,

- $250 < q' < 450$ W/cm,

- $400 < T_{co} < 550$ $°C$,

- $e_{Pu} < 30$ $wt.\%$,

- $e_{MA} < 1$ $wt.\%$,

- UTOP characteristic time around 10 s,

- ULOF characteristic time around 1 h,

where e_{Pu} and e_{MA} are, respectively, the plutonium and MA enrichment.

The characteristic transient times have been fixed according to the following criteria:

- for the UTOP, typically, the highest energy releases are achieved for fast transients, where the only negative feedback able to counterbalance the inserted reactivity is the Doppler effect; for this reason, the most conservative time for reaching the maximum fuel temperature has been set around 10 s [9];

- for the ULOF, according to the **W**estern **E**uropean **N**uclear **R**egulators **A**ssociation (WENRA) recommendations, no operators' intervention can be credited for the first 30 minutes into an accident; accordingly, the required grace time for this kind of accident is typically assumed in the order of one hour, to credibly match with the manual actuation of the SCRAM.

....

Which equations and models to adopt given the decided validity domain?

The answer to this question is much more complicated than the one in Section 7.1 due to the higher complexities and interdependence present in the fuel pin thermo-mechanic problem, not allowing an easy interpretation for all the terms in the governing equations. To allow a rational choice involving the equations and models to be implemented in TEMIDE, so to truly achieve all the DOC requirements, a sensitivity analysis has been performed, as presented in Chapter 13.

. . . .

SENSITIVITY ANALYSIS

The final step before the actual coding of any DOC is the selection of the most appropriate set of equations and models so to reach the desired accuracy while keeping complexity at reasonably low levels. To this aim, the governing equations and phenomena must be analyzed, inside the anticipated validity domain, so to retrieve the first order relations to keep and model. Unfortunately, the typical interdependency among parameters is depicted in Figure 13.1 where the complexity of the problem at hand is apparent.

To simplify and make more readable Figure 13.1, the first step is, therefore, to compile a ranking of physical phenomena by importance relatively to a target parameter whom accuracy we are trying to preserve; this can be done via a dedicated sensitivity study. In order to make the ranking possible, the different effects must be separated, the use of already existing fuel performance code is therefore not suited for this kind of sensitivity analysis because they are often black boxes or do not allow for effects separation [135]. To overcome this limitation, an (almost) analytical approach has been followed, avoiding most of the non-linearity, and so losing some completeness, but gaining in clarity and, possibly, generality.

13.1 Domain of the study

Given the intended use of TEMIDE, the decided validity domain and the will to study possibilities of fuel melting in UTOP and clad failure in ULOF, the target parameters for the sensitivity analysis have been pinpointed in the

. . . .

Figure 13.1: Typical dependency scheme among the main parameters
characterizing the fuel pin behavior under irradiation [82].

maximum fuel temperature $T = T_{fi} - T_{co}$[1] and in the clad mechanical state
summarized by the effective stress σ_{eff} and the total strain ε_t. Moreover,
for the cladding the focus will be on the end of the active region where
temperatures are higher, especially in ULOF conditions, while for the fuel,
the midplane of the active region will be the reference, being the section
where the maximum fuel temperature occurs and so, the most challenging,
especially in UTOP conditions.

To ease the analysis even further, only the two extreme conditions (from
the fuel pin thermo-mechanic point of view) will be studied: **B**eginning **o**f
Life (BoL) and **E**nd **o**f **L**ife (EoL). In the present context, with BoL, it is
intended the first days at full power when instantaneous or fast phenomena,
like fuel cracking and relocation, have already taken place.

13.1.1   General approach

In order to perform a comprehensive analysis, including all the factors in-
fluencing the target parameters, a top-down approach has been adopted;
starting from an analytical equation describing the parameter of interest,

---

[1]The difference between the maximum fuel temperature and the clad outer temperature
is the actual quantity calculated by fuel pin thermo-mechanics codes, being the latter,
an input value. T is therefore the parameter really affected by the code and materials
uncertainties.

. . . .

all the factors influencing it can be identified. The process is then repeated for each factor until some elementary quantity of interest is found, meaning a parameter or process which must be ultimately modeled. Material properties are also included in the analysis for highlighting where care in their selection must be applied and, mostly, to put modeling error contribution into perspective. On the other hand, input (e.g. flux level) or boundary conditions (e.g. outer clad temperature) are not directly included because they are assumed to come from other DOCs build with the same logics described in this thesis.

To better comprehend the adopted methodology, a brief example is given.

Example: T can generally be expressed as

$$T = T_{fi} - T_{co} = \Delta T_c + \Delta T_{gap} + \Delta T_f \quad , \tag{13.1}$$

where ΔT_c is the temperature difference across the clad, ΔT_{gap} is the temperature difference across the gap and ΔT_f is the temperature difference across the fuel. Each term can be further decomposed, like ΔT_f:

$$\Delta T_f \rightarrow \int_{T_{fo}}^{T_{fi}} k_f(T) dT = q''' \int_{r_{fi}}^{r_{fo}} \frac{1}{r'} \int_{r_{fi}}^{r'} r'' f(r'') dr'' dr', \tag{13.2}$$

where T_{fo} is the fuel surface temperature, k_f is the fuel thermal conductivity, q''' is the radially averaged power density, per unit volume, r_{fo} and r_{fi} are the external and internal pellet radii respectively and $f(r)$ is the power radial distribution function. Regarding $f(r)$, in a FR[2], can be simply formulated as

$$f(r) = \frac{e(r)}{\overline{e}} \frac{\rho_f(r)}{\overline{\rho_f}}, \tag{13.3}$$

where $e(r)$ and $\overline{e}$ are the local and average plutonium enrichment respectively and $\rho_f(r)$ and $\overline{\rho_f}$ are the local and average fuel density respectively. The elementary models involving the plutonium redistribution and the density variations due to restructuring have been identified and the analysis continues further decomposing all the other terms in equation (13.2).

Systematically applying the just reviewed top-down approach, the final results reported in Figures 13.2 and 13.3 respectively for the fuel temperature and clad mechanics in nominal conditions have been obtained; the parallel results for the UTOP and ULOF transients are instead reported in Figures 13.4 and 13.5.

....
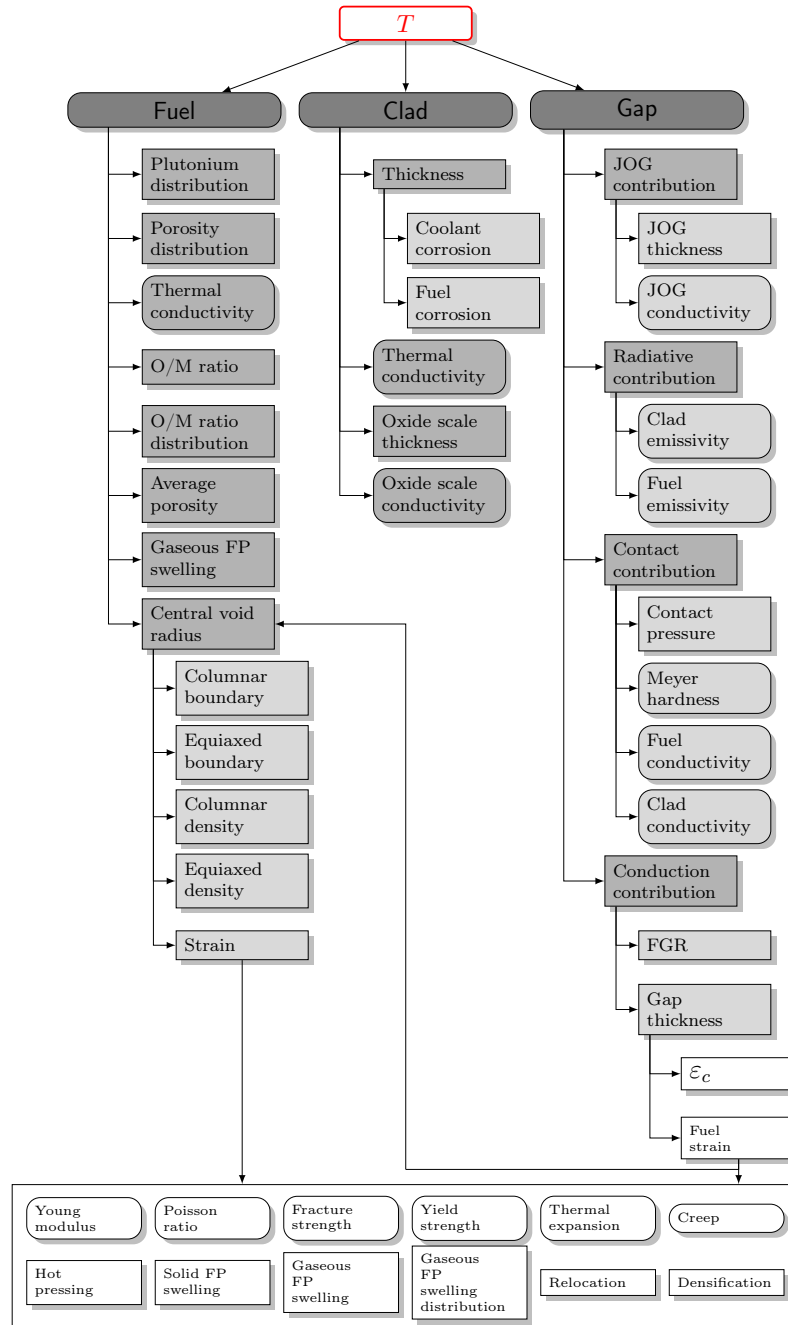
Figure 13.2: Results for the top-down analysis on T in nominal conditions. Rounded corners highlight material properties. The nomenclature is: **F**ission **P**roducts (FP) and **O**xygen-to-**M**etal (O/M).
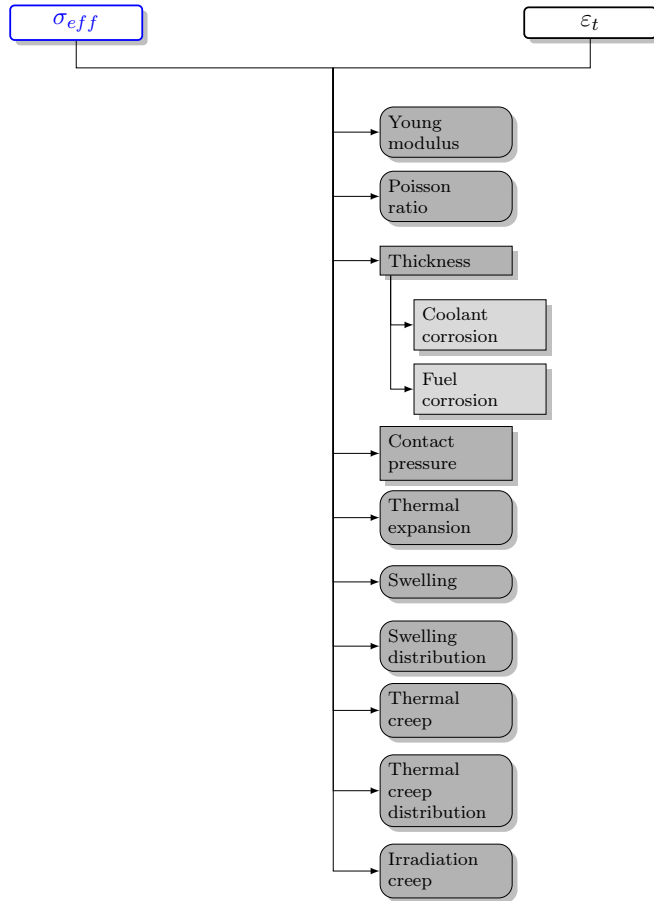
Figure 13.3: Results for the top-down analysis on σ_{eff} and ε_t in nominal conditions. Rounded corners highlight material properties.

. . . .
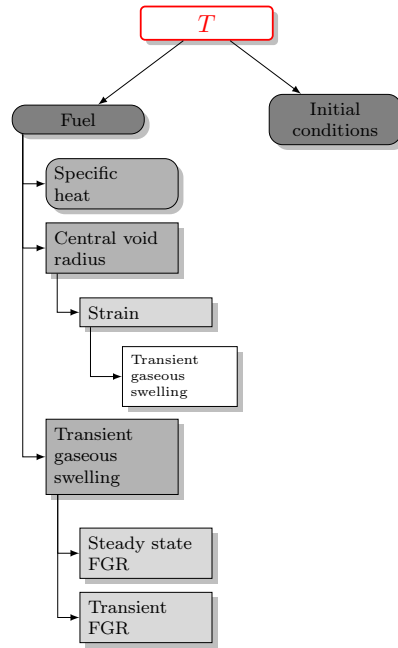
Figure 13.4: Results for the top-down analysis on T in UTOP conditions. Rounded corners highlight material properties.
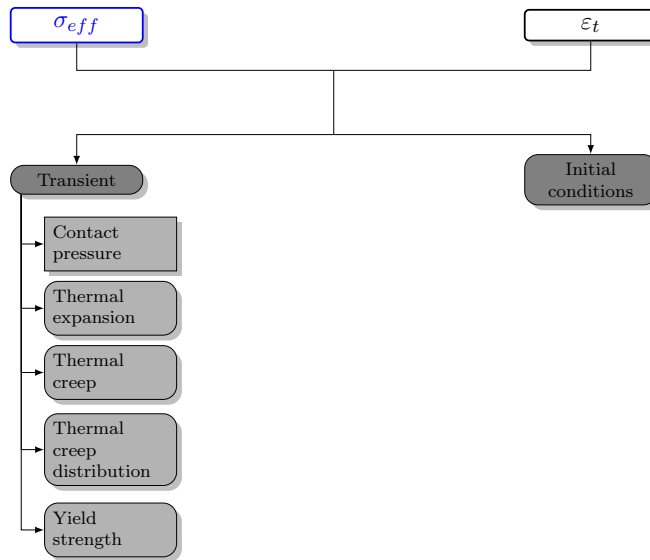
Figure 13.5: Results for the top-down analysis on σ_{eff} and ε_t in ULOF conditions. Rounded corners highlight material properties.

. . . .

All the results in this chapter will be presented in terms of the sensitivity coefficient $I_{x,y}$ defined as

$$I_{x,y} = \left| \frac{\delta y/y}{\delta x/x} \right| \quad , \tag{13.4}$$

where x is the parameter whose influence we are assessing (e.g. plutonium distribution) while y is the target parameter (e.g. maximum fuel temperature).

In the following, to keep this chapter more clean and easy to understand, not all the phenomena in Figures 13.2, 13.3, Figures 13.4 and 13.5 will be explicitly discussed (though investigated), but only the ones that better highlight the adopted analytical approach.

13.2 Fuel temperature - Nominal conditions

For the fuel temperature in nominal conditions, significant cases regard the effect of plutonium and density redistribution on the power density distribution across the pellet, as previously outlined, along with the effects of FGR, gap thickness and **J**oint **O**xide **G**ain (JOG) formation.

13.2.1 Plutonium distribution

A typical radial Plutonium distribution for the power range described in Section 12.2 is reported in Figure 13.6, where the increase in concentration inside the radius (r_{col}) characterizing the beginning of the columnar grain region is apparent. Various mechanisms have been proposed for explaining such a phenomenon going from the redistribution by vapor transport in an evaporation-condensation mechanism concomitant with pore migration and fuel restructuring, to redistribution by solid-state diffusion driven by the thermal gradient inside the pellet; the former is believed to dominate the BoL contribution while the latter to dominate in the long term [88]. Given that the overall redistribution at BoL is bound to be lower than the one at EoL, the latter is taken as reference, and so, the evaporation-condensation mechanism can be neglected.

An analytical solution to the solid-state thermally driven diffusion process has been put forward in [29], but is only valid for short times, making it not suited for EoL applications in fuel pin thermo-mechanics codes. For the

---

[2]The flux spatial self-shielding effect can be disregarded in a FR being the neutron mean free path much higher than a single pellet.

. . . .

present sensitivity purposes, however, the interest focuses more on studying the effects that an error on $f(r)$ has on T - so to assess the importance of plutonium redistribution -, meaning that $f(r)$ is actually imposed and then, consequences of its variations studied; for this reason the solution proposed in [29] could suffice. Unfortunately, two main problems arises if the solution in [29] is to be used:

- $f(r)$ would, correctly, depend on temperature creating an unwanted non-linear effect;

- the form of $f(r)$ would not be analytically integrable in equation (13.2).

For these reasons, a much simpler shape is assumed for $f(r)$[3], namely

$$f(r) = \begin{cases} A - Br & r \leq r_b \\ C & r \geq r_b, \end{cases} \tag{13.5}$$

where r_b is the radius inside which significant redistribution has occurred and, taken equal to r_{col} in first approximation. The proposed function is also represented in Figure 13.7. This form does not account for the depletion of plutonium near the columnar region boundary predicted by more sophisticated methods [87], however, this effect is not always present, as depicted in Figure 13.6 and reported in [88], possibly lying inside experimental or fabrication uncertainties; for the present purposes the adopted shape of $f(r)$ is therefore deemed acceptable.

Applying the condition of maximum Pu (e_{max}) near the central hole, continuity at r_{col} and preservation of the average enrichment ($\overline{e}$), the coefficients in equation (13.5) can be expressed as

$$\begin{aligned} A &= \frac{e_{max}}{\overline{e}} + \frac{3r_{fi}(\overline{e}-e_{max})(r_{fo}^2-r_{fi}^2)}{(r_{col}^3-r_{fi}^3+3r_{fi}r_{fo}^2-3r_{col}r_{fo}^2)\overline{e}} \quad, \\ B &= \frac{3(\overline{e}-e_{max})(r_{fo}^2-r_{fi}^2)}{(r_{col}^3-r_{fi}^3+3r_{fi}r_{fo}^2-3r_{col}r_{fo}^2)\overline{e}} \quad, \\ C &= \frac{e_{max}}{\overline{e}} + \frac{3(r_{fi}-r_{col})(\overline{e}-e_{max})(r_{fo}^2-r_{fi}^2)}{(r_{col}^3-r_{fi}^3+3r_{fi}r_{fo}^2-3r_{col}r_{fo}^2)\overline{e}} \quad. \end{aligned} \tag{13.6}$$

Putting these expressions into (13.2), the integral can be performed and the importance coefficient $I_{e_{max},\Delta T_f}$ calculated. $I_{e_{max},\Delta T_f}$[4] as a function of the

---

[3]To enforce effects separation, the contribution of the density distribution to $f(r)$ has been neglected (i.e. $\frac{\rho_f(r)}{\rho_f} = 1$).

[4]e_{max} in the sensitivity coefficient is in reality $\frac{e_{max}}{\overline{e}}$, but the former is adopted to keep the notation more compact.

. . . .
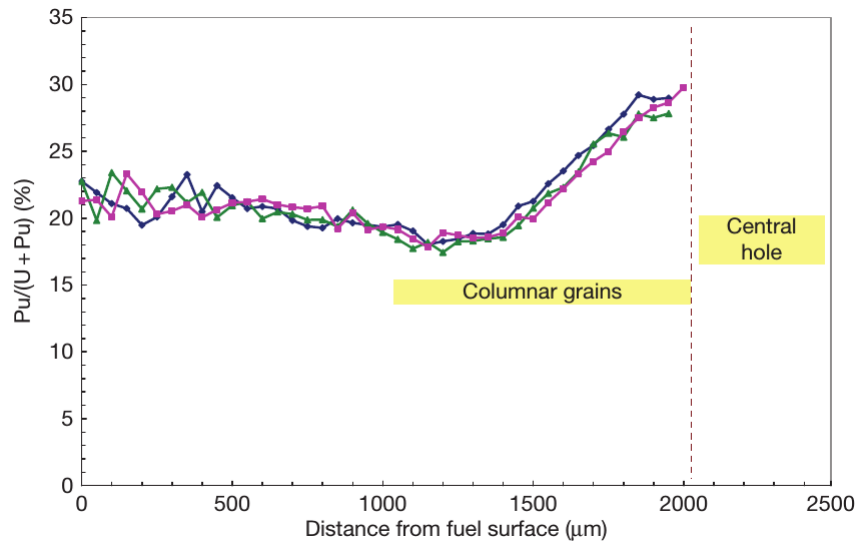
Figure 13.6: Typical Plutonium radial profile for an oxide pellet irradiated in Phénix at 15 at.%. Taken from [47].
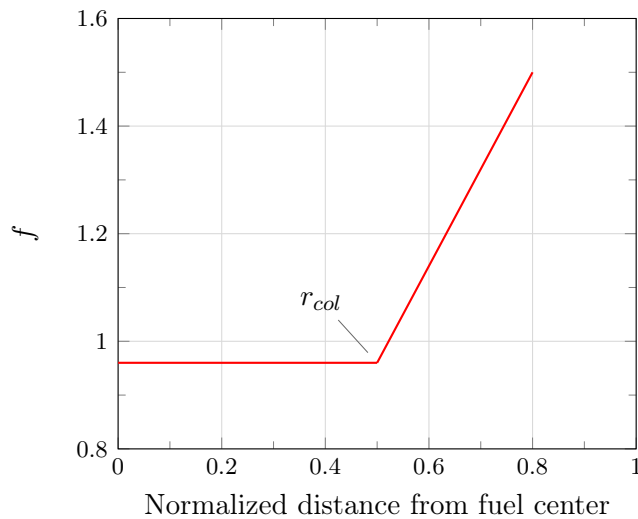
Figure 13.7: Assumed shaped of the radial power distribution factor due to Pu redistribution: an example.

normalized (relatively to r_{fo}) r_{col} and r_{fi} is plotted in Figure 13.8. The value of $I_{e_{max},\Delta T_f}$ slightly depends on $\frac{e_{max}}{\bar{e}}$, increasing for growing redistribution, ...

but this effect is overshadowed by the dependency on r_{col}. The increasing trend with r_{col} is clearly visible in Figure 13.8 and it generally corresponds to an increasing importance of plutonium redistribution for higher powers and temperatures; it can also be seen how the sensitivity coefficient decreases for higher r_{fi} mainly because this reduces the pellet area affected by redistribution - approximately $r_{col}^2 - r_{fi}^2$.
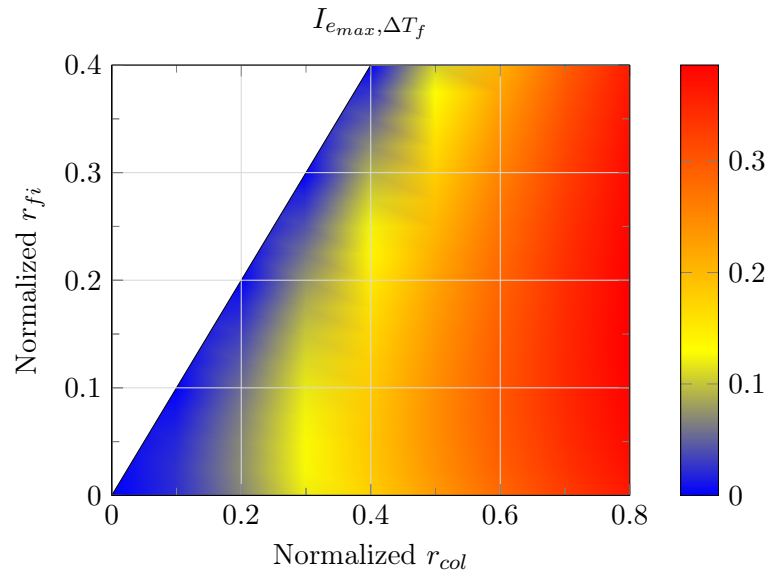
Figure 13.8: $I_{e_{max}, \Delta T_f}$ as a function of the internal fuel radius and the columnar boundary. Normalizations are relative to the fuel outer radius.

As an example, taking r_{fi} equal to 0.25 and r_{col} equal to 0.6, results in a sensitivity coefficient around 0.25 which means that an error of 20% in the prediction of e_{max} will results in a 5% error on ΔT_f finally translating in a lower error on the T (it must be weighted with the relative contribution of ΔT_f to T, namely $I_{\Delta T_f, T}$). Due to the nature of the analysis, the effect is possibly overestimated, but for the present work, it is still deemed acceptable.

Strictly speaking, some other actinides like americium have been shown to redistributes similarly to plutonium, but because a low concentration of these elements ($e_{MA} < 1 \ wt.\%$) has been assumed in Section 12.2, the effect on the power density distribution can be neglected.

. . . .

13.2.2   Density distribution

The density distribution is mainly linked to the restructuring process - if the influences of gaseous swelling and thermal expansion are neglected - which shifts porosity from the pellet to the central hole; the net effect is therefore a densification of the interior of the pellet which results in an increased heat generation in that region. A typical distribution for an initially high-porous pellet is reported in Figure 13.9, where the density distribution is complementary to the porosity one.
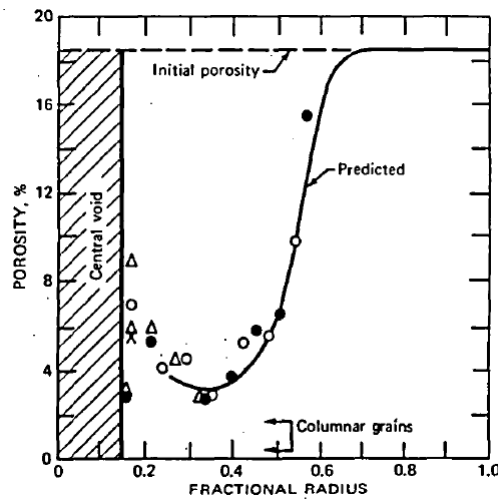
Figure 13.9: Porosity distribution for a Sphere-Pac stoichiometric MOX fuel at 0.7 at.% BU operated at a linear power of 450 W/cm. Taken from [96].

In analogy with Section 13.2.1, instead of using models based on the pore velocity migration [59], which would make an analytical approach impossible, a simpler, more manageable approach is selected: the three zones model. The pellet is therefore divided in three different regions of constant density: the unrestructured, equiaxed and columnar regions. The equation representing $f(r)$ is thus given by

$$f(r) = \begin{cases} \frac{\rho_{col}}{\rho_f} & r \leq r_{col} \\ \frac{\rho_{col}}{\rho_f} + \frac{\rho_{col}-\rho_{unr}}{\rho_f(r_{col}-r_{eq})}(r - r_{col}) & r_{col} \leq r \leq r_{eq} \\ \frac{\rho_{unr}}{\rho_f} & r \geq r_{eq}, \end{cases} \qquad (13.7)$$

where ρ_{col} and ρ_{unr} are the columnar and unrestructured densities respectively while r_{eq} is the equiaxed zone outer boundary radius. In equation

....

([13.7](#)) the equiaxed region density has been assumed as the average between the columnar and unrestructured ones. An example of $f(r)$ is given in Figure [13.10](#).
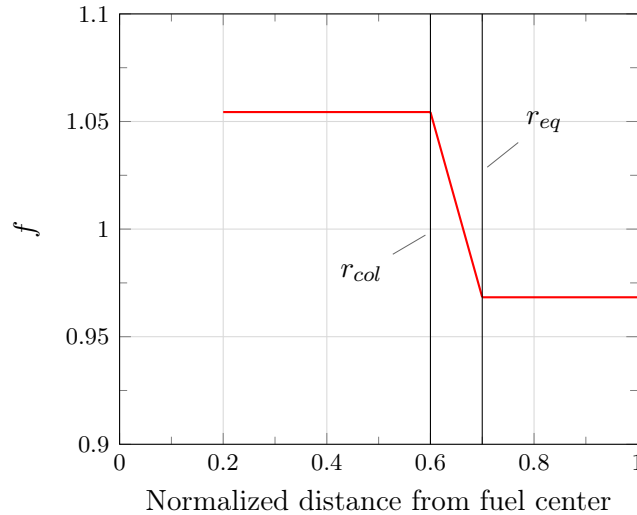
Figure 13.10: Assumed shaped of the radial power distribution factor due to porosity redistribution: an example.

Putting these expressions into equation ([13.2](#)), the integral can be performed and the sensitivity coefficient $I_{Po_{max}, \Delta T_f}$[5] calculated. The results of such a procedure are reported in Figure [13.11](#); $I_{Po_{max}, \Delta T_f}$ slightly depends on the fuel inner radius, increasing for lower r_{fi}, but the main factors are r_{col} and r_{eq}. It can be seen how the impact of the density distribution remains negligible as long as the columnar boundary is in the inner region of the pellet; this stems from the small amount of fuel mass involved in the redistribution in that case. It can be concluded that, similarly to the plutonium, but with an overall higher impact, the density redistribution process is important for increasing powers and temperatures and for pellets with a small, initial, r_{fi} (e.g. solid pellets).

As typically happens, the equiaxed and columnar boundaries are not particularly distant also due to the strong temperature gradient in the central zone of the pellet where they approximately lie; if the relation between r_{col} and r_{eq} is actually known, the physical space in Figure [13.11](#) is drastically

---

[5]Because the density and porosity distributions are the complement to one of each other, the sensitivity coefficient has been referenced to Po_{max} instead of ρ_{max}. Similarly to $I_{e_{max}, \Delta T_f}$, Po_{max} is actually $\frac{Po_{max}}{Po_{ave}}$ with Po_{ave} indicating the average pellet porosity.

. . . .
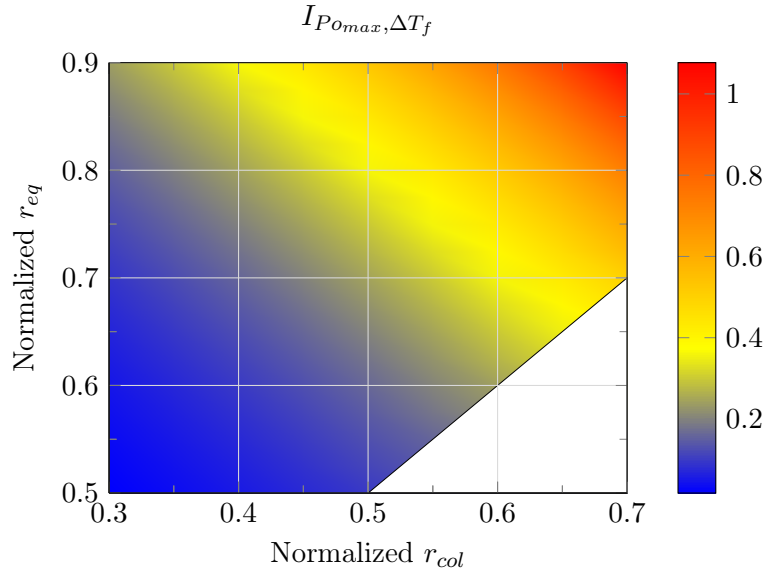
Figure 13.11: $I_{Po_{max},\Delta T_f}$ as a function of the normalized columnar and equiaxed boundaries. Normalizations are relative to the fuel outer radius.

reduced and: as an example, Figure 13.12 can be consulted.

13.2.3   FGR

Under high temperature conditions, the insoluble gases produced by the fission event, gain the necessary mobility to diffuse through the fuel structure, eventually reaching grain boundaries; if sufficient gas accumulates on such boundaries, a tunnel-like structure can be formed inter-grains potentially connecting the gas with open spaces, leading to a release in the plenum region [96]. These fission gases are characterized by low conductivity and thus contributes to the overall degradation of the thermal exchange dynamics between the clad and fuel; moreover, if released in significant quantities, the pressure inside the pin will increase potentially stressing the cladding.

The FGR, as visible in Figure 13.2, impacts T via the conductive contribution (h_{gas}) of the gap conductance (h_{gap}), in turn influencing ΔT_{gap} as summarized by equation (13.8)

$$FGR \to h_{gas} \to h_{gap} = h_{rad} + h_{gas} + h_{con} \to$$
$$\to \Delta T_{gap} = \frac{q'}{2\pi h_{gap} r_{gap}} \to T \quad , \tag{13.8}$$

. . . .
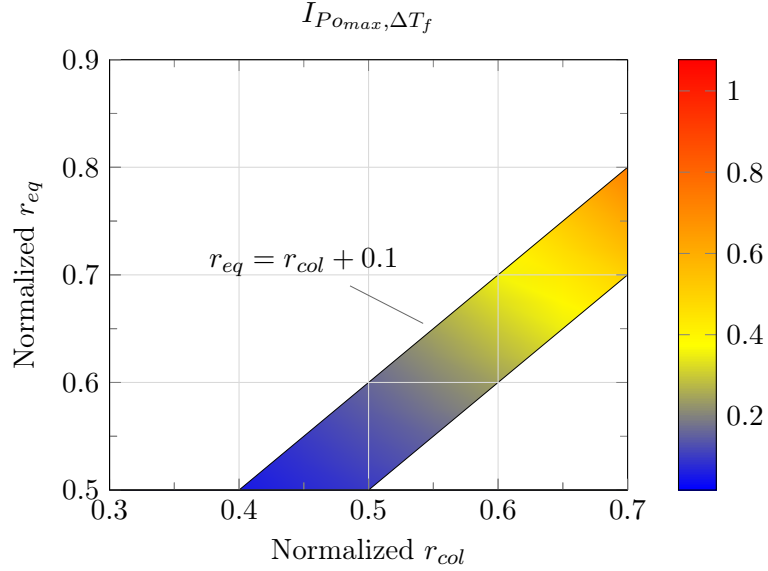
$$I_{Po_{max},\Delta T_f}$$

Figure 13.12: An example of physical domain inside the (r_{eq}, r_{col}) space for $I_{Po_{max},\Delta T_f}$.

where h_{rad} and h_{con} are the radiative and contact contribution to h_{gap} while r_{gap} is the gap radius defined as the average between the fuel outer and clad inner radii.

To better understand the role of FGR, it is worth recalling that the conductive contribution can be generally expressed as (even if a more general formula has been proposed in [63])

$$h_{gas} = \frac{k_{gas}}{s_{gap} + A(R_f + R_c) + (g_f + g_c)}, \tag{13.9}$$

where k_{gas} is the plenum gas mixture thermal conductivity, s_{gap} is the gap thickness, R_f and R_c are the fuel and cladding roughnesses respectively, A is a model coefficient, possibly function of contact pressure, and g_f and g_c are jump distances for the fuel and cladding respectively. The $g = g_f + g_c$ parameter accounts for the non-equilibrium condition between the gas molecules and the solid surfaces that originates due to the very small values of s_{gap}, comparable to the molecules mean free path.

Roughnesses are considered an input parameter and so not included in the analysis. Also, since the sensitivity coefficient $I_{k_{gas},h_{gas}}$ is unity, the effects which influence the gas conductivity are directly linked to h_{gas}; these

. . . .

are the gas mixture composition and plenum pressure. Finally, due to the fact that jump distances, as k_{gas}, depend on composition and pressure, their effect is embedded in the analysis of these two parameters; this is justified by the effect of g, which is indeed very small: as an example, considering the situation with closed gap - the most critical for the impact of the jump distances - we see that the effect of g, expressed as

$$I_{g,h_{gas}} = \frac{1}{1 + \frac{A(R_f + R_c)}{g}}, \tag{13.10}$$

is quite small given that $A(R_f + R_c)$ is usually higher than 10 µm while g is below 0.1 µm for usual closed gap plenum pressures.

Because both composition and pressure depend on the quantity of FG released by the fuel in the plenum, the effect of FGR on the gap conductance is actually double; both these effects will be now analyzed.

Composition

For oxide fuels the gap is usually pre-filled with helium at near atmospheric pressure; during irradiation, however, the fuel releases some of the insoluble gaseous fission products generated in the fuel matrix thus changing the plenum mixture composition. The main gaseous fission products included in such mixture are xenon and kripton; the former, in particular, is considered in the present analysis due to its higher cumulative fission yield, around thirteen times higher than kripton; this, has also a higher thermal conductivity than xenon thus making the present analysis slightly conservative. Helium is also produced and released from the fuel, but since its production rate from alpha decay is important only for fuels with significant fractions of actinides, and one of the working hypotheses is $e_{MA} < 1\ wt.\%$ this contribution will be neglected.

To link the mixture composition to h_{gas}, two models have been employed, namely: the URGAP model [63] and the MATPRO one [118]. Given that the MATPRO model does not include roughness, to obtain representative results in closed gap conditions, the gap thickness term input to the model has been modified as

$$s_{gap} \rightarrow s_{gap} + A(R_f + R_c). \tag{13.11}$$

A quick comparison of the two models is reported in Figure 13.13 where a satisfactory agreement can be seen; depending on the particular conditions,

....

the difference can increase, but as shown in this section, the sensitivity coefficients predicted by the two models are close to each other in a wide range of situations.

(a) k_{gas} by MATPRO and URGAP models as function of xenon concentration X_{Xe}.

(b) h_{gas} by MATPRO and URGAP models as function of xenon concentration X_{Xe}.
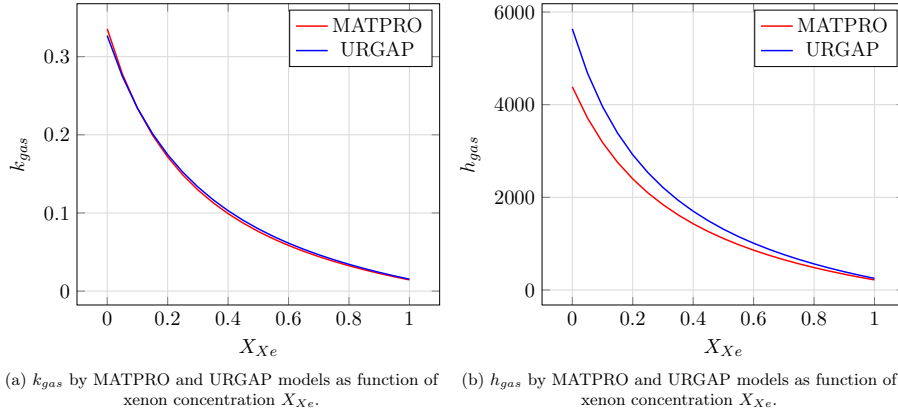
Figure 13.13: k_{gas} and h_{gas} as a function of xenon concentration X_{Xe} for $P_{gas} = 1\,\text{MPa}$, $T_{fo} = 1000\,\text{K}$, $T_{ci} = 800\,\text{K}$, $s_{gap} = 50\,\mu\text{m}$ and $A(R_f + R_c) = 10\,\mu\text{m}$.

The sensitivity coefficient $I_{X_{Xe},h_{gas}}$ for open and closed gap situations as a function of xenon concentration and plenum pressure P_{gas} is reported in Figure 13.14 for the two models. The temperature and roughness do not influence $I_{X_{Xe},h_{gas}}$ to any appreciable degree, even if, the latter can have a minor impact for closed gap conditions at very low pressures (i.e. $P_{gas} < 0.5$ MPa). The impact of pressure has the same rationale of the roughness and, as such, can basically be neglected; moreover, s_{gap} does not have a significant impact meaning that $I_{X_{Xe},h_{gas}}$ depends only on X_{Xe}, with an almost linear trend. Finally, it can be noted how the two models predict quite similar sensitivity coefficients.

In analogy with Section 13.2.1 the two parameters in Figure 13.14, namely, the P_{gas} and X_{Xe}, are related: accordingly the viable space in Figure 13.14 is smaller than the one shown; as an example, taking the pin free volume as 50 cm^3, the plenum temperature 800 K and mol_{He} as 1.5×10^{-3} the following relation is found

$$P_{gas} = \frac{0.2}{1 - X_{Xe}} \quad [\text{MPa}] \quad . \tag{13.12}$$

Figure 13.14, therefore, transforms as reported in Figure 13.15 where, for brevity, only results according to the MATPRO model are shown.

. . . .

(a) MATPRO - $s_{gap} = 150\,\mu m$ (b) URGAP - $s_{gap} = 150\,\mu m$

(c) MATPRO - closed gap   (d) URGAP - closed gap
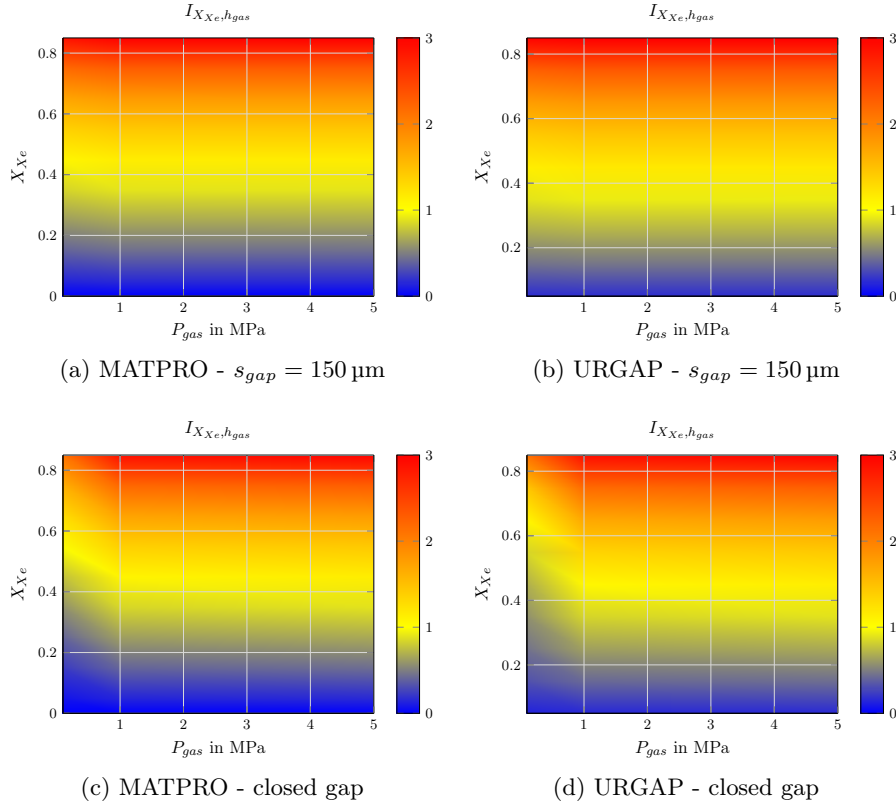
Figure 13.14: $I_{X_{Xe},h_{gas}}$ as a function of X_{Xe} and P_{gas} for the URGAP and MATPRO models in open and closed gap conditions.

Making a step further, the xenon concentration is linked to the predicted moles released by the fuel (i.e. FGR) and the sensitivity coefficient $I_{FGR,X_{Xe}}$[6] can be expressed as

$$I_{FGR,X_{Xe}} = \frac{1}{1 + \frac{mol_{Xe}}{mol_{He}}} = 1 - X_{Xe} \quad , \tag{13.13}$$

where mol_{Xe} represents the moles released by the fuel while mol_{He} indicates the moles of helium initially loaded in the pin. The decreasing trend of $I_{FGR,X_{Xe}}$ for higher released fractions is apparent. Looking at $I_{X_{Xe},h_{gas}}$ in Figure 13.14, it is seen that increases at high xenon fractions, but at the

---

[6]The correct notation would be $I_{mol_{Xe},X_{Xe}}$, but given that $I_{FGR,mol_{Xe}}$ is essentially unity, the two sensitivity coefficients can be, without errors, confused.

. . . .

(a) MATPRO - $s_{gap} = 150\,\mu\text{m}$ (b) MATPRO - closed gap
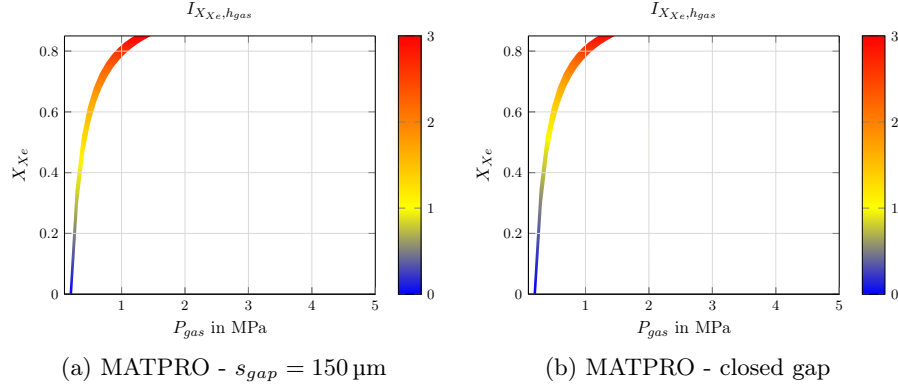
Figure 13.15: An example of a physically available domain for $I_{X_{Xe},h_{gas}}$ as a function of X_{Xe} and P_{gas} for MATPRO model in open and closed gap conditions.

same time, $I_{FGR,X_{Xe}}$ decreases and the overall behavior of

$$I_{FGR,h_{gas}} = I_{FGR,X_{Xe}} I_{X_{Xe},h_{gas}} \quad , \tag{13.14}$$

is reported in Figure 13.16.

To better understand how to read Figure 13.16 it should be considered that in a FR there are around 2.7×10^{21} fissions/MWd which means a production of some 1.2×10^{-3} mol_{Xe}/MWd assuming a xenon yield of 0.27 (which includes also the krypton contribution). The initial helium loading is usually between 1.5×10^{-3} and 2.5×10^{-3} mol_{He} meaning that around 1 or 2 MWd are necessary for reaching $mol_{Xe} = mol_{He}$ or $X_{Xe} = X_{He} = 0.5$; if the heavy metal loading in a pin oscillates between 0.2 and 0.4 kg, depending on the specif design[7], this translates in around 2.5-10 MWd/kg. Only a fraction of the produced xenon is released, but for the peak power pin, it is usually sufficiently high so that after 5-20 MWd/kg the condition $X_{Xe} = X_{He} = 0.5$ is reached and, as visible in Figure 13.16, this is close to the maximum point of $I_{FGR,X_{Xe}}$. The maximum is therefore reached early in life and $I_{FGR,X_{Xe}}$ can be basically considered a decreasing function of X_{Xe}. Another way yet to visualize the situation is to plot the necessary accuracy $A_{mol_{Xe}}$ on mol_{Xe} as a function of xenon concentration so to achieve a target accuracy $A_{h_{gas}}$ on h_{gas}, as done in Figure 13.17; for achieving an accuracy

---

[7]HLM cooled reactors usually have bigger pins and loose lattices, so the heavy metal loading per pin is high; this, however, is not a general rule [115].

. . . .
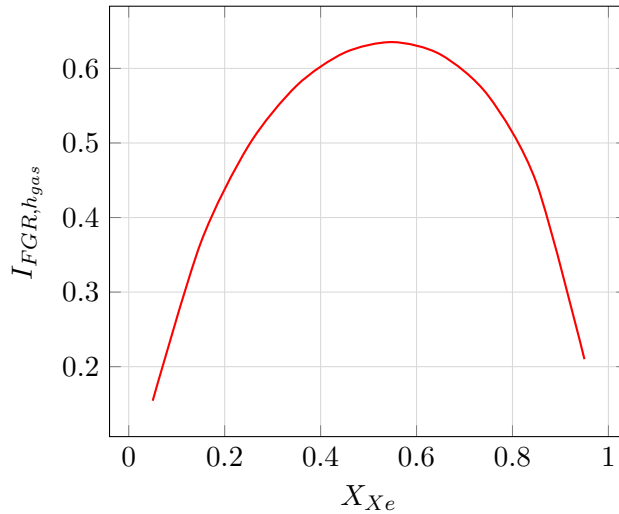
Figure 13.16: $I_{FGR,h_{gas}}$ as a function of xenon concentration X_{Xe}. The data are for a closed gap with the URGAP model, but as seen, only X_{Xe} has an impact on the sensitivity coefficient.

of 20% on h_{gas}, which is deemed a satisfactory figure, the error on mol_{Xe} can be higher than 30% and increases with further release. So it is clearly seen that further pushing on increased accuracy for FGR models - intimately connected to mol_{Xe} - is not actually worth for increasing the accuracy on the fuel temperature predictions of the peak pin under the assumptions listed in Sections 12.2 and 13.1.

Plenum pressure

As previously discussed, the pressure has a minor role, this can be easily seen from Figure 13.18 where only MATPRO results are reported. For an open gap $I_{P_{gas},h_{gas}}$ is basically non-negligible only for very small pressures, when significant release has not started yet; while for close gap the sensitivity increases, but again, remaining generally small and quickly decreasing as FGR progresses.

Because P_{gas} and X_{Xe} are indeed related, as previously shown, the viable space in Figure 13.18 is smaller than the one shown; taking as reference the relation in equation (13.12) the new domain in Figure 13.19 is obtained.

As equation (13.12) indicates, the plenum pressure is directly connected to FGR so, even if errors on the pressure have little impact on h_{gas}, they affect the value of the pressure itself which is an input parameter of the

....
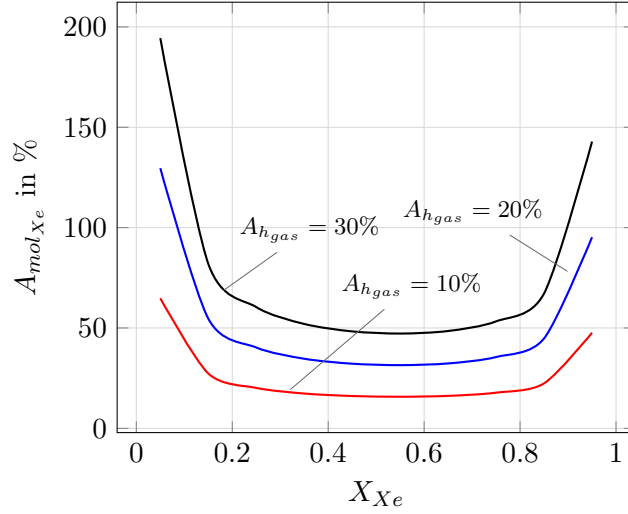
Figure 13.17: $A_{mol_{Xe}}$ as a function of Xenon concentration X_{Xe} for different target accuracies $A_{h_{gas}}$ on h_{gas}.

(a) MATPRO - $s_{gap} = 150\,\mu m$ (b) MATPRO - closed gap
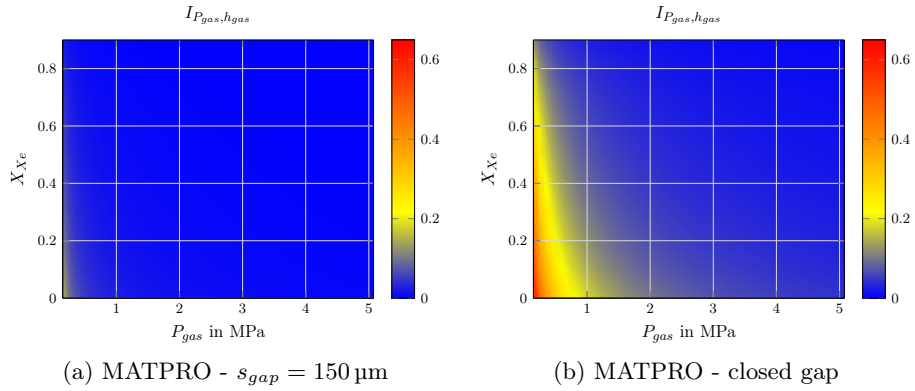
Figure 13.18: $I_{P_{gas},h_{gas}}$ as a function of X_{Xe} and P_{gas} for the MATPRO model in open and closed gap conditions.

mechanical analysis; taking advantage of the perfect gas law the importance coefficient $I_{FGR,P_{gas}}$[8] can be expressed as

$$I_{FGR,P_{gas}} = X_{Xe} \quad , \tag{13.15}$$

meaning that for a given error on mol_{Xe} the error on P_{gas} increases as release

---

[8]Exactly the same logic applied to $I_{FGR,X_{Xe}}$ has been used also for $I_{FGR,P_{gas}}$.

. . . .

(a) MATPRO - $s_{gap} = 150\,\mu\mathrm{m}$ (b) MATPRO - closed gap
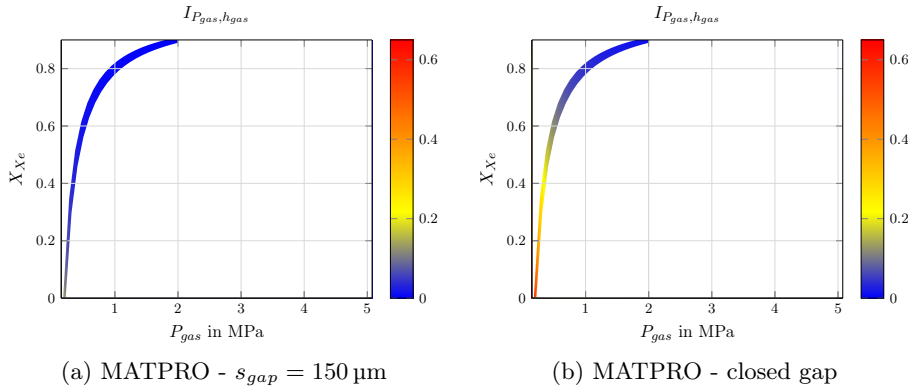
Figure 13.19: An example of a physically available domain for $I_{P_{gas},h_{gas}}$ as a function of X_{Xe} and P_{gas} for the MATPRO model in open and closed gap conditions.

progresses. So, for the peak pin, high FGR errors, while acceptable for h_{gas}, will entail high errors on the plenum pressure which is an input parameter of the mechanical analysis; fortunately, as will be shown in Section 13.3.3, plenum pressure inside the typical range of FRs (further remembering the condition BU $< 10\ at.\%$), is not a critical parameter, neither in nominal or ULOF conditions, relative to the cladding mechanical behavior.

13.2.4   Gap thickness

As seen from equation (13.9) the gap thickness contributes in determining the gap conductance; its value is, however, governed by the mechanical response of the fuel and cladding - at least in BoL conditions or in case of gap reopening due to clad swelling. The gap thickness is therefore a bridge between these two physical fields and so it is interesting to analyze how much they are influenced by s_{gap}.

Starting with the thermal field, the sensitivity coefficient $I_{s_{gap},h_{gas}}$, obtained by differentiating equation (13.9), is found to be independent from the plenum pressure, xenon concentration and temperature since they mainly act through the gas mixture thermal conductivity which is not present in the sensitivity coefficient formula, as seen from the following equation

$$I_{s_{gap},h_{gas}} = \frac{s_{gap}}{s_{gap} + A(R_f + R_c) + (g_f + g_c)} \quad . \tag{13.16}$$

Because, as discussed, the g term is significant only at low pressures it can

....
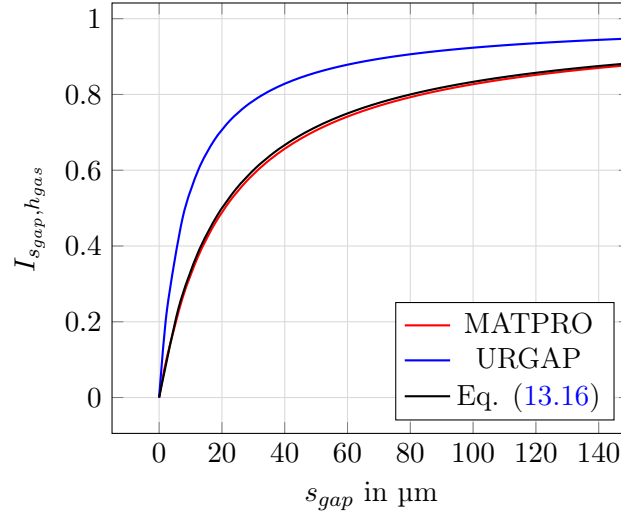
Figure 13.20: $I_{s_{gap},h_{gas}}$ as a function of the gap thickness s_{gap} for the MATPRO, URGAP and equation (13.16) for $A(R_f + R_c) = 20\,\mu\text{m}$.

be neglected in the following analysis. Results for $I_{s_{gap},h_{gas}}$ are reported in Figure 13.20, where equation (13.16), the MATPRO and the URGAP model are compared. It is seen the perfect agreement between equation (13.16) and the MATPRO model that uses an expression for h_{gas} very similar to (13.9) while the URGAP model has somewhat different results because of the more general expression adopted as explained in [63].

From Figure 13.20 it is apparent the decreasing trend of $I_{s_{gap},h_{gas}}$ as the gap closes, moreover, thanks to fuel cracking and relocation, the higher values can be excluded as soon as full power is reached; nonetheless, the impact at BoL is expected to be high.

Being s_{gap} the main bridge between the thermal and mechanical fields, errors on s_{gap} are mainly driven by the strain calculation of fuel and cladding. The gap thickness can then be simply stated as

$$s_{gap} = r_{ci} - r_{fo} \approx r_{ci0}(1 + \varepsilon_c) - r_{fo0}(1 + \varepsilon_f) \quad , \tag{13.17}$$

where r_{ci0} and r_{fo0} are the as-fabricated clad inner and fuel outer radii respectively. The sensitivity coefficients of the clad and fuel strains are of particular interest; the former, $I_{\varepsilon_c,s_{gap}}$, can be approximately calculated as

$$I_{\varepsilon_c,s_{gap}} \approx \frac{\varepsilon_c}{1 + \varepsilon_c - \frac{r_{fo0}}{r_{ci0}}(1 + \varepsilon_f)} \quad , \tag{13.18}$$

....
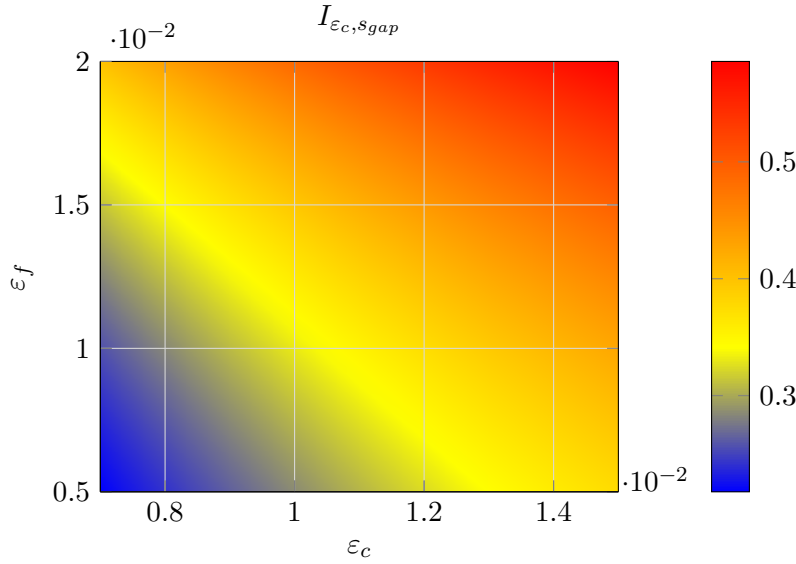
Figure 13.21: $I_{\varepsilon_c, s_{gap}}$ as a function of ε_c and ε_f for BoL range of values.

for BoL conditions, while it is zero once the gap closes. A graphical representation of the sensitivity coefficient is proposed in Figure 13.21 where it can be seen the increasing trend as the gap closes, point at which, the importance goes artificially to infinity since s_{gap} goes to zero.

In analogy, $I_{\varepsilon_f, s_{gap}}$ can be expressed as

$$I_{\varepsilon_f, s_{gap}} \approx \frac{\varepsilon_f}{\frac{r_{ci0}}{r_{fo0}}(1 + \varepsilon_c) - (1 + \varepsilon_f)} \quad . \tag{13.19}$$

In Figure 13.22 the behavior of such a function is reported. It can clearly be seen how values close to unity are reached, similarly to the $I_{s_{gap}, h_{gas}}$ coefficient; this implies a strong interaction between pin mechanics and gap conductance (and so the thermal field) in BoL situations.

As an example, a 30% error on ε_f at BoL will translate in a 30% error on s_{gap} taking $I_{\varepsilon_f, s_{gap}}$ around 1, which is a reasonable value for the the midplane of the active region; with $I_{s_{gap}, h_{gas}}$ around 0.8 we have an error on h_{gas} of 24% becoming 21.6% on the ΔT_{gap} for $I_{h_{gas}, h_{gap}}$ around 0.9. Finally, an error of 3.24% on T can be found assuming a $I_{\Delta T_{gap}, T}$ around 0.15.

. . . .
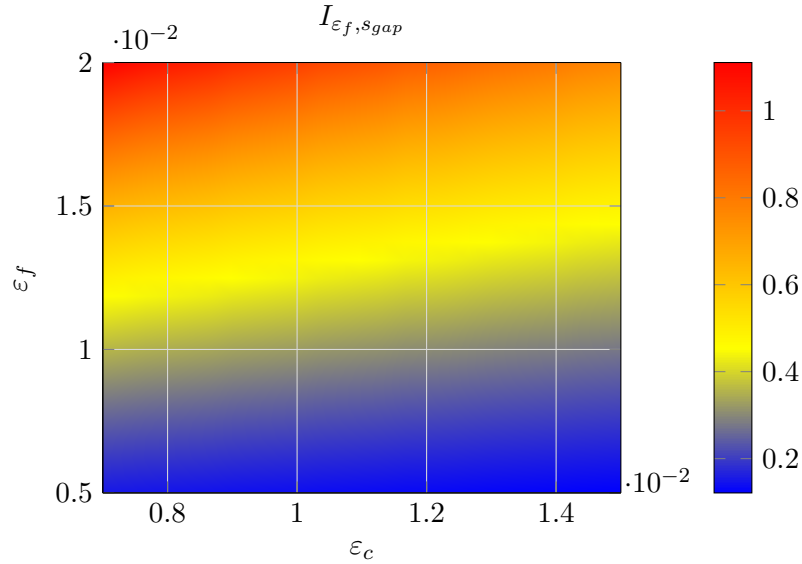
Figure 13.22: $I_{\varepsilon_f, s_{gap}}$ as a function of ε_c and ε_f for BoL range of values.

13.2.5   JOG

The JOG is generally supposed to form at a BU between 6 and 9 at.% when a limiting FP intra-grain concentration is reached and the solid fission products oxide are able to deposit in the gap. Because FP migration is low at low temperatures, the critical concentration is firstly reached by the unrestructured zone of the pellet leading to grain polygonalization and to a new microstructure with much smaller grains and enhanced porosity. This process is simultaneous to the JOG formation and it is believed that this restructuring is responsible for the additional release of FPs that condense in the JOG, feeding its thickness [47]. The JOG formation, in particular, alters the gap conductance, the fuel swelling and FGR.

Gap conductance

The effect of the JOG on the gap conductance can be expressed considering a parallel of thermal conductances [98] as

$$h_{gap} \rightarrow \frac{h_{gap} h_{JOG}}{h_{gap} + h_{JOG}} \quad , \tag{13.20}$$

. . . .

where h_{JOG} is the JOG conductance expressed as

$$h_{JOG} = \frac{k_{JOG}}{s_{JOG}} \quad , \tag{13.21}$$

where k_{JOG} is the JOG thermal conductivity and s_{JOG} is the JOG thickness.

Because a parallel of conductances is always lower than each of the individual components, this implies that the JOG effect, as modeled in this study, is always detrimental to the overall gap thermal exchange dynamic; if this is actually the case, however, is still object of debate. The JOG formation, indeed, seems to entail a shrinkage of the fuel pellet consequent to the mass lost in the process [132] and thus favoring a gap increase [73]; this gap is however filled with the JOG which has an higher thermal conductivity then the plenum gas mixture [98]. The gap conductance is therefore, on one hand, increased relatively to a situation with the same gas-filled gap, but on the other hand, the JOG grows to the detriment of the fuel[9] meaning that the newly formed gap would have not been present but for the JOG itself. The present approach seems therefore reasonable, in first approximation, to conservatively take into account the JOG effect especially considering the high degree of uncertainty currently surrounding this phenomenon.

With this in mind, it can be noted from equation (13.21) how the influence of the JOG on the overall h_{gap} comes from its thickness and conductivity. Regarding the former, the sensitivity coefficient $I_{s_{JOG},h_{gap}}$ can be expressed as

$$I_{s_{JOG},h_{gap}} = \frac{1}{1 + \frac{h_{JOG}}{h_{gap}}} = \frac{1}{1 + \frac{k_{JOG}}{h_{gap}s_{JOG}}} \quad . \tag{13.22}$$

$I_{s_{JOG},h_{gap}}$ is reported in Figure 13.23 where the k_{JOG} interval was selected based on the correlation proposed in [98] for cesium molybdate, believed to be the JOG main constituent. It is visible from Figure 13.23 how the sensitivity increases for increased JOG thickness and for high h_{gap}; the latter could be attained when strong contact exists between fuel and cladding; however, due to the fact that the JOG formation brings about a fuel shrinkage, such contact, should be possible only at the early moments of the JOG growth implying, a position on the upper-right corner of Figure 13.23 and so, a low value of $I_{s_{JOG},h_{gap}}$. It can also be appreciated the modest impact of k_{JOG} on the sensitivity, which is relevant only for very small values of h_{gap}.

---

[9]Because the JOG has lower conductivity than the fuel this, by itself, would be unfavorable from the thermal point of view.

. . . .

(a) $k_{JOG} = 0.2\,\mathrm{W/m\,K}$ (b) $k_{JOG} = 0.5\,\mathrm{W/m\,K}$
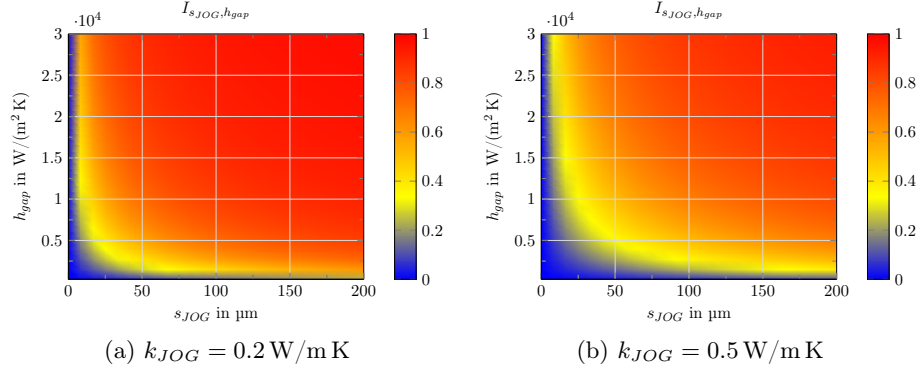
Figure 13.23: $I_{s_{JOG},h_{gap}}$ as a function of s_{JOG} and h_{gap} for two different k_{JOG}.

Regarding the effect of k_{JOG}, the sensitivity coefficient $I_{k_{JOG},h_{gap}}$ is the complement to one of $I_{s_{JOG},h_{gap}}$ meaning that all the previous discussion is perfectly reversed.

Fuel swelling

Because it is assumed that during the fuel pellet periphery restructuring, a fraction of the volatile FPs is released to the plenum forming the JOG and, because one of its main constituents is cesium, which is also an important contributor to the fuel FP solid swelling [96], it can be can seen that the JOG formation is expected to influence the swelling behavior of an oxide fuel. When the JOG is formed, its formation entails a reduction of the pellet diameter due to the release of a considerable fraction of FP, however, the overall pellet diameter (JOG+fuel) remains more or less constant (see previous Section); this pellet shrinkage, however, is not treated in this section which focuses on the effect of JOG on the solid FP swelling rate (and thus integral swelling).

Based on [55], the solid FP swelling rate $\dot{\varepsilon}^{sw,s}$ can be expressed as the sum of the dissolved and volatile FP

$$\dot{\varepsilon}^{sw,s} = 0.2 + 0.45(1 - VP) \quad [\%/at.\%], \qquad (13.23)$$

where VP is the fraction of volatile FP released from the pellet. Differentiating and taking into account that the swelling rate is influenced by the JOG only for a fraction of the whole pin in-reactor life, the sensitivity coefficient

....

$I_{VP,\varepsilon^{sw,s}}$ for the integrated swelling strain $\varepsilon^{sw,s}$ can be obtained as

$$I_{VP,\varepsilon^{sw,s}} = \frac{0.45VP}{0.2 + 0.45(1 - VP)} \frac{BU_{max} - BU_{JOG}}{BU_{max}} A_{unr}, \qquad (13.24)$$

where BU_{max} is the maximum BU reached by the pellet and BU_{JOG} is the BU at which JOG formation starts. The unrestructured fractional area A_{unr} takes into account the fact that only a fraction of the pellet undergoes JOG restructuring. $I_{VP,\varepsilon^{sw,s}}$ is plotted in Figure 13.24 where it can be seen the increasing trend with VP. VP can be calculated assuming it equal to the FGR in the unrestructured zone minus a fraction to account for cesium trapped in cracks, this means that VP is expected to be lower than 0.7 for the BU range identified in section 12.2 and thus, assuming a BU_{JOG} around 7 at.% [132], $I_{VP,\varepsilon^{sw,s}}$ should be lower than $0.3A_{unr}$.
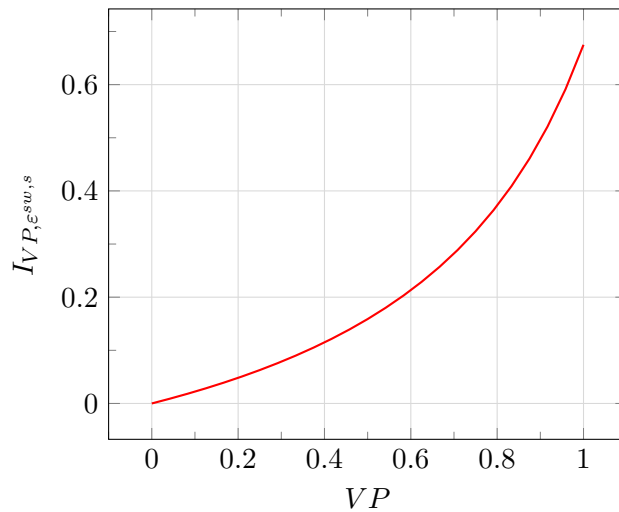
Figure 13.24: $I_{VP,\varepsilon^{sw,s}}$ as a function of VP for $\frac{BU_{max}-BU_{JOG}}{BU_{max}}$ =0.3 and assuming A_{unr} =1.

13.3 Clad mechanics - Nominal conditions

The main objective of the mechanical analysis is the evaluation of the cladding stresses (σ) and strains (ε); design criteria for the cladding are generally based on these parameters under steady state and transient conditions. The study of the function g in equation (12.3), indeed, requires their knowledge

. . . .

and so, it is important to identify the main contributors to their value so to correctly focus modeling efforts.

In the current section, concerning the mechanical behavior of the cladding in nominal conditions, after having presented the almost analytical approach followed in the sensitivity study, significant examples concerning the Young modulus and the clad internal pressure will be discussed.

13.3.1   Rationale of the mechanical analysis

The mechanical analysis is possibly more complicated than the thermal one, previously presented, due to the more complex mathematical framework characterizing it so, in order to make the analysis suitable for the present work scope, some simplifications have been introduced trying to preserve accuracy in the evaluation of the sensitivity coefficients of interest. Starting from the usual set of, 1D, axially symmetric equations solved by fuel thermo-mechanics codes under the plain strain hypothesis and neglecting axial coupling between pin sections, the set of equations to be solved can be expressed as the system composed by: the equilibrium condition

$$\frac{d\sigma_r}{dr} = \frac{\sigma_t - \sigma_r}{r} \quad , \tag{13.25}$$

the linear compatibility condition

$$\frac{d\varepsilon_t}{dr} = \frac{\varepsilon_r - \varepsilon_t}{r} \quad , \tag{13.26}$$

and the constitutive equations

$$\varepsilon_i = \varepsilon_i^{el} + \varepsilon_i^{th} + \varepsilon_i^{sw} + \varepsilon_i^{cr} + \varepsilon_i^{pl} \quad i = r, t, a \quad , \tag{13.27}$$

where the subscripts r, t, and a represent the radial, tangential and axial directions respectively, while the superscripts el, th, sw, cr and pl indicates elastic, thermal, swelling, creep and plastic components of the strain respectively. The quantities of interest are

$$\sigma_{eff} = \frac{1}{\sqrt{2}}\sqrt{(\sigma_r^2 - \sigma_t^2)^2 + (\sigma_r^2 - \sigma_a^2)^2 + (\sigma_t^2 - \sigma_a^2)^2} \quad , \tag{13.28}$$

the radially averaged effective stress and ε_t, the radially averaged tangential strain, because related to the radial displacement by $\varepsilon_t = \frac{u}{r}$. The previous set of equations can be analytically solved obtaining, as an example[10], the

---

[10]the complete solution is reported in [32].

....

tangential stress as

$$
\begin{aligned}
\sigma_t = & \frac{E}{1+\nu}\left(\frac{C_1}{1-2\nu}+\frac{C_2}{r}+\frac{\nu C_3}{1-2\nu}-\frac{\varepsilon_t^{ex}+\nu\varepsilon_a^{ex}}{1-\nu}\right)+ \\
& \frac{E}{2(1-\nu^2)r^2}\left((1-2\nu)\int_{r_{ci}}^{r_{co}}r(\varepsilon_r^{ex}(r)+\varepsilon_t^{ex}(r))dr+\right. \\
& \left. r^2\int_{r_{ci}}^{r_{co}}\frac{\varepsilon_r^{ex}(r)-\varepsilon_t^{ex}(r)}{r}dr+2\nu\int_{r_{ci}}^{r_{co}}\varepsilon_{tot}^{ex}(r)rdr\right) \quad,
\end{aligned}
\tag{13.29}
$$

where E is the elastic constant, ν is the Poisson ratio, C's are integration constants to be determined, the ε^{ex} are non-elastic components of the strain and the subscript *tot* indicates the sum of the strains in all directions. The integration constants are determined by imposing the following boundary conditions

$$
\begin{aligned}
\sigma_r(r_{ci}) &= -P_i \quad, \\
\sigma_r(r_{co}) &= -P_o \quad, \\
2\pi\int_{r_{ci}}^{r_{co}}\sigma_a(r)rdr &= F_a \quad,
\end{aligned}
\tag{13.30}
$$

where P_i and P_o are the inner and outer cladding pressures respectively while F_a is the axial force. The last term should depend on the contact condition between fuel and cladding of every axial section composing the pin, but as previously stated, this will be ignored and the conditions for a closed end cylinder will be used effectively relating F_a to P_i and P_o. Moreover, the boundary conditions in case of **F**uel **C**lad **M**echanical **I**nteraction (FCMI) should be different, but they will be kept unchanged, and the pressure P_i will be shifted from the plenum pressure value P_{gas} to the contact value P_{con} effectively decoupling the fuel and clad mechanical analysis. Finally, the internal pin pressure P_i is supposed to vary linearly from the initial atmospheric value to the final imposed one, so to simulate the pressure build-up due to FGR[11]. In analogy with Section 13.2, indeed, the boundary conditions for the cladding will not be consistently derived, but imposed, so to span the domain of interest, as outlined in Section 12.2, and so gaining understanding in the main contributors to the particular physics.

To tackle the analytical solution of equation (13.29) some approximations have been introduced, especially regarding the term $\varepsilon_i^{ex}(r)$ (only the integral for thermal expansion can be performed analytically):

- because the cladding has been divided in one node only, so to analytically apply the boundary conditions, the integrals are performed

---

[11]This is necessary to decouple the analysis from the thermal conditions of the whole pin.

. . . .

assuming the non-elastic strains are constant and equal to their radially averaged value;

- the real distribution is taken into account by an internal subdivision of the cladding when evaluating ε^{ex} outside the integrals, so to preserve the effect of strain gradients on stresses;

- to evaluate the creep term, a time discretization has been necessary, along with the adoption of an explicit approach using the stress distribution of the preceding time step;

- finally, plasticity has not been taken into account because supposed negligible in nominal conditions.

To verify that the above explained modeling of the cladding effectively preserves the sensitivity coefficients, a comparison, against a complete numerical solution of the mechanical equations, has been carried out and an example is given in Figure 13.25 for the case of the elastic constant sensitivity coefficient for the austenitic stainless steel 15-15Ti. From Figure 13.25 it is visible the good agreement between the two models especially near the border where the boundary conditions are imposed. In the present study, however, interest is mostly in the radially averaged values of σ_{eff} and the relative sensitivity coefficients and they are indeed well predicted by the semi-analytical model: for $I_{E,\sigma_{eff}}$ it is found 0.469 versus 0.462 for the complete and approximate solutions respectively, while for I_{E,ε_t} it is 0.0211 versus 0.0207.

The agreement on the radial distribution can decrease in case of very high swelling or strong creep due to high DPA reached or for high P_i in the contact pressure range at EoL, but the average value is generally well calculated.

From equation (13.29) and the boundary conditions it is seen that the parameters influencing the clad mechanical analysis are E, ν, α, $s_c = r_{co}-r_{ci}$, P_i, P_o, ε_i^{ex} and $\varepsilon_i^{ex}(r)$, where α represent the thermal expansion coefficient while $s_c = r_{co}-r_{ci}$ the clad thickness. From this list, E, ν and α are material properties while P_o is an input parameter and will not be studied; the creep and swelling properties are also, *de facto*, material properties and so the only model parameters are P_i - which is either the internal gas pressure and so linked to the FGR, or the contact pressure and so linked to the fuel mechanics - and the cladding thickness s_c which changes due to fuel and coolant corrosion.

For brevity, in the present thesis, only results for the austenitic stainless steel 15-15Ti are going to be presented, being the reference for almost all the

....

(a) Elastic constant importance for the effective stress.

(b) Elastic constant importance for the tangential strain.
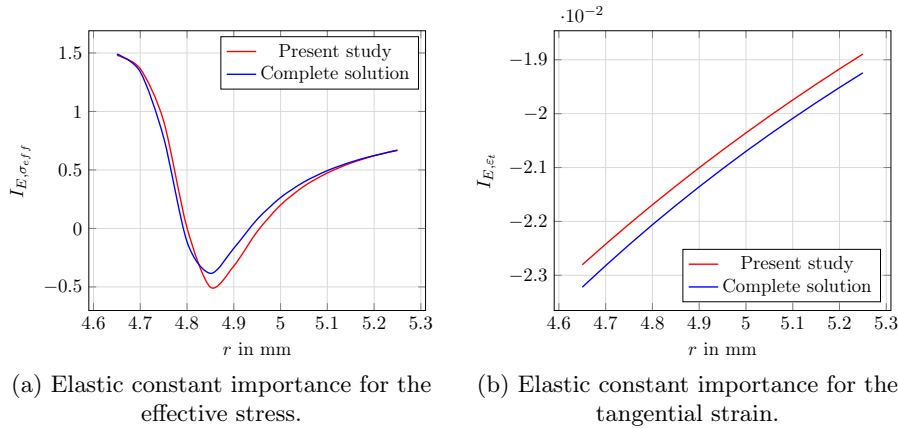
Figure 13.25: Comparison between calculations of a sensitivity coefficient by means of the approximate approach used in this study and of a complete numerical solution.

short-term deployment concepts, thanks to the already performed qualification campaign in the Phènix reactor; although, calculations for the ferritic T91 have also been carried out. The two clad materials have opposite characteristic and so they envelop well the spectra of possible advanced claddings: indeed, 15-15Ti is characterized by a high (relative to T91) swelling but very low creep; on the contrary T91 has virtually no swelling below 100 DPA, but a much higher thermal creep rate for identical conditions.

13.3.2   Young modulus

The reference value used for E has been 160 GPa which is an average value for the clad temperature range shown in section 12.2, even if, the Young modulus is weakly dependent on temperature in that range [121]. Results for the sensitivity coefficients $I_{E,\sigma_{eff}}$ and I_{E,ε_t} are presented in Figure 13.26 where weak dependencies on the Poisson ratio, clad thickness and outer pressure have been found, especially for σ_{eff}. The DPA_{max} label on the x-axis means the EoL DPA level coincident with the point where the indicated value of P_i is reached; the different DPA_{max} have been obtained changing the flux level for a fixed 5 years simulated period and this is acceptable because the thermal creep level is low enough and swelling is the main contributor. For high P_i in the contact range, thermal creep can become more significant, but the sensitivity coefficients are only weakly effected.

. . . .

$I_{E,\sigma_{eff}}$ is close to unity at BoL and this is in agreement with the simple thermo-elastic approximation

$$\sigma_t \approx \frac{P_i r_{ci} - P_o r_{co}}{s_c} - \frac{\alpha(T(r) - \overline{T})E}{1 - \nu}, \tag{13.31}$$

which implies a $I_{E,\sigma_{eff}} \approx 1$ at BoL when the pressure difference term is small compared to the thermal gradient contribution; the importance then decreases with DPA because the pressure builds up and the first term in equation (13.31) increases; moreover, stress relaxation due to creep reduces BoL influence. At some point, as DPA increases, the swelling contribution starts to increase (could be expressed in a similar way to the thermal component) and $I_{E,\sigma_{eff}}$ increases until stresses are so high that creep relaxation is not negligible anymore thus decreasing the sensitivity coefficient. The trend is the same for increasing pressures, but much faster, due to the faster increase of the pressure term in equation (13.31) and to the creep relaxation. At contact pressure values ($P_i > 10\,\text{MPa}$) the pressure term dominates and the sensitivity stays close to zero even when swelling starts.

For I_{E,ε_t} the situation is more straightforward because it is negligible for low pressures where the elastic strain component is small and increases at contact values until the swelling term kicks in, eventually bringing the importance back to zero.
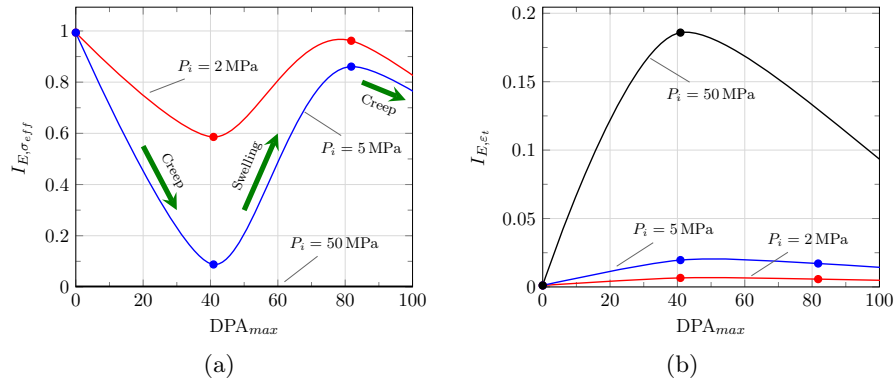
Figure 13.26: $I_{E,\sigma_{eff}}$ and I_{E,ε_t} for different inner pressures as a function of DPA_{max}.

....

13.3.3   Internal pressure

Because at BoL P_i is an input parameter, results in Figure 13.27 are only presented for EoL conditions. In the typical range reached by plenum pressure due to FGR (i.e. 1 MPa $< P_i <$ 10 MPa) $I_{P_i,\sigma_{eff}}$ increases with P_i - theoretically towards unity as reported in equation (13.31) -, but decreases as DPA$_{max}$ increases and, at the target value of 100, is basically negligible due to the swelling dominance; in the contact range, on the other hand, it remains important even at high DPA (see equation (13.31)).

I_{P_i,ε_t} is almost zero in the FGR range and then increase with pressure in the contact one; it weakly depends on DPA$_{max}$.

As previously discussed in Section 13.2.3, high errors on FGR will translate in high errors on the internal pressure at EoL but, due to the fact that in the typical P_i range of values (i.e. 1 MPa $< P_i <$ 10 MPa) the sensitivity coefficients $I_{P_i,\sigma_{eff}}$ and I_{P_i,ε_t} are relatively smalls, as visible from Figure 13.27, such errors will not significantly propagate on the final clad mechanical state and thus, they can be deemed acceptable.

As a quick check we can compare the importance calculated in the present study with the one graphically retrievable from [70] regarding the thermo-mechanical analysis of the ALFRED reactor pin with the TRANSURANUS code [62]: in the peak rod last cycle, the contact pressure goes from around 35 MPa to 55 MPa while the average clad stress goes from 280 MPa to 430 MPa which results in a $I_{P_i,\sigma_{eff}}$ around 0.85 which well matches the one reported in Figure 13.27 for that P_i range at around 100 DPA.

13.4   Fuel temperature - UTOP

As stated in Section 12.1, the reference transient for the fuel temperature is the UTOP, since it challenges fuel un-melting and sets the limit on the maximum linear power acceptable during normal operations; the reference time frame assumed critical for this transient has been selected around 10 s (see Section 12.1). Given the time scale of interest, all phenomena with a much higher characteristic time can be safely ignored, and thus borrowed from steady-state, so that the transient sensitivity analysis can focus only on the relevant effects.

As an example, the plutonium migration can be expressed by the following diffusion equation

$$\frac{\partial e(r,t)}{\partial t} = D\nabla^2 e(r,t) + D\nabla \cdot \left(e(r,t)(1 - e(r,t)) \left(\frac{Q^+}{RT^2} \right) \nabla T \right), \quad (13.32)$$

....

(a) $I_{P_i,\sigma_{eff}}$ for P_i in the FGR range.

(b) I_{P_i,ε_t} for P_i in the FGR range.

(c) $I_{P_i,\sigma_{eff}}$ for P_i in the conctact range.

(d) I_{P_i,ε_t} for P_i in the contact range.
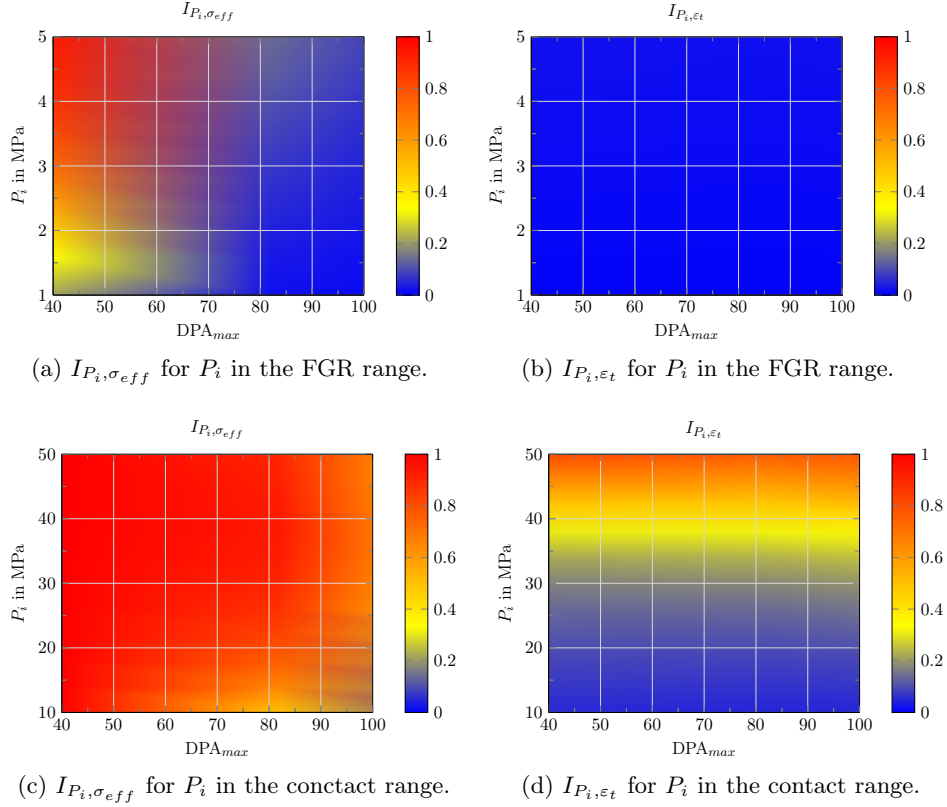
Figure 13.27: $I_{P_i,\sigma_{eff}}$ and I_{P_i,ε_t} as a fucntion of DPA_{max} for pressure in the gas and contact ranges.

where e is the volumetric enrichment, D the plutonium diffusion coefficient and Q^+ is a characteristic heat of transport. This equation neglects the pore migration contribution because, as will be later shown, the restructuring process is also negligible in a fast UTOP. Trying to put in evidence the time constants equation (14.47) can be cast in the form

$$\frac{\partial e(r,t)}{\partial t} = \frac{\nabla^{*2}e(r,t)}{\tau_D} + \frac{e}{\tau_T}, \qquad (13.33)$$

where τ_D is the concentration gradient diffusion time constant, τ_T is the temperature gradient diffusion time constant and the superscript * denotes a non-dimensional operator. The two time constants can be roughly expressed

. . . .

as

$$\begin{aligned}
\tau_D &= \frac{L^2}{D}, \\
\tau_T &= \frac{RT^2 L^2 (1-e)}{D|Q^+|\Delta T},
\end{aligned} \qquad (13.34)$$

where L is a characteristic length taken equal to the radius of the pellet. For the D and Q^+ proposed in [55] and considering as average temperature 2000 K and a temperature difference of 2000 we have that τ_D is higher than 10^9 s and τ_T is higher than 10^6 s and so negligible in an UTOP.

The same identical approach can be used for the oxygen-to-metal ratio radial redistribution where, taking as reference the data in [55] and for the same condition used for the plutonium analysis, we have τ_D higher than 10^5 s and τ_T higher than 10^4 s and so negligible in an UTOP.

For the restructuring dynamics, the pore migration velocity v_p can be taken and the characteristic time τ_p calculated as

$$\tau_p = \frac{L}{3v_p}, \qquad (13.35)$$

where only one third of the characteristic length is taken because columnar grains have approximately this size. Taking v_p from [96] and again using the same conditions as before we find a τ_p greater than 10^4 and so negligible in an UTOP.

On the other hand, a phenomenon which is believed to be particularly fast [102] in the case of power ramps is fuel gaseous swelling; the exact time scale of this effect is, however, difficult to estimate and possibly higher than the assumed reference time frame. Due to these kind of uncertainties, it is, nonetheless, - conservatively - inserted in the transient sensitivity analysis.

In the following, therefore, only the effects of transient fuel gaseous swelling and specif heat will be explicitly analyzed.

13.4.1   Specific heat

The heat equation for transient situations can be stated as

$$\frac{1}{\alpha_f} \frac{\partial T(r,t)}{\partial t} = \frac{1}{r} \frac{\partial}{\partial r} \left(r \frac{\partial T(r,t)}{\partial r} \right) + \frac{q'''(t)}{k_f}, \qquad (13.36)$$

where α_f is the fuel thermal diffusivity and q''' is the power density assumed to be of the form $q'''(t) = q_0'''(1 + \frac{t}{\tau_{tr}})$ where τ_{tr} is the characteristic transient time after which the initial power has doubled. Averaging the heat

....

equation over the pellet cross section, the following equation for the average temperature can be formulated

$$\frac{1}{\alpha_f}\frac{\partial \tilde{T}(t)}{\partial t} = -\frac{2r_{fo}}{k_f(r_{fo}^2 - r_{fi}^2)}q''(t) + \frac{q'''(t)}{k_f}, \qquad (13.37)$$

where q'' is the thermal flux at the pellet periphery and adiabaticity at the central void has been assumed. In order to understand how to model the heat flux during the transient, the characteristic time for the heat transport inside the pellet can be used and it is given by

$$\tau_f = \frac{(r_{fo} - r_{fi})^2}{\alpha_f} = \frac{\rho_f c_p (r_{fo} - r_{fi})^2}{k_f}, \qquad (13.38)$$

where ρ_f is the fuel density and c_p its specific heat. Considering that ρ_f is somewhat higher than 10000 kg/m^3 and that c_p during transient is around 375 J/(kg K) [97], a τ_f around 25 s results. From $\tau_f > \tau_{tr}$ it can be made the assumption that the temperature surrounding the pellet remains constant during the power ramp and thus formulating equation (13.37) as

$$\frac{1}{\alpha_f}\frac{\partial \tilde{T}(t)}{\partial t} = -\frac{2r_{fo}h}{k_f(r_{fo}^2 - r_{fi}^2)}(\tilde{T}(t) - T_\infty) + \frac{q'''(t)}{k_f}, \qquad (13.39)$$

where T_∞ is the environment temperature for heat exchange while h is the heat transfer coefficient between the pellet and the environment. The solution coupled with the initial condition $\tilde{T}(t=0) = \tilde{T}_0$ can be finally stated as

$$\begin{aligned}
\tilde{T}(t) =& T_\infty + \left(\tilde{T}_0 - T_\infty - \frac{q_0'''\tau_h}{\rho_f c_p}\right)e^{-\frac{t}{\tau_h}} + \frac{q_0'''\tau_h}{\rho_f c_p} + \\
& \frac{q_0'''\tau_h^2}{\rho_f c_p \tau_{tr}}\left(\frac{t}{\tau_h} - 1 + e^{-\frac{t}{\tau_h}}\right),
\end{aligned} \qquad (13.40)$$

where $\tau_h = \frac{2r_{fo}h}{\rho_f c_p(r_{fo}^2 - r_{fi}^2)}$ includes the parameter of interest, the specific heat c_p.

In order to refer the sensitivity coefficient to the temperature difference inside the pellet, T_∞ can be taken as the fuel outer temperature; moreover, to find the maximum temperature from the average one, the difference $\tilde{T} - T_{fo}$ is multiplied by the ratio between the maximum and average temperature which is 2 for a solid pellet and something less for an annular one (depending on the pellet inner to outer radii ratio). The sensitivity coefficient $I_{c_p,T_{fi}-T_{fo}}$,

. . . .

coming from the derivative of (13.40), is reported in Figure 13.28 where the convergence towards unity can be seen. Considering the 10 s reference frame, a value of 0.9 seems acceptable. The sensitivity is weakly dependent on c_p, τ_{tr} and the linear power and so the proposed value can be taken as reference. Even considering the pellet as completely adiabatic, does not change the importance significantly because it always tends towards unity; more generally it can be said that the higher the degree of heat lost by the pellet, compared to the one given, the lower is the value of $I_{c_p,T_{fi}-T_{fo}}$ that, nonetheless, tends towards unity.
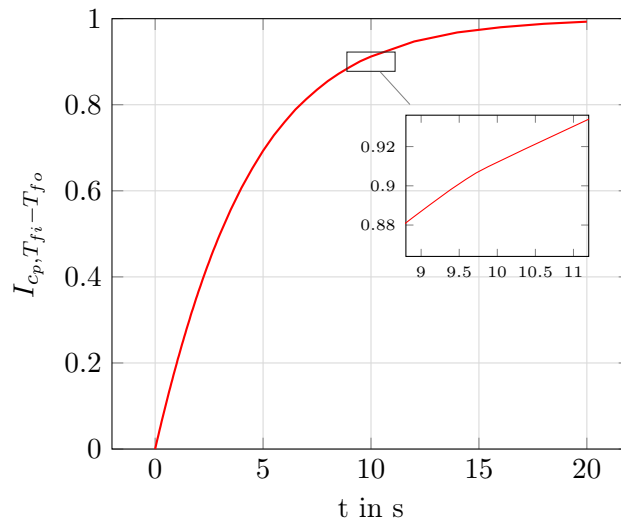
Figure 13.28: $I_{c_p,T_{fi}-T_{fo}}$ as a function of time for a fast UTOP.

13.4.2   Fuel swelling

During a power ramp, the bubbles with the retained fission gases get over-pressurized by the temperature increase and, for inter-granular bubbles, by migration of intra-granular gases[12]. Assuming that the bubble overpressure is instantaneously relaxed by vacancies diffusion and consequent bubble growth and that all the retained FGs are inside bubbles, the transient volumetric swelling could be very roughly expressed as

$$\varepsilon_{tr}^{sw,g} = \frac{mol_{ret}\Delta TR}{P_h + P_\gamma} = \frac{mol_g(1 - FGR)\Delta TR}{P_h + P_\gamma}, \qquad (13.41)$$

---

[12]the last phenomenon is possibly negligible in the present analysis due to the very short time frame of interest.

. . . .

where mol_{ret} is the number of moles retained per unit volume in the fuel matrix, P_h is the hydrostatic pressure and P_γ is the bubble surface tension. The latter depends on the bubble radius, but the simple correlation from [20], is used in this work and is reported in Table 13.1. It is seen the high value used for the unrestructured zone, to account for the small bubble size; this, however, does not reflect the change in structure after the JOG formation, but this detail will be ignored in the present context and the correlation used as it is.

Considering mol_{ret} for the unrestructured zone around 150 mol/m^3 ([132] and [134]) and the FGR around 0.85 and 0.95 for the equiaxed and columnar regions respectively and remembering that around 1.2×10^{-3} mol/MWd are produced, considering an EoL burnup of 100 MWd/kg, the plot in Figure 13.29 can be drawn. It is seen that for a ΔT around 1000 K the pellet average transient swelling strain is bound to be lower than 0.1[13].

Table 13.1: Correlation used for P_γ in the present work. The values have been taken from [20].

Zone	P_γ [MPa]
Unrestructured	6895
Equiaxed	6.895
Columnar	3.447

The main swelling effect on the maximum fuel temperature, besides the influence on the central void radius (effect borrowed from the steady state analysis), is through the porosity enhancement [21] and consequent thermal conductivity reduction. The real effect should take into account the porosity distribution, and integrate the local sensitivity factor on the temperature distribution. Nevertheless, in the present context, the average transient swelling will be taken as reference and its effect, through the average porosity on the fuel thermal conductivity, analyzed; this, means to assume a sensitivity coefficient for the porosity (Po) of

$$I_{Po,\Delta T_f} = \frac{3Po}{1 + Po - 2Po^2}, \tag{13.42}$$

stemming from the typical factor of $\frac{1-Po}{1+\beta Po}$, with β around 2, influencing the fuel thermal conductivity [105].

---

[13]The faster the transient the lower the swelling expected, everything else being equal.

....
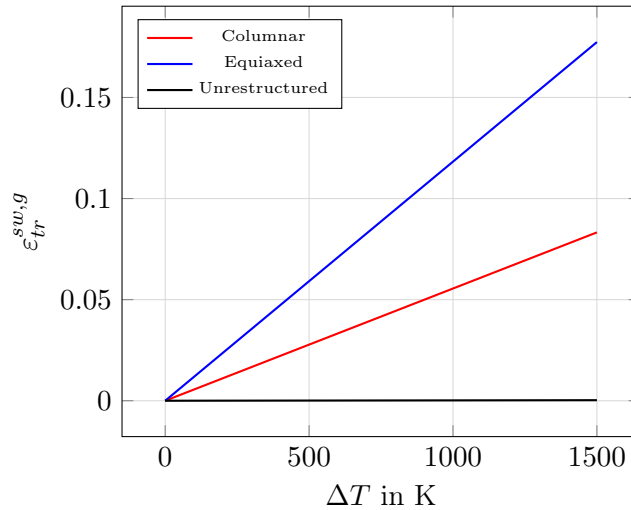
Figure 13.29: $\varepsilon_{tr}^{sw,g}$ for the different pellet zones as a function of the temperature increase during the power ramp. P_h has been assumed 5 MPa for the equiaxed and columnar regions.

With this in mind, the sensitivity coefficient $I_{\varepsilon_{tr}^{sw,g},\Delta T_f}$ can be expressed as

$$I_{\varepsilon_{tr}^{sw,g},\Delta T_f} = I_{\varepsilon_{tr}^{sw,g},Po}I_{Po,\Delta T_f} = \frac{\varepsilon_{tr}^{sw,g}}{\varepsilon_{tr}^{sw,g} + \varepsilon_{ss}^{sw,g}} \frac{3Po}{1 + Po - 2Po^2}, \qquad (13.43)$$

where $\varepsilon_{ss}^{sw,g}$ is the gaseous swelling during steady-state operations, which can be expressed as $Po - Po_{sin}$, where Po_{sin} is the sintered porosity. The sensitivity for typical EoL conditions is reported in Figure 13.30 where it can be seen a weak dependence on porosity for low $\varepsilon_{tr}^{sw,g}$, which increases at high transient swelling values.

13.5   Clad mechanics - ULOF

As stated in Section 12.1, the reference transient for the clad mechanical behavior is the ULOF, since it challenges cladding integrity and sets the relationship between active height, pin pitch, coolant velocity and clad thickness through the link of the first and second member of equation (12.3). The reference axial position for such a transient is the top of the fuel column where clad temperatures are higher and so is the probability of failure by

....
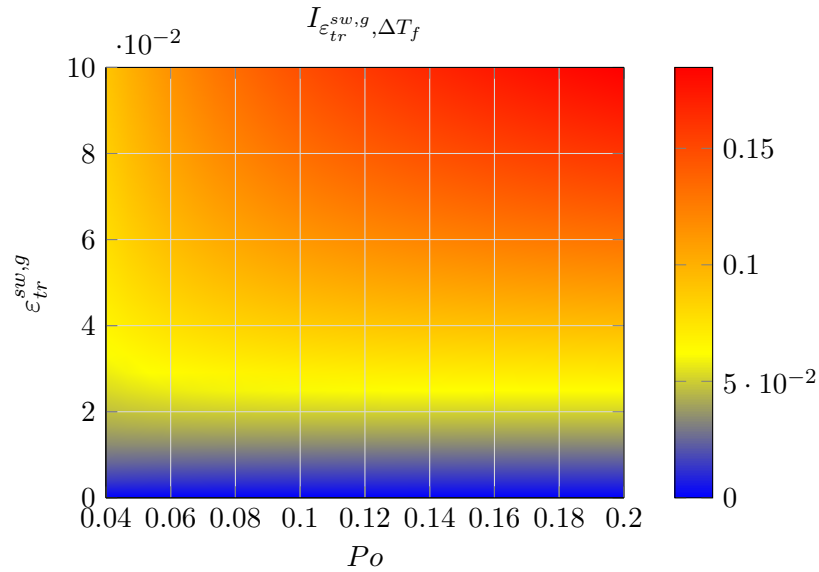
Figure 13.30: $I_{\varepsilon_{tr}^{sw,g},\Delta T_f}$ as a function of porosity and transient swelling. Po_{sin} taken equal to 0.01.

creep or plastic instability. The reference time frame assumed critical for this transient is around 1 h, as discussed in Section 12.2.

For brevity, only results for the austenitic stainless steel 15-15Ti will be presented, as done for the analysis in nominal conditions. During the aforementioned time frame swelling and irradiation creep are negligible; indeed, their time constants, the inverse of the strain rates, are τ_{sw} >10^{11} s and $\tau_{cr,ir}$ >10^{11} s, considering clad temperature higher than 700 °C (similarly to Section 13.4). The phenomena to analyze, being quantitatively different from the steady-state conditions, are therefore the thermal creep, the thermal expansion strain along with its distribution, the contact pressure, clad thickness and the plastic strain via the yield strength; in the following, for compactness, only thermal creep and yield strength will be explicitly discussed.

13.5.1   Rationale of the ULOF mechanical analysis

Because creep is much stronger during an ULOF, and plasticity comes into play, the semi-analytical method described in Section 13.3.1 can not be applied. A simple numerical approach has been therefore adopted, passing through the finite-differences discretization of the governing equations (see

. . . .
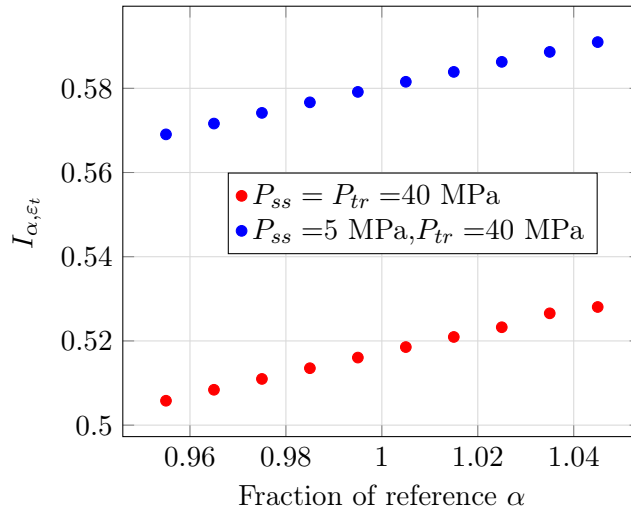
Figure 13.31: Influence of pressure histories on the importance coefficients. P_{ss} is the steady-state pressure while P_{tr} is the ULOF pressure.

Section 14.3 for further details on the numerical approach).

The clad is therefore irradiated at the maximum allowable steady-state temperature (see Section 12.2), namely 550 °C and, at EoL (i.e. 100 DPA), the temperature is quickly raised (i.e. 10 s) to the ULOF value of 750 °C; the choice of the ramp rate and temperature stems from the safety calculation done in [9] for the ALFRED reactor. The internal pressure is unchanged during the transient so, contact pressure[14] increase or decrease due to the fuel action is not directly included, but it has been found that the pressure history is not particularly relevant for the sensitivity coefficients calculation and so, the simplification is acceptable. As an example, the sensitivity coefficients for the thermal strain, calculated with a constant transient pressure of 40 MPa, on one hand, and from a steady state value of 5 MPa and a 1 h ramp until 40 MPa on the other, are reported in Figure 13.31, where the similarity can be noted even for so markedly different pressure histories. The motivation behind this behavior is the good creep resistance characterizing austenitic stainless steels so that the overall behavior is much more sensitive to swelling (and thus temperature) than to pressure.

---

[14]Similarly to the nominal clad mechanics analysis, pressure boundary conditions are imposed rather than consistently calculated, so to isolate the clad behavior from the overall pin dynamics.

. . . .

(a)   (b)
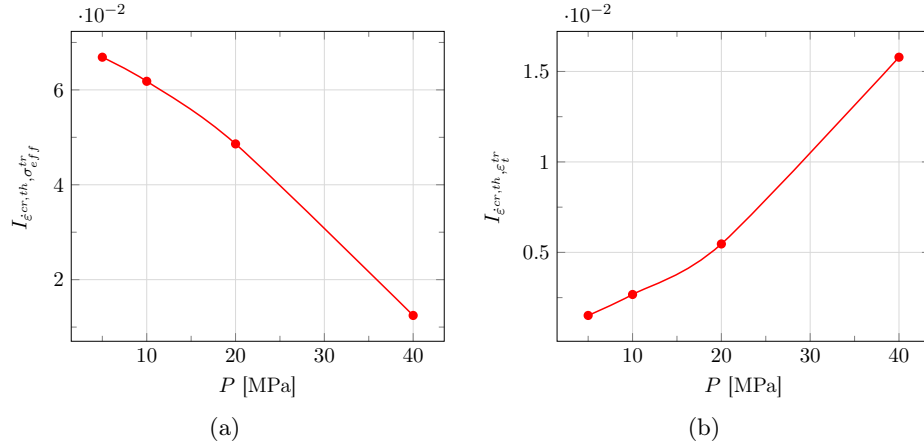
Figure 13.32: $I_{\dot{\varepsilon}^{cr,th},\varepsilon_t^{tr}}$ and $I_{\dot{\varepsilon}^{cr,th},\sigma_{eff}^{tr}}$ as a function of pressure for an ULOF-like transient.

13.5.2   Thermal creep

The sensitivity coefficients $I_{\dot{\varepsilon}^{cr,th},\varepsilon_t^{tr}}$ and $I_{\dot{\varepsilon}^{cr,th},\sigma_{eff}^{tr}}$ are presented in Figure 13.32, where the low values can be seen with a decreasing trend for the stress and an increasing one for the strain, the latter rapidly increasing with pressure. The value of the sensitivity coefficients are low even in ULOF conditions due to the great creep resistance of the austenitic stainless steels 15-15Ti.

13.5.3   Yield strength

The correlation adopted for the reference yield strength is the following [121]:

$$\sigma_Y = 1560 - 5.86T + 1.2 \times 10^{-2}T^2 - 1.04 \times 10^{-5}T^3 + 3.06 \times 10^{-9}T^4, \quad (13.44)$$

with temperature in K, also reported in Figure 13.33.

The sensitivity coefficients $I_{\sigma_Y,\varepsilon_t^{tr}}$ and $I_{\sigma_Y,\sigma_{eff}^{tr}}$ are presented in Figure 13.34 where a real complex pattern can be seen. Failure problems arise when the yield strength becomes lower than the primary stress $\frac{P_i r_{ci} - P_o r_{co}}{s_c}$, due to the fact that such high stresses are obtained from imposed boundary conditions (i.e. P_i and P_o) rather than from the fuel-cladding interaction and so the feedback of the plastic deformation to the contact pressure is lost; for this, results are presented for a maximum pressure of 30 MPa.

....
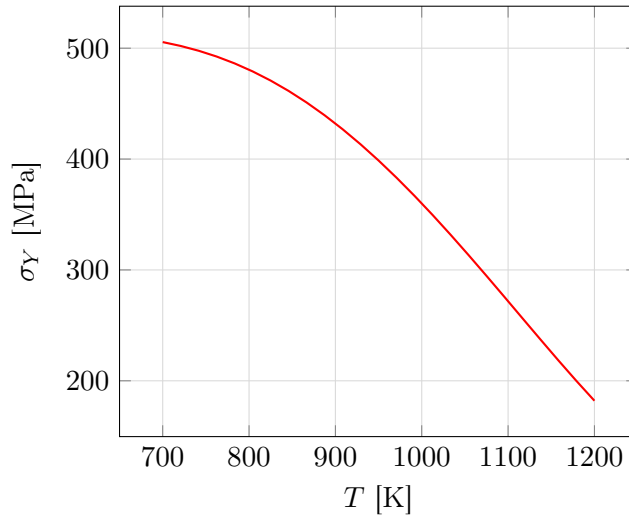
Figure 13.33: The reference σ_Y correlation as a function of temperature.

$I_{\sigma_Y,\varepsilon_t^{tr}}$ increases with pressure and if σ_Y decreases; fortunately, thanks to irradiation hardening, which has not been taken into account, higher yield strengths are expected and so lower values of the importance. $I_{\sigma_Y,\sigma_{eff}^{tr}}$ firstly decreases with pressure and then increases due to relaxation by creep; then increases again when plastic deformation is also necessary for relaxing the increasing stress level.

It must be said that, if the core and its restraint system have been carefully designed, in the case of ULOF-like transients the outlet core[15] temperature increase will produce a core expansion and consequent negative reactivity insertion sufficient to significantly reduce core power and thus fuel temperature; the last effect would imply a thermal contraction of the pellet itself, partially relieving any PCMI present. The exact condition for this to happen, however, depends on the evolution of the ratio between the power - influencing the fuel temperature - and the core mass flow - influencing the clad temperature - during the transient. In the case of such a favorable event, the internal clad pressure will drop to values close to the FGR range, with sensitivity coefficients much lower for both the yield strength and thermal creep (and all ULOF related parameters in general) as visible from Figures 13.32 and 13.34.

---

[15]In the case of loss of heat sink also the inlet core temperature, but with higher time scales.

. . . .
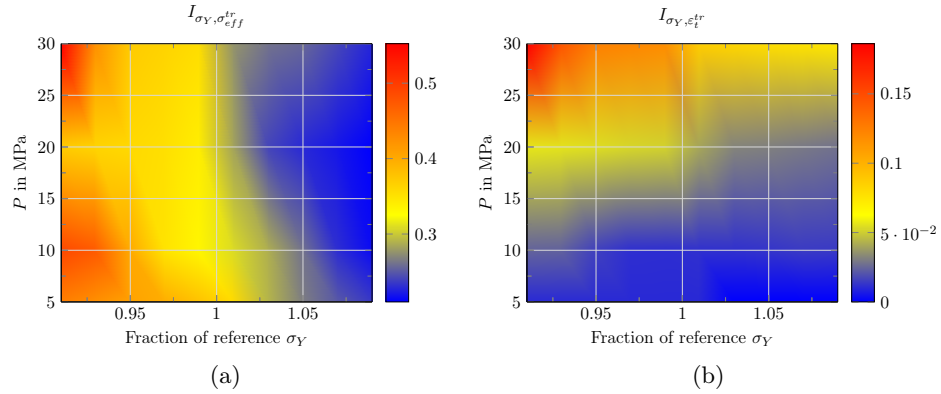
Figure 13.34: $I_{\sigma_Y, \varepsilon_t^{tr}}$ and $I_{\sigma_Y, \sigma_{eff}^{tr}}$ as a function of pressure and the fraction of the reference σ_Y for an ULOF transient.

13.6   Results

In this section, all the sensitivity coefficients previously derived in Figures from 13.2 to 13.5 are put together so to understand what are the main phenomena determining the fuel maximum temperature and the clad stresses and strains in nominal and transient conditions. This will also allow to form a ranking indicating where priorities in modeling effort should be concentrated enabling a balanced fuel pin thermo-mechanic DOC to be developed. Finally, by making the distinction between modeling and material properties contributions, the former can be put into perspective so to guide future R&D efforts to improve predictive capabilities for conditions which fall inside the validity domain addressed in Section 12.2.

13.6.1   General assumptions

Given the quite general framework under which the sensitivity coefficients have been derived, in order to perform a more quantitative analysis of the results, some assumptions are put forward for what concerns the power, fuel surface temperature and clad inner pressures at BoL and EoL having as reference the mid-plane and the top of the active region for the fuel and clad respectively.

   The power at the peak node is supposed to be 400 W/cm with a fuel surface temperature of 1200 K and 1000 K at BoL and EoL respectively; the lower T_{fo} at EoL stems from the assumed gap closure; under these conditions,

. . . .

Table 13.2: Columnar
and equiaxed boundaries
used in the analysis for
BoL and EoL conditions.

Zone	BoL	EoL
Equiaxed	0.72	0.75
Columnar	0.68	0.72

the normalized radii of the columnar and equiaxed zones are reported in
Table 13.2. They were calculated with the help of the equations

$$
\begin{aligned}
T_{eq} &= \frac{62000}{2.3\log_{10}(t)+26} \quad [\text{K}], \\
T_{col} &= \frac{68400}{2.3\log_{10}(t)+28} \quad [\text{K}],
\end{aligned}
\tag{13.45}
$$

with time t in hours, proposed in [139], for the boundary temperature of the
equiaxed, T_{eq}, and columnar, T_{col}, regions respectively.

The xenon concentration X_{Xe} in the plenum is assumed to be 0.4 at
BoL and 0.8 at EoL which are credible values for the peak pin as previously
discussed. For what concerns the contact pressure P_{con} it is supposed that
at EoL contact is established all over the pin length and that values around
50 and 25 MPa are attained for the mid-plane and top of the active region
respectively. Finally, for the strains it is supposed that at BoL the clad
strain is around 1 % (mainly thermal expansion) while the fuel inner and
outer strains are respectively 5 % and 2 % (mainly via cracking, thermal
expansion and relocation). At EoL the gap is closed so the only strain of
interest is the inner fuel one which is supposed around -30 % due to the high
creep and contact pressures reached at the peak node [98].

Even though the transient results are focused on EoL, the steady state
ones are also presented for BoL and the most stringent among the two is
taken as reference so to have a balanced code, at least in nominal condi-
tions. For the maximum fuel temperature, indeed, at BoL, the gap has some
influence, but at EoL, only the fuel pellet phenomena are important and
so, to not totally miss the gap effect, the choice of conservatively combine
the two conditions has been taken. For the cladding, on the other hand,
only EoL results are taken into account because at BoL the only parame-
ters of interest are E, ν and α that are material properties. At BoL the
clad is basically under thermo-elastic load with pressure boundaries close to
as-fabricated conditions and, for this, it is not a situation of interest for the

. . . .

present sensitivity analysis being almost an input condition.

A final consideration involves the maximum fuel temperature sensitivity coefficients: while the analysis focuses on the peak node, it has been found that for lower powers, the sensitivities (especially the modeling ones) are lower and so the peak node is, indeed, the most penalizing situation from that point of view.

13.6.2   Fuel temperature - Nominal condition

In Table 13.3 the assembly of all the sensitivities is presented for the fuel maximum temperature in nominal conditions. To keep compactness and ease reading and the overall discussion, the fuel strain is not decomposed as in Figure 13.2 but, kept as a model indicator. The meaning of symbols in Table 13.3 is the following: x represents the average O/M ratio, x_{max} the O/M ratio radial distribution, ρ_{col} and ρ_{eq} the columnar and equiaxed densities respectively, e_f and e_c the fuel and clad emissivities respectively, P_{con} the contact pressure, H the Meyer hardness, k_c the clad conductivity, s_{ox} and k_{ox} the oxide scale thickness and conductivity due to coolant corrosion, s_w the cladding wastage thickness due to fuel corrosion.

Multiplying the nested sensitivities recursively and selecting the maximum between BoL and EoL, results in Table 13.4 can be calculated; for phenomena (e.g. FGR) influencing more variables, results have been condensed by making the root of the sum of the squared individual contributions. This does not change the final results for the fuel temperature because each term is squared again in the final sum as later shown (see equation (13.46)).

From Table 13.4 it can be seen that, besides the (largely) dominant effect of the fuel thermal conductivity, the most important models include the porosity and plutonium distributions together with the boundary of the equiaxed and columnar regions. Finally, the gaseous swelling induced porosity is worth mentioning.

Table 13.3: Overall sensitivity picture for the
maximum fuel temperature $(T = T_{fi} - T_{co})$
in nominal conditions.

Importance	BoL	EoL
$I_{\Delta T_f, T}$	0.850	0.950
$\hookrightarrow I_{e_{max}, \Delta T_f}$	0.270	0.270
$\hookrightarrow I_{Po_{max}, \Delta T_f}$	0.350	0.400
$\hookrightarrow I_{r_{fi}, \Delta T_f}$	0.300	0.300

. . . .

$\hookrightarrow I_{r_{col},r_{fi}}$	0.470	0.480
$\hookrightarrow I_{r_{eq},r_{fi}}$	0.530	0.520
$\hookrightarrow I_{\rho_{col},r_{fi}}$	0.100	0.100
$\hookrightarrow I_{\rho_{eq},r_{fi}}$	0.050	0.040
$\hookrightarrow I_{\varepsilon_f^i,r_{fi}}$	0.050	0.400
$\hookrightarrow I_{k_f,\Delta T_f}$	1.000	1.000
$\hookrightarrow I_{x,\Delta T_f}$	0.050	0.010
$\hookrightarrow I_{x_{max},\Delta T_f}$	0.100	0.070
$\hookrightarrow I_{Po,\Delta T_f}$	0.030	0.030
$\hookrightarrow I_{\varepsilon^{sw,g},\Delta T_f}$	0.000	0.120
$I_{\Delta T_{gap},T}$	0.140	0.035
$\hookrightarrow I_{s_{JOG},h_{gap}}$	0.000	0.500
$\hookrightarrow I_{k_{JOG},h_{gap}}$	0.000	0.500
$\hookrightarrow I_{h_{rad},h_{gap}}$	0.100	0.020
$\hookrightarrow I_{e_f,h_{rad}}$	0.900	0.900
$\hookrightarrow I_{e_c,h_{rad}}$	0.850	0.850
$\hookrightarrow I_{h_{gas},h_{gap}}$	0.900	0.850
$\hookrightarrow I_{mol_{Xe},h_{gas}}$	0.600	0.500
$\hookrightarrow I_{FGR,mol_{Xe}}$	1.000	1.000
$\hookrightarrow I_{P_{gas},h_{gas}}$	0.030	0.020
$\hookrightarrow I_{mol_{Xe},P_{gas}}$	0.400	0.800
$\hookrightarrow I_{FGR,mol_{Xe}}$	1.000	1.000
$\hookrightarrow I_{s_{gap},h_{gas}}$	0.700	0.000
$\hookrightarrow I_{\varepsilon_t,s_{gap}}$	0.450	0.000
$\hookrightarrow I_{\alpha,\varepsilon_t}$	1.000	0.000
$\hookrightarrow I_{\varepsilon_f^o,s_{gap}}$	0.850	0.000
$\hookrightarrow I_{h_{con},h_{gap}}$	0.000	0.130
$\hookrightarrow I_{P_{con},h_{con}}$	0.000	0.700
$\hookrightarrow I_{H,h_{con}}$	0.000	0.700
$\hookrightarrow I_{k_f,h_{con}}$	0.000	0.900
$\hookrightarrow I_{k_c,h_{con}}$	0.000	0.100
$I_{\Delta T_c,T}$	0.020	0.020
$\hookrightarrow I_{s_c,\Delta T_c}$	0.940	0.970
$\hookrightarrow I_{s_{ox},s_c}$	0.000	0.020
$\hookrightarrow I_{s_w,s_c}$	0.000	0.120
$\hookrightarrow I_{k_c,\Delta T_c}$	1.000	1.000
$\hookrightarrow I_{k_{ox},\Delta T_c}$	0.000	0.100
$\hookrightarrow I_{s_{ox},\Delta T_c}$	0.000	0.100

. . . .

13.6.3   Clad mechanics - Nominal condition

In Table 13.5 a resume of all the sensitivity coefficients is presented for the clad stresses and strains in nominal conditions. Multiplying the nested sensitivities recursively, results in Table 13.6 can be calculated. It can be seen that the stresses are dominated by the swelling distribution and the contact pressure while the strains by thermal expansion and swelling, being the reference stainless steel an austenitic one. Finally, the strain in nominal conditions is mostly dominated by material properties being the only models with a non-negligible impact the cladding wastage by the fuel due to FCCI and the contact pressure.

13.6.4   Fuel temperature - UTOP

In Table 13.7 a summary of all the sensitivity coefficients is presented for the fuel maximum temperature in UTOP conditions. Multiplying the nested sensitivities recursively, results in Table 13.8 can be calculated. It can be seen how the ranking is dominated by the specific heat, a material property. The steady state FGR plays here a non negligible role because it decides the retained gas available for fuel swelling. It must also be said that due to the approximation adopted in Section 13.4.2, that considers all the retained gas available for swelling in the UTOP time frame, the effect could be overestimated; nevertheless it can be one of the main contributors to the global transient behavior.

13.6.5   Clad mechanics - ULOF

In Table 13.9 all the sensitivity coefficients are presented for the clad mechanics in ULOF conditions. Multiplying the nested sensitivities recursively, results in Table 13.10 can be calculated; while for the stresses model and material properties' sensitivities are on the same level, for the strains, the latter are always more important, but relatively to the steady state, the modeling contribution is higher in ULOF.

13.6.6   Summary

Remembering that the present analysis started from the deeply complex and interconnected behavior depicted in Figure 13.1, the main dependencies can now be better visualized as in Figure 13.35, where the arrow thickness is proportional to the relative sensitivity coefficient. Figure 13.35 is basically the linearized version of Figure 13.1 where the linearization has been performed

....

Table 13.4: Sensitivity summary for the fuel temperature in nominal conditions. Blue quantities indicate material properties.

Parameter	$I_{i,T}$
k_f	0.950
Po_{max}	0.380
e_{max}	0.257
r_{eq}	0.148
r_{col}	0.137
ε_f	0.119
$\varepsilon^{sw,g}$	0.115
x	0.085
FGR	0.076
x_{max}	0.043
α_c	0.040
s_{JOG}	0.035
k_{JOG}	0.035
Po_{col}	0.029
Po	0.029
k_c	0.020
Po_{eq}	0.013
e_f	0.013
e_c	0.012
H	0.003
P_{con}	0.003
s_w	0.002
s_{ox}	0.002
k_{ox}	0.002

. . . .

Table 13.5: Overall
sensitivity picture for the
clad stresses and strains in
nominal conditions.

Importance	σ_{eff}	ε_t
$I_{E,j}$	0.000	0.100
$I_{\nu,j}$	0.000	0.010
$I_{s_c,j}$	0.900	1.000
$\hookrightarrow I_{s_{ox},s_c}$	0.030	0.030
$\hookrightarrow I_{s_w,s_c}$	0.120	0.120
$I_{P_{con},j}$	0.700	0.100
$I_{\alpha,j}$	0.000	0.500
$I_{\varepsilon^{sw},j}$	0.050	0.200
$I_{\varepsilon^{sw}_{max},j}$	1.000	0.050
$I_{\dot{\varepsilon}^{cr,th},j}$	0.010	0.100
$I_{\dot{\varepsilon}^{cr,th}_{max},j}$	0.030	0.150
$I_{\dot{\varepsilon}^{cr,ir},j}$	0.000	0.000

Table 13.6: Importance summary for the
clad mechanic in nominal conditions.
Blue quantities indicate material
properties.

Parameter	$I_{i,\sigma_{eff}}$	Parameter	I_{i,ε_t}
ε^{sw}_{max}	1.000	α	0.500
P_{con}	0.700	ε^{sw}	0.200
s_w	0.110	$\dot{\varepsilon}^{cr,th}_{max}$	0.150
ε^{sw}	0.050	s_w	0.120
$\dot{\varepsilon}^{cr,th}_{max}$	0.030	E	0.100
s_{ox}	0.030	P_{con}	0.100
$\dot{\varepsilon}^{cr,th}$	0.010	$\dot{\varepsilon}^{cr,th}$	0.100
E	0.000	ε^{sw}_{max}	0.050
ν	0.000	s_{ox}	0.030
α	0.000	ν	0.010
$\dot{\varepsilon}^{cr,ir}$	0.000	$\dot{\varepsilon}^{cr,ir}$	0.000

. . . .

Table 13.7: Overall sensitivity
picture for the fuel temperature in
UTOP conditions.

Importance	UTOP - EoL
$I_{\Delta T_f, T}$	0.950
$\hookrightarrow I_{c_p, \Delta T_f}$	0.900
$\hookrightarrow I_{r_{fi}, \Delta T_f}$	0.300
$\hookrightarrow I_{\varepsilon_f^i, r_{fi}}$	0.400
$\hookrightarrow I_{\varepsilon_{tr}^{sw,g}, r_{fi}}$ [a]	0.075
$\hookrightarrow I_{\varepsilon_{tr}^{sw,g}, \Delta T_f}$	0.050
$\hookrightarrow I_{FGR_{tr}, \Delta T_f}$ [b]	0.050
$\hookrightarrow I_{FGR_{ss}, \Delta T_f}$	0.400

[a] Taken as half the steady state values to account for the ratio $\frac{\varepsilon_{tr}^{sw,g}}{\varepsilon_{tr}^{sw,g} + \varepsilon_{ss}^{sw,g}}$.

[b] $I_{FGR_{tr}, \varepsilon_{tr}^{sw,g}}$ taken as unity given the high release expected for the peak pin with JOG formation.

Table 13.8: Sensitivity summary
for the fuel temperature in
UTOP conditions. Blue
quantities indicate material
properties.

Parameter	$I_{i,T}$
c_p	0.855
FGR_{ss}	0.342
$\varepsilon_{tr}^{sw,g}$	0.044
FGR_{tr}	0.043

. . . .

Table 13.9: Overall sensitivity picture for the clad stresses and strains in ULOF conditions.

Importance	σ_{eff}	ε_t
$I_{s_c,j}$	0.250	0.200
$\hookrightarrow I_{s_{ox},s_c}$	0.030	0.030
$\hookrightarrow I_{s_w,s_c}$	0.120	0.120
$I_{P_{con},j}$	0.350	0.200
$I_{\alpha,j}$	0.020	0.600
$I_{\dot{\varepsilon}^{cr,th},j}$	0.050	0.010
$I_{\dot{\varepsilon}^{cr,th}_{max},j}$	0.000	0.000
$I_{\sigma_Y,j}$	0.350	0.050

Table 13.10: Sensitivity summary for the clad mechanic in ULOF conditions. Blue quantities indicate material properties.

Parameter	$I_{i,\sigma_{eff}}$	Parameter	I_{i,ε_t}
P_{con}	0.350	α	0.600
σ_Y	0.350	P_{con}	0.200
$\dot{\varepsilon}^{cr,th}$	0.050	σ_Y	0.050
s_w	0.030	s_w	0.240
α	0.020	$\dot{\varepsilon}^{cr,th}$	0.100
s_{ox}	0.008	s_{ox}	0.006

. . . .

on the three parameters inside the domain bounded by the conditions of Section 12.2.

13.6.7   Quantitative guidelines

Making a step further from the previous sections, all the gathered sensitivity coefficients can be effectively used to derive guidelines helping in building a balanced DOC. The concept of "balance" is here the same as in Section 4.2.1, meaning an equilibrium between the material and modeling errors contribution to the overall uncertainties on the target parameters of interest along with an internal balance between models; the latter implying investing modeling efforts proportionally to the importance of that model allowing marginal contributions to be roughly approximated or disregarded. To achieve this, an inverse uncertainty problem must be solved, starting with a target accuracy on T, σ_{eff} and ε_t so to derive the needed accuracy on models and material properties; the further constraint of similar contributions, to the final uncertainty, of materials and models is added.

The inverse uncertainty problem to be solved is similar to the one used in cross section analysis [101] and it assumes the following form

$$\text{MIN}\left(\sum_{i=1}^{N}\frac{\lambda_i}{d_i^2}\right) \quad \text{subject to} \quad \sum_{i=1}^{N}I_{i,j}^2 d_i^2 \leq R_j^2 \quad j = T, \sigma_{eff}, \varepsilon_t \quad , \quad (13.46)$$

where d_i is the uncertainty of the quantity i, λ_i is a cost parameter related to i and should give a figure of merit of the difficulty in improving that parameter while R_j is the target uncertainty on the performance parameter j (e.g. the maximum fuel temperature). Finally, the following condition is also imposed

$$R_{j,Mod}^2 \simeq R_{j,Mat}^2, \tag{13.47}$$

where $R_{j,Mod}$ and $R_{j,Mat}$ are the modeling and material properties contributions to the uncertainty. This condition actually enforces homogeneity of code development ensuring that extremely accurate models are not coupled to rough material properties or, better, that for given material properties accuracies, the modeling effort is consistent and optimized.

The transient and steady state analyses are combined deterministically, so decoupling them, as

$$1 + R_{j,Tot} = (1 + R_{j,Ss})(1 + R_{j,Tr}) \tag{13.48}$$

where $R_{j,Tot}$ is the global uncertainty on the j performance parameter, $R_{j,Ss}$ is the steady state uncertainty and $R_{j,Tr}$ is the transient uncertainty. This

. . . .
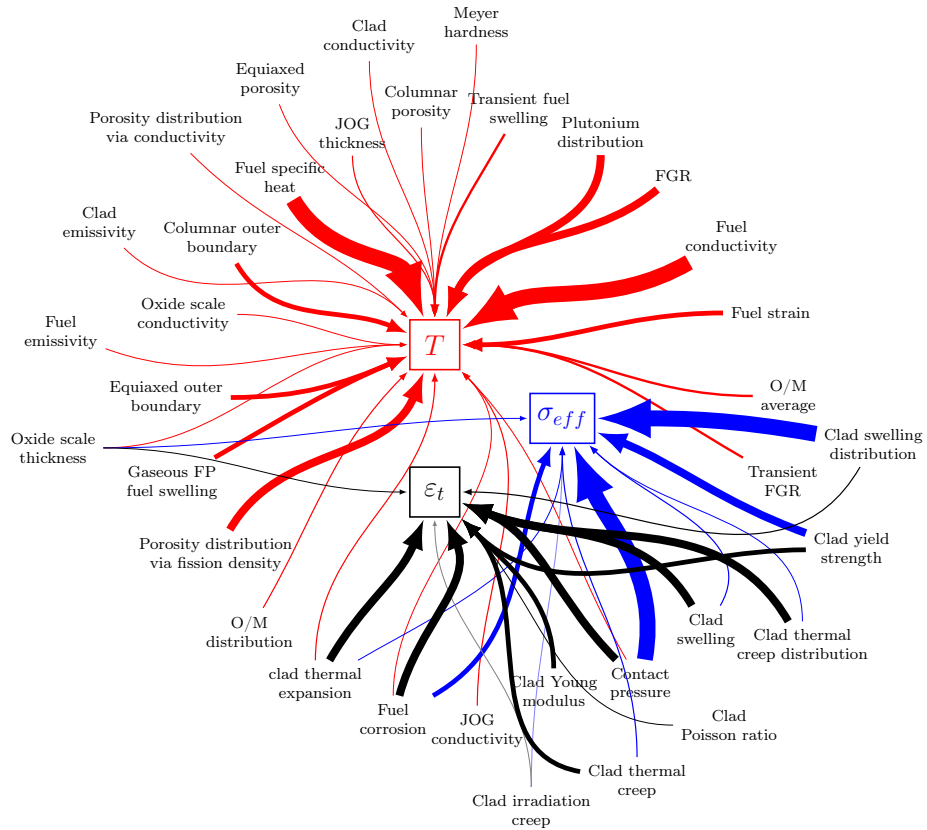
Figure 13.35: Importance representation of the various phenomena contributing to the fuel maximum temperature (in red), the clad stress (in blue) and strain (in black). Arrow thickness proportional to the relative sensitivity coefficient.

combination basically assumes that the initial conditions for the transient are always perturbed.

Guidelines

For the target uncertainties reported in Table 13.11, the constrained optimum problem in equation (13.46) has been solved and results presented in Table 13.12 finally obtained, where uncertainties have been bounded to be lower than 50%. As seen from Table 13.11, the transient target accuracy of the fuel temperature has been taken higher than the corresponding ones for the clad mechanics because of the much more uncertain nature of the former.

The final values of the target accuracies, differentiating steady and transient conditions and modeling and material properties contributions, are presented in Table 13.13. As can be seen, the higher contribution comes from normal operations which basically decides the transient initial conditions; only for T the situation is more balanced meaning that the transient itself has an equally important role. For what concerns the balance between modeling and material properties errors, we can see that equation (13.47) is well satisfied for the clad mechanics while for the temperature the modeling component slightly dominates in both steady state and transient conditions.

Is it interesting to note that:

- some of the target errors on material properties are actually higher than what has already been achieved with current data sets (e.g. e_c) implying, that no further (or at least with very low priority) effort is needed in their evaluation;

- on the contrary, other material properties represent the most stringent accuracy requirements due to their high sensitivity coefficient (e.g. k_f);

- the required accuracy for FGR is actually dictated by transient conditions more than nominal ones; this is due to the high importance of this phenomenon on the transient swelling and thus on the fuel porosity. This effect is possibly overestimated, as discussed in Section 13.4.2, for the fast UTOP assumed as reference.

Table 13.12: Proposed set of uncertainties
for the main parameters of a fuel pin
safety-informed design-oriented tool.

Parameter	d_i
....	

k_f	0.13
Po_{max}	0.20
e_{max}	0.20
r_{eq}	0.30
r_{col}	0.30
ε_f	0.35
$\varepsilon_f^{sw,g}$	0.20
x	0.40
FGR	0.30
x_{max}	0.50
α_c	0.05
s_{JOG}	0.50
k_{JOG}	0.50
Po_{col}	0.50
Po	0.20
k_c	0.05
e_f	0.50
e_c	0.50
Po_{eq}	0.50
H	0.50
P_{con}	0.15
s_w	0.40
s_{ox}	0.50
k_{ox}	0.50
c_p	0.10
$\varepsilon_{tr,f}^{sw,g}$	0.30
FGR_{tr}	0.30
$\sigma_{Y,c}$	0.15
$\varepsilon_{max,c}^{sw}$	0.11
ε_c^{sw}	0.20
$\dot{\varepsilon}_{max,c}^{cr,th}$	0.20
$\dot{\varepsilon}_c^{cr,th}$	0.20
E_c	0.20
ν_c	0.20
$\dot{\varepsilon}_c^{cr,ir}$	0.50

. . . .

Table 13.11: Target uncertainties for the maximum fuel temperature and clad stresses and strains for a safety-informed design-oriented pin thermo-mechanic tool.

Target accuracy	Nominal condition	Transient[a]
R_T	0.20	0.15
$R_{\sigma_{eff}}$	0.20	0.10
R_{ε_c}	0.20	0.10

[a] Transient referes to UTOP and ULOF for the temperature and clad mechanical quantities respectively.

Table 13.13: Contribution of transient and steady state and modelling and material properties uncertainties to the performance parameters.

Target accuracy	T	σ_{eff}	ε_t
$R_{j,Ss}$	0.18	0.16	0.08
Modelling	0.13	0.11	0.05
Material	0.12	0.11	0.06
$R_{j,Tr}$	0.13	0.08	0.04
Modelling	0.10	0.05	0.03
Material	0.09	0.05	0.03
$R_{j,Tot}$	0.34	0.25	0.13
Modelling	0.25	0.17	0.08
Material	0.22	0.17	0.09

Discussion

Given the whole set of data presented in the previous sections some general considerations can be drawn: material properties contribution to the overall error is quite high both in nominal and transient conditions; for this, as the modeling effort increases, material knowledge must follow, otherwise the

. . . .

aforementioned effort is bound to be less rewarding. Indeed, when models are built, during the calibration phase, errors of the material properties are indirectly included thus bounding the calibration to the set of properties used; this procedure is acceptable as long as those errors are reasonably low and, if that is not the case, the whole code development procedure can become questionable and this is an ulterior incentive to promote a better knowledge of material properties before undertaking further modeling efforts. It is also worth noticing that, in the present analysis, input and fabrication uncertainties have not been considered and they could potentially be another major source of error. Ideally, if most of the input parameters are elaborations of other codes build with the same logics described in the present work, the magnitude of the impact of such parameters should be similar - or at least easily quantifiable - to the modeling error, thus ensuring code homogeneity.

Another important point stems from the desire of having a balanced DOC, not only from the point of view of modeling versus material properties, but also, among the different models (see Section 4.2.1). This will ensure a homogeneous modeling effort throughout the code and thus considerably simplifying and speeding up the tool development itself. As an example, it does not actually make much sense to have a rough model for the restructuring and thus for the porosity distribution, while implementing an extremely accurate and complex model for the Oxygen-to-Metal redistribution as long as the global error will be dominated by the restructuring due to its higher importance; the modeling effort should then be proportional to the position occupied by the phenomenon in question in ranking tables like Table 13.4 and similar. This is indeed one of the main motivations of the present sensitivity study: to understand where development efforts should be stressed for a given set of conditions and aimed performances.

Finally, it must be reminded that the guidelines in Table 13.12 must not be interpreted analytically, due to the approximate nature of their derivation and the fact that individually proving that each model has actually achieved the wanted accuracy is almost impossible; this is due to the interconnected nature of many phenomena and the lack - along with difficulties in reliably collecting them - of dedicated data. They, instead, have to be used as beacons to rationally orient choices during models selection and construction.

. . . .

CODE STRUCTURE

Thanks to the sensitivity study of Chapter 13 and the consequent guidelines, it has been possible to develop a balanced safety-informed DOC, respecting the equilibrium and fast running conditions of Section 4.2, as outlined in this chapter.

In particular, the implemented material properties will not be directly presented, but discussed only on a case by case basis during the validation stage in Chapter 15; this in order to keep the model presentation clean and not overshadowed by the great number of physical parameters required, which must be multiplied by the many materials implemented accounting for the possibility of multiple choices for the same material property. For the same reasons, all the correlations implemented will not be listed, but models will be discussed only for highlighting the criteria behind their selection along with the main assumptions and simplifications adopted.

14.1   General structure

As anticipated in Section 12.2, the selected numerical approach is of the 1.5D type, meaning that an axial segmentation of the pellet stack and fuel clad is performed, with each slice additionally subdivided in the radial direction for both clad and fuel. From the adopted numerical method and the sensitivity analysis of Chapter 13 TEMIDE's structure has been conceived as reported in Figure 14.1, where the general flow diagram of TEMIDE calculation scheme is presented.

. . . .

After having read the input geometrical, materials and boundary conditions the initialization of all the needed variables starts:

- boundary conditions, in particular, consist in the power[1] and clad outer temperature histories, including transients, both in the form of an axial distribution[2]. If the clad temperature is not directly available, an acceptable substitute is the couple formed by the inlet coolant temperature and the elementary cell mass flow rate.

- Geometric information encompasses the internal pin structure - clad, gap and pellet dimensions - along with the upper and/or lower plenum volumes together with the fuel active height and, eventually, the elementary cell flow area (or lattice pitch).

- Materials includes mostly the fuel, clad, coolant and the plenum mixture initial composition and quantity (or loading pressure).

After the global initialization, the time loop starts, spanning over the given history; a time step check is present to test if the current Δt is below some threshold values in order to ensure smooth convergence or to speed up the calculation, if possible (see Section 14.13). Once the time step is set, the loop over the various axial slices starts updating variables like local power, BU and clad (or coolant) temperature; after this, the most important loop of the code, the gap loop, starts (the rationales behind the selected convergence criteria and the loop structure are discussed in Section 14.1.1) iterating between the thermal (see Section 14.2) and mechanical (see Section 14.3) fields. When convergence is achieved in the loop, the new state is tested against fuel melting and clad failure (see Section 14.4); indeed, if failure is, detected the calculation stops, otherwise all remaining phenomena of interest, encompassing grain growth (see Section 14.5), clad corrosion due to fuel and coolant action (see Section 14.6), oxygen-to-metal ratio change and redistribution (see Section 14.7), plutonium migration (see Section 14.8), restructuring (see Section 14.9), FGR (see Section 14.10) and JOG formation (see Section 14.11) are addressed. The procedure is then repeated for all the remaining axial nodes; when all the slices have been analyzed the new plenum pressure is evaluated and the next time step started until the whole simulated period is spanned or failure is detected.

---

[1]Since during the pin design phase such information is only tentatively available, a simple linear guess between BoL and EoL could suffice for the nominal conditions.

[2]Inferred from the axial form factor.

. . . .
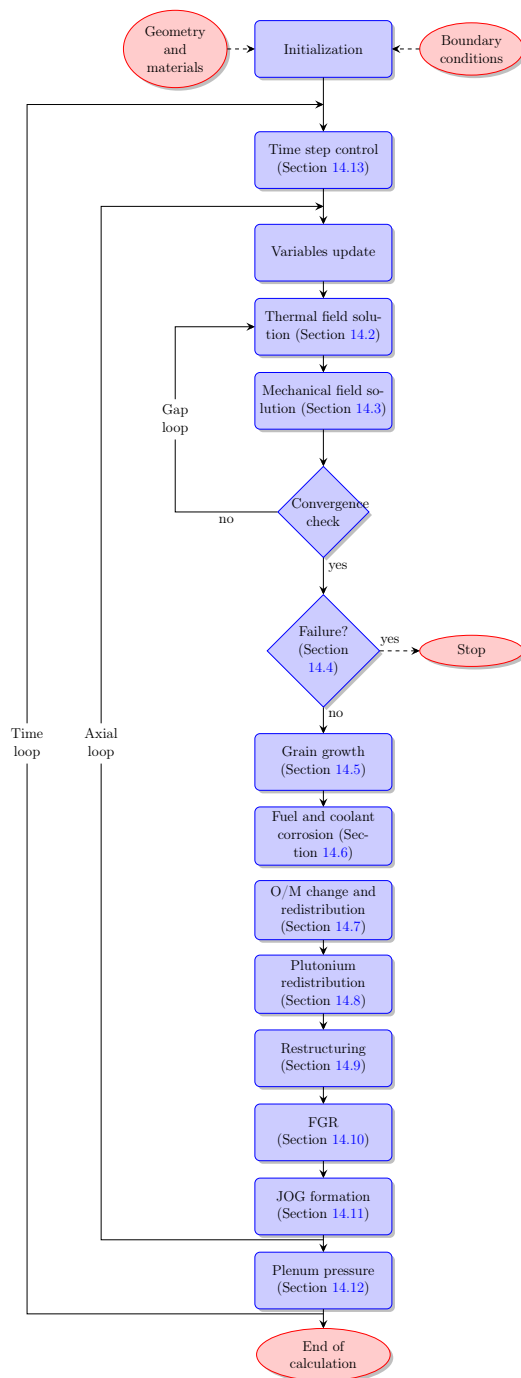
Figure 14.1: General flow diagram of TEMIDE calculation scheme.

. . . .

14.1.1   Rationales

Fuel pin thermo-mechanics codes encompass a variety of interconnected phenomena; in numerical language, this interconnection requires iterations to be performed. This iteration loop is at the core of such codes and establishes which are the phenomena implicitly coupled[3]. On one hand, the greater the number of physical aspects included in the loop, the higher the accuracy for a given time step, but on the other hand, the greater the convergence and numerical difficulties. Being equilibrium the keyword (and also remembering the intrinsic impact of material properties), a balance must be established; this can be done exploiting the sensitivity analysis of Chapter 13.

As discussed in Section 13.2.4, the interaction between the fuel and clad thermal fields is, indeed, dictated by the geometry, in particular, by the gap dynamics - at least when it is open - which in turn is driven by the fuel and clad mechanics; this link has a considerable importance, especially in BoL conditions and related transients. For this reason, a loop to couple the thermal and mechanical fields via the gap has been adopted. A similar effect is present for the central void radius, as reported in Table 13.3, and being essentially of the same nature it is automatically included in the loop.

For what concerns the other phenomena in Figure 14.1 - which are mainly temperature dependent -, the rationales behind the decision to include them or not in the coupling has been the following:

- grain growth has a negligible impact on the overall pin dynamics (see Section 14.5) and, as such, could be directly disregarded or at least roughly modeled; its coupling with other phenomena is therefore not needed.

- As seen in Section 13.6, fuel and coolant[4] corrosion have a low impact on the fuel temperature - while a modest one on the clad mechanics - and so they can be safely considered outside of the gap loop.

- Both the oxygen-to-metal ratio and its distribution have a low impact on T, as visible in Table 13.4; moreover, the time scale of the O/M average change is linked to BU and so relatively slow making an implicit coupling in the gap loop not necessary.

---

[3]Coupled, in this section, identifies a two-way coupling, in contrast to the simple one-way linkage for properties put outside the loop.

[4]Coolant corrosion has been studied under the hypothesis that protective measures have been taken so to avoid direct contact between HLM and clad so to protect the micro-structure of the latter.

. . . .

- The plutonium redistribution effect on T, via the power distribution distortion, can be significant (see Section 13.2.1), but is characterized by high time scales, as seen in Section 13.4, and so it can effectively be decoupled from the thermal calculation.

- Similarly to plutonium redistribution, the restructuring process has an overall high impact on T via the power distribution, the thermal conductivity and the central void (see Table 13.4); inserting it in the loop could be a reasonable choice, but, nonetheless, in TEMIDE a one-way coupling has been adopted so to speed up the calculation, having care to select the time step so to guarantee a sufficient accuracy (see Section 14.13).

- As seen in Section 13.2.3, FGR in nominal conditions impacts T, in a sensible way, via the FG moles released (mol_{Xe}), only for a limited time frame; besides, mol_{Xe} is actually a property of the whole pin rather than of a single axial slice, making it intrinsically less dependent on local conditions and so safely accountable without iterating with the temperature field. Tor what concerns UTOP-like conditions, the local impact of steady-state FGR could be higher, but given the conservative estimation trying to target the uncertainty in Table 13.12, it should suffice even not inserting it in the gap loop.

- Exactly the same logic of FGR can be applied to the plenum pressure, being aware that its impact on both fuel temperature and clad mechanics is even lower.

- Finally, JOG formation has been decoupled from the thermal and mechanical analyses since the effect on the former should be contained[5], but mostly because of the high uncertainties surrounding this phenomenon, not justifying any significant increase in numerical complexity.

All the just mentioned phenomena are primary linked to the fuel temperature and feature time scales higher than the reference UTOP one (see Section 13.4), implying that the proposed decoupling should be acceptable even in such a transient; for what concerns the ULOF, time scales are much higher, but there the accent is on the clad mechanics and so, again (see Section 13.5), the introduced TEMIDE structure seems adequate even in this case.

---

[5]The effect of JOG formation on the fuel pin mechanics is still object of debate and no definitive conclusion can be formulated.

. . . .

The gap loop in Figure 14.1, therefore, involves only the gap thickness and central void radius and it is believed to be converged when their pseudo-errors (the difference between two iterations), relative or absolute, are below threshold values. The absolute convergence requirement stems from the necessity to avoid difficulties for a nearly closed gap ($s_{gap} \to 0$) or central void, where relative requirements could be too stringent.

Thanks to the simple structure of TEMIDE, further outlined in the following sections, convergence is easily achieved in all, envisaged, situations of interest (i.e. with less than 10 iterations). It must also be noted that, generally, moving farther from BoL implies a lower gap importance making convergence even simpler[6].

14.2   Thermal field

The thermal field, being the object of interest in UTOP conditions and fundamental in determining the evolution of many of the phenomena previously discussed, has been carefully modeled - inside the possibilities of 1.5D codes - both in nominal and transient conditions, implying that axial conduction is neglected.

The overall scheme of the thermal calculation is reported in Figure 14.2 where the symbols meaning is explained later in the section. The depicted scheme is fairly simple: after a check on the given boundary conditions, the clad outer temperature is taken, if available, or calculated from the coolant one; the calculation of the internal fuel pin temperature follows with the building of the necessary matrices, updated to take into account transient conditions (if necessary); finally the temperature field is solved. Iterations are performed, until convergence, to ensure consistency between temperature and material properties that depend on the former.

14.2.1   Coolant

In case the axial distribution of the clad outer temperature is not available and the input consists of the elementary cell mass flow rate and coolant inlet temperature, the thermal model includes the coolant axial temperature calculation both in nominal and transient conditions.

---

[6]This could not hold true if the gap reopens due to clad swelling, although the gap loop convergence is always achieved in a reasonably fast way.

. . . .
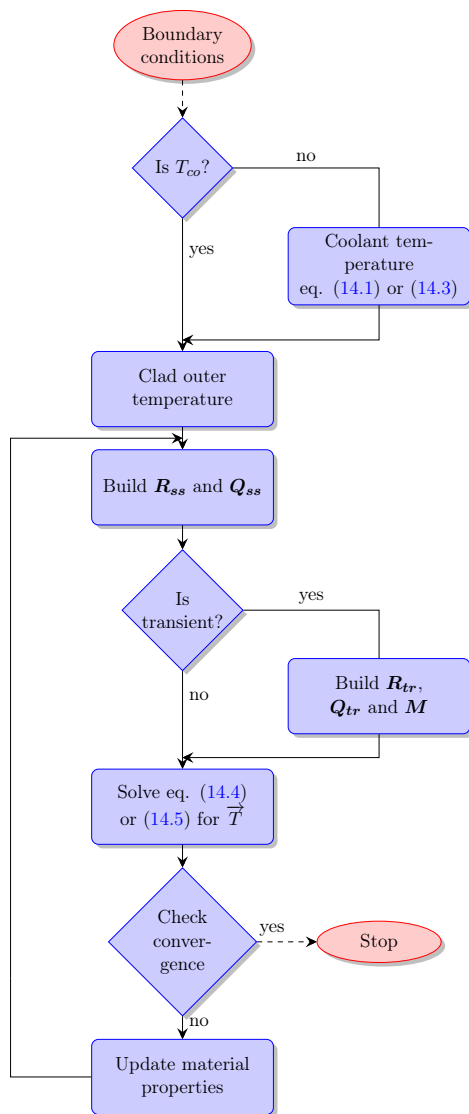
Figure 14.2: Flow diagram of TEMIDE thermal calculation.

. . . .

Nominal

The equation to solve in nominal conditions stems from equation 7.7 in the case of a single isolated channel as

$$\frac{dT_c(z)}{dz} = \frac{\chi(z)}{\dot{m}c_p} \quad , \tag{14.1}$$

which can be trivially discretized and solved starting from the inlet temperature boundary condition. The outer clad temperature can then be calculated with the aid of equation (7.9) and the Nusselt's number of Section 7.2.6 plus the correction term due to coolant corrosion as discussed in Section 14.6.

Transient

The equation to solve in transient conditions moves from equation (14.1) added of the thermal inertia term, resulting in

$$\frac{\partial T_c(z,t)}{\partial z} + \frac{1}{v(t)}\frac{\partial T_c(z,t)}{\partial t} = \frac{\chi(z,t)}{\dot{m}(t)c_p} \quad , \tag{14.2}$$

where v is the coolant velocity; instead of numerically solving equation (14.2) directly, a different approach has been followed, and the analytical solution in case of constant v, $\dot{m}$ and χ taken as reference, arriving at

$$T_{c,z+\Delta z}^{t+\Delta t} = T_{c,z+\Delta z}^{t}e^{-\frac{v\Delta t}{\Delta z}} + \left(\frac{\chi\Delta z}{\dot{m}c_p} + T_{c,z}^{t+\Delta t}\right)\left(1 - e^{-\frac{v\Delta t}{\Delta z}}\right) \quad , \tag{14.3}$$

where Δz and Δt indicate the axial and time discretizations respectively. This explicit treatment features a higher numerical accuracy, for a given time step, relatively to the direct discretization of equation 14.2 as shown in Section 15. Similarly to the nominal conditions, the clad outer temperature calculation follows with the aid of equation (7.9).

In the above mentioned calculation scheme, the coupling between coolant and solid (i.e. pin) thermal field is neglected, meaning that the former influence the latter, but not vice versa.

14.2.2   Fuel pin

The thermal field inside the pin results from the solution of the standard 1D (radial) heat transfer equations in cylindrical geometry [139] both in nominal and transient conditions, having as boundary conditions the outer clad temperature and adiabaticity at the inner pellet radius.

. . . .

Nominal

In nominal conditions a standard finite-differences discretization of the steady-state heat transfer equations [139] is performed, resulting in a system of the form

$$\boldsymbol{R_{ss}}\overrightarrow{T} = \boldsymbol{Q_{ss}} \quad , \tag{14.4}$$

where $\boldsymbol{R_{ss}}$ and $\boldsymbol{Q_{ss}}$ are the resistance and power matrices respectively, while $\overrightarrow{T}$ is the temperature vector. Exploiting the three-diagonal nature of $\boldsymbol{R_{ss}}$, the system is solved by a dedicated LAPACK package procedure [94]. Due to the non-linear dependence between the thermal conductivities - the fuel one in particular - and the temperature, some Picard's iteration is required before reaching convergence, but thanks to the very favorable nature of the heat equations (featuring the Laplacian operator in particular), it is always easily achieved.

Transient

Similarly to the coolant, in transient conditions the thermal inertia term must be added, resulting in an equation similar to (13.36); to minimize the impact of transient calculations, the main requirement its to use a numerical approach that is simply additive relatively to the nominal (steady-state) conditions (equation (14.4)). This results in a system of the form

$$\boldsymbol{R_{tr}}\overrightarrow{T}^{t+\Delta t} = \boldsymbol{Q_{tr}} \rightarrow \left(\frac{\boldsymbol{R_{ss}}}{2} - \boldsymbol{M}\right)\overrightarrow{T}^{t+\Delta t} = \boldsymbol{Q_{ss}} - \boldsymbol{M}\overrightarrow{T}^{t} - \frac{\boldsymbol{R_{ss}}}{2}\overrightarrow{T}^{t} \quad , \tag{14.5}$$

where $\boldsymbol{M}$ is the inertia matrix. Again the system is solved via a LAPACK procedure and iterations performed to take into account the materials properties dependence on temperature.

14.3   Mechanical field

The other component of the gap loop is the mechanical analysis of the fuel and cladding system, which is one of the main models of any thermo-mechanics code; it is also necessary to evaluate the clad state both in nominal and ULOF conditions. As it will be shown, differently from the temperature field, the developed model is used for both nominal and transient conditions.

The overall scheme of the mechanical calculation is reported in Figure 14.3, where using the available thermal field, and the stress ($\boldsymbol{\sigma^p}$) and strain ($\boldsymbol{\varepsilon^p}$) states from the previous time step or gap loop iteration, along

. . . .
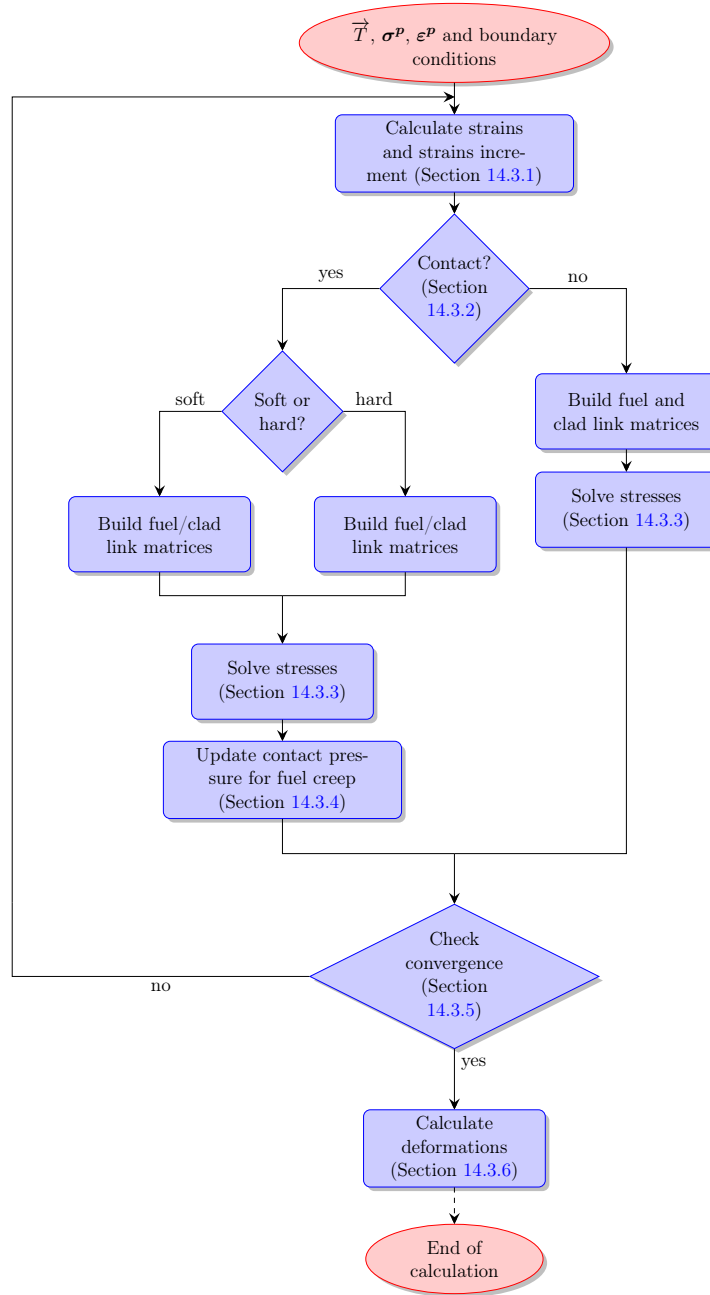
Figure 14.3: Flow diagram of TEMIDE mechanical calculation.

. . . .

with the given boundary conditions, fuel and clad strains are calculated (see Section 14.3.1); after having checked against contact (see Section 14.3.2), link matrices are properly assembled and the system solved for the stresses (see Section 14.3.3). In case of contact, the model for fuel creep is used to correct the calculated contact pressure (see Section 14.3.4); convergence is then tested (see Section 14.3.5) and, if not yet achieved, the procedure is repeated updating strains with the new stress state. When convergence is finally met, deformations are calculated and applied to the geometry (see Section 14.3.6) so that a new thermal field can be calculated until the gap loop converges.

14.3.1   Strains calculation

The strains calculation descends from the constitutive equation (13.27) for both the fuel and clad.

Clad

In the case of cladding strains (ε_c), equation (13.27) can be decomposed as

$$
\begin{aligned}
\varepsilon_{c,i} = & \varepsilon_{c,i}^{el}(\overrightarrow{\sigma}) + \varepsilon_{c,i}^{th} + \varepsilon_{c,i}^{sw,t} + \Delta\varepsilon_{c,i}^{sw,t} + \varepsilon_{c,i}^{cr,t} + \\
& \Delta\varepsilon_{c,i}^{cr,t}(\overrightarrow{\sigma}) + \varepsilon_{c,i}^{pl,t} + \Delta\varepsilon_{c,i}^{pl,t}(\overrightarrow{\sigma}) \quad i = r, t, a \quad ,
\end{aligned}
\tag{14.6}
$$

where the non-thermo-elastic strains have been explicitly stated as the sum of their value at the beginning of the time step (e.g. $\varepsilon_{c,i}^{sw,t}$) and the variation inside the step (e.g. $\Delta\varepsilon_{c,i}^{sw,t}$); the dependence on the stress state has also been clearly highlighted. Given that the values at time t are input parameters, the clad strains calculation is limited to the variation inside the step. Apart from the trivial thermo-elastic strains, the calculation encompasses the isotropic void swelling, creep and plastic increments; the first will not be discussed being a material property, as previously explained, while, the general approach and approximations regarding the other two will be briefly presented.

Creep   Creep is the sum of the irradiation and thermally driven components, with the former typically much lower than the latter (see Figure 13.35). The main features of creep are the high dependence on temperature and the strong link with the stress state of the component; while the former comes from the thermal field calculation, the latter is evaluated inside the mechanic loop creating a non-linearity between strains and stresses. This relation can

....

be tackled explicitly, borrowing the stress state in the evaluation of $\Delta\varepsilon_{c,i}^{cr,t}(\overrightarrow{\sigma})$ from the previous time step, or implicitly, updating $\overrightarrow{\sigma}$ with the new one calculated in the mechanic loop; since for austenitic stainless steels the creep rates, in nominal conditions, are particularly low, the explicit treatment is acceptable; when using ferritic-martensitic steels or during ULOF-like transients, higher creep rates are expected and so the implicit treatment could be preferable. Given however that, generally, the differences between the explicit and implicit approaches to creep have been found negligible both from a numerical accuracy and computational time standpoints, the latter has been preferred due to its higher generality.

Finally, to link the effective creep rate, the one available from experiments and correlations, with its directional counterparts (along $i = r, t, a$) the standard, stress-based Prandtl-Reuss flow rules have been adopted.

Plasticity The plastic strain develops when the local effective stress σ_{eff} (defined in equation (13.28)) is greater than the material yield strength σ_Y; if this happens, to actually evaluate the magnitude of the resulting plastic strain, stress-strain curves, like the one in Figure 14.4, are necessary. Unfortunately, such curves are complicated to use directly and depend on temperature, irradiation conditions and strain rates; in the present context, to make plasticity more manageable and given the fact that it is expected to contribute only in transient conditions (see Section 13.5), the perfect plasticity assumption proposed in [78] has been adopted. According to [78] a modified total strain can be defined as

$$\varepsilon_{c,i}^{'} = \varepsilon_{c,i}^{el} + \Delta\varepsilon_{c,i}^{pl,t}   , \tag{14.7}$$

where the plastic component has been subtracted. Applying Hooke's law, the Prandtl-Reuss flow rules and linearly expanding the relation between stresses and strains, the following relation for the plastic strain increment can be derived

$$\Delta\varepsilon_c^{pl,t} = \frac{\varepsilon^{et} - \frac{2}{3}\frac{(1+\nu)\sigma_{eff}}{E}}{1 + \frac{2}{3}\frac{(1+\nu)}{E}\left(\frac{d\sigma_{eff}}{d\varepsilon_c^{pl,t}}\right)}   , \tag{14.8}$$

where ε^{et} is the effective modified total strain. Neglecting work hardening[7], the derivative at the denominator is zero, further simplifying the relation and entailing that σ_{eff} is bounded by σ_Y. Equation (14.8) must be coupled

---

[7]Including work hardening in the present model would not require substantial modifications, but presently, the lack of reliable data, justifies the simpler method.

. . . .

with flow rules based on strains, rather than stresses, in the form

$$
\begin{aligned}
\Delta\varepsilon_{c,r}^{pl} &= \frac{\Delta\varepsilon_c^{pl,t}}{3\varepsilon^{et}}(2\varepsilon_{c,r}^{'} - \varepsilon_{c,t}^{'} - \varepsilon_{c,a}^{'}) \quad, \\
\Delta\varepsilon_{c,t}^{pl} &= \frac{\Delta\varepsilon_c^{pl,t}}{3\varepsilon^{et}}(2\varepsilon_{c,t}^{'} - \varepsilon_{c,r}^{'} - \varepsilon_{c,a}^{'}) \quad, \\
\Delta\varepsilon_{c,a}^{pl} &= -(\Delta\varepsilon_{c,r} + \Delta\varepsilon_{c,t}) \quad.
\end{aligned}
\tag{14.9}
$$

The main advantage of the present approach is that strains are evaluated without passing through stresses and thus considerably speeding up convergence [78]; indeed, in the case of a flat stress-strain curve, small variations of stresses implies high variations of strains complicating convergence.
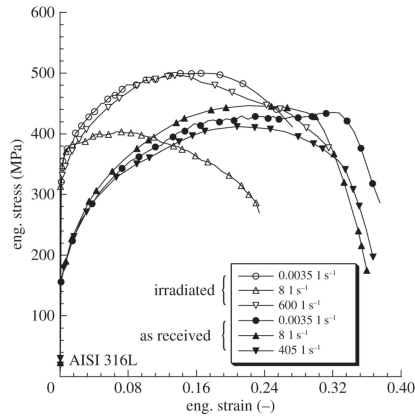
Figure 14.4: An example of stress-strain curves for the stainless steel AISI 316L as a function of strain rate and irradiation. Taken from [5].

Fuel

In the case of fuel strains (ε_f), equation (13.27) must be reformulated as

$$
\begin{aligned}
\varepsilon_{f,i} =&\varepsilon_{f,i}^{el} + \varepsilon_{f,i}^{th} + \varepsilon_{f,i}^{sw,g} + \varepsilon_{f,i}^{sw,s} + \varepsilon_{f,i}^{cr}+ \\
&\varepsilon_{f,i}^{hp} + \varepsilon_{f,i}^{pl} + \varepsilon_{f,i}^{re} + \varepsilon_{f,i}^{de} + \varepsilon_{f,i}^{crack} \quad i = r,t,a \quad,
\end{aligned}
\tag{14.10}
$$

where $\varepsilon_{f,i}^{hp}$ is the fuel hot-pressing strain, $\varepsilon_{f,i}^{re}$ is the fuel relocation strain, $\varepsilon_{f,i}^{de}$ is the fuel densification strain and $\varepsilon_{f,i}^{crack}$ is the fuel cracking strain. Due to the numerous phenomena involved and their intrinsic complexity, fuel mechanics is possibly the most strenuous field to model; to tackle the

....

problem, therefore, various simplifications have been put forward, in line with the overall impact on the temperature field (Table 13.4) and contact pressure.

Before arriving at an equation similar to (14.6) for the fuel, the terms in equation (14.10) that have been discarded or considerably simplified will be discussed.

Creep   Due to the high temperatures reached in the peak power pin, even the brittle ceramic fuel can exhibit high creep rates which are able to relax stresses so that the fuel pellet is almost stress-free during steady-state operations. Fuel creep acts in both relaxing PCMI and modifying the central void radius (and thus fuel temperature); the latter effect is linked to the former being the central void a sort of "mechanical sink" for contact-induced stresses.

Three main problems arises for this phenomenon:

- As for the clad, fuel creep depends on the stress state of the pellet creating a non-linearity in the mechanics loop; due to the high creep rates, especially in the central, hottest, part of the pellet, only implicit treatments are a viable option. To ensure numerical stability, however, the allowable creep in a time step must be substantially lower than the elastic strain [32] (see Section 14.13), implying that for increasingly higher creep rates, increasingly lower time steps have to be adopted; for typical fuel creep strain rates this results in unacceptably low times steps (i.e. lower than a millisecond), especially at BoL.

- The second point stems from the fact that the local stress state of the pellet is incredibly complex and subject to considerable uncertainties in general, but particularly for 1.5D codes. Relying on such stress state, therefore, does not guarantee an overall improvement.

- The third point concerns the possibility of exiting the small deformations assumption inherent in TEMIDE (see Section 14.3.3); for high creep strains, the central void deformation could be so high (i.e. greater than 10%) that linear approaches are not anymore applicable with risks of numerical divergence. In this situation, large-strains models have to be adopted [89], considerably complicating code structure and impairing calculation times.

For these reasons, and given the target uncertainty of around 35% for the fuel strain, creep has been neglected in the fuel mechanical analysis. As will be

. . . .

described in Section 14.3.4, a model to include creep in the evaluation of the contact pressure in case of PCMI has been devised so to cope with the target uncertainty of around 15% for the contact pressure; this means that the only missed phenomenon (among those affected by creep), compatibly with the guidelines of Table 13.12, is central the void closure and its consequent impact on the fuel temperature.

Hot pressing   When the fuel is subject to high temperatures and pressures a sintering process starts, in analogy with the one during pellet fabrication, which reduces the porosity until some minimum porosity is reached; this phenomenon is called hot pressing or stress-induced densification. The process is linked to the ability of the material to creep or plastify inside pores, thus reducing them and increasing fuel density [109].

This phenomenon is strictly linked with creep [48] and, having neglected the latter, it has also been discarded. Given that the main repercussion of hot pressing is, indeed, the porosity reduction and consequent power distribution distortion and thermal conductivity modification (similarly to restructuring), and given the fact that the latter phenomenon is believed to dominate from a time scale point of view, disregarding hot pressing seems an acceptable approximation.

Plasticity   For analogous motivations as those put forward in the creep discussion, the plastic strain has been neglected; given the high interaction with the uncertain stress field along with uncertainties surrounding the yield strength, especially at high temperatures, the approximation seems in line with the target uncertainty of 35%.

Cracking   In a way, cracking is the brittle analog of plasticity and, as such, is strongly interconnected with the stress field, besides being, inherently, a 3D phenomenon. Ceramic materials, like oxides, are, indeed, brittle at room temperature, meaning that if, locally, a stress is greater than the fracture strength - the same is true for the strains -, the material can crack; for increasing temperature this is true until the so called brittle-to-ductile transition temperature is reached, above which the material gains some ductility and plastic deformation becomes possible; this transition temperature varies with the strain rate, but is generally around half the oxide melting temperature [97].

Due to the strong radial thermal gradients in oxide pellets, in the peak power pin, stresses can be high enough to create cracks at the first ramp-

....

up to power - and possibly in all subsequent power cycling events - in the brittle region of the fuel, with a resulting situation of the kind reported in Figure 14.5. This can lead both to a faster gap closure, consequent to the increased thermal expansion driven by the hotter internal plastic core not restrained by the external, cracked region [96], and to locally enhanced stresses during PCMI near cracks surface in the case of power cycling [42].
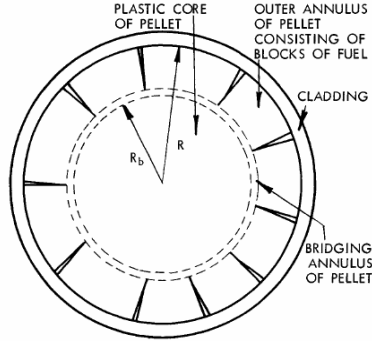
Figure 14.5: A simplified picture of the pellet state at full power. Taken from [42].

In [54], the attempt to model such a complex phenomenon in a 1.5D code has given rise to a modification of the pellet elastic constants (E_f and ν_f) so to reproduce the correct stress state after cracking while maintaining the isotropic nature of the fuel material; the crack strain is therefore not directly taken into account, but modeled via the following expressions:

$$
\begin{aligned}
E_f &\to E_f \left(\tfrac{2}{3}\right)^{N_{cr}} \quad, \\
\nu_f &\to \nu_f \left(\tfrac{1}{2}\right)^{N_{cr}} \quad,
\end{aligned}
\tag{14.11}
$$

where N_{cr} is the number of cracks which can be assumed either as a function of power or fixed at a constant values. This is a very rough model with feeble theoretical bases, but, nonetheless, it was proven to be adequate [62], particularly considering the impossibility of axially symmetric codes to tackle the phenomenon in its essence.

In the light of the above mentioned considerations, and related simplifications, the fuel strain can therefore be expressed as

$$
\begin{aligned}
\varepsilon_{f,i} =& \varepsilon_{f,i}^{el}(\overrightarrow{\sigma}) + \varepsilon_{f,i}^{th} + \varepsilon_{f,i}^{sw,g,t} + \Delta\varepsilon_{f,i}^{sw,g,t} + \varepsilon_{f,i}^{sw,s,t} + \\
& \Delta\varepsilon_{f,i}^{sw,s,t} + \varepsilon_{f,i}^{re,t} + \Delta\varepsilon_{f,i}^{re,t} + \varepsilon_{f,i}^{de,t} + \Delta\varepsilon_{f,i}^{de,t} \quad i = r, t, a \quad ,
\end{aligned}
\tag{14.12}
$$

....

where the same strain separation performed on equation (14.6) for the clad strains has been proposed for the fuel. In the following, each term, besides the thermo-elastic strains, will be described to outline the adopted approach in its modeling.

Gaseous FP swelling Due to the fission events the number of atoms inside the fuel changes, with a consequent variation in the pellet density; this phenomenon is known as swelling. From observations, it is now understood that swelling has two main contributors: solid fission product swelling and gaseous swelling. Concerning the latter, it originates from the ability of gaseous fission products to condensate in bubbles; given that preferential sites for bubbles growth are grain boundaries, since they are perfect sinks for mobile atoms or intra-granular bubbles, it is supposed that inter-granular bubbles are major contributors to the gaseous swelling; some role is also played by intra-granular bubbles which are, however, significantly smaller than their inter-granular counterpart and thus appointing only a limited contribution to the overall swelling [103].

For its very nature gaseous swelling is strongly connected with FGR implying that a balance between the two phenomena exists, indeed: on one hand, at high enough temperatures, the elevated atoms mobility causes a fast inter-granular bubbles inter-linkage leading to FGR in a very short amount of time and, therefore, limited bubble growth and swelling; on the other hand, at too low temperatures, mobility decreases so much that inter-granular bubbles growth rates become insignificant and swelling does accordingly. The critical region for gaseous swelling is, therefore, the one characterized by in-between temperatures, usually coinciding with the equiaxed region. All these aspects are included in models relying on bubbles pressure balances, like the one of equation 13.41, here reported as

$$\varepsilon_{f,i}^{sw,g,\infty} = \frac{mol_{ret}TR}{P_h + P_\gamma} = \frac{mol_g(1 - FGR)F_{intra}TR}{3(P_h + P_\gamma)} \quad , \quad (14.13)$$

where $\varepsilon_{f,i}^{sw,g,\infty}$ represents the equilibrium swelling strain, F_{intra} is a corrective term suggested in [7] and the factor 3 in the denominator is used to convert volumetric to linear strain under the isotropic swelling assumption. To avoid relying on the fuel stress state, P_h is taken equal to the negative of the pure elastic radial stress analytically computable from the pressure boundary conditions. To infer the needed $\Delta\varepsilon_{f,i}^{sw,g,t}$ from $\varepsilon_{f,i}^{sw,g,\infty}$ the further assumption of a creep-driven bubble relaxation towards equilibrium is introduced [7],

....

resulting in

$$\Delta\varepsilon_{f,i}^{sw,g,t} = (\varepsilon_{f,i}^{sw,g,\infty} - \varepsilon_{f,i}^{sw,g,t})(1 - e^{\dot{\varepsilon}_{f,i}^{cr}\Delta t}) \quad , \qquad (14.14)$$

where $\dot{\varepsilon}_{f,i}^{cr}$ is the creep rate. This model can be, in principle, applied to transient as well, so to tackle UTOP-like situations (see Section 13.4.2). If of interest, correlation-based approaches, like the one in [118] or [70], are also available in TEMIDE.

Finally, it is to be noted that the volumetric swelling is supposed to contribute to the gaseous part of the pellet porosity and is, therefore, added to the latter contributing to the thermal conductivity reduction, in sharp contrast to the restructuring process (see Section 14.9).

Solid FP swelling   The second form of swelling originates, as suggested by experimental evidence, from the difference, in density, of some of the FPs and the fuel atoms; performing a sum of all the fission products which stay in the fuel matrix for a period comparable to the pellet in-reactor lifetime, weighted by the corresponding fission yield, results in a value around 0.65 %/at.% for the volumetric strain. Such constant, averaged over the whole pellet life, can be decomposed like in equation (13.23) to make explicit the contribution of volatile FPs, like cesium, possibly affected by JOG formation.

Relocation   When a pellet cracks due to the stress distribution induced by thermal strains, a number of fragments is formed which are loosely coupled to each other and can move independently, to some degree, due to thermal cycling and fuel rod vibrations [62]. This gross outward movement of pellet fragments is called relocation and helps in substantially reducing the gap thickness as soon as full power is reached. Because the phenomenon is connected with the number of fragments, which is a function of pellet power, and to the gap size, which sets the upper bound of relocation (if there were no clad a cracked fuel column could not exist), many correlations developed in literature are functions of these two parameters (e.g. [12]).

For its very nature, relocation is important at BoL, but, in theory, could also play some role during PCMI; the fragmented fuel, under the restraining action of the clad, could compact itself, alleviating the mechanical action on the cladding. In TEMIDE, relocation is conservatively assumed zero when fuel and clad are in contact, with the same rationale used for fuel cracking being essentially a 3D phenomena; presently, therefore, any role in PCMI - which is, anyway, dominated by creep (at least in nominal conditions of the peak power pin) - is disregarded.

. . . .

Densification   The densification process of the fuel is dominated by restructuring, therefore, the calculation of the relative strain is postponed until the latter phenomenon is indirectly treated outside of the main loop (see Section 14.9).

14.3.2   Contact conditions

Contact between fuel and clad is assumed to occur when the fuel outer radius is higher than the clad inner one; once contact occurs, it can either be soft or hard depending on the relation between the contact (P_{con}) and plenum (P_p) pressures:

- if $P_{con} < P_p$, contact is supposed to be soft, meaning that fuel and clad are not axially locked, but relative slip is allowed;

- if, on the other hand, $P_{con} > P_p$, fuel and clad are considered axially locked and expand, axially, in a homologous way;

- finally, if $P_{con} < 0$, thus implying a separation of the component in contact, fuel and clad are supposed to detach from each another.

The distinction between soft and hard contact is rather artificial because it should be based on a friction force balance, possibly including other axial slices; for the present purposes, however, it is deemed sufficient to target the 15% error on the evaluation of P_{con}. Due to the approximate nature of the soft/hard differentiation criteria, contact pressure can slightly jump passing from a condition to the other; this stems from the further contribution originating from the imposed axial locking which can increase or decrease the contact pressure depending on the relative fuel-clad movement.

14.3.3   Matrix build-up and solution scheme

Once the strains and contact conditions are known, the system of equations reported in Section 13.3.1, along with the appropriate boundary conditions, can be solved for the stresses under the following hypotheses:

- axially symmetric conditions;

- small deformations assumption, implying linear relations between deformations and strains;

- plain strains approximation, so to have radially constant axial strains;

- perfect plasticity for the cladding;

. . . .

- mechanical decoupling of the various axial slices so that frictions originating from PCMI at different elevations are neglected.

The adopted numerical approach takes the moves from the one reported in [80] which, after a finite-differences discretization of the system and some matrix manipulations, is able to relate the stress state of any point to the boundary conditions like

$$\overrightarrow{\sigma}_{i+1} = \boldsymbol{A}_i \overrightarrow{\sigma}_1 + \overrightarrow{B}_i \quad i = 1, N-1 \quad , \tag{14.15}$$

where N is the number of points of the discretization, $\overrightarrow{\sigma}_{i+1}$ is the principal stress vector (i.e. radial, tangential and axial components) at point $i+1$, $\overrightarrow{\sigma}_1$ is the boundary conditions stress vector, depending on the contact condition, while $\boldsymbol{A}_i$ and $\overrightarrow{B}_i$ are link matrices and vectors based on the system geometry, material properties and strains (via the constitutive equations (14.6) and (14.12)); $\overrightarrow{\sigma}_1$ is found by solving the discrete version of the appropriate boundary conditions in the form

$$\boldsymbol{C} \overrightarrow{\sigma}_1 = \overrightarrow{D} \quad , \tag{14.16}$$

where $\boldsymbol{C}$ and $\overrightarrow{D}$ are boundary conditions matrix and vectors. The main advantage of this approach descends from avoiding to solve all the points together, in one big $3N \times 3N$ sparse matrix, in favor of one 3×3[8] system inversion, which can be done analytically, and a series of $(N-1)$ 3×3 multiplications (i.e. the dimensions of the link matrix).

No contact

When the fuel and clad are not in contact, they represent two completely decoupled systems from the mechanical point of view; the boundary conditions of equation (13.30) are the correct set for both components where, only in the case of a solid pellet, the first equation of (13.30) must be substituted by

$$\sigma_t(r_{fi}) = \sigma_r(r_{fi}) \quad . \tag{14.17}$$

Thanks to equations of the form of (14.15), the stress of any point can be related to the innermost point of the fuel/clad and the boundary conditions put in the form of equation (14.16); when the boundary conditions have been solved, the stress at the innermost node ($\overrightarrow{\sigma}_1$) is known and the stress $\overrightarrow{\sigma}_{i+1}$ at any point can be calculated with the aid of equations of the form of (14.15).

---

[8]In the case of soft contact the boundary matrices are 5×5

....

Soft contact

When soft contact is detected, the appropriate set of boundary conditions is

$$
\begin{aligned}
&\sigma_r(r_{fi}) = -P_i \\
&\sigma_r(r_{co}) = -P_o \\
&2\pi \int_{r_{ci}}^{r_{co}} \sigma_a(r)r\,dr = F_{a,c} \\
&2\pi \int_{r_{fi}}^{r_{fo}} \sigma_a(r)r\,dr = F_{a,f} \\
&r_{fo} = r_{ci},
\end{aligned}
\tag{14.18}
$$

where the last equation represents continuity at the fuel-clad interface. For a solid pellet, the first equation of (14.18) must be substituted by equation (14.17).

Since there are 5 boundary conditions, the matrix C is a 5×5 and its inversion is performed via a LAPACK routine. From the solution of the boundary conditions, the stress state at the innermost node of the fuel is known and the stress at any point calculated; requiring radial stress continuity between fuel and clad along with the other two stress components from the boundary conditions solution, the stress state at the innermost clad point is known and can, therefore, be calculated accordingly for all the other points.

Hard contact

When hard contact is detected, the appropriate set of boundary conditions is identical to the no-contact case, where the fuel/clad system is considered a single component; the main difference relative to the no-contact situation is that, to build the link matrix and vector, the continuity condition at the interface is called upon both in the radial and axial directions. The solution scheme is therefore: the 3×3 boundary conditions system is analytically solved and so the stress state at the innermost node of the fuel is available; recursively applying equations of the form (14.15), stresses at any point of the fuel and clad can be computed.

14.3.4   Contact pressure creep correction

As stated in Section 14.3.1, fuel creep has been neglected in the mechanical analysis, but it is believed to be an important contributor to the definition of the contact pressure, especially in the hottest part of the pin [98]. Given the importance of the contact pressure in the clad stress level definition, as discussed in Section 13.6, a model to include, *a posteriori* of the stress calculation, a correction accounting for fuel creep has been conceived.

. . . .

This model is based on the analytical solution proposed in [60] based upon a linear stress dependence of creep; the latter hypothesis is not valid at particularly high temperatures, but given its role in correcting the contact pressure at the periphery of the pellet - where temperatures are not particularly high -, it is believed to be adequate for fuel creep as more generally discussed in [62]. The contact pressure can then be expressed as

$$P_{con}(t) = P_{con}^*(t) + \int_{t_{con}}^{t} e^{-\lambda(t-\tau)} \lambda (P_{con}^\infty(\tau) - P_{con}^*(\tau)) d\tau \quad , \qquad (14.19)$$

where P_{con}^* is the contact pressure without fuel creep, t_{con} is the time at which contact started, λ is a relaxation constant while P_{con}^∞ is the asymptotic contact pressure. The exact expression of λ and P_{con}^∞ is not reported here and can be found in [60]; it is only worth mentioning that the former depends on the geometry, elastic constants and creep rate, while the latter, in addition to the parameters already mentioned, depends on the pressure boundary conditions.

Equation (14.19) has all the features expected from creep, starting with its relaxing effect which reduces the pressure, theoretically, to the value P_{con}^∞ along with the "fading memory" characteristic, thanks to the convolution integral, with more recent pressures weighted more heavily than older ones. In TEMIDE, equation (14.19) has been discretized as

$$P_{con} = P_{con}^\infty + (P_{con}^* - P_{con}^\infty) e^{-\lambda \Delta t} \quad , \qquad (14.20)$$

where P_{con}^* must now be interpreted as the pressure in the absence of creep in the time step Δt.

The procedure starts, therefore, with the calculation of P_{con}^* which results from the system solution described in Section 14.3.3; the parameters λ and P_{con}^∞ are, conservatively, calculated with properties (e.g. elastic and creep constants) based on the point of contact (e.g. the outer and inner radii of the fuel and clad respectively). Equation 14.20 is applied to find P_{con} and a fictitious strain ε_{con} calculated as

$$\varepsilon_{con}^{j+1} = \varepsilon_{con}^j + \left(\frac{d\varepsilon_{con}}{dP_{con}}\right)(P_{con}^{j+1} - P_{con}^j) \quad , \qquad (14.21)$$

where j is the mechanical loop iteration index. The derivative $\frac{d\varepsilon_{con}}{dP_{con}}$ is updated as

$$\frac{d\varepsilon_{con}}{dP_{con}} = \frac{\varepsilon_{con}^j - \varepsilon_{con}^{j-1}}{P_{con}^j - P_{con}^{j-1}} \quad . \qquad (14.22)$$

....

The mechanical loop then starts again with the strains evaluation and subsequent link and boundary conditions matrices construction where, now, in the continuity condition, in the radial direction, ε_{con} is present, with the purpose of modifying the contact pressure P_{con}^* so to match the creep-relaxed value P_{con}; this strain is fictitious because its purpose is just to allow for contact pressure adjustments. All the process is repeated until convergence is achieved as described in Section 14.3.5.

The detailed procedure which is followed, therefore, is:

1. calculate the contact pressure in the absence of fuel creep in the time step;

2. correct the pressure for the relaxation effect with equation (14.20);

3. calculate the fictitious strain with equation (14.21);

4. update the derivative;

5. solve the stress system with the new fictitious strain;

6. repeat steps 3. to 5. until convergence.

14.3.5 Convergence check

The mechanical loop is believed to be converged when relative errors on stresses and total strains are below threshold values; moreover, a check on the relative error on the fictitious strain ε_{con} is performed so to guarantee convergence of the pressure correction procedure.

Numerical provisions have also been taken to assure a smooth convergence like: under-relaxation in the case of excessive creep in the first iteration, or the use of the previous time step stresses when starting the mechanical analysis for the the new time step so to assure the closest possible mechanical state to the expected one, and thus significantly easing convergence. The described procedure converges well in all the tested situations encompassing credible scenarios, falling inside TEMIDE anticipated validity domain, also thanks to time step control procedure described in Section 14.13.

14.3.6 Deformations

Once the mechanical loop has converged, the new deformed geometry can be calculated based on the small strains approximation (see Section 14.3.3)

. . . .

as

$$u_i = \varepsilon_t r_i \quad ,$$
$$dw_k = \varepsilon_a \Delta z_k \quad , \tag{14.23}$$

where u_i is the radial displacement of point i, dw_k is the axial displacement of slice k (radially constant from the plain strain assumption) while ε_t and ε_a are the total tangential and axial strains respectively, either of the fuel (equation (14.12)) or the cladding (equation (14.6)). The deformed geometry is finally deduced from applying the displacements to the as-input geometry as

$$r_i = r_{i,0} + u_i \quad ,$$
$$\Delta z_k = \Delta z_{k,0} + dw_k \quad , \tag{14.24}$$

where the subscript 0 indicates as-input values. Once the new dimensions of the central void and gap are known the thermal field can be calculated again until the gap loop converges.

14.4   Failure criteria

The failure criteria are, clearly, related to the fuel temperature and clad stresses and strains; in the following, the main options currently implemented in TEMIDE are discussed.

14.4.1   Fuel temperature

The only discriminant available for the fuel temperature is melting; this can be translated in

$$f_{melt} > f_{failure} \quad , \tag{14.25}$$

where f_{melt} is the molten area fraction (of a generic slice k) and $f_{failure}$ is the failure fraction above which the calculation should stop. Given the intended use of TEMIDE (see Section 12.1) the recommended value of $f_{failure}$ is zero, implying the calculation should interrupt as soon as melting is detected.

14.4.2   Clad mechanic

Regarding the clad mechanics, numerous criteria have been proposed for detecting cladding failure either based on stresses or strains. In TEMIDE a variety of possibilities has been implemented so to give the user a broad spectrum of choices, spanning both short - mainly transients - and long term requirements, namely:

- short-term requirements:

. . . .

> – based on primary stress
>
> – based on plastic strain or **C**umulative **D**amage **F**unction (CDF)

- long-term requirements:

> – based on time-to-rupture or CDF.

This list is far from being comprehensive, but should be broad enough for TEMIDE intended applications[9].

Short-term failure criteria

Based on stress   Following the suggestion in [136], the stress-based failure condition regarding the primary hoop stress, σ_t, (i.e. in the tangential direction) can be expressed as

$$\sigma_t > MIN(f_Y \sigma_Y, f_U \sigma_U) \tag{14.26}$$

where σ_U is the ultimate tensile strength while f_Y and f_U are safety factors for the yield and ultimate tensile strength respectively. The values of the safety factors depend on the particular failure probability target of the design, the envisaged role of the reactor under considerations and the experimental values obtained, for the specific steel of interest, during the qualification campaign. This criterion is mostly related to elastic-type analysis being based on primary stresses.

Based on plastic strain   Criteria based on plastic strain are formally linked to the ones based on stresses, as reported in Figure 14.6, but have the advantage of directly involving the (approximate) cladding inelastic analysis in TEMIDE. The criterion reads

$$\varepsilon^p_{eff} > \varepsilon^p_{failure} \quad , \tag{14.27}$$

where ε^p_{eff} and $\varepsilon^p_{failure}$ are the calculated and allowable effective plastic strains respectively; the generic effective strain is defined as

$$\varepsilon_{eff} = \frac{\sqrt{2}}{3}\sqrt{(\varepsilon^2_r - \varepsilon^2_t)^2 + (\varepsilon^2_r - \varepsilon^2_a)^2 + (\varepsilon^2_t - \varepsilon^2_a)^2} \quad . \tag{14.28}$$

The plastic strain limitation has been categorized, for convenience, as a short term requirement, although a long-term version could also be used. Given

---

[9]Being failure criteria essentially post-processing actions of calculation data, any additional one can be easily implemented in TEMIDE.

. . . .
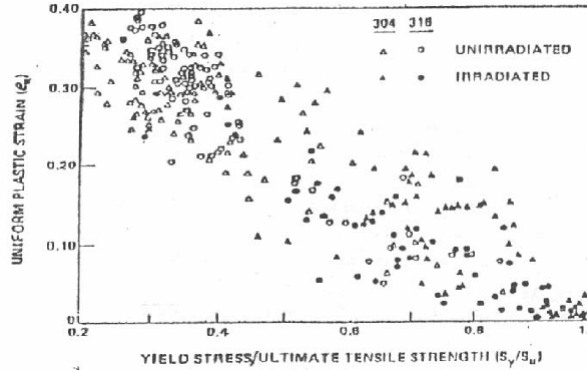
Figure 14.6: Approximate relation between uniform elongation and the $\frac{\sigma_Y}{\sigma_U}$ ratio. Taken from [107].

TEMIDE's application domain is, however, not expected for plasticity to play a considerable role during normal operation and so the short-term character should be maintained.

The same criterion can be expressed in the form of a CDF as

$$CDF = \sum \frac{\Delta \varepsilon_{eff}^p}{\varepsilon_{failure}^p} > 1 \quad , \tag{14.29}$$

where the sum spans all the simulated time steps. The advantage of the CDF is that it can, naturally, take into account criteria based on a varying $\varepsilon_{failure}^p$ (e.g. as a function of temperature or irradiation).

Long-term failure

Based on time-to-rupture   For the long-term resistance of the cladding, criteria based on the time-to-rupture $t_{rupture}$ due to creep action have been developed [139], they can be stated as

$$CDF = \sum \frac{\Delta t}{t_{rupture}} > 1 \quad . \tag{14.30}$$

The CDF is the natural definition for this phenomenon, since $t_{rupture}$ strongly depends on stress and temperature (being creep-related). This criterion is particularly important for ULOF conditions so to guarantee the target grace time before operators' intervention as discussed in 12.1.

. . . .

Finally, the time-to-rupture and plastic criteria could be combined, as previously hinted, in a single expression as

$$CDF = \sum \left(\frac{\Delta t}{t_{rupture}} + \frac{\Delta \varepsilon^p_{eff}}{\varepsilon^p_{failure}} \right) > 1 \quad . \tag{14.31}$$

14.5   Grain growth

Grain growth stems from the tendency of bigger grains to grow further, at the expenses of smaller ones, in virtue of atoms thermal agitation and energy minimization logics. The grain growth process is thus strongly linked to the thermal field of the pellet.

As already stated, however, grain growth has a minor role in TEMIDE, slightly influencing the creep rate of the fuel[10]. The latter, indeed, comes into play only in the contact pressure model, where creep is evaluated at the outer fuel radius, a position where grain growth is negligible.

Broadly speaking, FGR, at a microscopic level, depends on grains size, roughly deciding the length of the diffusion path necessary before reaching the grain boundary; moreover, the sweeping effect brought about by the growing grains can influence the inter-granulars bubbles coalescence rates and thus FGR. As will be detailed in Section 14.10, however, the adopted FGR model does not rely on grains size, being constructed at a pin level and so, inherently including it. The latter point, is actually an advantage, from the DOC point of view, because grain size is a very specific, fabrication dependent, parameter not really known at the early design stages; relying as little as possible on unknown, microscopically dependent, elements is an added value for a DOC.

For these reasons, grain growth can be either disregarded or simply modeled as in [97]:

$$D_g^n = D_{g0}^n + Ke^{-\frac{Q}{RT}}t \quad , \tag{14.32}$$

where D_g is the grain diameter, D_{g0} is the as-fabricated grain diameter while Q is a characteristic activation energy and K and n are model parameters.

14.6   Corrosion

Corrosion phenomena act either to reduce the cladding mechanical resistance, via changes of its micro-structure, or to reduce the available thickness

---

[10]Creep of the Nabarro-Herring type is, indeed, inversely proportional to grain surface, and so, to grain diameter [96].

. . . .

able to withstand loadings (or both). Being physically adjacent to the fuel and coolant, the cladding can suffer corrosion from both. As seen in Section 13.6, fuel corrosion is more important than the coolant one[11] for what concerns the cladding stresses ans strains; this is mainly due to the greater cladding wasted thickness fuel-side. Finally, the oxide scale forming on the cladding surface has a lower thermal conductivity than the steel substrate, increasing the temperature at the outer clad surface.

14.6.1 Coolant

Due to the solubility of some of the cladding constituents (e.g. nickel) in lead or lead-bismuth, and due to the presence of a thermal gradient inside the reactor primary circuit, the cladding metal can be subject to corrosion. Corrosion dynamics is strongly related to temperature and the time scale of the phenomenon becomes comparable to in-reactor service life above 400 °C. To limit corrosion effects, an accurate control of the coolant chemistry (notably to what concerns oxygen) is therefore necessary; a viable range for the oxygen concentration - depending on the reference temperatures - is typically identified, the limits being set: for the upper limit, so to prohibit the formation of lead oxide particles, which could cause pipe and FA plugging (see Section 3.4.1); for the lower limit, so to favor the formation of an oxide layer which limits the diffusion rate of the clad constituents. Such a stringent oxygen control is quite a challenging task due to the size of the primary circuit and possible stratification and stagnation phenomena; moreover, even if accomplished, standard austenitic stainless steels would anyway not survive long for temperature higher than 500 °C. Various solutions to this problem have been proposed, going from silicon/aluminum doping to allow for the formation of a stable silica oxide layer, to protective superficial coating based on aluminium alloys.

In TEMIDE, the effect of coating is not considered because it will depend on the specific design choice and R&D development in the near future; therefore, the clad is supposed to form *in situ* a protective oxide layer which affects the clad outer temperature and its thickness. Moreover, due to the slow dynamics of the reference transients, coolant corrosion is neglected in such events; it does only contribute to define the initial state of the system.

---

[11]True under the hypothesis that protective measures have been taken so to avoid direct contact between HLM and clad, thereby protecting the micro-structure of the latter.

. . . .

Clad outer temperature

With the aid of experimental correlations for the oxide scale growth rate, on the particular steel adopted, as functions of temperature and oxygen concentrations, like the one proposed in [140], the oxide scale thickness, s_{ox}, can be calculated and the clad outer temperature, during the thermal field calculation phase of Section 14.2, corrected with the term

$$\Delta T_{ox} = \frac{q'' r_{co}}{k_{ox}} \ln \left(1 + \frac{s_{ox}}{r_{co}} \right) \quad , \tag{14.33}$$

as

$$T_{co} \to T_{co} + \Delta T_{ox} \quad . \tag{14.34}$$

Clad thickness

The oxide grows at the expenses of the cladding mass (and volume) and so reducing its thickness, s_c, with time, namely

$$s_c \to s_c - s_{ox}/2.07 \quad , \tag{14.35}$$

where 2.07 is the Pilling-Bedworth ratio [3]. The cladding outer radius is therefore simply reduced accordingly.

14.6.2 Fuel

One of the possible life limiting factors for oxide-fueled pins are the chemical interactions that develop at the fuel cladding interface. They are the result of the increased oxygen activity with BU due to the oxidizing nature of the fission event which produces FPs not able to consume the just liberated oxygen atoms; given the great number of species present inside the cladding, with increasing oxygen activity, reaction between the FPs - in particular cesium, tellurium and iodine - and the cladding constituents becomes possible giving rise to what are called **F**uel-**C**lad **C**hemical **I**nteractions (FCCI) [96]. As already introduced, one of the main macroscopic expressions of FCCI is the internal clad corrosion due to inter-granular or matrix attack by FPs, which limits the clad thickness actually able to sustain stresses [43].

In analogy with coolant corrosion, also the fuel one is neglected during transients.

....

Clad wastage

The reduction of the available clad thickness due to FCCI can be expressed, similarly to the corrosion one, as

$$s_c \rightarrow s_c - s_w \quad , \tag{14.36}$$

where the wastage thickness, s_w, is calculated based on correlations like the ones reported in [138]. To simulate the reduced thickness, the clad inner radius is increased by s_w; because, differently from corrosion, the clad mass is not supposed to change, but only to lose mechanical capabilities, in order to preserve the gap thickness two geometries are used: one for the thermal field and one for the mechanical analysis. They are, *de facto*, identical but for the inner clad radius, and are related by

$$r_{ci}^{thermal} = r_{ci}^{mech}(1 - \varepsilon_w) \quad , \tag{14.37}$$

where $r_{ci}^{thermal}$ and r_{ci}^{mech} are the thermal and mechanical fields clad inner radii, while ε_w is the fictitious wastage strain, calculated incrementally as

$$\Delta\varepsilon_w^t = \frac{r_{ci}^{mech,t+\Delta t} - r_{ci}^{mech,t}}{r_{ci}^{mech,t+\Delta t}} \quad , \tag{14.38}$$

and

$$\varepsilon_w^{t+\Delta t} = \varepsilon_w^t + \Delta\varepsilon_w^t \quad , \tag{14.39}$$

where $\Delta\varepsilon_w^t$ is the strain increment in the time step Δt. The strain is labeled "fictitious" since it does not enter, directly, in the mechanical analysis (i.e. equation (14.6)), being just used to retrieve the correct gap thickness. Finally, to preserve the strains distribution and gradients inside the clad, a linear interpolation is performed, for the strains and temperature, between the thermal and mechanical inner radii. The mentioned interpolation is performed incrementally, meaning that the last available r_{ci}^{mech} (i.e. $r_{ci}^{mech,t}$) is used as starting point; this permits to restrict the interpolation distance to $r_{ci}^{mech,t+\Delta t} - r_{ci}^{mech,t}$ which is much lower then $r_{ci}^{mech,t+\Delta t} - r_{ci}^{thermal}$ assuring high precision of the procedure. It has been found, indeed, that the proposed linear interpolation scheme suffices in all the investigated cases, also thanks to the generally smooth behavior of clad strains[12].

---

[12]The only exception is, possibly, the plastic strain, not relevant, however, for nominal conditions; it has, nonetheless, been found that also this strain is well interpolated by this incremental procedure.

. . . .
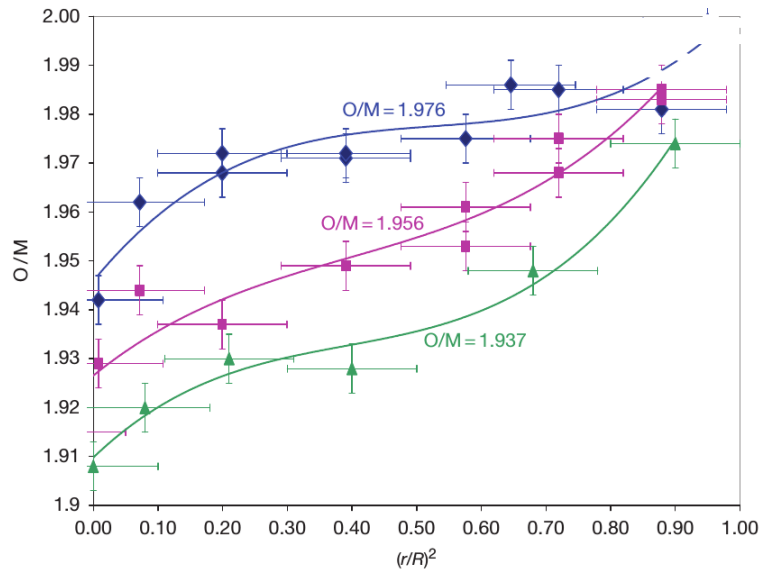
Figure 14.7: Typical O/M radial distribution for a hypostoichiometric MOX pellet. Taken from [47].

14.7   O/M change and redistribution

As introduced in Section 14.6.2, fissions are oxidizing events, implying an increase in the average O/M ratio as BU progresses; moreover, similarly to plutonium, the oxygen redistributes radially across the pellet. Conversely from oxygen, however, the direction of plutonium migration is inward: oxygen, indeed, actually moves down the temperature gradient[13] thus increasing the concentration at the cold periphery and, contextually, reducing it at the hotter inner part (see Figure 14.7). The mechanisms behind this redistribution process are not well understood, but it seems that solid-state oxygen diffusion is the dominant contributor for hypostoichiometric fuels [59].

   Due to the dependence of the fuel thermal conductivity on the O/M, its change and redistribution affect the thermal field[14]; in Section 13.6, it has been shown the low impact of both the average and distribution changes of

---

[13]This is true for hypostoichiometric pellets; the opposite would hold for hyperstoichiometries. Since the interest in FR fuels is more on the hypostoichiometric side, to reduce FCCI, only the latter will be discussed.

[14]Since diffusion properties of other species can depend on the local O/M ratio, nonlinear interactions could be generated, but they are assumed to be a second order effect if compared to the direct impact on the thermal conductivity.

. . . .

the O/M ratio and so, they have been modeled, accordingly, in TEMIDE.

14.7.1   Average value change

The average O/M can, in principle, be found from a charge balance of the fuel oxide phase along with a partitioning balance of the molybdenum between the metallic and oxide phases [96]; due to the target uncertainty of 40% (see Table 13.12), however, a simpler approach has been preferred. Given that $x = 2-\text{O/M}$ decreases around 0.003-0.005 per at.% of BU [47], the average pellet O/M (or its complement to 2) is found as

$$x_{ave}^{t+\Delta t} = x_{ave}^{t} - C\Delta(BU) \quad , \tag{14.40}$$

where the subscript *ave* indicates the average pellet value and C is a number between 0.003-0.005 per at.% of BU.

14.7.2   Redistribution

The solution of the oxygen redistribution problem should pass through an equation similar to (14.47), but, given the target 50% error, a more appropriate approach has been used, avoiding to directly solve a partial differential equation; the model proposed in [59] has therefore been adopted. The main rationale behind the model is that the deviation from stoichiometry of two different points can be expressed as

$$\frac{x_i}{x_{i+1}} = e^{\left(\frac{Q_{ox}}{R}\left(\frac{1}{T_i} - \frac{1}{T_{i+1}}\right)\right)} \quad , \tag{14.41}$$

where Q_{ox} is a characteristic heat of transport depending on the average O/M and, possibly, the plutonium enrichment. Having the possibility of relating any two points and knowing that the average value is preserved in the redistribution process, the correct x distribution can be, iteratively, found as depicted in Figure 14.8.

The scheme starts with the calculation of the characteristic time for oxygen migration, τ_{ox}, recommended in [61], as

$$\tau_{ox} = \frac{r_{fo}^2 - r_{fi}^2}{17.2D_{ox}} \quad , \tag{14.42}$$

where D_{ox} is the oxygen diffusion coefficient; the use of τ_{ox} permits to include the transient characteristic of the phenomenon, without increasing model
....
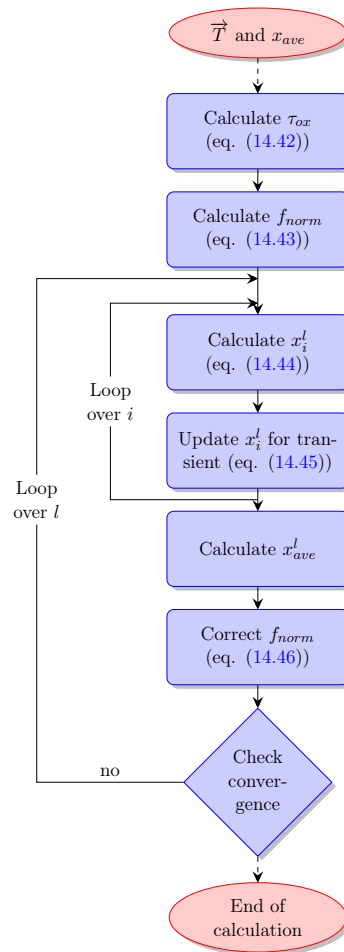
Figure 14.8: Flow diagram of TEMIDE oxygen redistribution calculation.

complexity, computational burden or running times, as will be explained below. The calculation of the normalization factor, f_{norm}, follows as

$$f_{norm} = \frac{x_{ave}}{\int e^{\left(\frac{Q_{ox}}{RT_i}\right)} dr} \quad .$$

(14.43)

The purpose of f_{norm} is to scale the x distribution so to preserve the average value x_{max}. After the initialization part, the iterative loop can start with the calculation of x at the points i at iteration l as

$$x_i^l = f_{norm} e^{\left(\frac{Q_{ox}}{RT_i}\right)} \quad ,$$

(14.44)

. . . .

corrected for transient effects as

$$x_i^l \to x_i^l + (x_i^t - x_i^l)e^{\left(-\frac{\Delta t}{\tau_{ox}}\right)} \quad , \tag{14.45}$$

where x_i^t is the deviation from stoichiometry at point i of the previous time step.

When all the fuel mesh points have been evaluated, the average can be found and compared to the target one, so to correct the normalization factor as

$$f_{norm} \to f_{norm}\frac{x_{ave}}{x_{ave}^l} \quad , \tag{14.46}$$

where x_{ave}^l is the calculated average value at iteration l. The new distribution over all the points i can be computed again, until convergence is achieved; to reach the latter, two criteria are used:

- the absolute difference between two $x_i^{l+1} - x_i^l$ at all the points i, and

- the absolute difference between $x_{ave} - x_{ave}^l$

must be below some threshold value. The last condition is important only for average O/M close to perfect stoichiometry, $x_{ave} \to 0$ so to smoothly translate to the state with a zero x_{ave} and so zero redistribution.

This procedure has been found to quickly converge (i.e. less than 10 iterations or even faster) especially after major restructuring has taken place.

14.8   Plutonium redistribution

As already discussed in Section 13.2.1, plutonium redistributes, radially, under the action of a temperature gradient or of pores movement; in Table 13.12 the importance of this phenomenon, inside the foreseen TEMIDE application domain, has been outlined and, consequently, a proper model implemented, following the derived guideline.

Similarly to the O/M ratio, also the plutonium average value in the pellet changes as a consequence of the fission events in proportion to its concentration and absorption cross-section; in TEMIDE, however, this plutonium depletion has been neglected in virtue of the fact that it is only the relative distribution that influences the power density radial profile (see equation (13.3)). The absolute concentration of plutonium, indeed, has not been found to significantly modify the fuel thermal conductivity, inside the typical enrichment's range of FRs [105], nor the melting temperature [97], as historically believed.

. . . .

14.8.1   Model

The model presented in [87] has been implemented, but neglecting the restructuring contribution to the overall redistribution, since, as discussed in Section 13.2.1, it does not significantly influence EoL which is the moment of interest - being the point of maximum importance - for this phenomenon.

It is also worth noticing that, as discussed in Section 13.4, the time scale of plutonium migration is higher than the majority of the other phenomena involving the fuel, meaning that the time step is actually much lower than the plutonium characteristic diffusion time (see Section 14.13); this can be exploited to further reduce the computational burden of solving equation (14.47). Instead of calculating the amount of plutonium diffusion at each time step, the radial profile can be updated only when

$$t_{Pu} = \sum \left(\frac{\Delta t}{\tau_T} \right) > F \quad , \tag{14.47}$$

where t_{Pu} is the normalized time relative to the plutonium time constant τ_T defined in equation (13.34) or, in analogy with the O/M redistribution, as in equation (14.42), and F is a user defined fraction; after the plutonium calculation, t_{Pu} is re-initialized to zero and the process can be repeated again. It has been found that a good compromise for F can be 0.01 with a slight reduction of (TEMIDE overall) running times without impairing results.

Given the slow dynamics, plutonium migration is not accounted for during transients [15].

14.9   Restructuring

Porosity migration brings an important contribution to the fuel pin thermo-mechanics as visible in Figure 13.35 and discussed in Section 13.2.2; it modifies the power radial profile, the porosity level - and so the thermal conductivity - and influences the size of the central void, significantly perturbing the temperature field. The steps involved in the restructuring model are schematically reported Figure 14.9.

The restructuring routine starts with the calculation of the radii and areas of the unrestructured, equiaxed and columnar regions (see Section 14.9.1); then, the new porosity distribution and the consequent densification process are evaluated with either a simple three zones model or a more complete solution of the porosity migration equations relying on pores velocity (see

---

[15]This will happen automatically if the t_{Pu} criterion is used.

. . . .
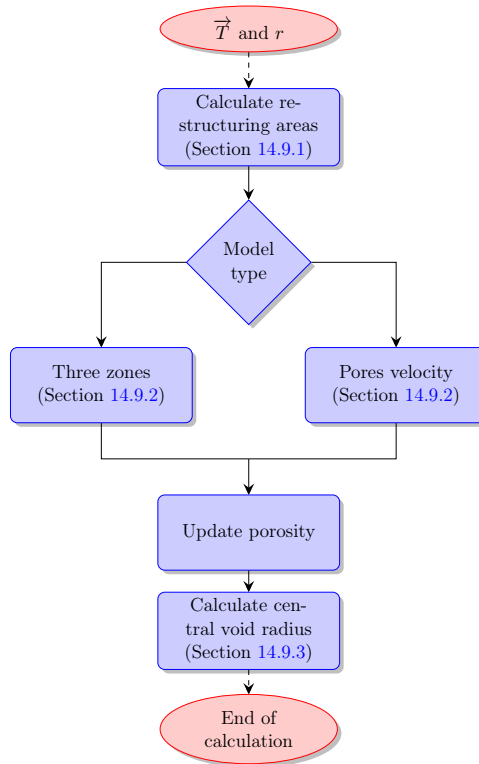
Figure 14.9: Flow diagram of TEMIDE restructuring calculation.

Section 14.9.2). Whatever the model, the pellet porosity is updated and the new central void radius calculated (see Section 14.9.3).

For what pertains to transient conditions, the restructuring dynamics has higher time scales than the reference UTOP and so the phenomenon can be safely neglected; if, however, the necessity to size its impact arises, the use of the pores velocity-based models is recommended.

In the following, details on each of the mentioned steps are given.

14.9.1   Restructuring area

The first step in the restructuring routine is the evaluation of the radii bounding the unrestructured, equiaxed and columnar regions along with their respective areas; they are needed input in the three zones model for fuel densification and for the FGR model (see Section 14.10). While various techniques have been proposed for discriminating the equiaxed region based on grain growth or the columnar zone based on the porosity change [7], they

. . . .

are all methods that, ultimately, depend on temperature; for this reason, in TEMIDE, only temperature is used for evaluating the regions boundaries (i.e. T_{eq} and T_{col}) with equations similar to (13.45).

14.9.2 Densification

The core of the restructuring model is the calculation of the porosity distribution evolution and consequent fuel densification. In TEMIDE two routes are possible: a simple three zones model or a more detail solution based on the pores migration velocity involving the integration of the relative conservation equation. Both models act, exclusively, on the sintered porosity portion of the total porosity, meaning that the fraction descending from bubbles due to gaseous swelling is not supposed to migrate (i.e. bubbles diffusion is neglected)[16].

Three zones model

Given the importance of restructuring, simple three zones models could be considered too approximate to reach the target accuracy regarding the porosity distribution; a suitably developed model, however, can have its own merits, thanks to the intrinsic simplicity. Starting from the region boundaries, available from Section 14.9.1, and given the fact that the unrestructured region is, by definition, unaffected and that the equiaxed region is considered as an average between the unrestructured and columnar zones, the porosity of the latter is the only quantity that needs to be evaluated; the accuracy of the model, therefore, heavily relies on the method used in its assessment. Fortunately, the target accuracy on the columnar porosity is quite low (see Table 13.12), allowing simple models to be viable[17]. To this regard, correlations that express the columnar porosity reduction as a function of BU can be used, like the on in [52].

An alternative method could be to calculate the zones porosity based on pores velocity, effectively integrating the porosity conservation equation over the three regions; this requires a suitably defined average velocity able to reproduce the correct zone average porosity. Such a model has not been implemented, yet, in TEMIDE; it is, however, an example of what should represent a good compromise between numerical efforts and accuracy.

---

[16]Cracks could be another source of internal porosity, but they are neglected due to the difficulties of systematically predicting cracking for a 1.5D code as discussed in Section 14.3.1.

[17]It seems, indeed, that a higher importance is allocated to the columnar region boundary rather than to the porosity.

. . . .

Pore velocity-based model

The more physically complete model based on the conservation equation for the sintered porosity, Po_{sin}, has also been implemented; the latter has the following form

$$\frac{\partial Po_{sin}}{\partial t} = \frac{1}{r}\frac{\partial}{\partial r}(rv_p Po_{sin}) \quad , \tag{14.48}$$

where v_p is the pores migration velocity. Employing a (forward) finite-differences discretization, equation (14.48) can be written as

$$\begin{aligned}
Po_{sin,i}^{t+\Delta t} = Po_{sin,i}^t + 2\Delta t &\left(\frac{(Po_{sin,i+1}^t - Po_{sin,min})v_{p,i+1}r_{i+1}}{r_{i+1}^2 - r_i^2} - \right. \\
&\left. \frac{(Po_{sin,i}^t - Po_{sin,min})v_{p,i}r_i}{r_{i+1}^2 - r_i^2} \right) \quad ,
\end{aligned} \tag{14.49}$$

where $Po_{sin,i}^{t+\Delta t}$ and $Po_{sin,i}^t$ are the sintered porosities at point i after and before the time step respectively, $v_{p,i}$ is the pores velocity at point i while $Po_{sin,min}$ is the minimum allowable sintered porosity in the pellet to take into account trapping effects by lattice defects. The velocity v_p, typically depending on temperature, temperature gradients and, possibly, O/M ratio can be retrieved from correlations like the ones reported in [96],[59] or [133].

It can be seen from equation (14.49) that the adopted numerical approach is completely explicit since, for updating the porosity, only values of the previous time step are adopted (the geometry and temperature are, however, the ones from the current time step); to keep numerical precision to acceptable levels, however, the time step ought to be limited as discussed in Section 14.13.

Whatever the model, after the change in the porosity distribution, the relative densification strain can be calculated as

$$\varepsilon_{de,i} = \frac{Po_{sin,i}^{t+\Delta t} - Po_{sin,i}^t}{3} \quad , \tag{14.50}$$

where $\varepsilon_{de,i}$ is the densification strain at point i and the assumption of isotropic densification has been performed in going from the volumetric to linear strain.

Finally, the total porosity - the one influencing the fuel thermal conductivity - can be calculated as

$$Po_{i,tot} = Po_{sin,i} + Po_{gas,i} \quad , \tag{14.51}$$

....

where $Po_{gas,i}$ is the bubble porosity fraction - and equal to the volumetric gaseous swelling strain - at point i.

14.9.3 Central void calculation

As known, one of the major effects of restructuring is the creation (or enlargement, if already present) of a central void resulting from the porosity movement towards the hottest part of the pellet. To estimate the void radius, the starting point is the mass balance

$$(r_{fo,0}^2 - r_{fi,0}^2)\rho_{f,0}\Delta z_0 = (r_{fo}^2 - r_{fi}^2)\rho_f\Delta z \quad , \tag{14.52}$$

where quantities without a subscript are evaluated at the current time step and ρ_f indicates the fuel density. Re-arranging the terms the void radius can be expressed as

$$r_{fi} = \sqrt{r_{fi,0}^2 \frac{\rho_{f,0}\Delta z_0}{\rho_f\Delta z} + r_{fo}^2 \left(1 - \frac{\rho_{f,0}\Delta z_0 r_{fo,0}^2}{\rho_f\Delta z r_{fo}^2}\right)} \quad , \tag{14.53}$$

where, leaving aside the ratio between the outer fuel radii - function of strains not related to densification -, it is seen that r_{fi} depends on the area change brought about by restructuring (i.e. the product $\rho_f\Delta z$ is indeed proportional to the area). To more easily allow superposition with the other strains in the mechanical analysis (e.g. thermal expansion), equation (14.53) can be cast in incremental form, after some algebraic manipulation, as

$$r_{fi} = \sqrt{\frac{\pi r_{fo}^2 - \sum_{i=1}^{N-1} \Delta A_{den,i}}{\pi}} \quad , \tag{14.54}$$

where $\Delta A_{den,i}$ is the area decrease due to densification expressed as

$$\Delta A_{den,i} = A_i(1 + 2\varepsilon_{de,i}) \quad . \tag{14.55}$$

where $\varepsilon_{de,i}$ is given by equation (14.50).

To avoid superposition problems between the newly calculated central void radius and the closest mesh point, the fuel grid is re-meshed near the cavity and all the strains and properties (e.g. O/M ratio, porosity etc.) interpolated, as discussed in Section 14.6.2.

. . . .

14.10   FGR

Introduced in Section 13.2.3, FGR is strongly related to the micro-structure of the fuel material, but, at the same time, its influence on the gap conductance and plenum pressure stems from the global behavior of the pin; as discussed in Section 13.4.2, however, the local effect can gain importance in transient situations.

It is generally recognized that the main parameters influencing FGR are BU, grain size and fuel temperature; the latter, in particular, has been modeled, in many 1.5D codes, via intra-granular diffusion coefficients [133] or fractional area coverage by the different restructured zones. This last category of models, based on the three zones approach, has been adopted. It is, by nature, optimal for the global character of FGR, but should be able to maintain sufficient accuracy even in establishing the initial conditions for transient, especially given the conservative nature of the value reported in Table 13.12. The only real parameter that is not, directly, modeled is the grain size even if, during the calibration stage of the model, grain growth is generally included and used to experimentally infer the temperature distribution [134].

14.10.1   Model formulation

The general expression at the foundation of models based on the three zones has the following form

$$
\begin{aligned}
mol_{FG,k} =& mol_{g,k} FGR_k = mol_{g,k}(F_{col}(BU_k)A_{col}(T_k)+ \\
& F_{eq}(BU_k)A_{eq}(T_k) + F_{unr}(BU_k)A_{unr}(T_k)) \quad,
\end{aligned}
\tag{14.56}
$$

where $mol_{FGR,k}$ and $mol_{g,k}$ are the number of FG moles released and generated in the fuel axial slice k, respectively; F_{col}, F_{eq} and F_{unr}, functions of BU, are the FGR from the columnar, equiaxed and unrestructured regions respectively while A_{col}, A_{eq} and A_{unr}, functions of temperature, are the respective fractional areas covered. While the fractional areas are calculated as discussed in Section 14.9.1, the zones FGR rates can be evaluated with the help of correlations like the ones in [134] or [139]. To actually find the total moles released, a summation over all the axial slices is necessary.

Finally, it is to be noted that this kind of model is, generally, not suited for transients calculations and, as such, FGR is not taken into account during the transient. Contrarily to the case of thermal reactors, for the peak power pin of a FR, given the high release expected during normal operations, the transient contribution - chiefly stemming from the gas trapped on

....

grain boundaries - should be negligible, especially considering the expected closed gap situation; indeed, even in recent experiments, definitive conclusions about the importance of additional release, in fast transients, were not possible due to the difficulties in separating the release from the melted and un-melted regions of the pin [38].

14.11 JOG formation

Typical of high BU oxide-fueled pins, the JOG formation is still surrounded by considerable uncertainties; a systematical understanding of the prerequisites for its development is not, currently, available and only few cornerstones are broadly accepted:

- there is a BU threshold for its formation and,

- the main constituents is cesium molybdenate (Cs_2MoO_4)[73].

Further experimental evidences, possibly suggest an influence of temperature in the gap region and fuel grain morphology [52], similarly to FGR.

Given the few reliable conclusions available, concerning JOG, only the most recent fuel performance tools have tried to tackle the phenomenon ([98],[55]); generally, JOG models rely on the fact that volatile cesium is able to radially migrate down the temperature gradient towards the cold pellet periphery, until some condition is fulfilled so that the accumulated cesium can condense in the JOG[18]. Considering the target uncertainty in Table 13.12, the effort to solve the cesium diffusion equation does not seem worth and a more simple model has been devised, as described in the following.

14.11.1 Thickness calculation

Being cesium a volatile FP, it is assumed to be released at the same rate of fission gases [77], and so following equation (14.56) where $mol_{g,k}$ must be substituted by $mol_{gCs,k}$, the moles of generated cesium in axial slice k; moreover, since only the unrestructured zone is supposed to contribute to the JOG formation, in equation (14.56) only the term $F_{unr}A_{unr}$ is used.

Once the released cesium in a time step, $\Delta mol_{Cs,k}$, is know the new JOG thickness can be calculated as

$$s_{JOG,k}^{t+\Delta t} = s_{JOG,k}^{t} + \frac{M_{JOG}\Delta mol_{Cs,k}(1 - f_{crack})}{2\pi r_{fo,k}dz_k} \quad , \qquad (14.57)$$

---

[18]Molybdenum is also an important constituent, but given the fact that for each mole of cesium only half mole of molybdenum is needed, the latter is assumed to be already available [98].

. . . .

where M_{JOG} is the JOG molar volume taken as 106.3 cm^3/mole [98] and f_{crack} is the fraction of cesium trapped in cracks as suggested in [77]. The JOG is supposed to form only if a set of conditions is fulfilled:

- F_{unr} must be different from zero and so, the BU threshold is linked to the used FGR correlation;

- $T_{fo} > 873$ K due to almost null mobility of cesium below this temperature;

- $T_{ci} < 873$ K to assure cesium remains in solid form, enabling JOG formation.

Effect on gap conductance

The same rationales behind the analysis in Section 13.2.5, have been employed in TEMIDE namely, a parallel of conductances. This approach, as discussed, should be on the conservative side; moreover, considering transient situations, if a JOG-filled gap is present, the sudden power increase in an UTOP should quickly reduce the gap thickness due to the fuel thermal expansion, effectively squeezing JOG from the high power region of the pin, increasing accordingly its conductance [77]. To model this process, the JOG thickness during a sudden power increase is reduced by the difference of the thermal expansion between the fuel and cladding as

$$s_{JOG,k}^{t+\Delta t} \to s_{JOG,k}^{t+\Delta t} + \Delta u_{th,c,k} - \Delta u_{th,f,k} \quad , \tag{14.58}$$

where $\Delta u_{th,c}$ and $\Delta u_{th,f}$ represent the thermal displacements of the clad and fuel respectively for the axial slice k. The squeezed mass should, indeed, be transported to adjacent slices, but this effect is presently neglected due to its low absolute impact if compared to the overall uncertainty existing in the JOG thickness evaluation.

Effect on swelling

In Section 13.2.5, the effect of JOG formation on the fuel solid swelling rate was addressed. Reporting equation (13.23) with the nomenclature of the present section it results in

$$\dot{\varepsilon}^{sw,s} = A + B \left(1 - \frac{mol_{Cs,k}}{mol_{gCs,k}} \right) \quad , \tag{14.59}$$

where A and B are constants representing the non-volatile and volatile contributions to the solid swelling rate. The pellet shrinkage subsequent to JOG

. . . .

formation is, therefore, not directly taken into account or better: the effect on the temperature field is partially accounted for with the modification of the gap conductance, while the possible effect of JOG on the mechanical interaction between fuel and clad is conservatively neglected due to the lack of systematic, reliable data supporting any modeling in that direction [47].

14.12 Plenum pressure

The plenum pressure calculation is based on the ideal gas law as

$$P_p = \frac{mol_{FG}R}{\left(\frac{V}{T}\right)_p} \quad , \tag{14.60}$$

where mol_{FG} are the moles of FGs released to the plenum by the whole pin - sum over k of the value calculated in equation (14.56) - while $\frac{V}{T}_p$ is the plenum volume-to-temperature ratio, defined as the sum of all the available cavities as

$$\left(\frac{V}{T}\right)_p = \left(\frac{V}{T}\right)_{lp} + \left(\frac{V}{T}\right)_{up} + \left(\frac{V}{T}\right)_{cv} + \left(\frac{V}{T}\right)_{gap} \quad , \tag{14.61}$$

where the subscripts lp, up, cv and gap indicates, respectively, the lower plenum, the upper plenum, the central void and the fuel-clad gap. In equation (14.61) the contribution of cracks to the plenum pressure has been neglected due to its low impact and to the overall low importance of P_p, as discussed in Chapter 13.

14.13 Time step control

As hinted throughout the chapter, a time step control is performed, at the beginning of the time loop so to guarantee a smooth convergence of the main time dependent phenomena, along with numerical stability and a sufficient precision. The main effects subject to control are:

- cladding creep (Δt_{creep}),

- geometrical variations (Δt_{geo}),

- boundary conditions variations (Δt_{bound}),

- restructuring (Δt_{res}),

....

- plutonium migration (Δt_{Pu}) and

- contact pressure adjustment ($\Delta t_{contact}$).

During a time loop iteration, all these effects are evaluated, for all the axial sections, and the minimum, taken as the reference Δt for the next time iteration, namely

$$\Delta t = MIN(\Delta t_{max}, \Delta t_{creep}, \Delta t_{geo}, \Delta t_{bound}, \Delta t_{res}, \Delta t_{Pu}, \Delta t_{contact}) \quad , \tag{14.62}$$

where Δt_{max} is the maximum allowable time step (e.g. 2 h) so to avoid excessive coarsening of the time discretization; moreover, to avoid sharp changes in Δt, when the constraint of equation (14.62) is higher than the previous Δt, a gradual increase is performed until the new upper bound is met.

In the following, the logics behind the introduced limitations are described.

Cladding creep

In Section 14.3.1, numerical stability problems in case of excessive creep in a time step were mentioned; in particular, creep must be lower than the corresponding elastic strain [32], so that Δt_{creep} is calculated as

$$\Delta t_{creep} = \frac{f_{cr}\varepsilon_{eff}^{el}}{\dot{\varepsilon}_{eff}^{cr}} \quad , \tag{14.63}$$

where f_{cr} is the, user defined, allowable creep fraction, usually around 0.2. The equation is evaluated for all the clad points (no creep is accounted for in the fuel) in all the axial slices, and the minimum is taken.

Geometrical variations

To avoid risks of overlapping radii in the geometrical mesh due to strong or sudden mechanical deformations, the time step is limited as

$$\Delta t_{geo} = \frac{f_{geo}(r_{i+1} - r_i)}{r_i \Delta \dot{\varepsilon}_{f,t,i}} \quad , \tag{14.64}$$

where f_{geo} is the, user defined, allowable displacement fraction. Similarly to Δt_{creep}, the equation is evaluated for all the points of the fuel and cladding in all the axial slices, and the minimum is taken.

....

Boundary conditions variations

In order to assure adequate time steps able to catch the variation of the boundary conditions, notably in transient situations, a time step control is performed as follows

$$\Delta t_{bound} = \frac{f_{bound}\Delta t}{\frac{\Delta y}{y}} \quad , \tag{14.65}$$

where f_{bound} is the, user defined, maximum acceptable variation of y which represents a boundary conditions either in the form of power, clad outer temperature, coolant inlet temperature or mass flow rate.

Restructuring

The time control on restructuring is fundamental in guaranteeing a precise numerical solution of the porosity conservation equation in case the explicit model based on the pores migration velocity is adopted. The constraint reads as follows:

$$\Delta t_{res} = \frac{f_{res}(r_{i+1} - r_i)}{v_{p,i}} \quad , \tag{14.66}$$

where f_{res} is the, user defined, allowable migration fraction and is recommended to be lower than 0.25 [7]. This equation is evaluated for all the fuel points and all axial sections, and the minimum is taken.

Plutonium migration

Although the characteristic time of plutonium redistribution is particularly high, relatively to others already mentioned, a check has been introduced for completeness, besides being fundamental for applying equation (14.47). To evaluate Δt_{Pu}, either equation (13.34) can be used, based on physical parameters, or the following expression, based on allowable variations,

$$\Delta t_{Pu} = \frac{f_{Pu}\Delta t}{\Delta e_i} \quad , \tag{14.67}$$

where f_{Pu} is the, user defined, maximum acceptable variation (e.g. 0.01 similarly to F in equation (14.47)) and Δe_i represents the plutonium concentration variation in a time step at point i. The equation is applied to all the points and axial slices, and the minimum is taken.

....

Contact pressure adjustment

Given the exponential nature of the contact pressure adjustment procedure, to allow sufficient precision in its evaluation, a time step limitation is adopted as

$$\Delta t_{contact} = \frac{f_{contact}}{\lambda} \quad , \tag{14.68}$$

where $f_{contact}$ is the, user defined, maximum allowed variation in the time step and λ was defined in equation (14.19). The expression is evaluated for all the axial section undergoing contact and the minimum is taken.

General comparison

Even if the value of all the outlined time step controls can vary greatly for different operative conditions and even during the pin irradiation, generally it has been found that:

- cladding creep, plutonium migration and contact pressure adjustment rarely are the most stringent requirements;

- geometrical variations are important only if an extremely refined mesh is used, but generally are not dominant;

- restructuring is the dominant limitation, especially close to BoL conditions and for high power rated pins;

- the boundary conditions control poses no limits during normal operation while is the dominant one both in ULOF and UTOP transients.

....

CHAPTER 15

VERIFICATION AND VALIDATION

After having delineated TEMIDE's general structure and the logics behind all the selected and implemented models, a verification and validation campaign has been conducted. V&V activities are of paramount importance for software quality control, for quantifying accuracy and cross checking consistently and homogeneously the correctness of the implementation from both the mathematical and intended point of view. Moreover, they are fundamental for assessing codes results confidence and so make the user aware of the representativeness of his conclusions as discussed in Chapter 8.

During the verification stage, all the models have been assessed, as described in Section 15.1 while, in the validation part, some preliminary comparison with experimental data has been performed in order to test if the adopted development methodology broadly fulfilled the DOC requirements upon which has been based, particularly concerning accuracy (see Section 15.2).

15.1 Verification

Based on [91], verification can be defined as *"the assessment of the software correctness and numerical accuracy of the solution to a given computational model. In the verification phase the association or relationship of the simulation to the real world is not an issue".* Thus, verification provides evidence, or substantiation, that the mathematical model which is derived from the conceptual one, is solved correctly by the computer code that is being assessed. The fundamental strategy in verification therefore is to identify, quantify,

. . . .

and reduce errors caused by the mapping of the mathematical model to a computer code.

Verification can be further divided in two activities [91]:

- numerical algorithm verification addresses the mathematical correctness of the software implementation of all the numerical algorithms that affect the numerical accuracy of the computational results. The major goal of numerical algorithm verification is to accumulate sufficient evidence to demonstrate that the numerical algorithms in the code are implemented correctly and function as intended;

- the emphasis in software quality engineering is on determining whether or not the code, as part of a software system, is reliable (implemented correctly) and produces repeatable results on specified computer hardware and in a specified software environment, including compilers, libraries, and so forth. Software quality engineering procedures are primarily needed during software development, testing, and modification.

The first one is usually performed comparing the code solution with highly accurate reference solutions, the latter is performed through software management and quality assurance procedures (like documentation requirements, planning, etc.). Although logically two independent tasks, they, in practice, overlap because coding errors or bad management will influence the algorithm verification.

Object of this section is the numerical algorithm verification, where some significant - not exhaustive - examples regarding the models described in Chapter 14 are presented. To keep compactness, indeed, only models concerning the solution of a differential equation are presented, meaning that grain growth, corrosion, FGR and JOG formation will not be discussed.

15.1.1   Thermal field

The thermal field model outlined in Section 14.2 has been tested in a variety of situations; here some illustrative cases, concerning the coolant and pin temperatures in nominal and transient situations are reported.

Fuel pin

Steady-state   The steady-state verification of the temperature distribution for an hollowed pellet is reported in Figure 15.1 where the pellet geometry of the ALFRED reactor has been taken. The analytical solution is the classical,

. . . .
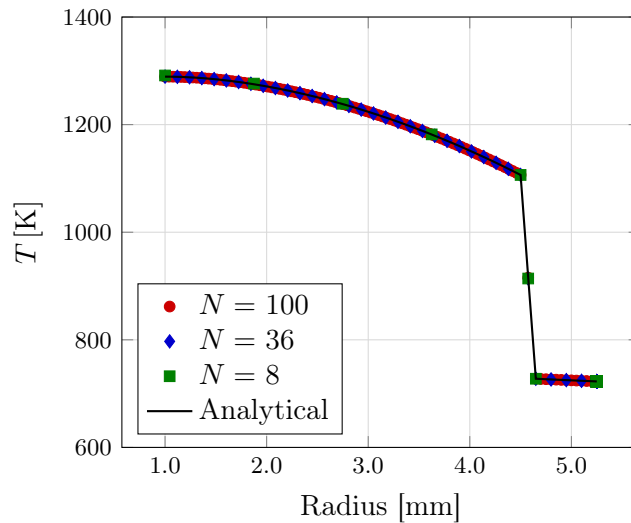
Figure 15.1: Fuel pin temperature solver verification in steady state conditions. N represents the number of points in the mesh.

almost, parabolic profile, derivable assuming constant material properties and a flat power profile [139].

The maximum relative errors are 0.39, $7.2 \cdot 10^{-3}$ and $7.5 \cdot 10^{-4}$%, respectively, for N equal to 8, 36 and 100. Given that, on one hand, the higher the number of mesh points, the higher the numerical precision, but, on the other hand, the grater the computational burden a balance have to be met; it can, therefore, be seen that discretizations with around 20 points should assure a sufficient precision without excessively penalizing running times.

Transient   For the pin transient test, a solid pellet with uniform initial temperature has been used; at time $t = 0$ s an uniform, exponentially decaying, heat source is activated as described in [137]. Results for this transient are reported in Figure 15.2 where T_{norm} is defined as

$$T_{norm} = \frac{(T - T_0)k_f}{r_{fo}^2 q_0'''} \quad , \tag{15.1}$$

being T_0 the initial temperature and q_0''' is power density of the source at time $t = 0$ s. The transient time constant, the characteristic time of the power exponential variation, is 10 s.

The maximum relative error, found near the outer periphery, where the gradient is higher, diminishes with time and goes from 8 to 0.5% for $\Delta t =$

....
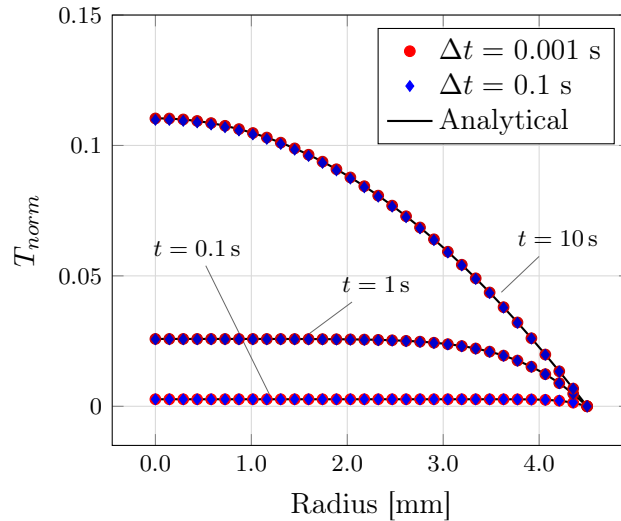
Figure 15.2: Fuel pin temperature solver verification in transient conditions. $N = 32$ has been used.

0.1 s while, for $\Delta t = 0.001$ s, goes from 1 to 0.05% (using $N = 32$). The error for smoother variations, like the ones expected in UTOP conditions, is, therefore expected to be lower, suggesting that a f_b in equation (14.65) around 0.001 should suffice.

Coolant

Transient   For the coolant model of Section 14.2.1, only a transient case is reported, being the steady-state solution just an algebraic operation. The studied case involves an axially constant, exponentially decaying, heat source activated at $t = 0$ s when the channel inlet temperature is T_0; results for this transient, compared to the analytical solution of equation (14.2) are reported in Figure 15.3 where the transient time constant is 20 s.

The maximum relative error is at the heat source activation and is around 20% for the direct, linear discretization of equation (14.2) while around 0.25% using the exponential method of equation (14.3); the advantage of the implemented discretization is apparent and assures high precision even with rough time steps.

....
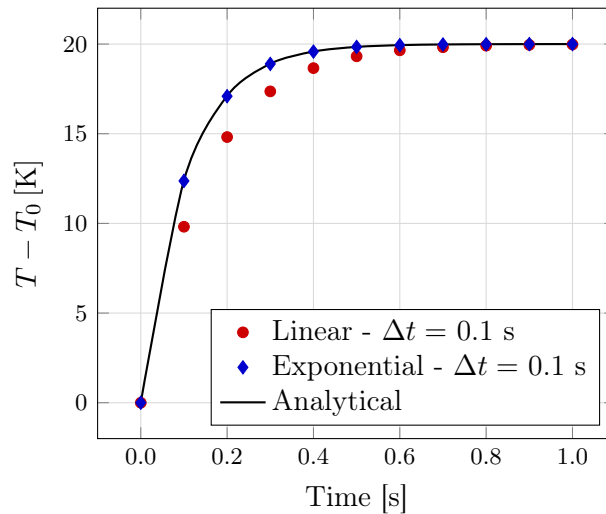
Figure 15.3: Coolant temperature solver verification in transient conditions.

15.1.2   Mechanical field

The mechanical field model outlined in Section 14.3 is more multifaceted than the thermal one due to the plurality of possible situations; in the following, only some representative cases are discussed, encompassing a thermo-elastic solution, a swelling-creep problem and a plastic analysis.

Thermo-elastic

Results for the verification in the case of a thermo-elastic problem with a linear temperature distribution are reported in Figure 15.4, where typical clad dimensions have been taken.

The maximum relative error goes from 0.92 to 0.21% passing from 5 ($\Delta r = 150$ µm) to 20 ($\Delta r = 32$ µm) mesh points.

Swelling and creep

To test the solver on a more complete problem, the analytical solution reported in [60], including simple correlations describing linear creep and swelling, is reported; a comparison with TEMIDE's mechanical solver is reported in Figure 15.5, as a function of BU.

The maximum relative error with 13 mesh points is 0.23% almost constant with BU. A clad discretization with around 10 points seems therefore

....
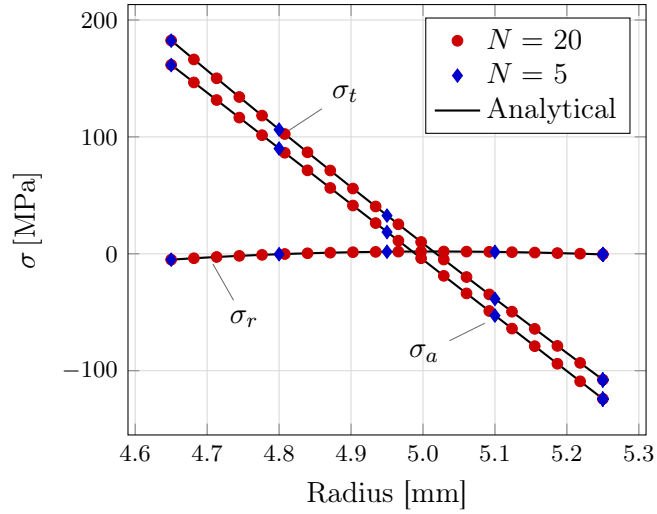
Figure 15.4: Mechanical solver verification for a cladding thermo-elastic problem; internal and external pressures are 5 and 0.5 MPa respectively.
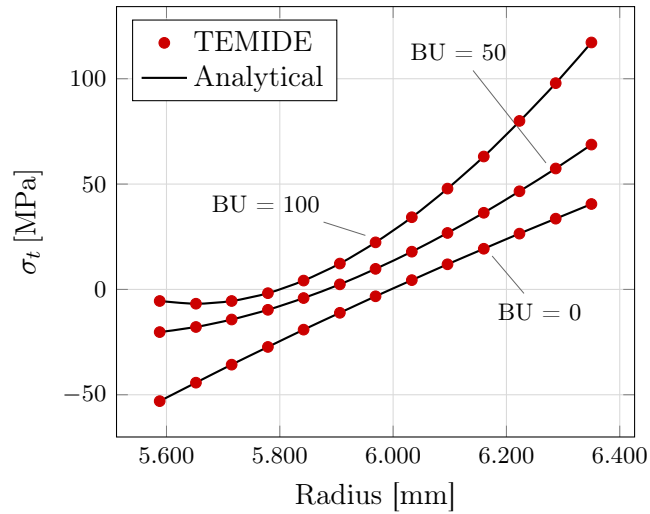
Figure 15.5: Mechanical solver verification for a cladding thermo-elastic problem with creep and swelling taken from [60]; BU is in MWd/kg and $N = 13$.

. . . .

sufficient for limiting numerical errors.

Plasticity

To test the perfect plasticity assumption implementation discussed in Section 14.3.1, a comparison with the solution reported in [80], also compared with ABAQUS [128], has been conducted. The benchmark is about a solid cylinder subject to a linear temperature gradient, which is increased and decreased as reported in Figure 15.6a, and to an external pressure pushing outward depicted in Figure 15.6b.

(a) Benchmark temperature history.

(b) Benchmark pressure history.
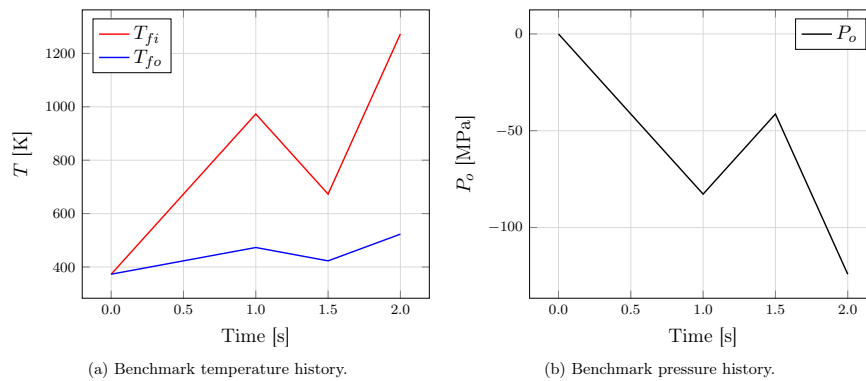
Figure 15.6: Temperature and pressure histories for the plasticity benchmark.

Results for this benchmark relatively to the fuel outer radius displacement are reported in Figure 15.7; the maximum relative error assesses at around 0.6%, confirming the correctness of the plasticity model implementation.

15.1.3 Oxygen redistribution

The model presented in Section 14.7 has been checked against the OXIRED model presented in [61] using the Q_{ox} proposed in [4]; the obtained results are plotted in Figure 15.8.

It is seen the perfect agreement between the models with a maximum relative error of $8.3 \cdot 10^{-4}\%$.

. . . .
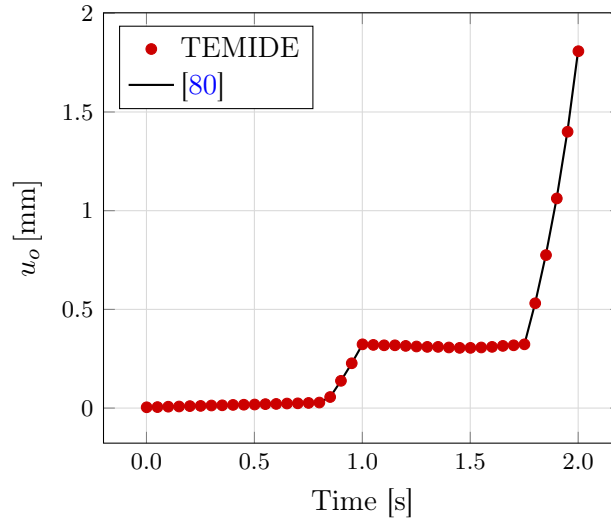
Figure 15.7: Mechanical solver verification for a solid cylinder under plastic deformation taken from [80]; $N = 11$.
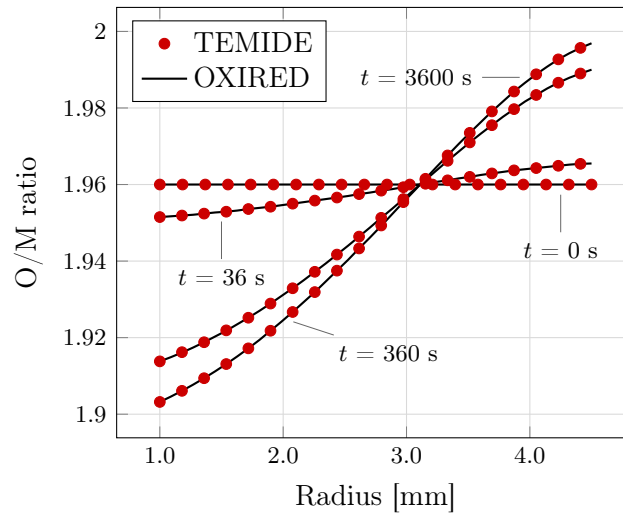
Figure 15.8: O/M redistribution solver verification against the OXIRED model with Q_{ox} taken from [4] for $O/M_{ave} = 1.96$.

....
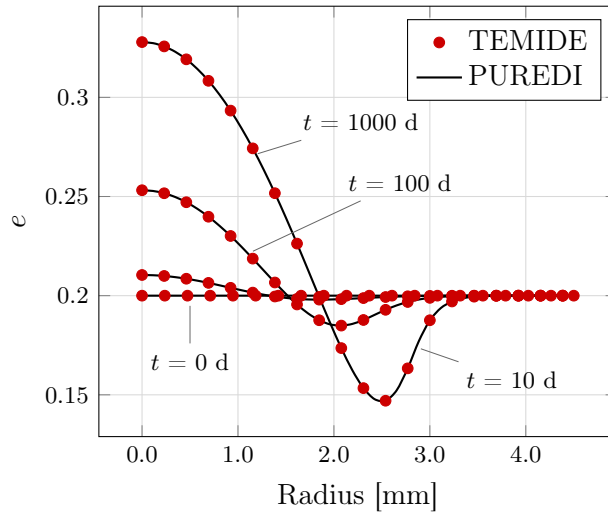
Figure 15.9: Plutonium redistribution solver verification against the PUREDI model with material constants taken from [11] for $e_{ave} = 0.2$.

15.1.4   Plutonium redistribution

Similarly to the oxygen migration, the plutonium redistribution model presented in Section 14.8, has been tested against the PUREDI model described in [87] - upon which is based - using the activation energy and diffusion coefficient reported in [11]. The comparison is reported in Figure 15.9.

The two models agree at round of errors, proving the correctness of the implementation.

15.1.5   Restructuring

The porosity distribution evaluation with the help of the model based on the pores migration velocity, explained in Section 14.9.2, is here verified against the analytical solution of the porosity conservation equation reported in [29]. The solution is based on a simplified formulation of the pores velocity as an exponential function of the pellet radius; results are reported in Figure 15.10.

The maximum relative error concerning the radial distribution goes from 15.7 to 3.1 and finally 1.2% using 10, 40 or 100 mesh points; the point of maximum error is close to the high gradient region and strongly diminishes with time. The slow spatial convergence hints a number of points close to 20 as an optimal trade-off for not losing too much precision in the early stages

. . . .

(a) Innermost point porosity evolution with time.

(b) Radial profiles comparison as a function of N.
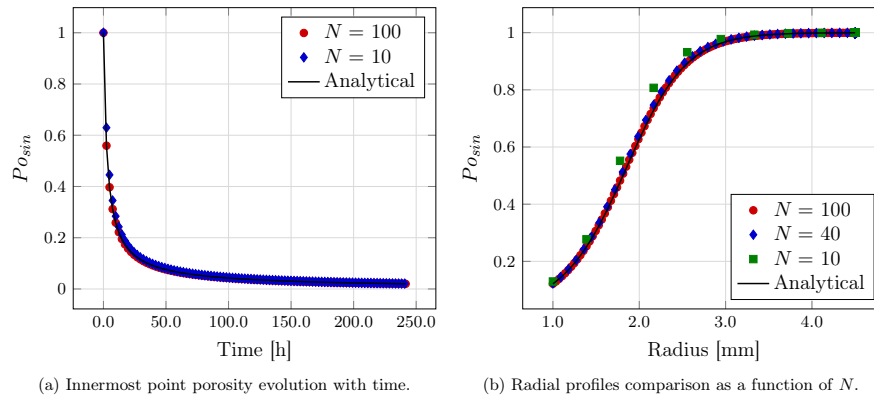
Figure 15.10: Porosity distribution solver verification against the analytical solution of [29].

of restructuring while assuring a manageable computational burden[1].

15.2 Validation

As described in Chapter 8, validation provides evidence, or substantiation, of how accurately the computational model simulates the real world for system responses of interest and is also crucial to test that the anticipated and actual validity domains coincides. In the present section the preliminary validation performed on TEMIDE is presented encompassing the experiment on the porosity distribution presented in [59] and the steady-state and UTOP tests reported in [21].

15.2.1 Porosity experiments

In [59], the radial porosity distribution for an initially high-porous Sphere-Pac[2] stoichiometric MOX fuel irradiated in the **E**ngineering **T**est **R**eactor (ETR) was measured; specifications are given in Table 15.1. Given the very low BU, the experiment was expressly designed so to avoid gaseous fuel swelling perturbations on the porosity distribution so to allow, as best as

---

[1]A mesh uniform over porosity rather than geometry has been implemented in TEMIDE so to further increase numerical precision, but it is still in the development phase.

[2]Pelletized and Sphere-Pac fuels have been shown to behave similarly during restructuring [59].

achievable, effects separation; this makes possible to test the densification models reported in Section 14.9.2.

Table 15.1: Specifications for the porosity distribution experiments in [59].

	Value
Fuel material	
e	0.15
O/M	2.0
Po_{sin}	0.186
Geometry	
$r_{fi,0}$	solid pellet
$r_{fo,0}$	2.9464 mm
Fuel height	76.2 mm
Irradiation conditions	
T_{fo}	833 K
q'	446.2 W/cm
BU	0.7 at.%
Power profile	flat

Using the fuel thermal conductivity suggested in [105], results in Figure 15.11 have been obtained for the three zones model using the columnar porosity evolution reported in [52], labeled as 3Z and for the pores velocity-based model using migration velocities from [59], labeled as LACKEY, [96], labeled as OLANDER, and [85], labeled as NICHOLS; a quantitative comparison is also given in Table 15.2.

Discussion Looking at Figure 15.11, it is visible the agreement between LACKEY and OLANDER pores velocities, while NICHOLS predicts lower velocities and so pushing the region unperturbed by restructuring further into the pellet center; the three zones model proposes results remarkably different from the velocity-based models underestimating restructuring and suggesting that the correlation in [52], built for low porosity pellets, is not scalable.

Compared with experimental data, even if the columnar boundary is

. . . .
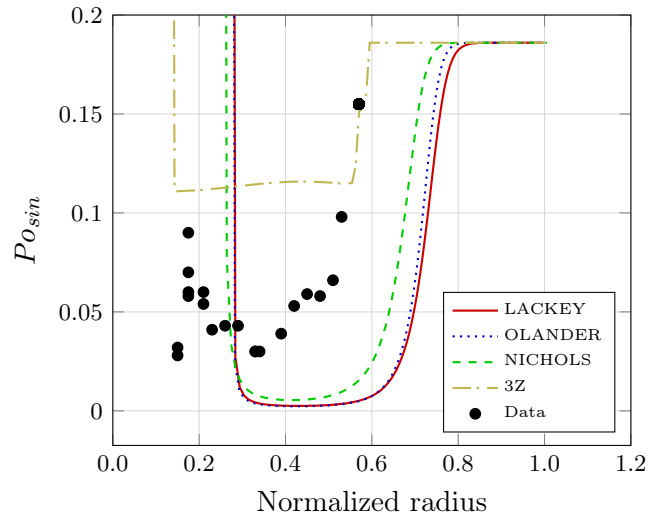
Figure 15.11: Comparison against experimental data for the porosity
distribution reported in [59] at 0.7 at.% BU.

Table 15.2: Quantitative
comparison against the porosity
distribution experiments in [59].

	r_{col}[a]	r_{fi}[a]
Data	0.53	0.15
LACKEY	0.43	0.27
OLANDER	0.45	0.27
NICHOLS	0.51	0.25
3Z	0.56	0.13

[a] Normalized to the fuel outer ra-
dius.

reasonably well predicted, the central void radius is generally overestimated,
with the exception of the three zones model thanks to the high remaining
porosities predicted; differences could be due to the predicted temperature
field, higher than the one actually present in the pellet, or to the underestima-
tion of the minimal porosity achievable by such a highly porous Sphere-Pac
fuel.

    For what concerns experimental uncertainties, using the reported average

. . . .

porosity for the columnar region at 5.9%, and the equiaxed outer radius at 0.68 [59] results, from the application of equation (14.53), a $r_{fi} = 0.18$ suggesting a good consistency of the experimental data.

15.2.2   Steady-state experiment

To include a more general validation comparison so to better test the full capabilities of TEMIDE, a complete irradiation experiments have been included in the database; in particular, pins irradiated in the french, sodium-cooled, Phénix reactor. Experiments in HLM environment are not currently available and so the validation must be based on sodium-cooled cases; this is acceptable in steady-state conditions, and for the domain outlined in Section 12.2, because the fuel pin thermo-mechanics is, neglecting corrosion or embrittlement issues, weakly dependent on the coolant. The situation for transients is, however, different as discussed in Section 15.2.5.

15.2.3   E9 - low smear density

The first pin used, labeled as E9[3], [21] represents a low smear density pellets stack in a high swelling stainless steel clad, and was irradiated at a relatively low BU for subsequent testing in the CABRI reactor (see Section 15.2.5).

The general specifications of the experiments are reported in Table 15.3 while a complete list of the material properties and models used is reported in Appendix A.

The obtained results for the E9 pin are presented in Table 15.4.

Discussion   As can be seen from Table 15.4, a satisfactory agreement is obtained between simulation and experiment; the central void radius is slightly overestimated, while FGR underestimated. The fuel smear density is very well matched while the plenum pressure is overestimated; due to the fact that FGR was under-predicted, possible explanations are uncertainties in the loading pressure or errors in the predicted moles generated by the fuel stack.

Being all the evaluated parameters strictly related to the temperature field, it can be inferred that the latter was actually well predicted. No information on the mechanical behavior of the cladding is available, besides swelling (see Appendix A), and so no conclusions regarding the mechanical model can be retrieved for the E9 pin.

---

[3]Of the so called Ophelie-6 type.

. . . .

Table 15.3: General specifications for
the E9 pin experiment.

	Value
Material	
Fuel	MOX
Clad	316SS[a]
Gap	He
Fuel specifications	
e	0.145
O/M	1.97
Po_{sin}	0.045
Geometry	
$r_{fi,0}$	1.000 mm
$r_{fo,0}$	3.635 mm
$r_{ci,0}$	3.750 mm
$r_{co,0}$	4.325 mm
Fuel height	750.0 mm
Plenum volume	38.23 cm^3
Irradiation conditions	
T_{in}[b]	673 K
$\dot{m}$[c]	0.1015 kg/s
q'_{max}	305.0 W/cm
BU_{max}	4.9 at.%
DPA_{max}	54
Power profile f_{ax}[d]	1.1

[a] Indicates the cold worked austenitic
   stainless steel grade 316.
[b] Is the coolant inlet temperature.
[c] Fixed so to preserve the coolant
   temperature rise reported in [50].
[d] Axial form factor.

Table 15.4: Comparison between
TEMIDE and the post-irradiation data
of the E9 pin; local values refers to the
peak power node.

	Data	TEMIDE
r_{fi}[a]	0.300	0.314
FGR	0.536	0.527
ρ_f[b]	0.800	0.803
P_p [MPa][c]	1.2	1.27

[a] Normalized to the fuel outer radius.

[b] Fuel smear density expressed as a fraction of the theoretical density.

[c] Evaluated at 673 K.

15.2.4 E12 - high smear density

The second pin, labeled as E12[4], [21] represents a high smear density pellets tack in a low swelling austenitic stainless steel clad, and was irradiated at a relatively high BU for subsequent testing in the CABRI reactor (see Section 15.2.5).

The general specifications of the experiments are reported in Table 15.5 while a complete list of the material properties and models used is reported in Appendix A.

The obtained results for the E12 pin are presented in Table 15.6 and Figure 15.12 where the profilometry data of the cladding, at EoL, are available.

Discussion Similarly to the E9 pin, results are, overall, satisfactory; the central void radius is under-predicted, in this case, while FGR is overestimated (exactly the opposite of the E9 pin). In analogy with the E9 pin, even overestimating FGR brings a (slightly) lower plenum pressure probably for the same reasons previously discussed.

For the E12 pin, details about the clad mechanical behavior are available, and it can be seen how the maximum deformation is well predicted both in magnitude and position; even if fuel-clad contact happened, for part of the clad life, the outer radius deformation is dominated by swelling. This means that the adopted correlation (see Appendix A) is able to catch the maximum

---

[4]Of the so called Viggen-4 type.

. . . .

Table 15.5: General specifications for the E12 pin experiment.

	Value
Material	
Fuel	MOX
Clad	15-15 Ti
Gap	He
Fuel specifications	
e	0.269
O/M	1.97
Po_{sin}	0.045
Geometry	
$r_{fi,0}$	solid pellet
$r_{fo,0}$	2.7135 mm
$r_{ci,0}$	2.8250 mm
$r_{co,0}$	3.2750 mm
Fuel height	850.0 mm
Plenum volume	14.34 cm^3
Irradiation conditions	
T_{in}[a]	673 K
m[b]	0.11 kg/s
q'_{max}	323.0 W/cm
BU_{max}	11.55 at.%
DPA_{max}	98
Power profile f_{ax}[c]	1.226

[a] Is the sodium coolant inlet temperature.

[b] Fixed so to preserve the coolant temperature rise reported in [50].

[c] Axial form factor.

point of deformation brought by a combination of temperature and fluence, but overestimates the effect of temperatures further away from the one giving the maximum; nonetheless, the prediction can be considered satisfactory.

. . . .
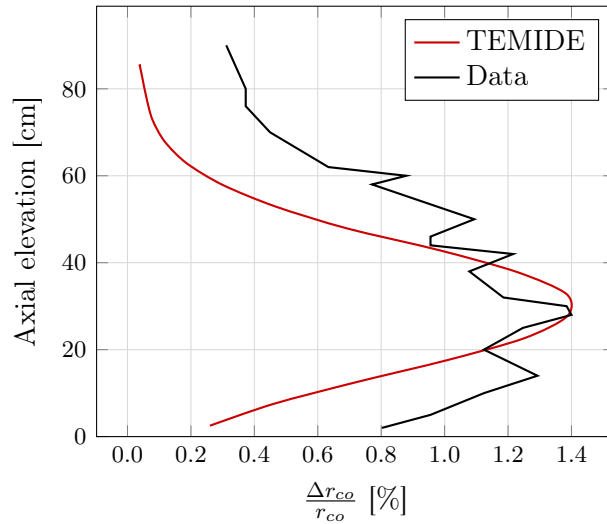
Figure 15.12: Comparison between TEMIDE and experimental data of the cladding profilometry of the E12 pin at EoL.

Table 15.6: Comparison between TEMIDE and the post-irradiation data of the E9 pin; local values refers to the peak power node.

	Data	TEMIDE
r_{fi}[a]	0.170	0.141
FGR	0.787	0.803
ρ_f[b]	0.910	0.903
P_p [MPa][c]	5.70	5.66
$\frac{\Delta r_{co}}{r_{co}}{}_{max}$	1.40	1.39

[a] Normalized to the fuel outer radius.
[b] Fuel smear density expressed as a fraction of the theoretical density.
[c] Evaluated at 673 K.

15.2.5   UTOP experiment

To test the transient capabilities of TEMIDE, a fast UTOP transient has been included in the validation. The experiment concerns the E12[5] pin previously presented that was, after the steady-state irradiation in the Phénix reactor, tested in the CABRI facility [17] under the CABRI-2 program [21]. CABRI, owned by CEA, is a pool-type research reactor dedicated to studying reactivity initiated accidents upon a section of highly-irradiated fuel; it was built in 1962 for safety studies of FR fuels, featuring a sodium-cooled test loop (exploited in the E12 pin experiment) and a water cooled core[6].

Given the fact that CABRI is characterized by a thermal spectrum, provisions have been taken to simulate the consequent self-shielding effect in TEMIDE as described in Appendix A.

As previously discussed, in transient conditions, the difference between sodium- and HLM-cooled pins is bounded to increase, as discussed in Sections 5.2 and 12.1, since the power and temperature evolutions can be remarkably different; the higher melting point of lead, indeed, strongly influences the events series of ULOF-like transients. Concerning UTOP, due to the fast dynamics, a lower impact of the coolant is expected - at least before failure -, making possible the transfer of validation conclusions from sodium to HLMs; they are therefore the only type of transient analyzed.

The specific boundary conditions applied during the transient are reported in Appendix A; in Table 15.7, only major specifications are given. It can be seen the lower ramp rate, relatively to the one assumed as reference for TEMIDE; the test characteristic time is, indeed, around 100 s falling outside the anticipated validity domain, nonetheless it should be useful for testing the implemented transient capabilities. Moreover, TEMIDE was developed to help the designer in avoiding melting while, in the E12 case, some (around 10% of the fuel mass in the pin) did happen; this, again, means that comparison with this experiment can only bring approximate conclusions.

All this said, results concerning the melt profile are reported in Figure 15.13 while, cladding profilometry, after the transient, is depicted in Figure 15.14a; the stress distribution at the end of the transient is presented in Figure 15.14b.

---

[5]The E9 pin was also tested in UTOP conditions, but due to the strongly diffuse melting, it is considered too far from TEMIDE's intended application domain.

[6]Recently, CABRI has been converted to light water conditions representative situations under the CABRI international program [17].

. . . .

Table 15.7: General specifications for the E12
pin in the CABRI-2 UTOP experiment.

	Value
Steady-state conditions CABRI	
T_{in}	659 K
q'_{max}	474.0 W/cm
Power profile $f_{ax}{}^{\text{c}}$	1.331
UTOP conditions CABRI	
Power ramp	0.9 [%/s]
$q'_{max}{}^{\text{a}}$	810.0 W/cm

[a] Value at the end of the transient coinciding
with clad failure.

Discussion Concerning melting, the axial profile is satisfactorily reproduced, especially considering that no model for the melted fuel is implemented in TEMIDE; indeed, during melting, part of the power deposited in the pellet should transform in latent heat and so not contributing to the temperature increase. In TEMIDE this phenomenon is completely missed and so, the overestimation of the melted fraction seems more than acceptable.

Regarding the cladding profilometry, the possibility of estimating the implemented PCMI model arises, since strong contact between the fuel and the clad is predicted to happen almost all over the active height. Considering that errors on the lower portion are memories of the steady-state simulation (see Figure 15.12) attention can be concentrated on the point of maximum deformation; the latter is 1.80% and 1.67% for the measurement and TEMIDE respectively. Given the excellent agreement at EoL previously discussed, the difference is mainly due to the transient where TEMIDE under-predicts the maximum deformation which happens very locally; the global behavior is, indeed, better predicted.

The failure location was experimentally predicted to be between 60 and 66 cm from the bottom, close to the end of the melted region; given the fast nature of the transient a short-term failure criteria, like the one based on stresses can be used. Particularly, as suggested in [133], failure can be assumed when the tangential stress is higher than σ_U[7]; the exact failure

---

[7]Implicitly, assuming failure is above σ_U and not σ_Y means that sufficient ductility of the cladding is believed to be retained.

. . . .
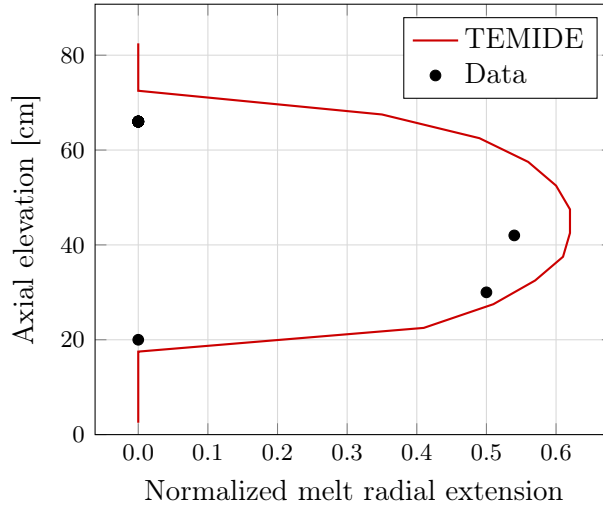
Figure 15.13: Comparison against experimental data for the melted
fraction profile of the E12 pin at the end of the UTOP.

(a) Cladding profilometry for the E12 pin at the end of   (b) Hoop stress axial profile at the end of the transient;
the UTOP. Only the bottom portion, far from the failure   comparison with σ_U taken from [70] and [122] is also given.
point, is available.
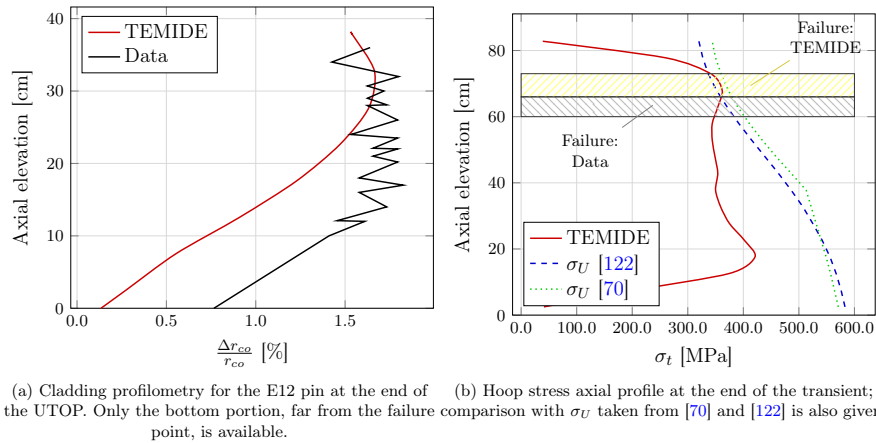
Figure 15.14: Comparison between TEMIDE resutls and experimental data
for the mechanical behavior of the cladding after UTOP for the E12 pin.

dynamics depends on the specific σ_U correlation used, like the ones reported
in Figure 15.14b. As seen, whatever the correlation, shifting in time the
moment of failure, the failure region is just above the experimental one. Of
course different failure criteria could produce slightly different results, but,
nonetheless TEMIDE prediction seems generally in line with the observed

. . . .

physical behavior; indeed, in [21], it is suggested that the cladding failure temperature should have been between 983 and 1013 K, which is very close to the range of temperatures at the failure location in Figure 15.14b. The fact that it is just shifted upward the observed failure location could hint on the errors in the evolution of the clad temperature from the boundary conditions, due to insufficient knowledge of the exchange geometry between the coolant and the clad (i.e. the elementary cell geometry).

Finally, it is mentioned that TEMIDE's running time for this case, including the steady-state in the Phénix reactor, and the successive preconditioning in the CABRI reactor (see Appendix A) is around 5 min on a standard personal computer.

15.3   Summary

The verification phase has been conducted, demonstrating the correct implementation of the models described in Chapter 14. For many models, a modest number of mesh points (i.e. around 20) has been found sufficient to guarantee acceptable numerical precision; others, like the porosity distribution one, require more points, particularly in the early phases of restructuring. Thanks to very low running times, however, the additional computational burden of a more refined mesh could be bearable, user side.

Regarding the validation phase, even if, in the experiment specifically dedicated to the porosity distribution, deficiencies have emerged; in the integral tests, both in steady-state and UTOP conditions satisfactory results were obtained for both thermal and mechanical fields.

The presented validation must be interpreted as a preliminary analysis - a first estimate - enabling the development approach described in the previous chapters to be tested, so to understand the validity of the methodology, in analogy to what has been done in Part II. To this aim, it can be said that first results are encouraging, motivating further validation work.

. . . .

. . . .

CONCLUSIONS ON TEMIDE

Part III has been dedicated to the fuel pin thermo-mechanics safety-informed DOC, TEMIDE. The main objectives and intended use of TEMIDE have been laid out, primarily involving the pin dimensioning so to cope with issues related to fuel melting in UTOP and clad failure in ULOF transients. The pursuing of answers to the three questions marking a DOC, as discussed in Part I, has pinpointed in the so called 1.5D codes the best trade-off approach to follow; to understand the main phenomena requiring attention during the development stage, a sensitivity analysis, inside the decided validity domain, has been performed, encompassing fuel temperature and clad stresses and strains, both in nominal and transients conditions. For this purpose, an analytical approach has been adopted and, where not practical, simple numerical models developed; even if simplified, the analysis provided quantitative explanations for the link between models and target parameters. In particular, for the fuel temperature, in nominal conditions, the most important models have been found to include restructuring and the effect of plutonium and porosity distributions; on the other hand, in UTOP, important contributions stemmed from the fuel gas retention capability. For what concerns the cladding, the dominant models have been identified in the contact pressure and swelling radial distribution, in nominal conditions, with the addition of the yield strength in ULOF-like situations. In almost all conditions, and for all TEMIDE's target parameters, a decisive contribution of material properties to the global uncertainty has been found, suggesting that modeling improvement of specific aspects (e.g. fission gas release) is not worth if not accompanied by a concomitant improvement of the material

. . . .

properties, refining the picture as a whole.

Another main achievement of the sensitivity study has been, via an inverse uncertainty problem solution, the derivation of guidelines expressing target uncertainties for the main phenomena so to act as beacons during the code layout construction, models simplification and selection. Based on these premises, TEMIDE's structure and rationales, spanning the main models like FGR, fuel restructuring and the thermal and mechanical analyses, have been described.

The preliminary verification and validation campaigns have also been presented; due to the important limitations on the availability of representative experimental data for HLMFRs in transient conditions, the conducted validation campaign must be interpreted as an early screening phase so to test, in first approximation, TEMIDE's capabilities in fulfilling the DOC requirements upon which has been built. Even if still in the embryonic stage, validation results are quite encouraging, suggesting the solidity of the undertaken development methodology and motivating a further expansion of the validation database.

....

Part IV

PhD thesis conclusions and future works

CHAPTER 17

CONCLUSIONS AND FUTURE WORKS

Looking at the many social, economical and environmental challenges ahead of humanity, there is not much doubt that the energy sector is going to play a prominent, catalyzing role. As part of the available range of options, nuclear energy can be an active player; to make this reality, of course, public and thus, political, support is a key aspect. Independently of the latter, however, research should strive for delivering systems ever more safe, economical and sustainable so to, lets say, *put the ball into* the policy maker *court*; broadly speaking, this was the object of the GIF initiative.

Among the systems fostered by the GIF, as potentially able to comply with their requirements, FRs are the ones ranking higher in the sustainability field, thanks to their intrinsic neutronics characteristics. More specifically, adopting a blank sheet approach, and weighting all the pros and cons of the GIF's proposed FR concepts, HLMFRs are believed to be promising candidates for reaching the ambitious Gen-IV objectives, in a relatively short time frame.

Under the umbrella of this new technological challenge, the opportunity can be seized to reset the standards of the nuclear scientific approach which is, almost by definition, instrumental to technological advancement and thus essential for delivering the wanted technological leap.

The present PhD thesis, in this generic framework, focuses on the core design approach rationalization; the latter is, indeed, a crucial component of any nuclear reactor system and, as such, it seems the most logical starting point of any innovation endeavor. Particularly, to help the designer in putting the approach into action, suitable tools must be used and, if not

. . . .

available, conceived.

Many questions were open at this point like: what exactly it is meant by "suitable"? How this tool should actually help? What is that a core designer truly wishes for? How such a tool should be developed? The attempt to answer these fundamental questions has brought to the definition of DOC along with broad guidelines helping in its conception and development[1].

The underlined methodology has been applied to close some of the gaps, currently present, involving instruments specifically dedicated to the core design stage of HLMFRs; the covered fields, in particular, have been the FA thermal-hydraulics and the fuel pin thermo-mechanics. Regarding the former, following the established guidelines, the SC code ANTEO+ has been conceived, with the main objective of delivering a code able to simplify the problem description without penalizing accuracy and with a clear interface for the user (i.e. the core designer) having an explicit and easily identifiable application domain so to ease the results interpretation phase - necessary in a rationale design process - and to increase confidence in them so to aid in the FA dimensioning.

Initially restricted to the forced convection regime and subsequently extended to the mixed one, ANTEO+ structure has been delineated along with the rationales behind equations simplification and models selection. The subsequent, thorough, validation campaign has been presented revealing the generally high level of ANTEO+ accuracy in its applicability domain; some concerns are still pending on HLM-cooled cases, mainly due to the lower availability of experiments truly dedicated to the validation of SC codes concerning these coolants; the first obtained results are, however, encouraging in this sense.

ANTEO+ has therefore been shown to satisfy all the main requirements for a DOC, effectively enabling a rationale approach to the FA thermal-hydraulics design.

To what pertains to the fuel pin thermo-mechanics, the will to include safety-related considerations at the outset of the pin dimensioning process, has given birth to the safety-informed DOC TEMIDE having, as principal objective, the clear translation of the main transients, concerning HLMFR, in constraints or relations among pin design parameters with a degree of accuracy and completeness superior to P&P methods, but without losing their degree of clarity, fundamental in a rationale design process.

The DOC development methodology, followed for ANTEO+, has been also applied to TEMIDE; given the complex interdependence patterns among

---

[1]Ironically, these guidelines have been formulated as questions.

. . . .

the numerous phenomena involved in the fuel pin during irradiation, to comply with the DOC's equilibrium requirement, a sensitivity analysis has been performed, in the anticipated TEMIDE's application domain; the objective was, on one hand, to pinpoint models and aspects requiring major attentions and, on the other hand, uncovering the phenomena not particularly contributing to the final results of interest so to, eventually, discard or roughly modeled them. Following an (almost) analytical approach and, via an inverse uncertainty problem solution, it was possible to derive guidelines expressing target uncertainties for the main phenomena so to act as beacons during the code layout construction, models simplification and selection.

The resulting structure and code layout were presented and subsequently tested in the verification and validation phase; the latter, was only a preliminary attempt to test, in first approximation, TEMIDE's capabilities in fulfilling the DOC requirements upon which it has been built. To this aim, validation results, even if embryonic, are quite encouraging, suggesting the solidity of the undertaken development methodology and motivating a further expansion of the validation database.

The conceived DOC development framework, at the core of the present PhD thesis, has therefore been proven successful and capable to deliver tools able to maintain sufficient accuracy in reproducing experimental data in a wide range of situations of interest, while keeping a simple structure entailing a very low computational burden and a clear interdependence among the main design parameters.

Ground for future work, specifically linked to the content of the present thesis, can be located in the further validation of both ANTEO+, for what concerns HLM-cooled experiments so to truly assess uncertainties to be recognized to the tool when applied to such coolants, and TEMIDE so to test, in more representative conditions the actual degree of reliability of the code, eventually highlighting areas where optimization can be needed (always inside the framework depicted in the thesis). Concerning modeling improvements, in

- ANTEO+ a better model for the near wall SCs for HLM-cooled bundles could be envisaged along with the possibility of directly including hot spot factors (i.e. uncertainties) calculations so to annex to the nominal design feedback, the required operational margin;

- for TEMIDE, only further validation results will definitely highlights the areas needing improvements, but, from the sensitivity analysis performed in this thesis, it can preliminarly be said that, after the necessary knowledge increase in material properties, the fuel creep (partic-

....

ularly concerning gap closures and contact pressure), JOG models and transient gaseous swelling are candidates for further advancements.

The developed DOCs will also be used, as partially already done, for further improving and advancing the design of the ALFRED reactor, with particular emphasis on the effect of uncertainties on design and safety performances.

More broadly, future work about the development of other DOCs, with the proposed methodology, covering HLMFRs core design aspects of interest, can be envisaged; the FA thermo-mechanics or the core thermal-hydraulics could be valuable candidates. The latter, in particular, entails the determination of optimal gagging schemes and/or the evaluation of the global (i.e. at core level) FAs by-pass flow and temperature distributions so to avoid hot or cold spots, reducing thermal gradients on core structures.

. . . .

Appendices

APPENDIX A

TEMIDE VALIDATION CASES: BOUNDARY CONDITIONS AND MODELS

In this appendix, the models and boundary conditions used in order to obtain the results presented in Section 15.2 are outlined for the E9 and E12 pins, both in nominal and transient conditions.

A.1   E9 - steady-state

In Section 15.2.3 the validation against the E9 pin irradiated in the Phénix reactor is presented and the general specifications outlined in Table 15.3. To complement the description, information, TEMIDE's side, must be given; a list of the used models and material properties is therefore reported in Table A.1.

From the discretization point of view, the active height was divided in 17 axial slices, each radially subdivided in 15 points for the fuel and 5 for the cladding.

Due to the fact that no swelling correlation was found in literature able to reproduce, at least approximately, the observed behavior for the specific 316SS adopted in the E9 pin [21] and to the fact that this, high swelling material, is of no interest for current design applications, it was decided to create a swelling correlation able to fit the profilometry data reported in [21]. This effort resulted in the following linear swelling correlation

$$\varepsilon_c^{sw} = 2.992 \cdot 10^{-25} \Phi \exp\left(-\frac{(T-750)^2}{1700}\right) \quad , \tag{A.1}$$

. . . .

Table A.1: Material properties and models used in TEMIDE for the simulation of the E9 irradiation test.

	Reference or value
Material Properties	
Fuel thermal conductivity	[105]
Fuel density	[144]
Fuel Young modulus	[97]
Fuel Poisson ratio	[97]
Fuel creep rate	[97]
Fuel thermal expansion[a]	[144] and [75]
Plutonium diffusion coefficient	[53]
O/M heat of transport	[61]
JOG conductivity	[98]
Plenum gases conductivity	[63]
Plenum gases viscosity	[63]
Gas mixture property	[64]
Clad thermal conductivity	[6]
Clad density	[6]
Clad Young modulus	[6]
Clad Poisson ratio	[6]
Clad creep rate	[125]
Clad thermal expansion	[6]
Clad swelling	See eq. (A.1)
Models	
Contact component gap conductance	[63]
Restructuring temperatures	[139]
FGR	[134]
Relocation	[82]
Densification	Pore velocity-based [96] and $Po_{sin,min} = 0.001$
Solid fuel swelling	Eq. (14.59) $A = 0.2$ at.% and $B = 0.45$ at.%
Gaseous fuel swelling	F_{intra} from [7] and P_γ from [20]
Corrosion	Not activated
Wastage	HEDL [138]
Grain growth	[97]

[a] The first for plutonium and the second for uranium.

....
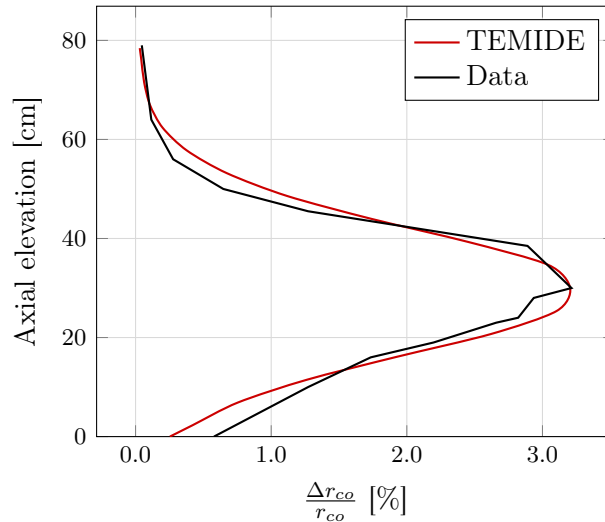
Figure A.1: Comparison between the fitted swelling correlation and experimental data of the cladding profilometry of the E9 pin at EoL.

where Φ is the fluence in $1/\text{cm}^2$ and T is in Kelvin. The calculated and experimental profilometries are reported in Figure A.1 where the good agreement can be noted.

A.2 E12 - steady-state

For the steady-state irradiation of the E12 pin, the same material properties and models were used, besides the cladding that was different as visible in Table 15.5. In Table A.2, therefore, only the used cladding properties are reported.

From the discretization point of view, the active height was divided in 17 axial slices, each radially subdivided in 15 points for the fuel and 5 for the cladding.

A.3 E12 - UTOP

After the base irradiation, the E12 pin was tested in the CABRI reactor, as described in Section 15.2.5; since boundary conditions are different among the Phénix and CABRI cores, the latter featuring a higher maximum power, to simulate the change, a linear interpolation between the two sets of bound-

. . . .

Table A.2: Material properties and models used
in TEMIDE for the simulation of the E12
irradiation test. Only differences with Table A.1
are reported.

	Reference or value
Material Properties	
Clad thermal conductivity	[122]
Clad density	[122]
Clad Young modulus	[122]
Clad Poisson ratio	[122]
Clad creep rate	[70]
Clad thermal expansion	[122]
Clad swelling	[70]

ary conditions has been used. The change has been supposed to last 10 min; arbitrarily, a 10 min holding time has been set to simulate the period spent, in the CABRI reactor, before the actual transient [1][21].

With boundary conditions, in this case, it is specifically meant power, indeed:

- the mass flow rate is identical,

- the coolant inlet temperature changes slightly from 673 K to 659 K and so the variation has been supposed instantaneous after EoL conditions are reached.

Finally, the CABRI-2 test was performed under a thermal spectrum, implying a great self-shielding effect and consequent power depression at the interior of the pellet; following [133], the radial power profile has been taken as reported in Figure A.2. To cope with the pellet changing conditions, the radial profile is normalized to one at each time step.

After the 10 min holding time, the actual UTOP starts with the power ramp rate reported in Table 15.7; when the linear power at the peak power node reaches the value 810.0 W/cm the simulation is stopped. During the transient all the phenomena outside the gap loop in Figure 14.1 are neglected, due to the fast dynamics of the transient itself; moreover, the additional set

---

[1]The duration of such a holding phase has not been found particularly impacting on the final results.

. . . .
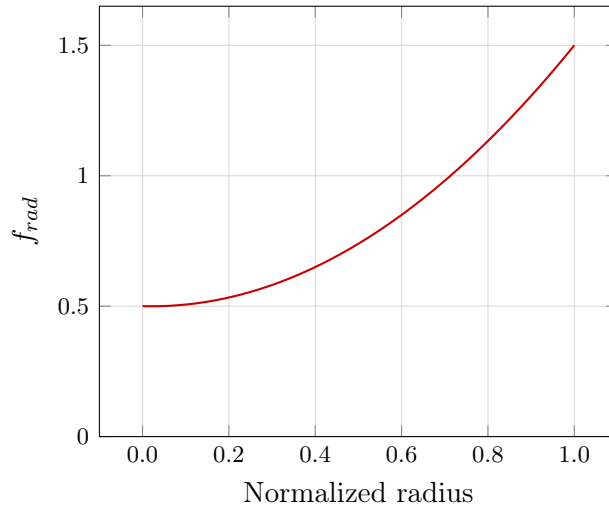
Figure A.2: Representation of the used pellet radial form factor, f_{rad}, due to the CABRI thermal spectrum as taken from [133].

of material properties, necessary in the transient simulations, is reported in Table A.3.

Table A.3: Additional material properties used in TEMIDE for the UTOP simulation of the E12 pin.

	Reference or value
Material Properties	
Fuel specific heat	[58]
Fuel melting temperature	3033 K
Clad specific heat	[10]
Clad yield strength	[122]

APPENDIX B

ACRONYMS

ADS   **A**ccelerator-**D**riven **S**ystem

ALFRED   **A**dvanced **L**ead-cooled **FR** **E**uropean **D**emonstrator

ANTEO   **AN**alisi **TE**rmoidraulica **O**ttimizzata

BoL   **B**eginning of **L**ife

BU   **B**urn-**U**p

CANDLE   **C**onstant **A**xial **N**eutron **D**uring the **L**ife of **E**nergy

CAS   **C**hinese **A**cademy of **S**ciences

CDA   **C**ore **D**isruptive **A**ccident

CDF   **C**umulative **D**amage **F**unction

CFD   **C**omputational **F**luid **D**ynamic

CLEAR   **C**hina **LEA**d-based **R**eactor

CT   **C**heng and **T**odreas

CTm   **C**heng and **T**odreas for **m**ixing

COP21   21th **C**onference **O**f the **P**arties

DFR   **D**ounreay **F**ast **R**eactor

....

DHR   **D**ecay **H**eat **R**emoval

DOC   **D**esign-**O**riented **C**ode

DPA   **D**isplacement **P**er **A**tom

EBR   **E**xperimental fast **B**reeder **R**eactor

EFIT   **E**uropean **F**acility for **I**ndustrial **T**ransmutation

ELSY   **E**uropean **L**ead-Cooled **SY**stem

EoL   **E**nd of **L**ife

ETR   **E**ngineering **T**est **R**eactor

EU   **E**uropean **U**nion

FALCON   **F**ostering **AL**FRED **CON**struction

FCCI   **F**uel-**C**lad **C**hemical **I**nteractions

FCMI   **F**uel **C**lad **M**echanical **I**nteraction

FEM   **F**inite **E**lements **M**ethods

FR   **F**ast **R**eactor

GFR   **G**as-cooled **FR**

GIF   **G**eneration IV **I**nternational **F**orum

HLM   **H**eavy **LM**

HYPER   **HY**brid **P**ower **E**xtraction **R**eactor

IAEA   **I**nternational **A**tomic **E**nergy **A**gency

ICE   **I**ntegral **C**irculation **E**xperiment

INEST   **I**nstitute of **N**uclear **E**nergy **S**afety **T**echnology

IPPE   **I**nstitute of **P**hysics and **P**ower **E**ngineering

JOG   **J**oint **O**xide **G**ain

KALLA   **KA**rlsruhe **L**iquid metal **LA**boratory

LFR   **L**ead-cooled **FR**

LEADER   **L**ead-Cooled **E**uropean **A**dvanced **DE**monstrator **R**eactor

LM   **L**iquid **M**etal

....

MA   **M**inor **A**ctinide

MHX   **M**ain **H**eat e**X**changer

MSFR   **M**olten **S**alt **FR**

MSR   **M**olten **S**alt **R**eactor

MYRRHA   **M**ulti-purpose H**Y**brid **R**esearch **R**eactor for **H**igh-tech
  Applications

N   **N**eutronics

NEA   **N**uclear **E**nergy **A**gency

OECD   **O**rganisation for **E**conomic **C**o-operation and **D**evelopment

P&P   **P**aper and **P**encil

PBWFR   **P**b–Bi-cooled direct-contact **B**oiling **W**ater **FR**

PEACER   **P**roliferation-resistant **E**nvironment-friendly **A**ccident-tolerant
  Continuable-energy **E**conomical **R**eactor

PFR   **P**rototype **FR**

PR&PP   **P**roliferation **R**esistance and **P**hysical **P**rotection

R&D   **R**esearch and **D**evelopment

SC   **S**ub-**C**hannel

SCWR   **S**uper**C**ritical **W**ater-cooled **R**eactor

SFR   **S**odium-cooled **FR**

SEALER   **S**w**E**dish **A**dvanced **LE**ad **R**eactor

SEARCH   **S**afe **E**xploit**A**tion **R**elated **C**hemistry for **H**LM

SGTR   **S**team **G**enerator **T**ube **R**upture

SSTAR   **S**mall **S**ecure **T**ransportable **A**utonomous **R**eactor

TEMIDE   **TE**ermo-**M**eccanica **I**mprontata al **DE**sign

TH   **T**hermal-**H**ydraulics

TM   **T**hermo-**M**echanics

ULOF   **U**nprotected **L**oss **O**f **F**low

. . . .

UTOP   Unprotected Transient of Over-Power

VHTR   Very High Temperature Reactor

VOC   Verification-Oriented Code

V&V   Verification and Validation

WARD   Westinghouse Advanced Reactors Division

WENRA   Western European Nuclear Regulators Association

. . . .

BIBLIOGRAPHY

[1] D. A. Afremov, V. P. Smirnov, and D. A. Yashnikov. Calculations using brs-tvs.r code as part of a standard problem "hydraulics and heat exchange in model rod assemblies with liquid-metal cooling", are including uncertainty analysis. In *Hydrodynamics and heat transfer in reactor components cooled by liquid metal coolants in single/two-phase*, pages 173–196. IAEA, 2004. 111

[2] International Energy Agency. Key world energy statistics. Technical report, IEA, 2016. 1

[3] F. Agosti et al. Extension of the TRANSURANUS code to the analysis of cladding materials for liquid metal cooled fast reactors: a preliminary approach. Technical Report CeSNEF-IN-02-2013, PoliMi, 2013. 251

[4] E. A. Aitken. Thermal diffusion in closed oxide fuel systems. *Journal of Nuclear Materials*, 30:62–73, 1969. xxv, 275, 276

[5] C. Albertini et al. Advances in the hopkinson bar testing of irradiated/non-irradiated nuclear materials and large specimens. *Philosofical Transaction of the Royal Society A*, 372, April 2014. xxv, 235

[6] ANL. Properties for LMFBR safet analysis. Technical Report ANL-CEN-RSD-76-1, ANL, 1979. 302

[7] ANL. The SAS4A/SASSYS-1 safety analysis code system - Chapter 8: DEFORM-4 steadu-state and transient pre-failure pin bahavior.

. . . .

Technical Report ANL/NE-12/4, ANL, January 2012. 239, 258, 267, 302

[8] C. Artioli et al. Elsy neutronic analysis by determinustuc and monte carlo methods: an innovative concepts for the control rod systems. In *Proceedings of 2009 International Congress on Andvances in Nuclear Power Plants (ICAPP,2009)*, Tokyo, Japan, May 10-14 2009. 23, 84

[9] G. Bandini and M. Polidori. Report of the results of the analysis of DEC events for the ETDR (ALFRED). Technical Report DEL022-2013, ENEA, 2013. xxii, 158, 159, 163, 205

[10] A. Banerjee et al. High temperature heat capacity of alloy D9 using drop calorimetry based enthalpy increment measurements. *International Journal of Themophysics*, 28:97–108, 2007. 306

[11] M. Bboer et al. Plutonium redistribution in fast reactor mixed oxide fuel pins. *Journal of Nuclear Materials*, 47:187–197, 1973. xxv, 277

[12] C.R. Beyer et al. GAPCON-THERMAL 2: a computer progrma for calculating the thermal behavior of an oxide fuel rod. Technical Report BNWL-1898, BNWL, 1975. 240

[13] Gromov B.F. et al. Designing the reactor installation with lead-bismuth coolant for nuclear submarines. the brief history summarized: Operation results. In *Proceedings of the Conference Heavy Liquid Metal Coolants in Nuclear Technology*, Obninsk, Russia, October 5-9 1998. 20

[14] P. R. H. Blasius. Das aehnlichkeitsgesetz bei reibungsvorgangen in flussigk eiten. *Forschungsheft*, 131:1–41, 1913. 64

[15] G. P. Bogoslovskaya, A. V. Zhukov, and A. P. Sorokin. Models and characteristics of interchannel exchange in pin bundles cooled by liquid metal. Technical Report TECDOC 1157, IAEA, Vienna, 2000. 74

[16] S. Bortot et al. BELLA: a multi-point dynamics code for safety-informed design of fast reactors. *Annals of Nuclear Energy*, 85:228–235, 2015. 46, 160

[17] J.C. Cabrillat et al. The CABRI facility: Implementation of a pressurized water loop and related safety review. Technical Report INIS-XA-C–030, IAEA, 2003. 286

. . . .

[18] J. Carlsson and H. Wider. Results of calculations of the standard problem "hydrodynamics and heat transfer in a subassembly model cooled by liquid metal coolant". In *Hydrodynamics and heat transfer in reactor components cooled by liquid metal coolants in single/two-phase*, pages 203–217, Obninsk, Russia, 2004. IAEA. xxi, 111, 112

[19] S. Cevolani. ANTEO : an optimised pc computer code for the steady state thermal hydraulic analysis of rod bundles. Technical Report RT/ERG/96/1, ENEA, 1996. 53

[20] L.K. Chang. A study of the life-i code. Technical Report ANL/EBR-064, ANL, 1973. xxix, 202, 302

[21] J. Charpenel et al. Fuel pin behavior under the slow power ramp transients in the CABRI-2 experiments. *Nuclear Technology*, 130:252–271, 2000. 202, 278, 281, 283, 286, 289, 301, 304

[22] S. K. Chen, N. E. Todreas, and N. T. Nguyen. Evaluation of existing correlations for the prediction of pressure drop in wire-wrapped hexagonal array pin bundles. *Nuclear Engineering and Design*, 267:109–131, 2014. 64, 66, 91

[23] S. K. Cheng. *Constitutive Correlations for wire-wrapped subchannel analysis under forced and mixed convection conditions*. PhD thesis, MIT, 9 1984. 60, 77, 87, 88, 89, 102, 129

[24] S. K. Cheng and N. E. Todreas. Hydrodynamic models and correlations for bare and wire-wrapped hexagonal rod bundles - bundle friction factors, subchannel friction factors and mixing parameters. *Nuclear Engineering and Design*, 92:227–251, 1986. 65, 66, 75, 90

[25] K. W. T. Chiu. *Fluid mixing studies in a hexagonal 37-pin, wire wrap rod bundle*. PhD thesis, MIT, 1977. 89

[26] M. H. Chun and K. W. Seo. An experimental study and assessment of existing friction factor correlations for wire-wrapped fuel assemblies. *Annals of Nuclear Energy*, 28:1683–1695, 2001. 66

[27] M. Cigarini and M. Dalle Donne. Thermohydraulic optimization of homogeneous and heterogeneous advanced pressurized reactors. *Nuclear Technology*, 80:107–132, 1988. 69

. . . .

[28] L. Cinotti et al. *Nuclear Engineering Handbook - Chapter 23: Lead-Cooled Fast Reactor (LFR) Design: Safety, Neutronics, Thermal-Hydraulics, Structural Mechanics, Fuel, Core, and Plant Design*, volume 4. Springer Science+Business Media, 2010. 21, 163

[29] C.F. Clement. Analytic solutions to mass transport equations for cylindrical nuclear fuel elements. *Journal of Nuclear Materials*, 68:54–62, 1977. xxv, 171, 172, 277, 278

[30] European Commission. Paris Agreement: Climate Action. http://ec.europa.eu/clima/policies/international/negotiations/paris_en, 2015. 1

[31] M. A. Connor and A.D. Carr. Heat transfer in vertical tubes under conditions of mixed free and forced convection. In *Proceeding of the 6th International Heat Transfer Conference*, Toronto, Canda, August 7 - 1 1978. 95

[32] EC/JRC. *TRANSURANUS handbook*. EC/JRC - V1M1J14, 2014. xxiii, 161, 192, 236, 266

[33] F. C. Engel et al. Characterization of heat transfer and temperature distributions in an electrically heated model of an lmfbr blanket assebmly. *Nuclear Engineering and Design*, 62:335–347, 1980. 96, 100, 138

[34] A. Epiney, K. Mikityuk, and R. Chawla. Trace qualification via analysis of the eir gas-loop experiments with smooth rods. *Annals of Nuclear Energy*, 37:875–887, 2010. 91

[35] M .H. Fontana et al. Temperature distribution in a 19-rod simulated lmfbr fuel assembly in a hexagonal duct (fuel failure mockup bundle 2a) - record of experimental data. Technical Report TM-4113, ORNL, 1973. 95, 96

[36] N. Forgione. Coupling between thermal system and cfd codes to support lfr. Presented at the 2nd ESNII+ Workshop, May 2016, Pisa. xix, 55

[37] J. W. Fricano. *Integrated fuel performance and thermal-hydraulic sub-channel models for analsis of sodium fast reactors*. PhD thesis, MIT, 2 2012. 87, 95, 98

[38] Y. Fukano et al. Fuel pin behavior up to cladding failure under pulse-type transient overpower in the CABRI-FAST and CABRI-RAFT experiments. *Journal of Nuclear Science and Technology*, 47:396–410, 2010. 263

[39] N. Garcia-Herranz et al. Impact of nuclear data uncertainties on the reactivity coefficients of ALFRED. In *Proceeding of the 3th International Conference on Fast Reactors and Related Fuel Cycles*, Yekaterinburg, Russia, June 26 - 29 2017. Accepted. 46

[40] K. J. Geelhood and W. G. Luscher. FRAPCON-3.5: A computer code for the calculation of steady-state, thermal-mechanical behavior of oxide fuel rods for high burnup. Technical Report NUREG/CR-7022, NRC, 2014. 161

[41] GIF. Generation iv International Forum. https://www.gen-4.org/gif/jcms/c_9260/public, 2017. xix, 7, 10, 11

[42] J. H. Gittus et al. Theoretical analysis of cladding stresses and strains produced by expansions of cracked fuel pellets. *Nuclear Applications and Technology*, 9:40–46, July 1970. xxv, 238

[43] O. Gotzmann. A thermodynamic model for the attack behaviour in stainless steel clad oxide fuel pins. *Journal of Nuclear Materials*, 84:39–54, September 1979. 251

[44] G. Grasso. *Neutronics Analyses for Fast Spectrum Nuclear Systems and Scenario Studies for Advanced Nuclear Fuel Cycles*. PhD thesis, UniBo, 3 2011. 26, 28, 34

[45] G. Grasso et al. The core design of ALFRED, a demonstrator for the european lead-cooled reactors. *Nuclear Engineering and Design*, 278:287–301, 2014. 23, 163

[46] T.E. Greene. *Development and evaluation of techniques for thermal-hydraulic analsis of LMFBR fuel assemblies*. PhD thesis, MIT, 7 1980. 131, 136

[47] Y. Guerin. *Comprehensive Nuclear Materials - Chapter: Fuel performance of fast spectrum oxide fuel*, volume 2. Elsevier, 2012. xxiii, xxv, 173, 188, 253, 254, 265

[48] J.D. Hales et al. BISON theory manual: the eqautions behind nuclear fuel analysis. Technical Report INL/EXT-13-29930, INL, 2014. 237

. . . .

[49] IAEA. Lmfr core and heat exchanger thermohydraulic design: Former ussr and present russian approaches. Technical Report TECDOC 1060, IAEA, Vienna, 1999. 77

[50] IAEA. Benchmark analyses on the natural circulation test performed during the PHENIX end-of-life experiments. Technical Report TECDOC-1703, IAEA, 2013. 282, 284

[51] V. Iannello, K.Y. Suh, and N.E. Todreas. Mixed convection friction factors and nusselt numbers in vertical annular and subchannel geometries. *International Journal of Heat and Mass Transfer*, 31:2175–2189, 1988. 128, 134

[52] M. Inoue et al. Fuel-to-cladding gap evolution and its impact on thermal performance of high burnup fast reactor type uranium–plutonium oxide fuel pins. *Journal of Nuclear Materials*, 326:59–73, 2004. 259, 263, 279

[53] T. Ishii and T. Asaga. An investigation of the Pu migration phenomena during irradiation in fast reactor. *Journal of Nuclear Materials*, 294:13–17, 2001. 302

[54] V.Z. Jankus and R.W. Weeks. LIFE-II: a computer analysis of fast reactor fuel-element behavior as a function of reactor operating history. *Nuclear Engineering and Design*, 18:83–96, 1972. 238

[55] A. Karahan. *Modeling of thermo-mechanical and irradiation behavior of metallic and fuels for sodium fast reactors*. PhD thesis, MIT, 6 2009. 190, 199, 263

[56] H. Kawamura et al. Dns of turbulent heat transfer in channel low with low to medium-high prandtl number fluid. *Int. J. of Heat and Fluid Flow*, 19:482–491, 1998. 83

[57] S. Kim and B. J. Chung. A scale analysis of the turbulent mixing rate for various prandtl number flow fields in rod bundles. *Nuclear Engineering and Design*, 205:281–294, 2001. 72

[58] O. L. Kruger and H. Savage. Heat capacity and thermodynamic properties of plutonium dioxide. 49(10):4540–4544, 1968. 306

[59] W. J. Lackey et al. Porosity and actinide redistribution during irradiation of (U, Pu)O$_2$. *Nuclear Technology*, 16:120–142, 1972. xxvi, xxx, 175, 253, 254, 260, 278, 279, 280, 281

. . . .

[60] D. E. Lamkin. *Analytical stress analysis solution for a simplified model of a reactor fuel element.* PhD thesis, University of Arizona, 1974. xxv, 244, 273, 274

[61] K. Lassmann. The OXIRED model for redistribution of oxygen in nonstoichiometric uranium-plutonium oxides. *Journal of Nuclear Materials*, 150:10–16, 1987. 254, 275, 302

[62] K. Lassmann and H. Blank. Modelling of fuel rod behavior and recent advances of the TRANSURANUS code. *Nuclear Engineering and Design*, 106:291–313, 1988. 161, 197, 238, 240, 244

[63] K. Lassmann and F. Hohlefeld. The revised URGAP model to describe the gap conductance between the fuel and cladding. *Nuclear Engineering and Design*, 103:215–221, 1987. 178, 179, 186, 302

[64] A. L. Lindsay and L.A. Bromley. Thermal conductivity of gas mixtures. *Industrial and Engineering Chemestry*, 42:1508–1511, 1950. 302

[65] K. Litfin et al. Investigation on heavy liquid metal cooling of ads fuel pin assemblies. *Journal of Nuclear Materials*, 415:425–432, 2011. xx, xxvii, 91, 93, 94

[66] F. Lodi. Anteo+ developer manual. Private Document. 53

[67] F. Lodi. Anteo+ user manual. Private Document. 53

[68] F. Lodi et al. ANTEO+: a subchannel code for thermal-hydraulic analysis of liquid metal coolant systems. *Nuclear Engineering and Design*, 301:128–152, May 2016. 53, 55, 62, 95

[69] F. Lodi et al. Evaluation of data and model uncertainties and their effect on the fuel assembly temperature field of the ALFRED lead-cooled fast reactor. In *Proceeding of the 3th International Conference on Fast Reactors and Related Fuel Cycles*, Yekaterinburg, Russia, June 26 - 29 2017. Accepted. 124

[70] L. Luzzi et al. Application of the TRANSURANUS code for the fuel pin design process of the ALFRED reactor. *Nuclear Engineering and Design*, 277:173–187, 2014. 197, 240, 288, 304

[71] K. Lyu et al. Preliminary thermal-hydraulic sub-channel analysis of 61 wire-wrapped bundle cooled by lead bismuth eutectic. *Annals of Nuclear Energy*, 92:243–250, 2016. 96, 114, 117, 138

. . . .

[72] Z. Ma et al. An innovative method for prediction of liquid metal heat transfer rate for rod bundles based on annuli. *Annals of Nuclear Energy*, 47:91–97, 2012. 77

[73] K. Maeda and T. Asaga. Change of fuel-to-cladding gap width with the burn-up in FBR MOX fuel irradiated to high burn-up. *Journal of Nuclear Materials*, 327:1–10, 2004. 189, 263

[74] D. Martelli et al. HLM fuel pin bundle experiments in the CIRCE pool facility. *Nuclear Engineering and Design*, 292:76–86, 2015. 117, 121, 138

[75] D. G. Martin. The thermal expansion of solid UO_2 and (U,Pu) mixed oxides - a review and recommendations. *Journal of Nuclear Materials*, 152:94–101, 1988. 302

[76] D. Mattioli and S. Cevolani. Anteo-lfr: a pc code for thermal-hydraulic optimized core analysis in a lead fast reactor. Technical Report UTFISSM-P000-007 Rev. 0, ENEA, 2012. 65

[77] J. C. Melis et al. Fuel modeling at high burn-up: recent development of the GERMINAL code. *Journal of Nuclear Materials*, 204:188–193, 1993. 263, 264

[78] A. Mendelson. *Plasticity: theory and application*. Krieger Pub Co, 1983. 234, 235

[79] K. Mikityuk. Heat transfer to liquid metal: Review of data and correlations for tube bundles. *Nuclear Engineering and Design*, 234:680–687, 2009. 77

[80] G.K. Miller. New mechanical model for the transmuation fuel performance code. Technical Report INL/EXT-08-14111, INL, 2008. xxv, 242, 275, 276

[81] K. Miyaguchi. Analysis of the how and temperature fields in locally blocked lmfbr fuel subassemblies. In *THERMODYNAMICS OF FBR FUEL SUBASSEMBLIES UNDER NOMINAL AND NON-NOMINAL OPERATING CONDITIONS*. IWGFR/29, 1979. 89

[82] C.L. Mohr et al. GAPCON-3 a computer code to analyze the path-dependent thermal and mechanical performance of nuclear fuel rods. Technical Report BNWL-SA-5962, 1976. xxiii, 166, 302

. . . .

[83] R. H. Morris et al. Single phase sodium test in 61-pin full-length simulated LMFBR assembly - record of phase 1 experimental data for THOR bundle 9. Technical Report TM-7313, ORNL, 1980. 96, 99, 138

[84] F. Namekawa, A. Ito, and K. Mawatari. Bouyancy effects on wire-wrapped rod bundle heat transfer in an lmfbr fuel assembly. In *AlChE Symposium Series*, pages 128–133, Niagra Falls, 1984. 96, 97

[85] F. A. Nichols. Theory of columnar grain growth and central void formation in oxide fuel rods. *Journal of Nuclear Materials*, 22:214–222, 1967. 279

[86] R. Nijsing and W. Eifler. A computation methid for the steady state thermohydraulic analysis of fuel rod budles with single pahse cooling. *Nuclear Engineering and Design*, 30:145–185, 1974. 73

[87] V. Di Marcello et al. Extension of the TRANSURANUS plutonium redistribution model for fast reactor performance analysis. *Nuclear Engineering and Design*, 248:149–155, 2012. 172, 257, 277

[88] V. Di Marcello et al. Modeling actinide redistribution in mixed oxide fuel for sodium fast reactor. *Progress in Nuclear Energy*, 72:83–90, 2014. 171, 172

[89] V. Di Marcello et al. The transuranus mechanical model for large strains analysis. *Nuclear Engineering and Design*, 276:19–29, September 2014. 236

[90] P. Van Uffelen and M. Suzuki. *Comprehensive Nuclear Materials - Chapter: Oxide fuel performance modeling and simulations*, volume 2. Elsevier, 2012. 161

[91] W. L. Oberkampf and T.G. Trucano. Verification and validation benchmarks. *Nuclear Engineering and Design*, 238:716–743, 2008. 269, 270

[92] OECD/NEA. *Handbook on Lead-Bismuth eutectic alloy and lead properties, materials compatibility, thermal-hydraulics and technologies*. OECD-AEN/NEA Report No. 6195, 2007. 83

[93] OECD/NEA. *Handbook on Lead-Bismuth eutectic alloy and lead properties, materials compatibility, thermal-hydraulics and technologies*. OECD-AEN/NEA Report No. 7268, 2015. 55

. . . .

[94] University of Tennessee and The University of Tennessee Research Foundation. LAPACK - Linear Algebra PACKage. http://www.netlib.org/lapack/, 2017. 231

[95] H. Ohshima and Y. Imai. Thermal hydraulic analysis of model pin bundle with liquid metal coolant - simulation results of standard problem. In *Hydrodynamics and heat transfer in reactor components cooled by liquid metal coolants in single/two-phase*, pages 188–202, Obninsk, Russia, 2004. IAEA. 111

[96] D.R. Olander. *Foundamentals aspects of nuclear reactor fuel elements.* National Technical Information Center, 1976. xxiii, 175, 177, 190, 199, 238, 249, 251, 254, 260, 279, 302

[97] J.P. Ottaviani et al. State of the art with a literature review of MOX fuel properties. Technical Report D7.11, WP7 Fuel Safety, ESNII Plus, CEA, 2015. 200, 237, 249, 256, 302

[98] T. Ozawa and T. Abe. Development and verifications of fast reactor fule design code CEPTAR. *Nuclear Technology*, 156:39–55, 2006. 161, 188, 189, 209, 243, 263, 264, 302

[99] J. Pacio et al. Heavy-liquid metal heat transfer experiment in a 19-rod bundle with grid spacers. *Nuclear Engineering and Design*, 273:33–46, 2014. 78

[100] J. Pacio et al. Thermal-hydraulic study of the LBE-cooled fuel assembly in the MYRRHA reactor: Experiments and simulations. *Nuclear Engineering and Design*, 2016. In Press. 96, 113, 117

[101] G. Palmiotti and M. Salvatores. Developments in sensitivity methodologies and the validation of reactor physics calculations. *Science and Technology of Nuclear Installations*, 2012(Article ID 529623):1–14, 2012. 217

[102] G. Pastore. *Modeling of fission gas swelling and release in oxide nuclear fuel and application to the TRANSURANUS code.* PhD thesis, PoliMi, 3 2012. 199

[103] G. Pastore et al. Uncertainty and sensitivity analysis of fission gas behavior in engineering-scale fuel modeling. *Journal of Nuclear Materials*, 456:398–408, 2015. 239

. . . .

[104] A. Pena and G. Esteban. Benchmark problem: hydraulics and heat transfer in the model pin bundles with liquid metal coolant upv-ehu calculations. In *Hydrodynamics and heat transfer in reactor components cooled by liquid metal coolants in single/two-phase*, pages 238–250, Obninsk, Russia, 2004. IAEA. 111

[105] Y. Philipponneau. Thermal conductivity of $(U,Pu)O_{2-x}$ mixed oxide fuel. *Journal of Nuclear Materials*, 232:166–180, 1996. 202, 256, 279, 302

[106] S. Pramuditya and M. Takahashi. Thermal-hydraulic analysis of wire-wrapped sfr test subassemblies by subchannel analysis method. *Annals of Nuclear Energy*, 54:109–119, 2013. 71, 110

[107] P. Puthiyavinayagam. Lectures on fast reactor core design - module 4:mechanical design. Technical Report ICTP/2055-10, ICTP, 2009. xxv, 248

[108] B. Rameau and B. Menant. Sodium thermal hydraulics under natural and mixed convection in bundle geometry. In *Proceedings of the ASME winter annual meeting*, New Orleans, 1984. 96, 107

[109] Y.R. Rashid et al. Mathematical treatment of hot pressing of reactor fuel. *Nuclear Engineering and Design*, 29:1–6, 1974. 237

[110] K. Rehme. Pressure drop correlations for fuel element spacers. *Nuclear Technology*, 17:15–23, 1973. 66

[111] K. Rehme. Simple method of predicting friction factors of turbolent flow in non-circular channels. *Int. J. of Heat and Mass Transfer*, 16:933–950, 1973. 64, 65

[112] K. Rehme and G. Trippe. Pressure drop and velocity distribution in rod bundles with spacer grid. *Nuclear Engineering and Design*, 62:349–359, 1980. 64, 65, 89

[113] G. Rimpault et al. The eranos code and data system for fast reactor neutronic analyses. In *Proceeding of the Int. Conf. New Frontiers of Nuclear Technology: reactor physics, safety and high-performance computing (PHYSOR 2002)*, Seoul, Korea, October 7 - 10 1983. 46

[114] T. S. Ro and N. E. Todreas. Energy transfer mechanisms in lmr rod bundles under mixed convection conditions. *Nuclear Engineering and Design*, 108:343–357, 1988. 135

. . . .

[115] M. Sarotto et al. The MYRRHA-FASTEF cores design for critical and sub-critical operational modes (EU FP7 central design team project). *Nuclear Engineering and Design*, 265:184–200, 2013. 113, 182

[116] M. Sarotto and G. Grasso. Results of the validation campaign of neutronic codes and reccomandations for the correct application to LFR systems. Technical Report ADPFISS - LP2 - 115, ENEA, 2015. 46

[117] M. Schikorr et al. Proposal for pressure drop prediction for a fuel bundle with grid spacers using rehme pressure drop correlations. *Nuclear Engineering and Design*, 240:1830–1842, 2010. 91

[118] L.J. Siefken et al. MATPRO - a library of materials properties for light-water-reactor accident analysis. Technical Report NUREG/CR-6150,Vol.4,Rev.2, NRC, 2001. 179, 240

[119] C. A. Sleicher and M. W. Rouse. A convenient correlation for heat transfer to constant and variable property fluids in turbolent pipe flow. *Int. J. of Heat and Mass Transfer*, 18:677–683, 1975. 83

[120] C. F. Smith et al. SSTAR: The US lead-cooled fast reactor (LFR). *Journal of Nuclear Materials*, 376:255–259, 2008. 23, 127

[121] V. Sobolev. Preliminary design variants for fuel rod, assembly and core of ELSY-600. Technical Report DEL/07/05, ANS/826/07-15, Rev. 1, ELSY project, SCK-CEN, 2007. 195, 206

[122] V. Sobolev. Database of thermophysical properties of liquid metal coolants for gen-iv. Technical Report BLG-1069, SCK-CEN, 2011. 288, 304, 306

[123] H. Son and K. Suh. Result of calculations of the standard problem hydraulics and heat transfer in a subassembly model cooled by liquid metal coolant. In *Hydrodynamics and heat transfer in reactor components cooled by liquid metal coolants in single/two-phase*, pages 218–237, Obninsk, Russia, 2004. IAEA. xxi, 111, 112

[124] A. P. Sorokin et al. Methods and codes for modeling thermalhydraulics of fast reactor core subassemblies under nominal and non-nominal operating conditions. Technical Report TECHDOC-1157, IAEA, Vienna, 2000. 55

[125] J. Standring et al. Microstructural instability and thermal creep in 20% CW m316 tubing. Brighton, UK, April 11 - 13 1983. 302

. . . .

[126] K.Y. Suh, N.E. Todreas, and W.M. Rohsenow. Mixed convective low flow pressure drop in vertical rod assemblies- i. predictive model and design correlation. *Journal of Heat Transfer*, 111:956–965, 1989. 128, 132

[127] K.Y. Suh, N.E. Todreas, and W.M. Rohsenow. Mixed convective low flow pressure drop in vertical rod assemblies- ii. experimental validation. *Journal of Heat Transfer*, 111:966–973, 1989. 128

[128] Dassault Systemes. Abaqus unified FEA. `https://www.3ds.com/products-services/simulia/products/abaqus/latest-release/`, 2017. 275

[129] Y. Tobita et al. Safety strategy of jsfr tocore disruptive accident establish the in-vessel retention of the. In *FAST REACTOR AND RELATED FUEL CYCLES: Safe Technologies and Sustainable Scenarios FR13*. IAEA, 3 2013. 84

[130] N.E. Todreas and M.S Kazimi. *Nuclear Systems*, volume 2. Taylor and Francis, 2001. 57

[131] A. Toti. Development and validation of system-code/cfd coupling for multi-scale thermal hydraulic analyses. Presented at the 2nd ESNII+ Workshop, May 2016, Pisa. xix, 55

[132] M. Tourasse et al. Fission product behavior in Phenix fule pins at high burnup. *Journal of Nuclear Materials*, 188:49–57, 1992. 189, 191, 202

[133] Y. Tsuboi et al. Analysis of fuel pin behavior under slow-ramp type transient overpower condition by using the fuel performance evaluation code 'FEMAXI-FBR'. *Journal of Nuclear Science and Technology*, 49:408–424, 2012. xxvi, 161, 260, 262, 287, 304, 305

[134] S. Ukai et al. Evaluation of the fission gas release behavior from fast reactor mixed oxide fuel based on local concentration measurement of retained Xenon. *Journal of Nuclear Materials*, 151:209–218, 1988. 202, 262, 302

[135] C. Unal et al. Application of advanced validation concepts to oxide fuel performance codes: LIFE-4 fast-reactor and FRAPCON thermal-reactor fuel performance codes. *Nuclear Engineering and Design*, 263:102–128, February 2013. 165

[136] T. Uwab and S. Ukai. Uncertainty and sensitivity analysis of fission gas behavior in engineering-scale fuel modeling. *Nuclear Engineering and Design*, 234:51–59, 2004. 247

[137] J. H. VanSant. Conduction heat transfer solution. Technical Report UCRL-52863, LLNL, 1980. 271

[138] R. Viswanathan. Fuel clad chemical interactions in fast reactor MOX fuel. *Journal of Nuclear Materials*, 444:101–111, 2014. 252, 302

[139] A. E. Waltar, D. R. Tood, and P. V. Tsvetkov. *Fast Spectrum Reactors*. Springer, 2013. 33, 73, 209, 230, 231, 248, 262, 271, 302

[140] A. Weisenburger. Compilation of existing data on the liquid lead oxygen control strategy. Technical Report LEADER-DEL-12.WP6, KIT, 2013. 251

[141] C. L. Wheeler. Cobra-IV-I: An interim version of cobra for thermal-hydraulic analysis of rod bundle fuel elements and cores. Technical Report BNWL-1962, Battel-Pacific Northwest Laboratories, Richland, Washington, 1976. 61

[142] X. Wu and A. C. Trupp. Spectral measurements and mixing correlation in simulated rod bundle. *Int. J. of Heat and Mass Transfer*, 37:1277–1281, 1994. 72

[143] Wu Y. Design and R&D progress of China LEA-based Reactor for ADS research facility. *Engineering*, 2:124–131, 2016. 24

[144] Yamashita et al. Thermal expansions of NpO_2 and some other actinide dioxides. *Journal of Nuclear Material*, 245:72–78, 1997. 302

[145] A. V. Zhukov et al. Specification of the benchmark problem "hydraulics and heat transfer in the model pin bundles with liquid metal coolant". In *Hydrodynamics and heat transfer in reactor components cooled by liquid metal coolants in single/two-phase*, pages 138–172, Obninsk, Russia, 2004. IAEA. 96, 111, 113, 117

[146] A. V. Zhukov, Y. A. Kuzina, and A. P. Sorokin. Analysis of a benchmark experiment on the hydraulics and heat transfer in a liquid-metal-cooled assembly of fuel element simulators. *Atomic Energy*, 99:770–781, 2005. 111, 112

. . . .